ENHANCING OXIDATION RESISTANCE OF Ni-BASED ALLOYS FOR HIGH TEMPERATURE APPLICATIONS

A Thesis Submitted to the College of

Graduate and Postdoctoral Studies

In Partial Fulfillment of the Requirements

For the Degree of Doctor of Philosophy

In the Department of Mechanical Engineering

University of Saskatchewan

By

Xu Wang

PERMISSION TO USE

In presenting this thesis in partial fulfilment of the requirements for a postgraduate degree from the University of Saskatchewan, I agree that the Libraries of this University may make it freely available for inspection. I further agree that permission for copying of this thesis in any manner, in whole or in part, for scholarly purpose may be granted by the professors who supervised my thesis work or, in their absence, by the Head of the Department or the Dean of the College in which my thesis work was done. It is understood that any copying or publication or use of this thesis or part thereof for financial gain shall not be allowed without my written permission. It is also understood that due recognition shall be given to me and to the University of Saskatchewan in any scholarly use which may be made of any material in my thesis.

Requests for permission to copy or to make other use of material in this thesis in whole or part should be addressed to:

Head of the Department of Mechanical Engineering

57 Campus Dr.

University of Saskatchewan

Saskatoon, Saskatchewan (S7N 5A9)

ABSTRACT

The demand for energy significantly increases with increasing of world population and industrial activity in developing countries. Nuclear energy can be considered to make an important contribution to future demands for electricity and thermal energy. In order to continue providing inexpensive and safe energy, the operation temperatures of the next generation nuclear reactors should be remarkably increased. Consequently, the alloys used in the high temperature environment will face oxidation degradation problems. Therefore, it is critical to find ways to improve the oxidation resistance of the alloys to be used for high temperature applications. In this thesis, two potential solutions are proposed to enhance the oxidation resistance of three Ni-based alloys.

The effect of crystallographic orientation on the oxidation behavior of Hastelloy 230 was investigated to evaluate if texture would affect the oxidation behavior of Ni-based alloys. The obtained results clearly demonstrate that the oxidation rate highly depends on the grain orientation. The oxidation resistance of grains are found to increase in the order of (100) < (110) < (111). The substrates with different grain sizes and similar textures were prepared to inspect the influence of grain sizes on the oxidation behavior of Hastelloy 230 and Hastelloy N. It is demonstrated that the grain size only has a small influence on the oxidation behavior of the high-Cr Hastelloy 230 while it significantly changes the oxidation behavior of the low-Cr Hastelloy N. The oxidation mechanisms of high and low-Cr alloys with coarse and fine grain sizes are discussed. Increasing of the grain boundary density of the low-Cr alloy is believed to promote the diffusivities of Cr ions which results in the formation of a uniform Cr-rich protective oxide layer. The grain refinement process can be an efficient way to enhance the oxidation resistance of investigated low-Cr alloy.

The effect of reactive element coating on oxidation behavior of chromium oxide forming alloy was examined. The parameters of electro-deposition process like the current density, deposition time and temperature were optimized to synthesize ceria coating. The coatings were applied to Hastelloy 230 and 625 to investigate the influence of this reactive element on the oxidation behavior. For both alloys, the coating significantly enhanced the oxidation resistance and adherence of the oxide to the substrate. The segregation of reactive element onto grain boundaries is linked to change of the oxidation mechanism from outward diffusion of cations to

inward diffusion of anions. Specifically for Hastelloy 230, the addition of ceria coating changed the chromium oxide morphology from columnar to equaxied structure and that is believed to enhance the spallation resistance. In Hastelloy 625, a porous and cracked oxide layer is observed on the uncoated sample, while a layer that is protective against oxidation is formed on the coated sample. The prepared coating suppressed the formation of iron oxide. The oxidation mechanism is suggested and discussed.

ACKNOWLEDGEMENT

I would love to sincerely appreciate my supervisor Prof. Jerzy Szpunar for his careful guidance and endless support in this whole project and writing of this thesis.

I also would like to thank my advisory committee members: Prof. Richard Evitts, Prof. Duncan Cree, Prof. Chris Zhang and Prof. Jim Bugg for their encouragements and worthy comments.

My thanks also go to Prof. Zhenghe Xu from University of Alberta and Dr. Frank Czerwinski from CanmetMATERIALS for their supports in the experimental parts.

Additionally, I appreciate the valuable discussions and helps of Dr. Fan Fan, Dr. Chunyu Zhou, Dr. Ming Song, Dr. Lina Zhang, Dr. Andy Hu, Dr. Ritwik Basu, A.A Tiamiyu and all the group members of Advanced Materials and Renewable Energy (AMRE).

Finally, I acknowledge the financial support from Canada Research Chair program and from China Scholarship Council (CSC).

Last but not least, I appreciate the patience and bottomless love of my parents, my sister and my wife Fan Zhang.

TABLE OF CONTENTS

LIST OF TABLES

LIST OF FIGURES

ACRONYMS

AFM	Atomic Force Microscope
BC	Band Contrast
CED	Cathodic Electrochemical Deposition
EBSD	Electron Backscattering Diffraction
EBPVD	Electron Beam Physical Vapour Deposition
EDA	Electrical Discharge Alloying
EDS	Energy Dispersive Spectroscopy
FCC	Face Centered Crystal
GFC	Gas-cooled Fast Reactor
HAGB	High Angle Grain Boundary
HGD	Hot Gas Duct
IHX	Intermediate Heat Exchanger
IPF	Inverse Pole Figure
KAM	Kernel Average Misorientation
MOCVD	Metal-organic Chemical Vapor Deposition
ND	Normal Direction
OM	Optical Microscope
RE	Reactive Element
REE	Rare Earth Effect
REE	Reactive Element Effect
RPV	Reactor Pressure Vessel
SCE	Saturated Calomel Electrode
SCW	Super-Critical Water
SEI	Secondary Electron Image
SPPS	Solution Precursor Plasma Spray
SEM	Scanning Electron Microscope
SOFC	Solid Oxide Fuel Cell
VHTR	Very High Temperature Reactor
XRD	X-ray Diffraction

Chapter 1 Introduction

1.1 Overview of Chapter 1

In this chapter, the motivation for research on this project is briefly discussed with emphasis on the importance of enhancing oxidation resistance of Ni-based alloys. The knowledge of high-temperature oxidation process is also presented here to facilitate understanding of the presented work. The previous work of enhancing the oxidation resistance of alloys is reviewed. The knowledge gaps are identified and the objectives of this project are proposed.

1.2 Motivations for research on improving oxidation resistance of Ni-based alloys

The need for energy is dramatically increasing with the increase of the population in the world. Therefore, it is critical to supply sustainable, safe and high-efficiency energy to satisfy the future demands. It was reported that the concept of next generation nuclear reactors is promising to furnish effective and continuous sources of energy [1]. To improve the efficiency of the nuclear systems, the operating temperatures should be significantly increased. For instance, the very high temperature reactor (VHTR) is supposed to be operated at 900 to 1000 ℃ for at least 60 years [1]. Consequently, the structural materials used in the reactors, that are expected to be Ni-based alloys, will face high-temperature degradation problems like high-temperature oxidation. The oxidation of the structural materials in the high-temperature service environment can significantly damage their surfaces and shorten their service times. Hence, it is critical to find solutions to enhance the oxidation resistance of these alloys.

1.3 Literature review

1.3.1 High-temperature oxidation

Investigations on the oxidation kinetics and oxidation mechanisms are of interest for researchers working on Ni-based alloys. However, the oxidation processes in these alloys are very complex owing to many factors. For instance, different elements in the alloys have different oxygen affinities which depend on the Gibbs free energies for forming the oxides. Consequently, several types of oxides can form at different times during the oxidation process. It is also possible that the oxidation reactions occur within the formed oxides and that result in the formation of new oxides. Further, different elements can have different diffusion coefficients when diffusing through the oxide layers or in the substrate. Subsequently, oxidation process might have several different oxidation stages and is often decided by the dominant diffusion element. Therefore, the oxidation mechanism of the alloy is simplified to consider the oxidation of different metals that are components of the alloys.

Generally, reaction 1.1 is used to describe the oxidation of a metal.

$$M(s) + \frac{1}{2}O_2(g) = MO(s) \qquad 1.1$$

Initially, the chemisorptions and ionization of the adsorbed oxygen on the metal surface will facilitate the reaction process in the high temperature atmosphere. The *MO* will consequently form as a reaction product which disconnects the substrate from the oxidizing environment as shown in the schematic diagram of Fig. 1.1 (a). Therefore, the element of *M* or *O* or both of them have to diffuse through the solid *MO* layer and react with each other in the oxidation process. Consequently, the element dominating the diffusion process will control the oxidation process and the oxidation rate. Fig. 1.1 (b) and (c) depict the schematic diagrams that present the mechanism of oxidation process with different dominant diffusion element. In the case of the dominating outward diffusion of *M*, the cation and electron will diffuse to the scale/gas interface where they can react with oxygen as shown in Fig. 1.1 (b). The *MO* will subsequently form as external oxide on the scale/gas interface. However, if the oxygen diffusion dominates, the *MO* will form as internal oxide on the alloy/scale which can be illustrated by Fig. 1.1 (c).

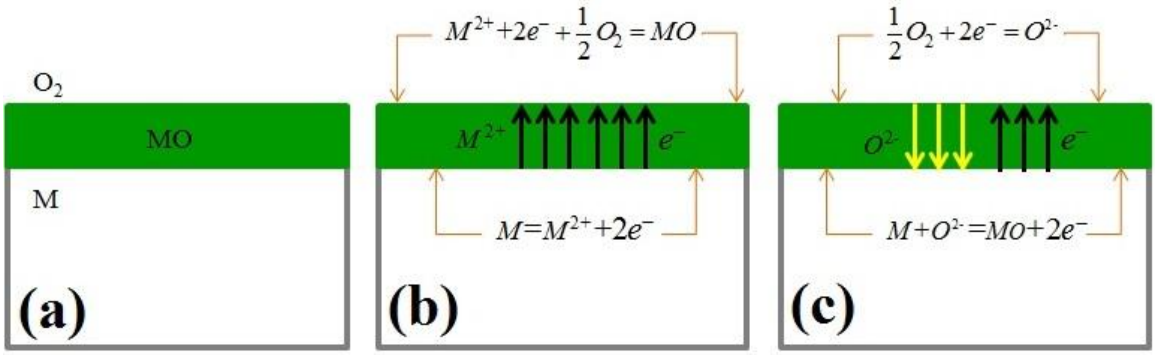

Fig. 1.1 Schematic diagrams of oxidation of metals

For alloys, diffusion of one or more elements can dominate the oxidation processes. However, the diffusion mechanisms discussed above can still be used where the diffusion of cations will result in the oxide forming on scale/gas interface and the diffusion of anions will trigger oxide formation on metal/scale interface.

1.3.2 Effect of grain size on oxidation behavior

Oxidation behavior of alloys with different grain sizes have been previously investigated [2–11]. The grain size, shape, boundary diffusion had a critical influence on the oxidation rates of metals like Fe, Cu and Zn [12]. It was reported that the oxidation resistance would be enhanced for small grain size since decreasing of grain size could decrease the critical amount of chromium needed for forming a protective oxide layer [13]. The grain refinement was demonstrated to enhance the adherence of the oxide layers because of the high grain boundary diffusion coefficient [11]. Furthermore, thermo-mechanical processing was used to produce substrates with different grain sizes and similar Σ3 grain boundary fractions for alloy 304 [14]. A pure Cr_2O_3 layer was observed on the sample with a grain size of 8.92 μm while a mixture Cr_2O_3 and Fe_2O_3 layer was found on larger grain size. The enhanced grain boundary diffusion of Cr was believed to promote the formation of a pure Cr_2O_3 layer which resulted in a higher oxidation resistance of refined grains in SS304 [14]. The grain size however changed the surface morphology and chemical composition of the oxide formed in alloy PM2000 but only a slight difference was found on the oxidation kinetics of coarse and fine-grained PM2000 [6]. Therefore, the effect of grain size on oxidation behavior of alloys is still uncertain and more investigations are required.

Additionally, samples with different grain sizes for investigating the oxidation behavior were mainly prepared through the traditional thermo-mechanical processing. During the rolling and heat treatment process, the microstructures and textures of the prepared samples with different grain sizes can be changed. However, the evolution of the texture with variation of the grain size was never considered in the previous works. It was reported that the micro-texture that refers to the crystallographic orientation of the substrate could have significant effects on various material properties such as deformation [15,16], hardness [17,18], creep [19], electrochemical activity [20], corrosion [21–27] and oxidation [28–39]. The previous works on the effect of grain orientation on the oxidation behavior of materials are summarized in Table 1.1. The first observation that the differently oriented crystal tended to have anisotropic rate of oxidation was suggested where the authors demonstrated that the colors of the oxidized copper were varying with the changing crystal planes [40]. It was also revealed that the oxidation reaction rates of large single crystal of copper were strikingly different for differently oriented crystal planes [41–43]. The attempt of determining the oxidation rate of several crystal planes of (100), (111), (110) and (311) at a temperature of 70 ℃, 106 ℃, 130 ℃, 159 ℃ and 178 ℃ were reported [44]. A polarizing spectrometer was used to measure the oxide thicknesses formed on those planes where it was concluded that the oxidation rate increased in the order of (311) < (110) < (111) < (100). The oxidation rate of (100) plane was 12.5 times higher than that of (311) plane. The effect of crystallographic orientation on oxidation behavior of single crystal of nickel was also discussed [45–50]. The authors measured the thicknesses of the NiO formed on single crystal of nickel oriented along (100), (111), (110), and (311) planes at a temperature of 400 ℃ to 600 ℃ [45]. They concluded that the anisotropy oxidation rate of Ni single crystal attributed to the contents and effectiveness of the short-circuit diffusion paths on various planes. Higher contribution of short circle path facilitated the oxidation process. It was finally summarized that the oxidation rate increased with the order of (311) < (111) < (001) < (110). Moreover, the oxidation resistance of the principle planes of (111), (100) and (110) of Ni single crystals was studied at a temperature of 500 ℃ to 800 ℃ for 100 h [46]. It was suggested that the oxidation rates not only depended on the crystal plane orientation but also was related to the temperature. For instance, the oxidation rate of single crystal Ni increased with the order of (111) < (110) < (100) at temperature of 500 ℃ to 600 ℃ but increased with the order of (110) < (111) < (100) at temperature of 700 ℃ to 800 ℃ [46]. Graham et.al compared the oxidation rate of

polycrystalline nickel with single crystal nickel of (100), (111) and (112) planes at a temperature of 600 ℃. It was demonstrated that the oxidation rate increased with the order of (112) < (111) < (Poly) < (001). Furthermore, the effect of microstructure, grain boundary distribution on the oxidation behavior of (100) and (111) Ni single crystals was studied [49,50]. The oxide formed on (100) plane always had higher grain boundary density than that on (111) crystal which acted as short-circuit diffusion paths that accelerated the oxidation velocity.

Table 1.1 Previous studies on effect of crystallographic orientation on oxidation

Metal	Environment	Rate	Ref.
Single crystal Cu	1000 ℃	(111) < (110) < (100)	[41]
	70 ℃/106 ℃/130 ℃/ 159 ℃/178 ℃	(311) < (011) < (111) < (001)	[44]
Single crystal Ni	400 ℃~600 ℃	(311) < (111) < (001) < (110)	[45]
Single crystal Ni	500 ℃/600 ℃	(111) < (110) < (001)	[46]
	700 ℃/800 ℃	(110) < (111) < (001)	
Single & Polycrystalline Ni	600 ℃	(112) < (111) < (Poly) < (001)	[47]
Single crystal Ni	500 ℃~800 ℃	(111) < (110)/(001)	[48]
Single crystal Ni	600 ℃ ~800 ℃	(111) < (001)	[49]
Single crystal Ni	800 ℃	(111) < (001)	[50]
Pure Ni	700 ℃	(111) < (110) < (001)	[30]
Pure Cr	950 ℃	(001) < (110) < (111)	[30]

Until now, most of the previous works on the influence of crystallographic orientation on oxidation behavior of materials are mainly focusing on single crystals. Recently, several works attempted to investigate the effects of micro-texture on the room temperature corrosion behavior of polycrystalline alloys [27,51] and pure metals [23,26]. However, the effect of texture on the high-temperature oxidation behavior of polycrystalline alloy was barely reported and needs further investigation.

Therefore, based on the discussion above, it is necessary to evaluate if the texture affects the oxidation behavior of Ni-based alloy before investigation on the effect of grain size on oxidation

behavior. Consequently, the substrate with different grain size and similar texture should be produced if the influence of the grain size on oxidation behavior of Ni-based alloy is investigated.

1.3.3 Effect of reactive element on oxidation behavior

The high-temperature oxidation resistance of alloys generally relies on the protective properties of the oxide layers that are formed at the surface. The protective layer must be high temperature stable, compact, continuous and have strong adherence to the substrate [52]. Chromium oxide (Cr_2O_3) and aluminum oxide (Al_2O_3) layers are well known as dense, adhesive and stable in the high-temperature environment. More importantly, they grow very slow at high temperature and that will impressively decrease the oxidation rate. Furthermore, they can act as diffusion barriers which prevent the diffusion of cations and anions. Consequently, those alloys that can form Cr_2O_3 and Al_2O_3 protective layers at elevated temperatures are named as Cr_2O_3-forming and Al_2O_3-forming alloys.

The addition of elements like Ce, Hf, Zr and Y could significantly improve the high-temperature oxidation resistance of Cr_2O_3 and Al_2O_3 forming alloys and this process of improvement is known as the rare earth effects (REEs). A lot of attention has been paid to investigate the effect since it was first patented by Pfeil [53]. Currently, it was observed that not only those rare earth elements but also many other elements can have similar influences on the oxidation behavior of Cr_2O_3 and Al_2O_3 forming alloys [54–57]. Consequently, the effects were named as reactive element effects (REEs). The reactive elements (REs) are defined as elements which have higher oxygen affinity than the oxide layer forming elements. Hereafter, all the REEs in this thesis refer to reactive element effects.

Numerous methods have been proposed to incorporate reactive elements into alloys in order to enhance their oxidation resistance. Table 1.2 illustrates a summary of the previously used elements for various alloys. Among these approaches, alloying [58–71] and surface modifications such as dip coating [49,72–79], sputtering [80], ion implantation [81,82], electro-deposition [83–89], metal-organic chemical vapor deposition (MOCVD) [90], electron beam physical vapour deposition (EB-PVD) [91], solution precursor plasma spray (SPPS) [92,93] were the most widely used and efficient ways for incorporating reactive elements. Golightly et.al studied the effect of alloying of Y in FeCrAl alloy and the authors concluded that the oxidation

resistance of FeCrAl was enhanced both by changing the oxide formation from scale/gas interface to alloy/scale interface and by inhibiting voids formation in the alloy/scale interface [58]. An alloying of 6 at % silicon reduced the critical amount of Al needed to form a continuous external Al_2O_3 after examining the incorporation of silicon in NiAl alloy [61]. Dispersion of Y through powder metallurgy slightly increased the oxidation rate of Ti at 700 ℃ to 800 ℃ while the rate was dramatically reduced at a temperature of 900 ℃. This change was attributed to the formation of a more dense and protective oxide layer after adding Y at higher temperature [65]. Alloying of REs of Dy, Hf, Zr, Y, Sm, Gd, Yb, Sc, Nd, Nb and Ta could efficiently improve the oxidation resistance of NiAl while La could not at 1200 ℃ [67,69]. The addition of Dy, Hf, Zr, Sm, Gd, Nd, Yb and Sc could further enhance the adhesion of Al_2O_3 layers to the NiAl substrate. Additionally, alloying of Zr, La, Dy and Hf into NiAl was also used for oxidation investigation at 1100 ℃ in dry and humid atmospheres [70]. It was found that different reactive elements can play different roles during the high-temperature oxidation of NiAl. Doping with Zr and Hf revealed much better oxidation resistance than doping with Dy and La which was attributed to the higher solubility of Zr and Hf.

Besides the alloying, many surface modification methods were applied to deposit REs onto various materials for high-temperature applications. Dip coating processes were widely used to prepare reactive element coatings either at room temperature [49] or high temperature [79]. The influence of RE oxide coatings on the oxidation behavior of austenitic stainless steels was also examined using dip coating method [72,76,79]. Hussey et.al sputter-coated several RE oxide coatings on pure Cr and several high Cr alloys [80]. They suggested that different RE oxide coatings would have different effectiveness on the oxidation of alloys. Y_2O_3 and CeO_2 would have better effectiveness than the addition of Sc_2O_3. Furthermore, electro-deposition method was reported to be a promising and environmental friendly way to produce RE or RE oxide coatings [83–86]. It was demonstrated that chemical composition, surface morphology and thickness of the coating can be easily controlled by variation of the deposition parameters like current density and time. However, until now, the effect of reactive element coating prepared through electro-deposition process was mainly concentrated on Al_2O_3-forming alloys. The influence of electro-deposited reactive element coating on high-temperature oxidation of Ni-based alloys and Cr_2O_3-forming alloys was hardly reported.

In addition, Wessel et.al evaluated the addition of Y and Zr on the microstructure of alumina scale formed on FeCrAl alloy at 1200 ℃ [60]. They stated that the importation of Y and Zr would highly increase the oxidation rate of FeCrAl alloy. Moreover, the addition of Y and Zr could alter the microstructure of Al_2O_3 grains from columnar to equiaxed shape that highly increased the grain boundary densities of the grains. Consequently, the higher density of grain boundaries in equiaxed grains enhanced the ion diffusion in oxidation reaction and this accelerated the oxidation process [60]. Even though many successful examples of REEs were reported, the improvement of oxidation resistance was not always achieved [73,81,90,91,94,95]. As a result, the effectiveness of REEs is still a controversial and needs more studies.

Finally, even though several cases of improvement were reported on the mechanisms of REEs, the reason why the addition of REs can have such effects on alloys is still not clearly understood [96]. Therefore, there is still a knowledge gap in investigation of the influence of RE coatings prepared through electro-deposition process on the high-temperature oxidation behavior of Ni-based Cr_2O_3-forming alloys.

Table 1.2 Previous investigations on reactive element effects (REEs)

Method	Substrate	REs Added	Main Oxides	Temp (℃)	Ref.
Alloying	FeCrAl	Y	Al_2O_3	1200	[58]
	NiCr	Ce/Si	Cr_2O_3	1250	[59]
	FeCrAl	Y/Zr	Al_2O_3	1200	[60]
	NiAl	Si	Al_2O_3	1000	[61]
	304L	Nd_2O_3/Y_2O_3/La_2O_3 /Yb_2O_3	Cr_2O_3	900	[62]
	FeCrMn	Y/Ce/La	Cr_2O_3	800	[64]
	Ti	Y_2O_3	TiO_2	700 - 900	[65]
	MoSiBAl	Ce	MoO_3/SiO_2	1100	[66]
	NiAl	Dy/Hf/Zr/Y/La	Al_2O_3	1200	[67]
		Hf		1100	[68]

Table 1.2 Previous investigations on reactive element effects (REEs) (continued)

Method	Substrate	REs Aadded	Main Oxides	Temp (℃)	Ref.
Alloying	NiAl	Sm/Gd/Yb/Sc/ Nd/Nb/Ta	Al_2O_3	1200	[69]
		Hf/Zr/Dy/La		1100	[70]
	CoReCr	Ni	Cr_2O_3	1000	[71]
Dip Coating	Ni	CeO_2	NiO	600 - 1000	[49]
	316/321/ 304	CeO_2	Cr_2O_3	1000 - 1050	[72]
	304/310/ IN718	Y/Ce/La/ Hf/Ca/Zr	Cr_2O_3	1000	[79]
	Co/Ni/Cu	CeO_2	CoO/NiO/ Cu_2O	700 - 1000	[73]
	FeCrMn	CeO_2	$CeCrO_3$/ $MnCr_2O_4$	900	[75]
	304	CeO_2/La_2O_3	Cr_2O_3/ Fe_3O_4	970	[76]
	FeCrAl	ZrO_2	Al_2O_3	1060	[78]
Sputtering	Cr/FeCr/ NiCr	$CeO_2/Y_2O_3/La_2O_3$/ $CaO/HfO_2/Sc_2O_3$	Cr_2O_3	900	[80]
Ion Implantation	304	Si/Mo/Ce	Cr_2O_3	900	[81]
Electro-deposition	CrNiTi	Y_2O_3	Cr_2O_3	900	[83]
	NiAl	CeO_2	Al_2O_3	1000	[84]
	TiAlV	Y_2O_3	TiO_2/Al_2O_3	600 - 850	[85]
	N5	CeO_2	Al_2O_3	1100	[88,97]
MOCVD	FeCrAl	Nd_2O_3/Y_2O_3	Al_2O_3	1050 - 1200	[90]
EB-PVD	NiAlDy	B	Al_2O_3	1200	[91]
SPPS	410/316L	CeO_2	Fe_2O_3/ Cr_2O_3	1000	[92,93]

1.4 Objectives of the project

With the emphasis on the motivation discussed above, the objectives of the current project are focused on finding ways to improve the high-temperature oxidation resistance of Ni-based alloys.

Two potential approaches are proposed here to study their effects on the high-temperature oxidation behavior of Ni-based alloys. Firstly, the grain refinement process might affect the diffusivity of Cr that promotes the formation of a protective oxide layer. However, the formation of the protective oxide layer may also depend on the Cr content in the alloy which can be a resource for supporting its diffusion. Consequently, a role of grain refinement in oxidation behavior of alloys with high and low Cr contents should be investigated. Furthermore, the crystallographic orientation of grain can also affect the oxidation behavior which was never considered in the investigation of grain size on the oxidation behavior. Therefore, the influence of crystallographic orientation on oxidation behavior of Ni-based alloys should be first examined before samples with different grain sizes are investigated. In the project, Ni-based Hastelloy 230 will be used to study the effect of crystallographic orientation on oxidation behavior since the selected alloys all have similar face centered crystal (FCC) structures. Secondly, synthesizing of RE coating via electro-deposition process might be a potential way to improve the oxidation resistance of the alloy. However, the effect of reactive element coating on the oxidation behavior of Ni-based Cr_2O_3-forming alloys was barely reported and the mechanisms of REEs are not clearly understood. As a result, the effect of RE coatings on oxidation resistance of Ni-based Hastelloy 230 and Hastelloy 625 will be evaluated.

Accordingly, to better understand and address the outlined problems, four objectives of this work are defined as follows:

- To determine the effect of crystallographic orientation on the oxidation behavior of polycrystalline Ni-based Hastelloy 230;
- To evaluate the oxidation resistance of different Cr contents Hastelloys 230 and N with different grain size and similar texture;
- To optimize the deposition parameters for synthesizing reactive element coating onto Ni-based alloy;

- To define a role of reactive element coating in controlling the oxidation resistance of Hastelloys 230 and 625.

Those realizations of the objectives listed above will be demonstrated in the following chapters of this manuscript-based thesis:

In Chapter 2, the influence of crystallographic orientation on oxidation behavior of Ni-based Hastelloy 230 is investigated that addresses the first objective. The content of this chapter is published in *Materials Characterization* and *Applied Surface Science*.

In Chapter 3, the effect of grain size on oxidation behavior of Ni-based Hastelloy 230 and N is inspected. This chapter fulfill the objective of studying the effect of grain size on different Cr content alloys. The content of this chapter is under reviewing in *Corrosion Science.*

In Chapter 4, the optimizing process of deposition of reactive element coating onto Ni-based Hastelloy 230 is described. This research is published in *Thin Solid Films.*

In Chapter 5, the issue of the effect of reactive element coating on oxidation behavior of Ni-based Hastelloy 230 is addressed. This describes the investigation on the influence of reactive element coating on the oxidation behavior of Cr_2O_3-forming alloy. The content of this chapter is accepted as a manuscript in *Oxidation of Metals*.

In Chapter 6, the effect of reactive element coating on oxidation behavior of another Ni-based Hastelloy 625 is discussed. The reason for this study is to establish the effect of reactive element coating on the oxidation behavior of a Cr_2O_3-forming alloy which also can form iron oxide. The research paper is under reviewing in *Corrosion Science*.

Chapter 2 Influence of grain orientation on the incipient oxidation behavior of Hastelloy 230 at 900 ℃

2.1 Overview of Chapter 2

This chapter concentrates on investigating the effect of crystallographic orientation on the oxidation behavior of Ni-based Hastelloy 230 and addresses the first objective of the project.

This chapter is shown as manuscript #1: Influence of grain orientation on the incipient oxidation behavior of Hastelloy 230 at 900 ℃. The contributions of the current Ph.D candidate are 1) preparing the samples; 2) doing optical microscope, scanning electron microscope and electron back-scattering diffraction scans; 3) analyzing the data and plot all the figures; 4) writing and revising the manuscript.

This research was published in the Journal of *Materials Characterization:*

- X. Wang, F. Fan, J.A. Szpunar, L. Zhang, Influence of grain orientation on the incipient oxidation behavior of Haynes 230 at 900 ℃, Materials Characterization, 107(2015) 33-42.

The differences of this chapter from the published manuscript are as follows:

- Fig.2.2 (a) is taken from another published manuscript #2 : X. Wang, J.A. Szpunar, L. Zhang, Effect of surface crystallographic orientation on the oxidation behavior of Ni-based alloy, Applied Surface Science, 327(2015) 532-536. The purpose of adding this image is described in the experiment section;

- Fig.2.4, Fig.2.5 and Fig.2.6 are re-plotted to make the figures clear;
- English writing of this manuscript is revised.

The copyright permissions of the two manuscripts were obtained and shown in the Appendix section. The references of the manuscript are listed at the end of this thesis.

Influence of grain orientation on the incipient oxidation behavior of Hastelloy 230 at 900 ℃

Xu Wang[a], Fan Fan[a], Jerzy.A. Szpunar[a], Lina Zhang[b]

[a]*Department of Mechanical Engineering, University of Saskatchewan, Saskatoon, SK, Canada*

[b] *School of Materials Science and Engineering, University of Science and Technology Beijing, Beijing, China*

2.2 Abstract

Ni-based Hastelloy 230 is used in many areas where it is exposed to the high-temperature environment. In order to improve its oxidation resistance for high temperature applications, the effect of crystallographic orientation on the early stage oxidation behavior is investigated. It is demonstrated that oxides with different thicknesses form on the grains with different orientations. Comparison of the electron back-scattering diffraction orientation maps before and after oxidation indicates that grains near (111) orientation, especially those grains with the deviation angles from <111> smaller than 20 °, are more oxidation resistant than grains with other orientations. Correlation between the results of electron backscattering diffraction and atomic force microscopy is used to compare the oxidation rate of grain with different crystallographic orientation. The oxidation rate is found to vary with the crystallographic orientation in the order of (111) < (110) < (100). It is further demonstrated that the variation of the oxidation rate has a nearly linear function of the deviation angle from <111> direction. The surface morphology of the oxide also depends on the orientation of grain.

Keywords: Oxidation; Ni-based alloy; Electron back-scattering diffraction (EBSD); Atomic force microscopy (AFM); Deviation angle;

2.3 Introduction

Significant researches have been done to develop the next generation nuclear reactors (Generation IV) [98–100]. The design of very high temperature reactor (VHTR) has been widely discussed by many researchers [101,102]. The reactor system contains several main structural components of the intermediate heat exchanger (IHX), hot gas ducts (HGD) and the reactor pressure vessel (RPV) that are exposed to very high temperatures. In order to achieve high working efficiency, the coolant temperature at the outlet of the reactor is planned to be increased to 1000 ℃ which is 200 ℃ and 450 ℃ higher than those of the Gas-Cooled Fast Reactor (GFC) and Supercritical Water-Cooled Reactor (SCW) [98]. During the running of the VHTR system, the HGD and IHX structural materials may face many high-temperature degradation problems especially the acceleration of high-temperature oxidation [103]. The extreme and severe operating conditions could significantly oxidize the surface and affect the properties of the structural materials. Consequently, their performance and service lifetimes at high-temperature will be affected. Therefore, the materials with high temperature oxidation resistance have to be developed for application in high temperature environments.

Nickel-based alloys are well known as combining high-temperature oxidation resistance and outstanding mechanical properties [104]. They are widely used as structural materials in many areas like combustion cans, turbine engines and nuclear reactors [105,106]. Ni-based alloy 230 was selected as one of the structural materials for the VHTR system. The application of this alloy at high-temperature environment was discussed by Dewson [107]. However, the high-temperature oxidation behavior and its related surface degradation properties are still the main problems and additional efforts should be made to improve the alloy performance at high-temperature atmosphere. Subsequently, it is important to understand the oxidation behavior of this alloy.

Many researchers have explored the oxidation properties of alloy 230 since it was manufactured in the 1980s. Tawancy et.al studied the oxidation behavior of Ni-Cr-W-Mn-Si-La alloy at 950 ℃, 1050 ℃ and 1150 ℃ and focused on measuring the weight change, metal loss and internal oxidation penetration depth before and after oxidation [108]. England and Virkar investigated the oxidation behavior of several alloys including alloy 230 in the humidified hydrogen and air between 700 and 1000 ℃ for almost 10000 hours [104,109]. Jian et.al

reported the multiple stages oxidation of alloy 230 at 650 ℃ to 850 ℃ for using in solid oxide fuel cells (SOFCs) [110–112]. Recently, Kim et.al investigated the oxidation and mechanical properties of alloy 230 and Inconel 617 at various environments at the temperatures of 900 ℃ and 1000 ℃ for 1000 hours [103,113–117]. Chien et.al investigated the cyclic oxidation behavior of alloy 230 at temperatures of 871 ℃, 982 ℃ and 1093 ℃ [118]. It was demonstrated that intergranular oxidation and internal oxidation occurred at 982 ℃ and 1093 ℃ after 300 hours exposure, respectively. Further, many researchers have tried to improve the oxidation behavior of alloy 230 by several methods either using alloying [119,120], electrical discharge alloying (EDA) [121,122], MOCVD [123] or various surface modification methods [124,125]. However, these previous works mainly concentrated on the long term oxidation behavior of alloy 230. Research concerning the initial oxidation behavior of this alloy was rarely reported. Nevertheless, it was recently documented that the long term exposure is highly affected by the initial oxidation stage for alloy 230 when the oxidation took place in the reducing environment at a temperature from 850 ℃ to 1000 ℃ [126]. Further, the previous research was mainly focused on the oxidation kinetics of bulk materials with unknown microstructures. The role of microstructures and orientations of grains on the oxidation behavior of this alloy were not investigated. Therefore, the present work focuses on the investigation of the role of crystallographic orientation in the initial oxidation stage of Ni-based Hastelloy 230.

2.4 Experimental

Hastelloy 230 with the nominal chemical composition shown in Table 2.1 was used in the present investigation. Hastelloy 230, as one of the most promising candidates for the VHTR structural materials, is a Ni-Cr-Mo-W alloy that has very good mechanical properties and oxidation resistance at high temperature. Fig. 2.1 shows the typical microstructure of Hastelloy 230 at low and high magnification. The mean grain size is around 50 μm. The precipitates like W and Cr-rich MC_6 and $M_{23}C_6$ carbides are often located at the grain boundaries within grains as marked in Fig. 2.1 (b). The similar findings were also reported by other researchers [127–129].

Table 2.1 Nominal chemical composition of Hastelloy 230 (wt %)

Ni	**Cr**	**W**	**Mo**	**Fe**	**Co**	**Mn**	**Si**	**Al**	**C**	**La**	**B**
Bal	22	14	2	3	5	0.5	0.4	0.3	0.1	0.02	0.01

In our work, a rectangle specimen with dimensions of 15 mm × 10 mm × 1.5mm was cut from an alloy sheet. To develop a strain free and flat surface for electron backscattering diffraction (EBSD) measurement, the sample was ground by SiC paper from 360# to 4000#. The sample was then subsequently polished with 3 μm and 1 μm diamond polishing and 0.04 μm colloidal silica solution for 30 min. Finally, the sample was polished by a Buehler VibroMet2 Vibratory polisher for 20 hours to make a stress free surface. After polishing, the sample was ultrasonically cleaned in acetone for 10 min, then washed with deionized water and ethanol and fast dried under flowing air. After the final polishing, a smooth and extremely flat surface was produced which could ensure the entire surface was at the same height level before any further treatment. Further, ZYGO NewViewTM 800 optical surface profiler was used to guarantee the specimen had a very low roughness.

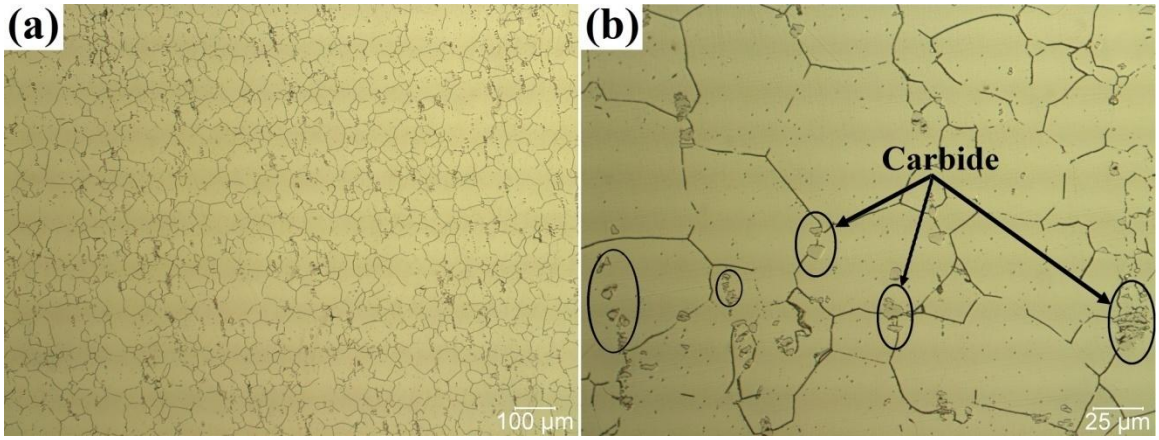

Fig. 2.1 Optical microscope (OM) images of the typical microstructure of Hastelloy 230: (a) low magnification (100 ×); (b) high magnification (500 ×) image.

To study the effect of crystallographic orientation on the oxidation behavior of alloys, it is important to know the orientations and the oxidation behavior of some specific grains. Therefore, a specific area was marked on the polished sample to investigate the oxidation behavior of selected grains. The marking method of the investigated area is shown in Fig. 2.2 (a). Firstly, a steel scriber was used to produce a rectangular marker on top of the specimen as marked by the blue rectangle in Fig. 2.2 (a). Next, several Vickers hardness indents were imprinted at the bottom of the rectangular area. Then a small area containing several of the indents inside the rectangular area was used to do the EBSD scans. Fig. 2.2 (b) depicts a typical surface profile scanning result of the marked area. The average roughness of the marked area is 2 to 3 nm after

polishing which clearly indicates that the heights of the grains are almost at the same level before oxidation experiment.

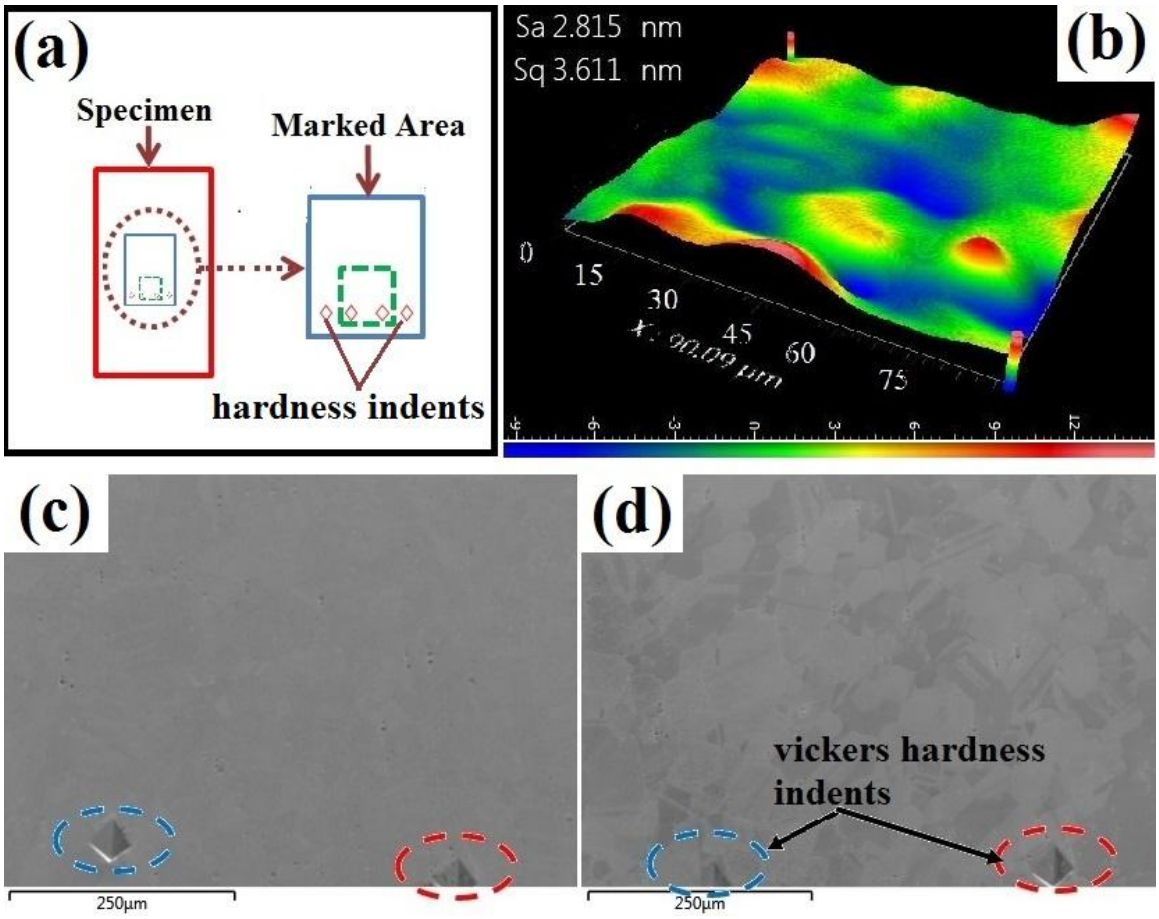

Fig. 2.2 Method of marking the specimen and surface roughness profile before oxidation (a) marking of the sample; (b) surface roughness profile before oxidation; secondary electron image (SEI) of the marked area (c) before oxidation; (d) after oxidation.

Grain orientation of the marked area was characterized using Hitachi SU6600 scanning electron microscopy (SEM) equipped with EBSD system at a voltage of 20 kV. The EBSD maps were recorded with a step size of 1.4 μm. After the EBSD mapping, the sample was oxidized in air for 5 min at 900 ℃ in a muffle furnace with a thermocouple very close to the specimen. Finally, the crystallographic orientation of the oxidized sample was measured by EBSD again on the same area as previously scanned. To compare the results of orientation measurements before and after

oxidation, all parameters used for EBSD measurements were kept the same. No oxide phase pattern was used to characterize the grain orientation after oxidation. HKL Channel 5 software was used to visualize the EBSD map. Fig. 2.2 (c) and (d) demonstrate the surface morphology marked area for EBSD measurements before and after oxidation. The two visible Vickers hardness indentations used for marking the specimen clearly indicated that the EBSD measurements were scanned in the same area before and after oxidation.

To correlate the oxidation behavior of individual grain with its own orientation, atomic force microscopy (AFM) was used to analyze the topography of the oxidized area where EBSD was done. Then Nanoscope Analysis software was used to visualize the 2D and 3D AFM images. Section analysis was used to measure the oxide thickness of each grain. Finally, the height of the oxidized grain was correlated with the orientation of the substrate grain.

2.5 Results and Discussions

2.5.1 Comparison of EBSD results before and after oxidation

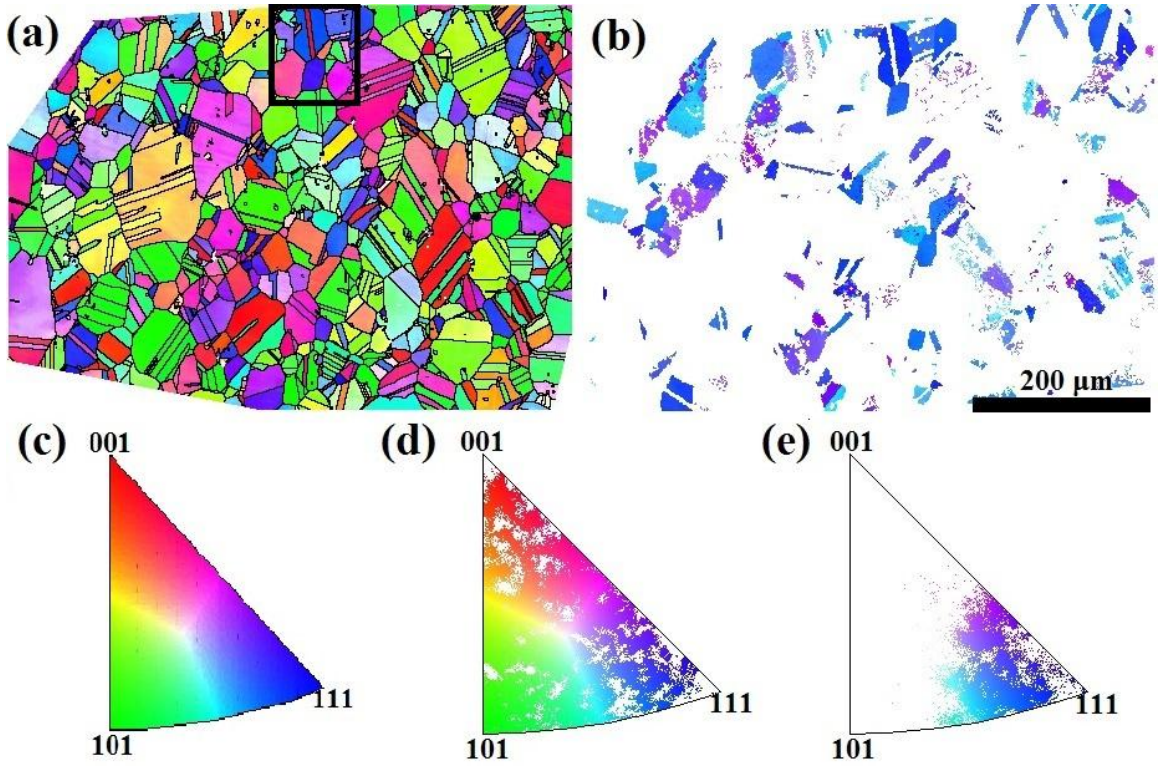

Fig. 2.3 EBSD orientation maps: (a) before oxidation; (b) after oxidation; (c) legend of the EBSD orientation maps; (d) inverse pole figure of (a); (e) inverse pole figure of (b).

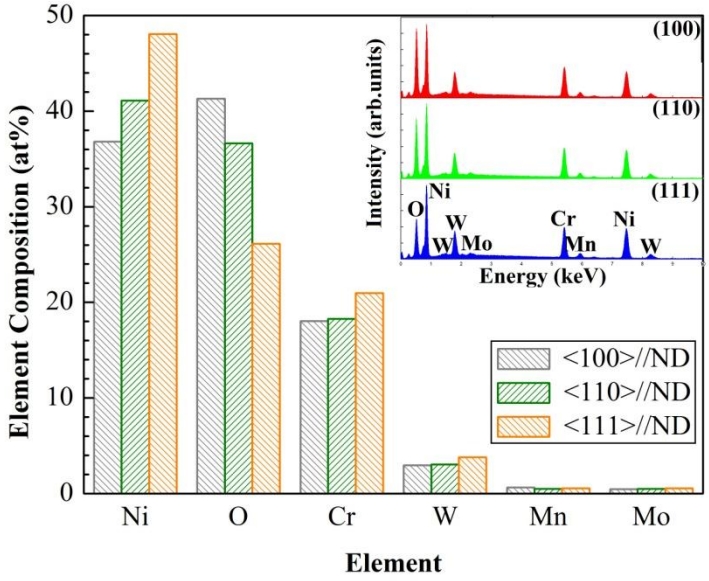

Fig. 2.4 EDS result to show the different element compositions of grains with different orientation after oxidation.

Fig. 2.3 presents the comparison of the EBSD orientation maps of the marked area before and after oxidation. In these color maps, the color corresponds to the crystallographic orientation of each grain which depicts the normal vector of the grain that is parallel to the normal direction (ND) of the specimen. For instance, the blue color grains correspond to <111>//ND, the green color grains correspond to <110>//ND and the red color grains have <100>//ND orientation. The legend of the color maps is shown in Fig. 2.3 (c). As seen in Fig. 2.3 (a) and (b), the grains imaged on both figures are identical and the grain size and shape did not change. All of the grains in this area were well-indexed before oxidation test. However, some of these grains could not be indexed after oxidation which is represented by the white area in Fig. 2.3 (b). This may indicate that different thicknesses of oxides formed on different grains. It is seen that only grains with near <111>//ND orientations (blue color grains) were indexed again after oxidation. This implies that the oxide layers formed on the grains with near <111>//ND orientations are much thinner than those on the grains that cannot be indexed. The diffraction signals of the other grains could not be detected by EBSD detector owing to the absorption of the thick oxide layer formed on their surfaces. Fig. 2.3 (d) and (e) are the inverse pole figure (IPF) triangles of orientation maps in Fig. 2.3 (a) and (b). From these figures, it is clear to see that the grains departure from

<111>//ND orientation are heavily oxidized and the diffraction patterns from them cannot be observed.

To verify the formation of oxides on the different grains, energy dispersive spectroscopy (EDS) was used to characterize the chemical compositions of three oxidized grains with <111>//ND, <110>//ND and <100>//ND orientations as shown in Fig. 2.4. The EDS spectra of these three grains were also shown as an inset image in Fig. 2.4. The EDS was performed at 20 kV. The signal of oxygen content in the element composition obviously confirms the formation of oxide on each grain. Further, it is clear to see that the signal intensity of oxygen on grain <100>//ND is much higher than those on grain <110>//ND and <111>//ND which indicates that a thicker oxide layer formed on grain with <100>//ND orientation.

Table 2.2 The Miller indices and deviation angles of selected grains

Grain	Orientation (Before Oxi)	Orientation (After Oxi)	Miller Indices (hkl)[uvw]	Deviation Angles from <111> (°)	Indexed or not after oxidation
1			(233)[$\bar{5}$21]	10 °	Yes
			(016)[5$\bar{3}$1]	48.4 °	No
2			(223)[$\bar{3}$12]	11.4 °	Yes
			(237)[8$\bar{1}\bar{2}$]	28.4 °	No
3			(324)[32$\bar{3}$]	15.2 °	Yes
			(012)[$\bar{1}$00]	39.2 °	No
4			(112)< $\bar{1}$3$\bar{1}$>	19.5 °	Yes
			(122)<22$\bar{3}$>	15.8 °	Yes
5			(101)[$\bar{1}\bar{5}$1]	35.3 °	No

To precisely know which grains are severely oxidized and therefore they cannot be indexed after oxidation, the deviation angles of indexed grains from <111> orientation were calculated. The deviation angle is defined as the angle between the normal direction of the indexed plane and ideal <111>//ND direction. For instance, for any Miller indices (hkl)[uvw], the deviation angle is the angle between the <hkl> direction and the <111> direction. Table 2.2 shows the orientation

maps, Miller indices and deviation angles of five grains selected in the EBSD scanned area. The Miller indices of these grains were converted from the Euler angles in the HKL Channel 5

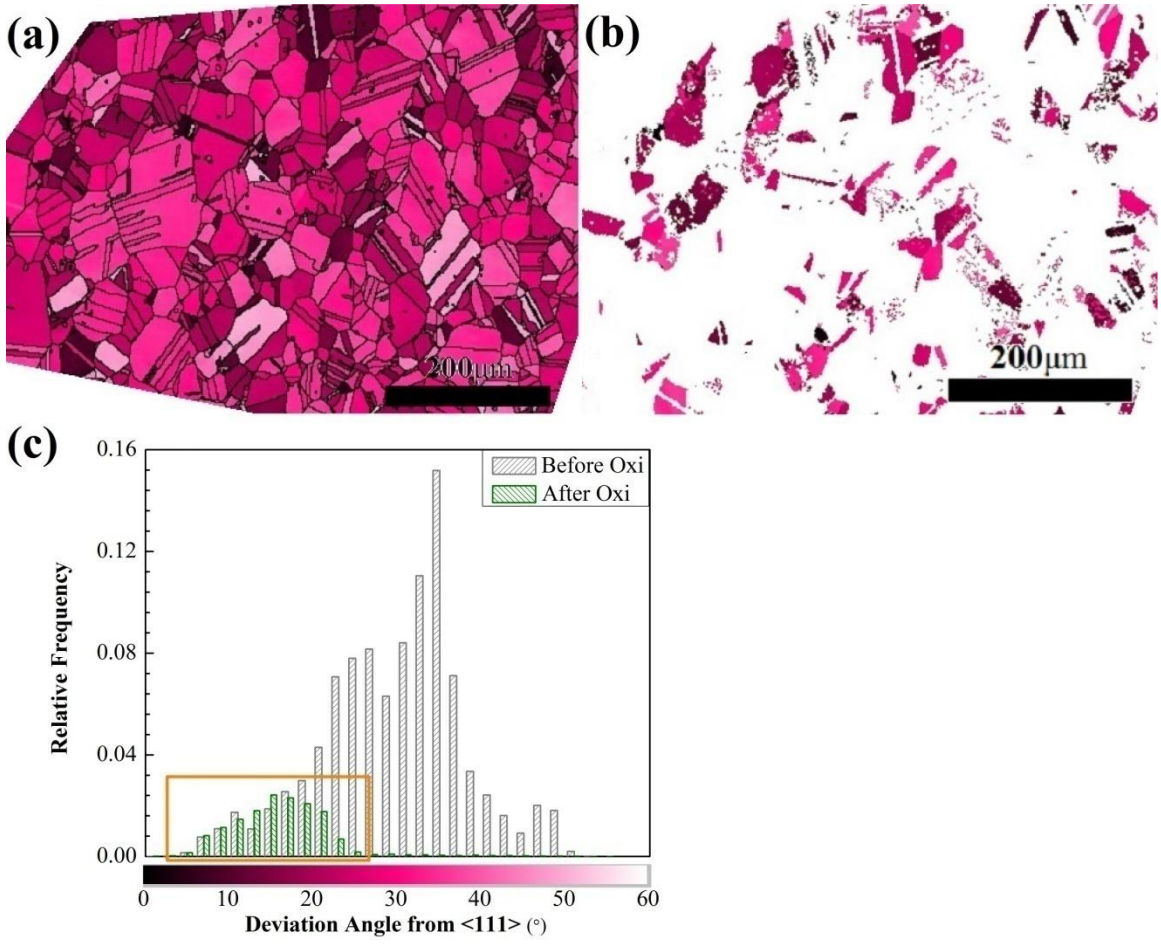

Fig. 2.5 Deviation angle maps of indexed grains from <111>//ND before and after oxidation: (a) before oxidation; (b) after oxidation and (c) deviation angle distribution of indexed grains.

software database by Textools software. The calculated (hkl)[uvw] values were automatically normalized to integers by the software. Therefore, the dot product between the direction vector and plane vector may not exactly equal to zero. For example, the calculated (hkl)[uvw] values for grain 1, twin in grain 1 and grain 3 are (0.44, 0.63, 0.64)[-0.88, 0.43, 0.18], (0.1, 0.17, 0.98)[-0.81, -0.56, 0.18] and (0.56, 0.35, 0.75)[0.64, 0.38, -0.67], respectively. However, the normalized integers of the calculated values are (233) [$\bar{5}$21], (016)[$\bar{5}\bar{3}$1] and (324)[32$\bar{3}$], respectively. As can be seen in this table, all the grains and the twin grains in grains 1 to 3 were well indexed before oxidation test. Nevertheless, these twin grains and grain 5 were not indexed after

oxidation. The background colors of Miller indices in the table are described according to the orientation map colors of the grains. For instance, the Miller indices of the grain 1 is (233)[$\bar{5}$21] which is marked as blue color according to its orientation map color. It is found that only those grains with lower deviation angles can be indexed after oxidation as seen in Table 2.2. Those grains with higher deviation angles could not be well indexed after oxidation. Fig. 2.5 (a) and (b) shows the comparison of the deviation angle maps of all the indexed grains before and after oxidation. The color legend of these maps is described in Fig. 2.5 (c) which demonstrates the deviation angle distribution of the indexed grains before and after oxidation. It can be found that the deviation angles of most indexed grains after oxidation are lower than 20 °. This clearly indicates that these grains with deviation angles lower than 20 ° can have higher oxidation resistance than other grains with larger deviation angles.

2.5.2 Correlation of grain orientation with grain oxidation rate

2.5.2.1 Orientation dependent oxidation of individual grains

To correlate the oxidation behavior of grains with their orientations, it is critical to known the oxide thicknesses formed on the grains after we know their orientations. Therefore, AFM was used to measure the surface roughness of the EBSD scanned area after oxidation with the assumption of same types of oxides formed on different grains. AFM is well known as an excellent characterization technique to know the 3D surface topography at a very high resolution [130]. Fig. 2.6 depicts the AFM result scanned from the area marked in Fig. 2.3 (a) as also shown as an inset image. Generally, it is easy to find the EBSD scanned area for AFM measurement with the indents that facilitate us to correlate them together.

Similarly to EBSD orientation maps where different colors correspond to different orientations, the different colors relate to the different surface heights of each grain for AFM measurements. The legend of these colors is provided in the upper right corner of Fig. 2.6 (a). In the case of the oxidized sample, these different relative heights relate to the different oxidation rates of individual grains. As can be seen in Fig. 2.6 (a), those grains close to <111>//ND which correspond to the darkest areas in the AFM image are slightly oxidized, the grains close to <100>//ND which correspond to the lightest areas are severely oxidized and those grains with a closing <110>//ND tend to be intermediately oxidized. To correlate the oxidation behavior of grains with their grain orientations, Nanoscope analysis software was used to display the

thickness of the oxide formed on each grain. Five line scans were measured on each grain and the average relative height was used to represent its surface oxide height. Finally, all the surface heights of individual grains were normalized to a grain which has a deviation angle smaller than 10 ° from <111> direction. Then the normalized height was correlated to the orientation of individual grain. These normalized heights were called as the "relative thickness" of the oxide. As an example, Fig. 2.6 (b) shows the normalized relative oxide thickness along the green scanning line in Fig. 2.6 (a). It is much clear to see that the oxides formed on different oriented grains tended to have different oxide thicknesses.

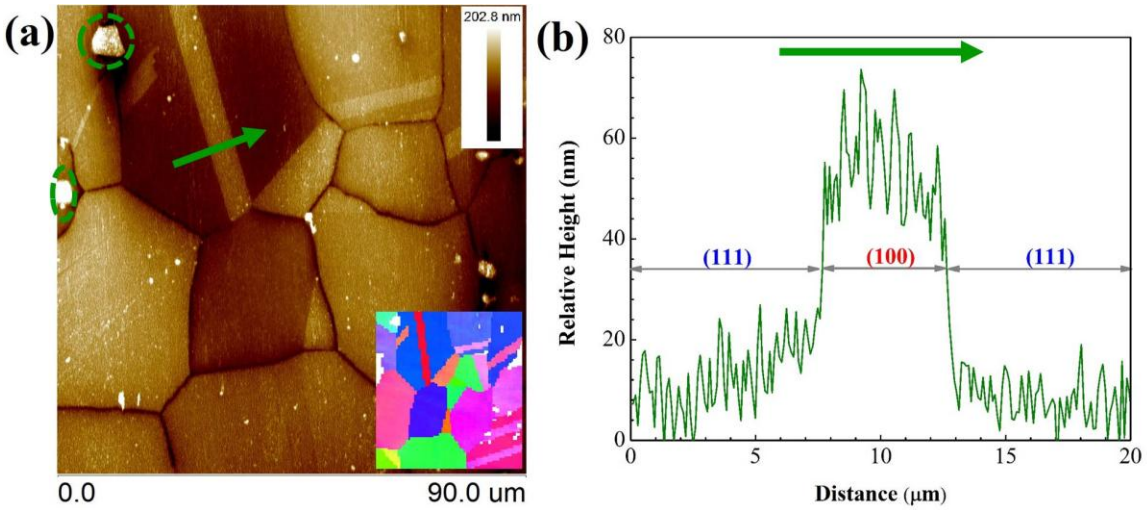

Fig. 2.6 AFM measurement to know the relative thickness of the oxide: (a) AFM result of the area marked in Fig. 2.3 (a); (d) AFM section analysis result in (a).

Moreover, the carbides were selectively oxidized as shown in the green circle marked areas in Fig. 2.6 (a). The selectively oxidized carbides always had higher relative heights than those oxides formed on the grains. The preferential oxidation of carbides has been reported by other researchers [110,116,128] in the case of oxidizing Ni-based alloys of Inconel 738 LC and Inconel 939 [131]. It was demonstrated that the oxidation rates of carbides were much higher than that of the matrix and the volume of the oxidized carbides would largely increase after oxidation. The increasing of the volume would result in the high shear stresses between their oxide products and Cr_2O_3, which may favor the internal oxidation in the carbide areas [131]. However, the fast oxidation rate of carbide is observed in the present study, the increase in the volume of their oxide products are not recorded since the oxidation time is very short.

To know the rules of how the orientation affects the oxidation behavior of grain, nine selected areas including 220 grains were scanned by AFM to obtain a statistic analysis. Six of the nine areas are displayed here since all the areas tend to show similar trends as shown in Fig. 2.7. These six areas were all scanned inside the area where EBSD was done before oxidation. It is seen that the heights of oxides formed on each grain are well defined. Further, it is clear to see that the carbides (white cylinder areas) are fast oxidized.

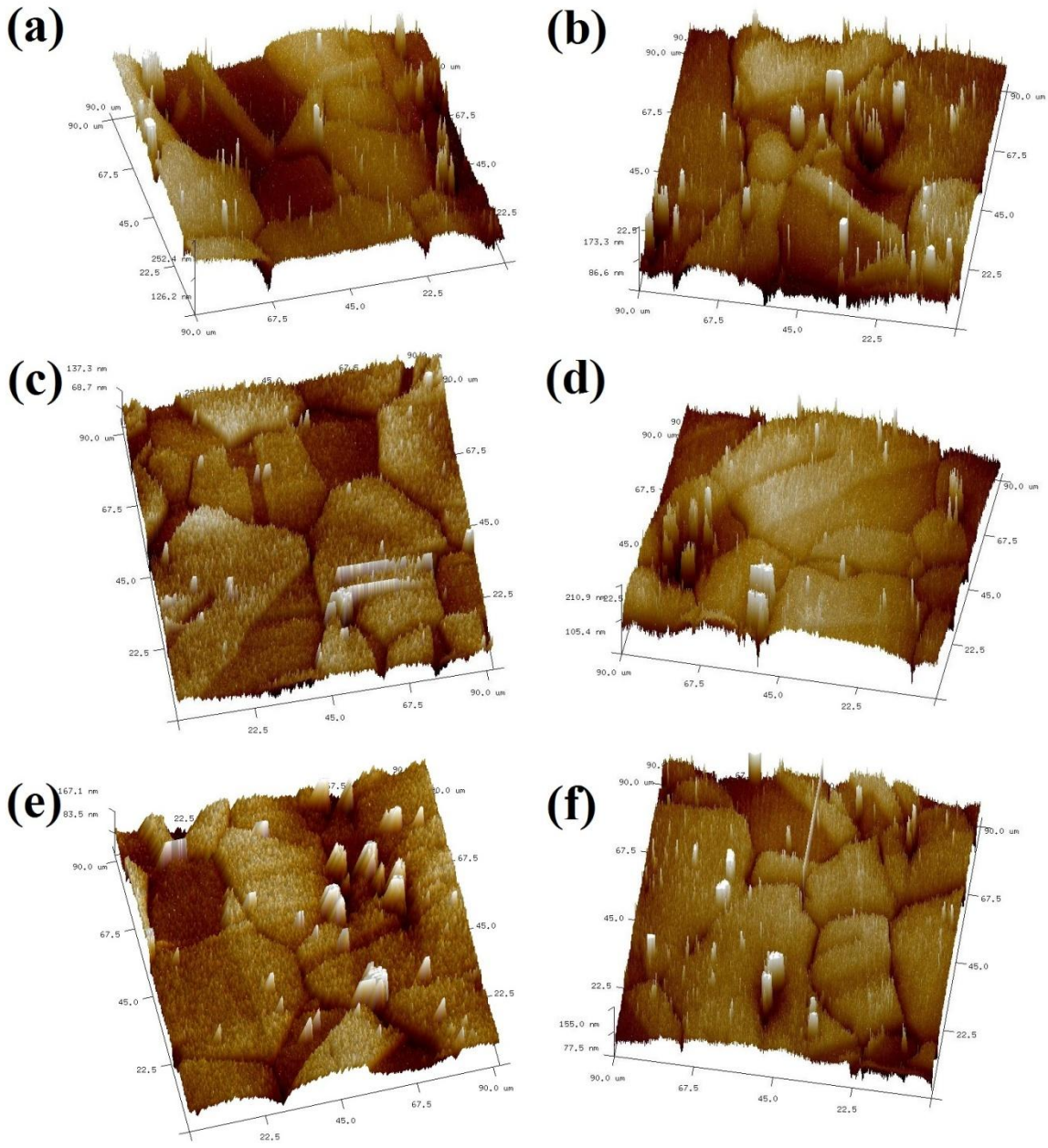

Fig. 2.7 Typical AFM results scanned inside the EBSD area after oxidation.

2.5.2.2 Correlation of grain orientation with oxide thickness

To correlate the grain orientation with the oxide thickness, the measured relative heights were normalized to a grain close to <111>//ND orientation as described earlier. Then the standard stereographic IPF triangle was used to describe both of the grain orientation and the oxide thickness. Fig. 2.8 shows the IPF triangles correspond to the areas presented in Fig. 2.7 and also in the EBSD scanned area. In these triangles, each point corresponds to one grain. The position of the point in the IPF triangle represents the crystallographic orientation of the oxidized grain and the color of the point demonstrates the relative thickness of the oxide formed on the grain. The color legend of the relative thickness is shown as inset image in each area. In all the areas, it is found that grains with orientation close to <111>//ND always have lower relative thicknesses, grains near <100>//ND always have higher relative thicknesses and the oxides on planes close to <110>//ND tend to obtain intermediate relative thicknesses.

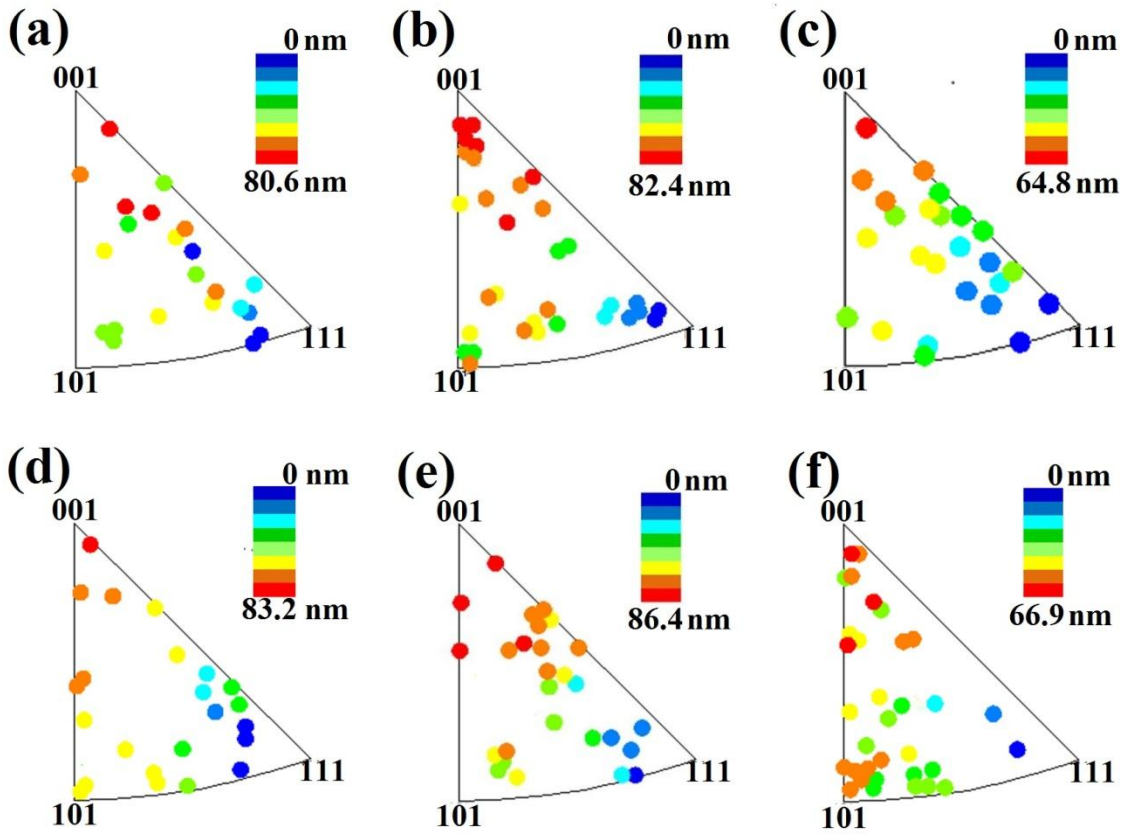

Fig. 2.8 Dependence of relative height on crystallographic orientation

Fig. 2.9 plots the dependence of relative oxide thicknesses on the deviation angles of the oxidized planes from (111) plane. Obviously, there is a nearly linear relationship between the thickness of the oxide formed on the grain and its deviation angle from (111) plane although the results are scattered. It is clear to see that the oxidation rates of grains are in the order of (111) < (110) < (100). The effect of grain orientation on the oxidation behavior was previously studied in many crystals, e.g. single crystal Fe [22], Cu [44], and Ni [49]. It was observed that (100) face was more easily oxidized than (111) face in the case of oxidation of Ni [49]. The authors suggested that the oxides formed on the (100) face tended to produce a high concentration of high-angle grain boundaries (HAGBs). The HAGBs were considered as short-circuit diffusion paths of metal ions which therefore accelerated the oxidation process. Studies on the impact of surface orientation on the oxidation behavior of TiN demonstrated that the oxide islands were favorably formed on (100) surfaces, while the islands were barely observed on the (111) planes [31]. Furthermore, the sizes and areas of oxide islands that covering the (100) planes were much larger than those on the (110) and (111) planes. Planes with different atomic densities resulting in the different binding energies were used to explain these results. Therefore, for face-centered crystal (FCC) material, the oxidation resistance of grains were reasonably in the order of (111) > (100) > (110). However, this is not in agreement with the present work since the oxidation rate is found in the order of (111) < (110) < (100). Here, although the oxidation velocity may still relate to the atomic density of different planes like near (111) grains always obtain higher resistance than other grains, it may also relate to the surface morphology of the oxides formed on the grains.

FCC materials obtaining similar oxidation trends with the present work were reported by other researchers [30]. After investigation of the initial oxidation of polycrystalline Ni and Cr, it was reported that oxidation rate in Ni changed with crystal orientation in the following order of (111) < (110) < (100) while for polycrystalline Cr changed with crystal orientation in the order of (111) > (110) > (100) [30]. Orme et.al investigated the anisotropic corrosion behavior of Inconel 600 [27] and alloy 22 [51] in HCl solution. The corrosion rate was reported to be in the order of (111) < (100) < (110) in 3M HCl solution which was reasonably explained by the atomic density theory. However, in 1M HCl solution, they concluded that the corrosion rates of Inconel 600 and alloy 22 were in the order of (111) < (110) < (100). The result was attributed to how fast the passive film could form on grains with different orientations. Nevertheless, it is not negligible that the oxidation behavior variation of grain is correlated with the deviation angle between its

normal vector of the crystallographic planes and <111>//ND direction at the surface of the specimen.

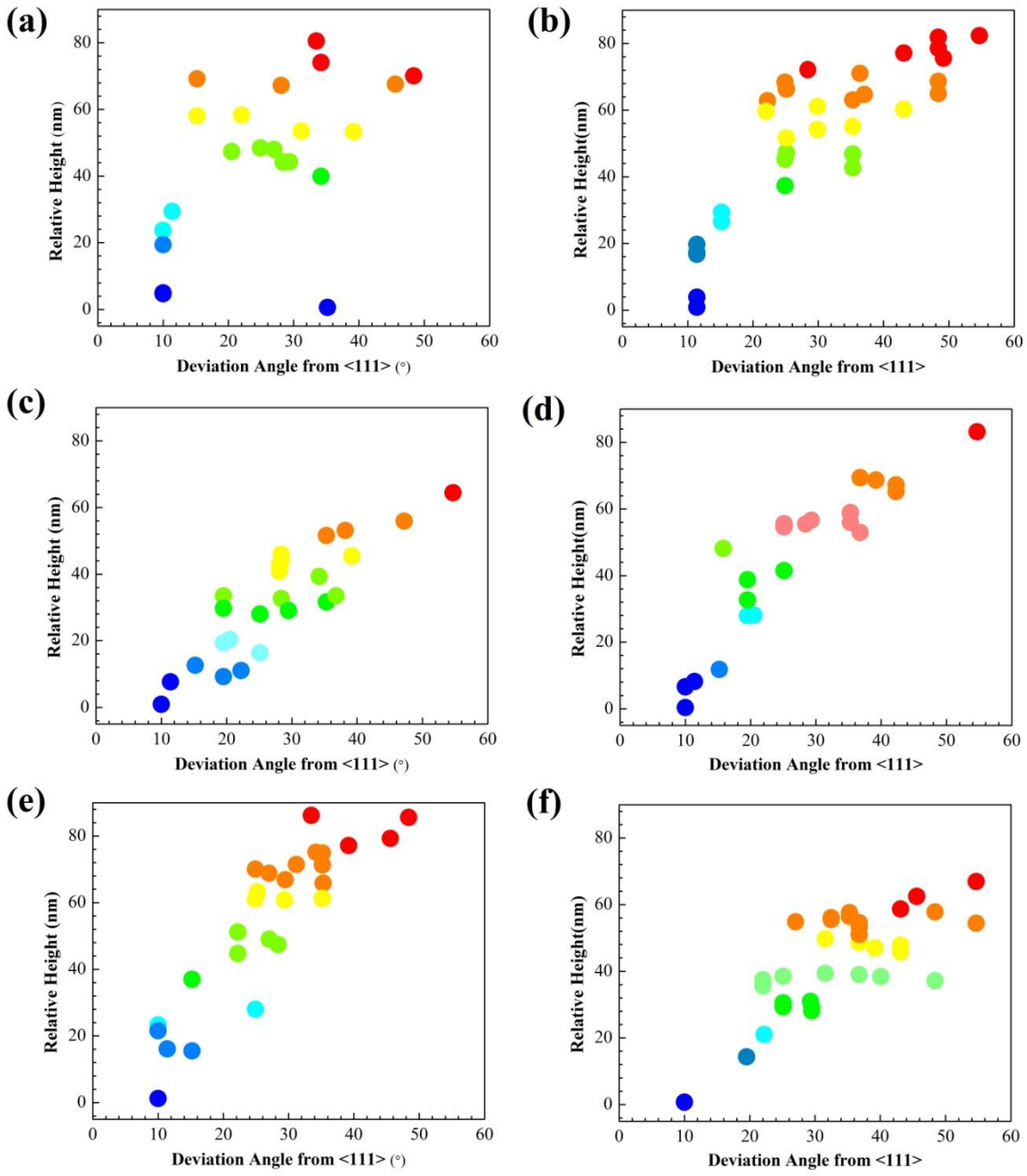

Fig. 2.9 Dependence of relative height on deviation angle of indexed planes from <111>.

2.5.3 Correlation of grain orientation with grain surface morphology

Fig. 2.10 depicts the surface morphology of the EBSD scanned area. Fig. 2.10 (a) shows the SEM image of the whole EBSD scanned area. It is observed that grain with near <111>//ND orientation has a dark color, grain near <100>//ND has light color and grain close to <110>//ND has gray color after comparing this image with the orientation image map. Fig. 2.10 (b) represents the high magnification surface morphology image of the area marked in Fig. 2.10 (a). It is clear to see that the oxide formed on carbide has similar contrast with that formed on grain having <100>//ND orientation. Further, the oxide morphology seems to be also orientation dependent as seen in Fig. 2.10 (c) which shows the different morphology of two neighbor grains with near <100>//ND and <111>//ND orientation marked in Fig. 2.10 (b). Consequently, Fig. 2.10 (d), (e) and (f) display the images scanned from grains with near (100), (110) and (111) orientations. Coarse-grained oxides formed on grains with near (111) orientations, much fine-grained oxides formed on grains with near (110) orientations and oxides on grains with (100) orientations seem to have both coarse and fine grains. The orientation-dependent surface morphology was also reported for Inconel 600 after corrosion in HCl acid [27]. In that paper, smooth and uniform oxides were observed on the grain with near (111) orientation, porous oxides formed on the grain with near (100) orientation and stripped oxide morphology was observed on the grain with near (110) orientation. In our case, the oxides formed on near (111) grains seems also flat and uniform and the oxide morphology may suggest us clues why the oxidation velocity is in the order of (111) < (110) < (100). As could be seen in these three images, oxides formed on grains (111) and (110) are tightly compact but oxide on grain (100) seems loose and non-compacted since the coarse oxide grains cannot well fit with fine grains. Therefore, some gaps or voids will form between those coarse oxide grains and fine oxide grains as seen in Fig. 2.10 (d). These gaps or voids therefore directly introduce the oxidation environment to contact with the substrate grains which will accelerate their oxidation velocities. Further, the grains boundary concentration on fine oxide grains formed on <110>//ND may explain why it has a higher oxidation rate than coarse grains formed on <111>//ND. The grain boundary was found to act as short-circuit diffusion path for ions during oxidation reaction and the grain size will significantly affect the oxidation behavior of alloys [10]. Therefore, the smaller oxide grains with higher grain boundary densities tend to facilitate the oxidation process.

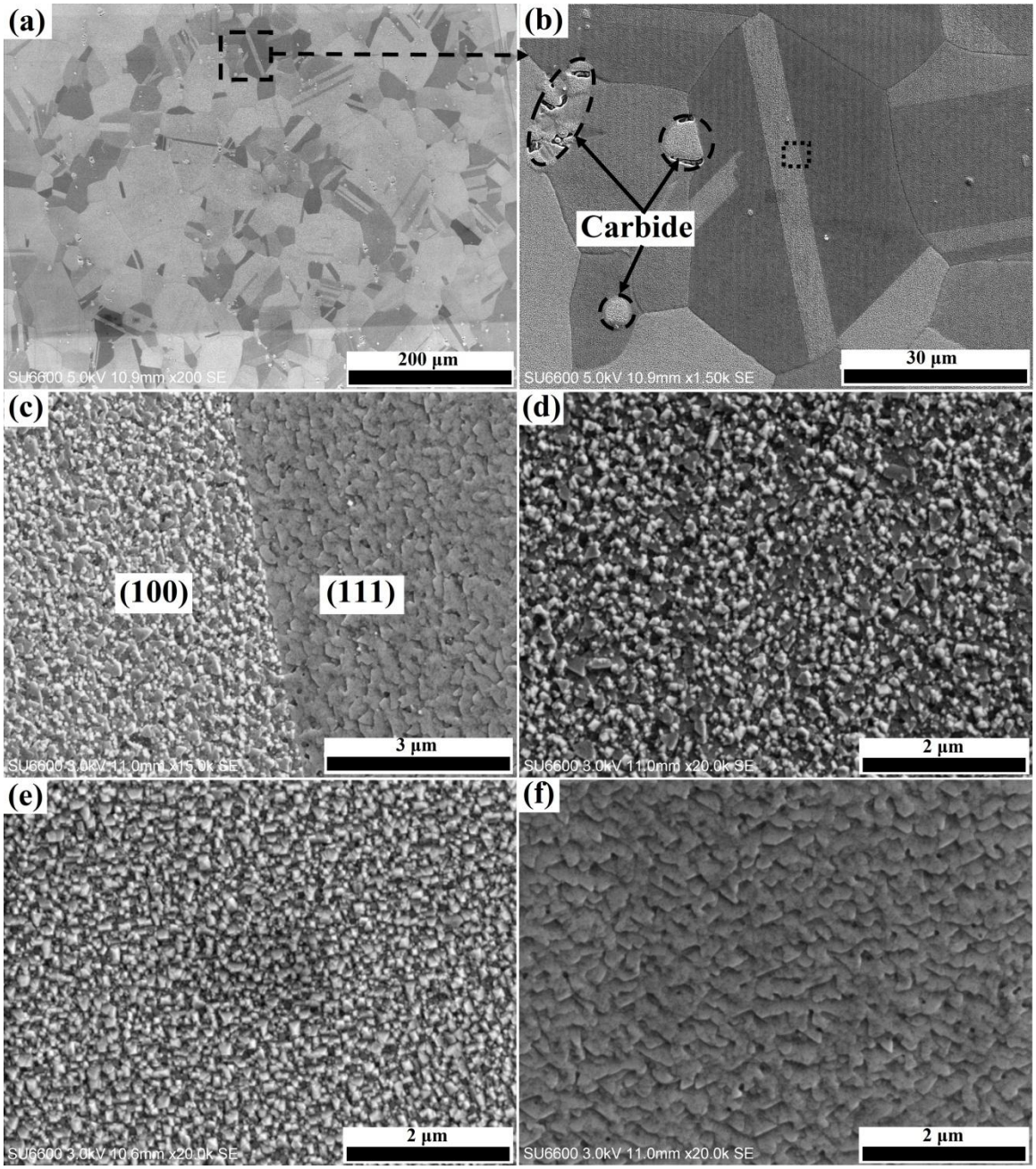

Fig. 2.10 Dependence of surface morphology on grain orientation.

2.6. Conclusions

The oxidation behavior of Hastelloy 230 at 900 ℃ was investigated by combining of EBSD orientation maps and AFM measurements. The crystal planes with deviation angles smaller than 20 °from ideal <111> direction can be indexed again after oxidation which indicates that those grains with orientation close to (111) tend to have higher oxidation resistance than the others. In

addition, the correlation between the relative oxide thicknesses formed and crystallographic orientations of the individual grains are investigated by combining the information collected from EBSD and AFM techniques. The thicknesses of the oxides formed on (100) grains are the thickest which are much thinner on the (110) oriented grains and (111) oriented grains. The oxidation rate of the grain is found in the order of (111) < (110) < (100). This conclusion suggests that changing the surface crystallographic orientation might be a novel way to enhance the oxidation behavior of alloys, e.g a surface with dominant (111) orientation grains might highly enhance the oxidation resistance of the alloys. Finally, the morphology of the oxide formed on differently grain is also dependent on the grain orientation.

Chapter 3 Effects of grain size on the oxidation behavior of Ni-based alloys with low and high Cr contents

3.1 Overview of Chapter 3

In the last chapter, the influence of texture on the oxidation behavior of FCC-structured Hastelloy 230 was investigated. It is demonstrated that the texture has a significant effect on the oxidation of the FCC-structured material. Therefore, the objective of this chapter is to explore the effect of grain size on the oxidation behavior of FCC structure alloys that have different Cr contents and similar textures.

This chapter was submitted as a manuscript #3: Effect of grain size on the oxidation behavior of Ni-based alloys with low and high Cr contents. The PhD candidate's contributions to the manuscript are a) preparing of the samples; b) performing the oxidation experiments; c) characterizing the oxidized samples by XRD, SEM, EDS and EBSD; d) writing and revising the manuscript.

The manuscript is under review status in *Corrosion Science*:

- X. Wang, J.A Szpunar, Effects of grain size on the oxidation behavior of Ni-based alloys with low and high Cr contents, Corrosion Science, (2016) under review.

The difference of this chapter from the submitted manuscript is as follows:

- The chemical composition of Hastelloy 230 in Table 3.1 is removed.

The references and the copyright permission are attached at the end of the thesis.

Effects of grain size on the oxidation behavior of Ni-based alloys with low and high Cr contents

Xu Wang*, Jerzy A. Szpunar

Department of Mechanical Engineering, University of Saskatchewan, Saskatoon, SK S7N5A9, Canada

3.2 Abstract

The effects of grain size on the oxidation behavior of a high Cr Hastelloy 230 and a low Cr Hastelloy N are investigated with the consideration of texture. The grain refinement process only has a slight influence on the oxidation kinetic of Hastelloy 230 while it significantly changes the oxidation behavior of Hastelloy N. Oxide spallation is observed after oxidizing coarse-grained Hastelloy N for 100 h but there is no spallation on the fine-grained Hastelloy N even after oxidizing for 1000 h. Furthermore, the oxide formed on the Hastelloy 230 with a small grain size has similar surface morphology and chemical composition with those formed on the coarse-grained Hastelloy 230. For coarse-grained Hastelloy N, thicker and cracked oxide layers form in the grain interiors and thin Cr-rich oxide films form at the grain boundary areas. A homogeneous Cr-rich oxide layer covers the entire surface of the Hastelloy N with a small grain size which clearly implies that the diffusivity of Cr is enhanced owing to the grain refinement process. Schematic models are developed to manifest the oxidation mechanisms of the high and low Cr alloy with large and small grain sizes.

Keywords: High-temperature oxidation; Grain size; Texture; Ni-based alloy; Electron back-scattering diffraction (EBSD).

3.3 Introduction

High-temperature oxidation resistance is one of the most important properties of materials for high-temperature applications. Finding ways of enhancing the oxidation resistance of alloy is always very important for material servicing in the high-temperature environment. Generally, the oxidation resistance of alloys depends on the protective properties of the oxide layers formed on their surfaces in the oxidizing atmospheres. The protective layer can decrease the transportation rate of the cations and anions through the oxide which reduces the oxidation rate of the alloy. However, the formation of the oxide layer significantly varies with the microstructure, chemical

composition and surface condition of the alloy [2]. Therefore, various methods have been proposed to enhance the oxidation resistance of alloys either through changing the structures of alloys [2,7,9,10,132,133] or altering the chemical compositions of materials [71,134,135]. Among these methods, grain refinement was reported as an efficient way to enhance the oxidation resistance of alloys. Baer et.al investigated the oxidation behavior of SS304 with large and small grain sizes where they concluded that the fine-grained samples had much higher oxidation resistance than those of the coarse-grained samples [2]. It was reported that thick iron-rich oxide layers were found in the interior of the coarse grains and thin Cr_2O_3 layers were observed on the grain boundary areas. However, a homogeneous Cr-rich oxide layer covered the whole surface of the fine-grained sample [2]. Basu et.al suggested that the substrate with a small grain size facilitated the formation of a uniform silica layer that enhanced the oxidation resistance of an iron-based austenitic alloy [3]. The oxide formed on the grain-refined substrate only had a different morphology, chemical composition with that formed on the coarse-grained substrate while the oxidation kinetics of them were similar for alloy P2000 [6].

On the contrary, it was reported that the oxidation rate increased with the decreasing of grain size for an iron-based alloy with 2.25 wt% of Cr at 550 ℃ [4]. The authors suggested that the decreasing of grain boundary densities attributed to the lower inter-granular diffusion of ions. In another case, the coarse-grained 9Cr-1Mo alloy was more spallation resistance than the fine-grained substrate at 700 ℃ [136]. Therefore, the influence of grain size on the oxidation behavior of materials is still a controversial area that needs more investigations.

Furthermore, the formation of the Cr-rich oxide layer highly depends on the Cr content in the substrate. It was reported that 12 wt% content of Cr in the alloy is necessary to form a homogeneous and continuous protective Cr-rich oxide layer [57]. Therefore, the grain refinement processes might have different effects on the alloys with different contents of Cr. Nevertheless, the comparison study of grain sizes on the oxidation behavior of low and high Cr content alloys were seldom reported.

Finally, until now, the main methods of producing alloys with different grain sizes are through different deformation processes followed by various heat treatments. However, the preparation processes may change the textures of the alloys and texture also affects the oxidation resistance that was never considered in the previous works [137]. Therefore, the objective of present work

is to investigate the effect of grain size on the oxidation behavior of low and high Cr content alloys with the consideration of texture.

3.4 Experimental

Two Ni-based Hastelloys 230 and N were used in this work. The nominal chemical composition of Hastelloy230 is displayed in Table 2.1 and that of Hastelloy N is depicted in Table 3.1. Clearly, the Cr content in these two alloys are different and therefore Hastelloy 230 was used as high Cr alloy and Hastelloy N was used as low Cr alloy in present work.

Table 3.1 Nominal chemical composition of Hastelloy N (wt %)

	Ni	**Cr**	**W**	**Mo**	**Fe**	**Co**	**Mn**	**Al**	**C**	**Si**	**Cu**
N	Bal	7	0.5	16	5	0.2	0.8	0.35	0.08	1	0.35

To manufacture the substrates with different grain sizes, cold rolling processes followed with different heat treatments were used. In the case of Hastelloy 230, the as-received sample was used as coarse grain substrate which was cold rolled and annealed at 1200 ℃ for 30 min that was then named as coarse-grained 230 (CG230). The fine-grained 230 (FG230) was produced through rolling the as-received sample with a 70 % thickness reduction and annealing at 1000 ℃ for 40 min. For Hastelloy N, the as-received substrate was cold rolled to 70 % thickness reduction. Then, the coarse-grained (CGN) substrate was obtained by annealing the rolled substrate at 1100 ℃ for 2 h. The fine-grained N (FGN) was prepared by annealing the rolled sample at 1000 ℃ for 2 min.

To prepare samples for the oxidation tests, the manufactured substrates were cut into small pieces with dimensions of 18 × 12 × 0.5 mm. A hole with a diameter of 0.15 mm was drilled in each sample which allowed us to hang the sample in a crucible by a 0.08 mm diameter ceramic rod. All of the samples were ground with silicon carbide papers up to 1200 grit. To measure the grain sizes and textures of the samples, some of the samples were polished with 3 μm and 1 μm polishing solution and a BUEHLER Vibromet 2 vibratory polisher for 24 h. Then EBSD was used to measure the grain size distributions and microstructures of the prepared samples. Furthermore, the macro-textures of the prepared samples were measured by a D8 Bruker

discovery XRD with Cr irradiation. Two incomplete pole figures of (111) and (200) were used to calculate IPFs of all the samples.

For oxidation test, all the polished samples were ultrasonically cleaned in acetone for 10 min and washed with deionized water and alcohol. Then all the washed samples were fast dried and hold in the desiccator for 24 h before any further tests. Then all of the samples were suspended in the crucible and inserted into a high-temperature box furnace at the same time. The prepared samples of Hastelloy 230 and N were oxidized at 900 ℃ and 800 ℃, respectively. To test the oxidation kinetics of the alloys, the samples were regularly taken out from the furnace with interval times of 50 h, 100 h, 300 h, 500 h, 700 h and 1000 h. A Mettler Toledo XS205 analytical balance was used to measure the masses of the samples before and after oxidation. Three samples were prepared and the average mass gain was used for samples oxidized for 500 and 1000 h to show the repeatability of the oxidation process.

Finally, the XRD was used to determine the oxide phases of all the samples after oxidation. A SEM was used to characterize the surface and cross-section morphology of the oxidized samples. In the case of preparing the cross-sectional sample, the oxidized sample was firstly electro-plated with nickel which was assumed to protect the oxide from removal during the following polishing process. Then the Ni-plated sample was mounted with conductive resin powders and polished with the polishing process described above for further energy-dispersive spectroscopy (EDS) and EBSD analysis.

3.5 Results and Discussions

3.5.1 Characterization of the prepared samples

Fig. 3.1 shows the microstructures and grain size distributions of the prepared CG230 and FG230. Fig. 3.1 (a) and (b) show the orientation images of the CG230 and FG230. Obviously, it is observed that the grain sizes of CG230 and FG230 are significantly different while the textures are similar. Fig. 3.1 (c) and (d) depict the grain size distributions of CG230 and FG230 measured from the orientation image mappings. The misorientation angle higher than 15 °is defined as a grain boundary and the twin boundaries are disregarded to calculate grain size. The average grain sizes of CG230 and FG230 are 35.4 μm and 3.9 μm, respectively. The IPF triangles representing the textures of the CG230 and FG230 are displayed as inset images in Fig. 3.1 (c) and (d). The

maximum texture intensities of CG230 and FG230 are 1.9 and 1.8 times of random texture which indicates that no strong preferential orientations are formed.

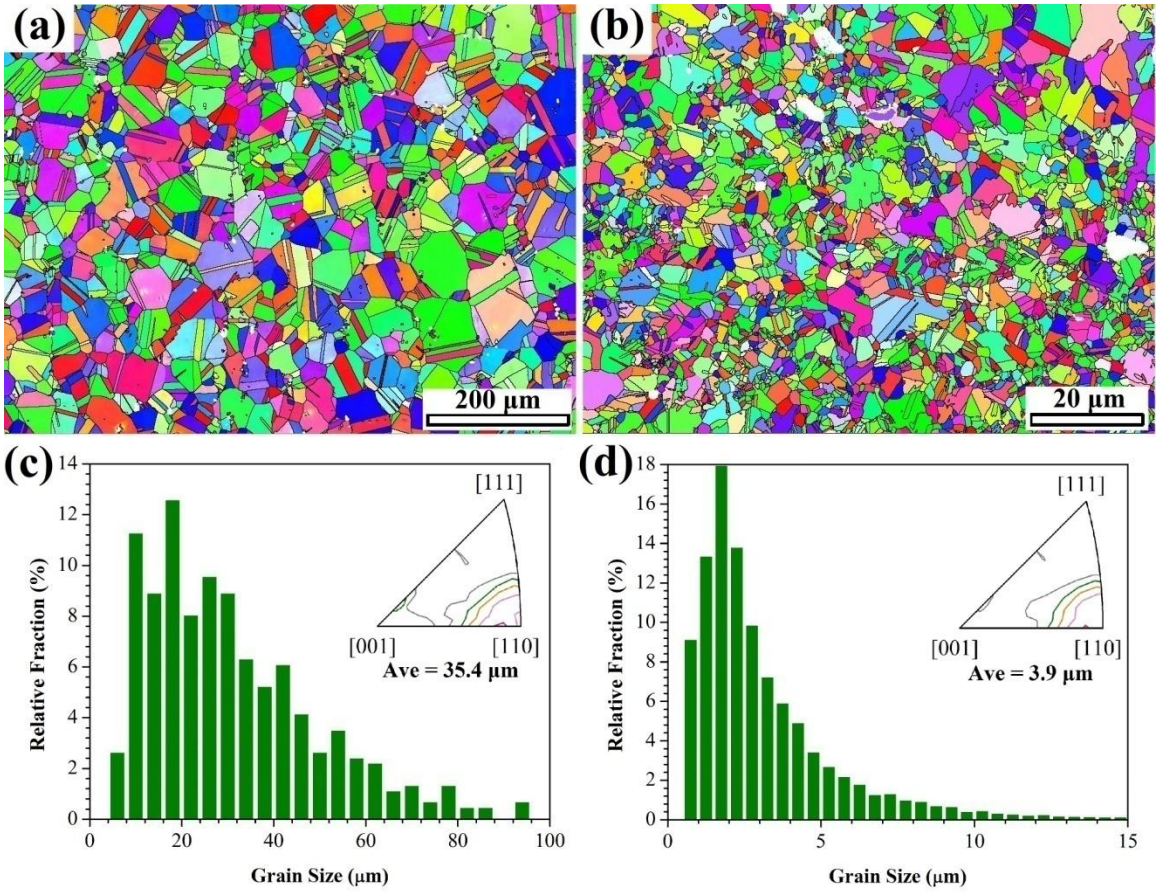

Fig. 3.1 Microstructure and grain size distribution of alloy 230: orientation image mapping (OIM) of (a) CG230 and (b) FG230; grain size distribution of (c) CG230 and (d) FG230.

Identically, Fig. 3.2 (a) and (b) display the orientation image mappings of the produced CGN and FGN. The grain size distributions without considering the twin grain boundaries measured from these images are presented in Fig. 3.2 (c) and (d). The calculated average grain sizes for the CGN and FGN are 51.6 µm and 4.7 µm. The IPF triangles of the CGN and FGN are also presented as inset images in Fig. 3.2 (c) and (d). Similar textures are observed for CGN and FGN since the maximum texture intensities of CGN and FGN are 1.8 and 2 times of the random grain orientation distribution.

Therefore, it can be concluded that the samples with different grain size and similar textures can be obtained through cold rolling and heat treatments for both alloy 230 and N.

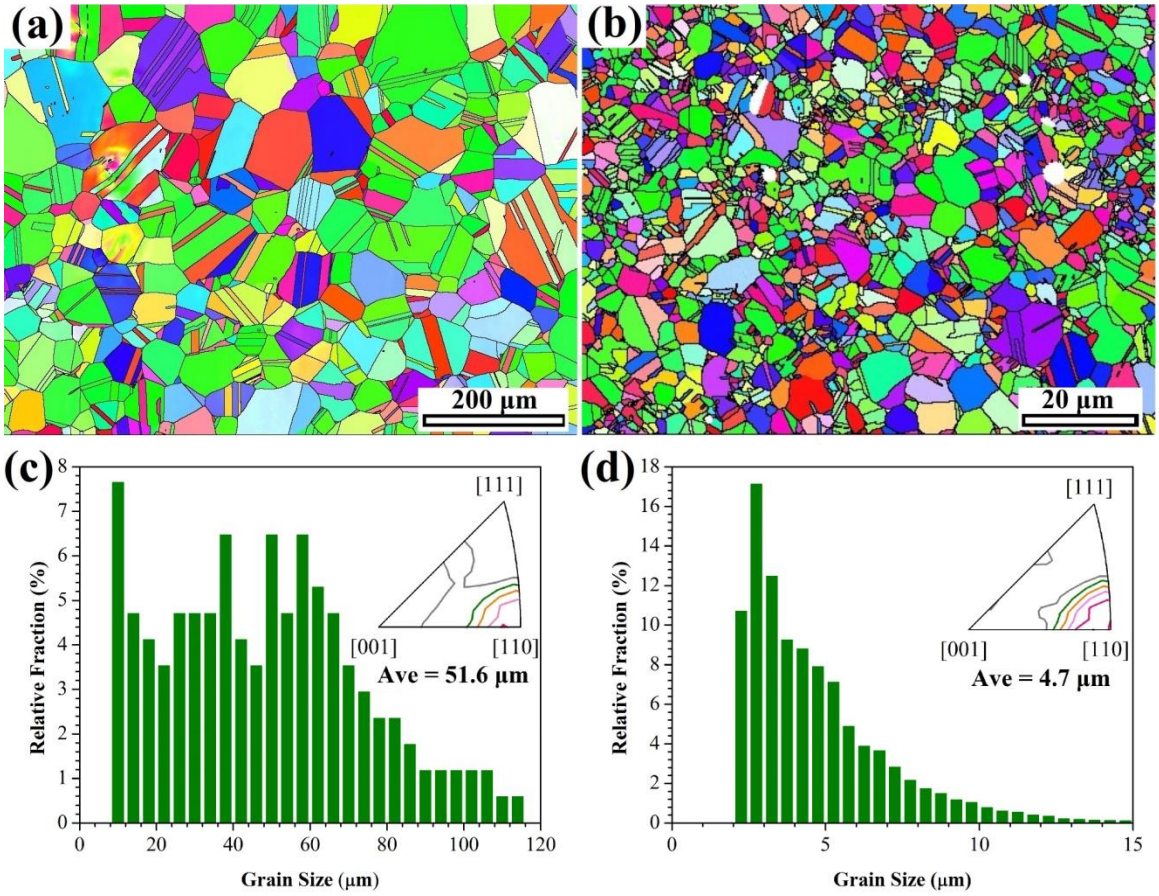

Fig. 3.2 Microstructure and grain size distribution of alloy N: orientation image mapping (OIM) maps (a) CGN and (b) FGN; grain size distribution of (c) CGN and (d) FGN.

3.5.2 Effect of grain size on the oxidation kinetics

Fig. 3.3 (a) and (b) show the oxidation kinetics of CG230, FG230, CGN and FGN. The oxidation kinetics of the CG230 and FG230 obtained similar trends with extending of exposure period as seen in Fig. 3.3 (a). The error bar shows the standard deviation of the mass gain of the oxidized samples. All of the substrates fast oxidized at the initial stage. Then, the oxidation processes of CG230 and FG230 gradually changed into the steady stage at which the mass gains for alloys increased slowly. However, the FG230 obtained a slightly higher mass gain than the CG230 at the later stage. This difference indicates that the grain size had little influence on the oxidation behavior of alloy 230 which has high Cr content.

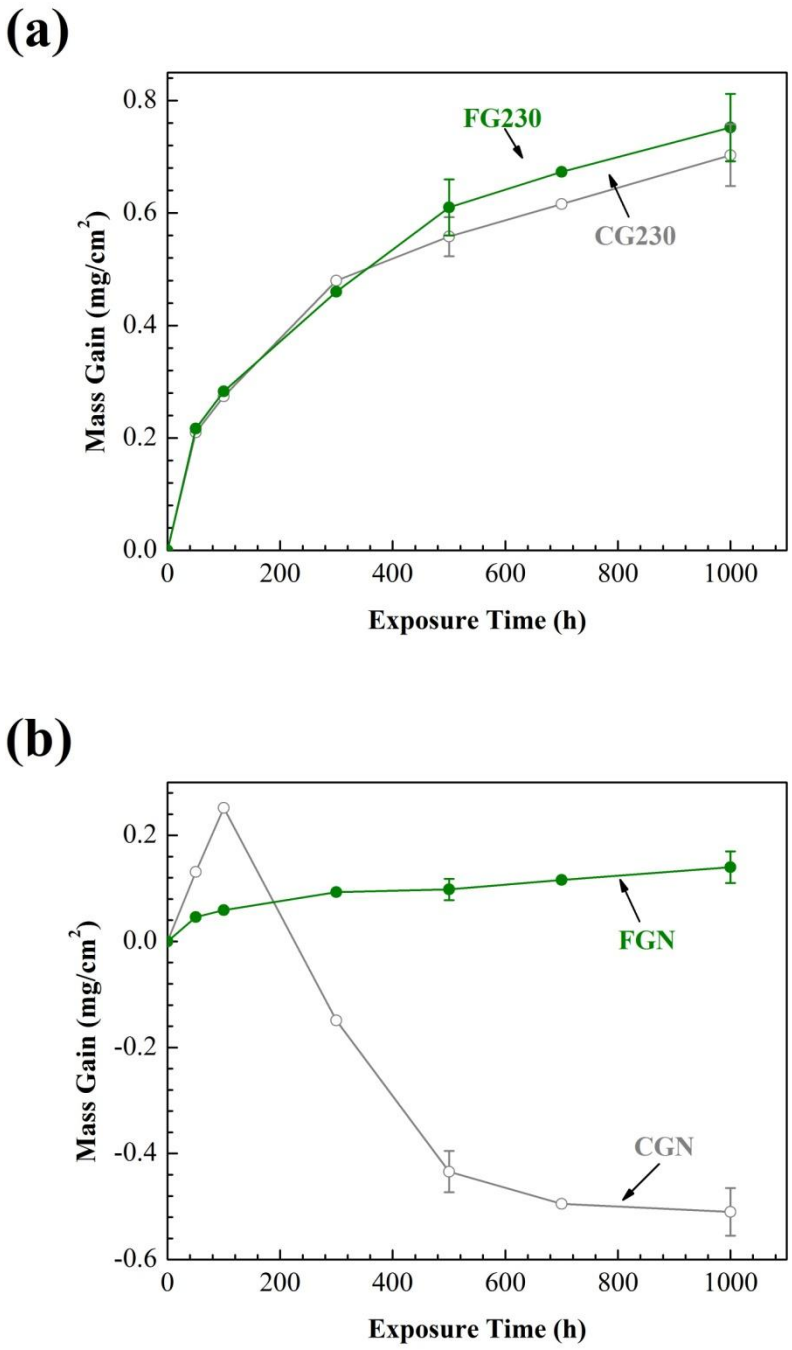

Fig. 3.3 Oxidation kinetic of alloys: (a) CG230 and FG230; (b) CGN and FGN;

In contrast, the oxidation behavior of alloy N with different grain sizes and similar textures are obviously different as seen in Fig. 3.3 (b). Similarly, both of the CGN and FGN fast oxidized at the initial stage where the mass gains of the samples rapidly increased. The FGN obtained most of its mass gain in the first 100 h which is almost five times lower than that of the CGN sample.

The lower mass gain clearly indicates that the grain refinement process enhanced the oxidation resistance of alloy N. Furthermore, a striking difference is found after oxidation the CGN and FGN for more than 100 h. Mass loss started to occur on the CGN which may because of the spallation of the oxide layers. Oppositely, the oxidation kinetic of the FGN steadily transformed to the steady stage and the mass gain of FGN increased slowly. The slow increasing of the mass gain implies that protective oxide layers formed on top of the FGN and no spallation are observed after oxidation of the FGN up to 1000 h. Therefore, this difference suggests that the adhesion of the oxide layer formed on the FGN was also enhanced.

3.5.3 Characterization of oxide

3.5.3.1 Surface Morphology

Fig. 3.4 shows the surface morphology of the CG230 and FG230 samples after oxidation up to 1000 h. Fig. 3.4 (a) to (f) depicts the surface morphology of the CG230 after oxidation for 50, 100, 300, 500, 700 and 1000 h. Fig. 3.4 (g) to (l) shows the surface morphology of the FG230 after oxidation. As can be seen from Fig. 3.4 (a) and (g), two different types of morphology are observed with the top granular-grained oxide and the flat morphology beneath it for both the CG230 and FG230 after oxidation for 50 h. Then, the granular oxides spread over the outermost surface of the oxidized samples with the extending of oxidation period. Furthermore, the grain sizes of the granular grains also increased with the increasing oxidation time. Different surface morphology was observed after oxidizing the CG230 and FG230 for 700 h. Oxide spallation started to occur on the CG230 while no spallation was found on the FG230 as seen in Fig. 3.4 (e) and (k). The oxide spallation on the CG230 confirms the slightly smaller mass gain observed than that of the FG230 after oxidation for 500 h shown in the Fig. 3.3 (a). However, the surface morphology and mass gain of the CG230 and FG230 tended to show the similar trends which indicate that the grain refinement process will not have a significant effect on the oxidation behavior of alloy 230. In other words, the grain refining might not an efficient way to enhance the oxidation behavior of the alloys with high Cr contents.

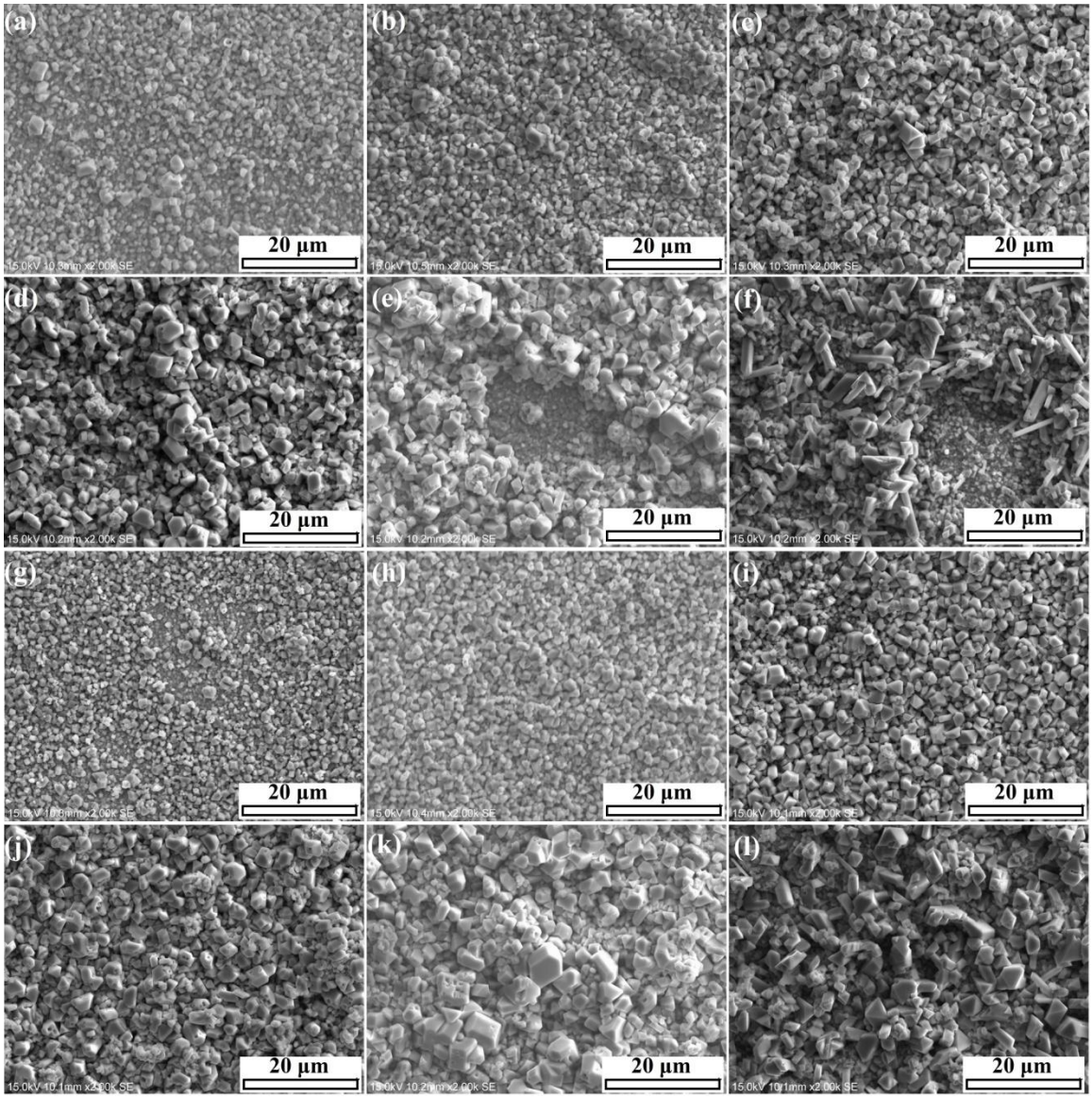

Fig. 3.4 Surface morphology of CG230 and FG230 after oxidation at 900 ℃: oxidation of CG230 (a) to (f) and oxidation of FG230 (g) to (l) for 50, 100, 300, 500, 700 and 1000 h.

Fig. 3.5 depicts the surface morphology of the oxidized CGN up to 1000 h. Fig. 3.6 shows the higher magnification image of the CGN after oxidation for 50, 100, 300 and 500 h. Oxide islands started to form on the sample surface after oxidation for 50 h as seen in Fig. 3.5 (a). It is worth to mention that some oxide islands tended to form inside the grains and some formed on the grain boundaries as seen in Fig. 3.5 (a). Two different morphology of oxide was detected at higher magnification as seen in Fig. 3.6 (a). The granular oxides tended to form in the grain interior and the smooth oxides were prone to appear on the grain boundary areas when combing Fig. 3.5 (a)

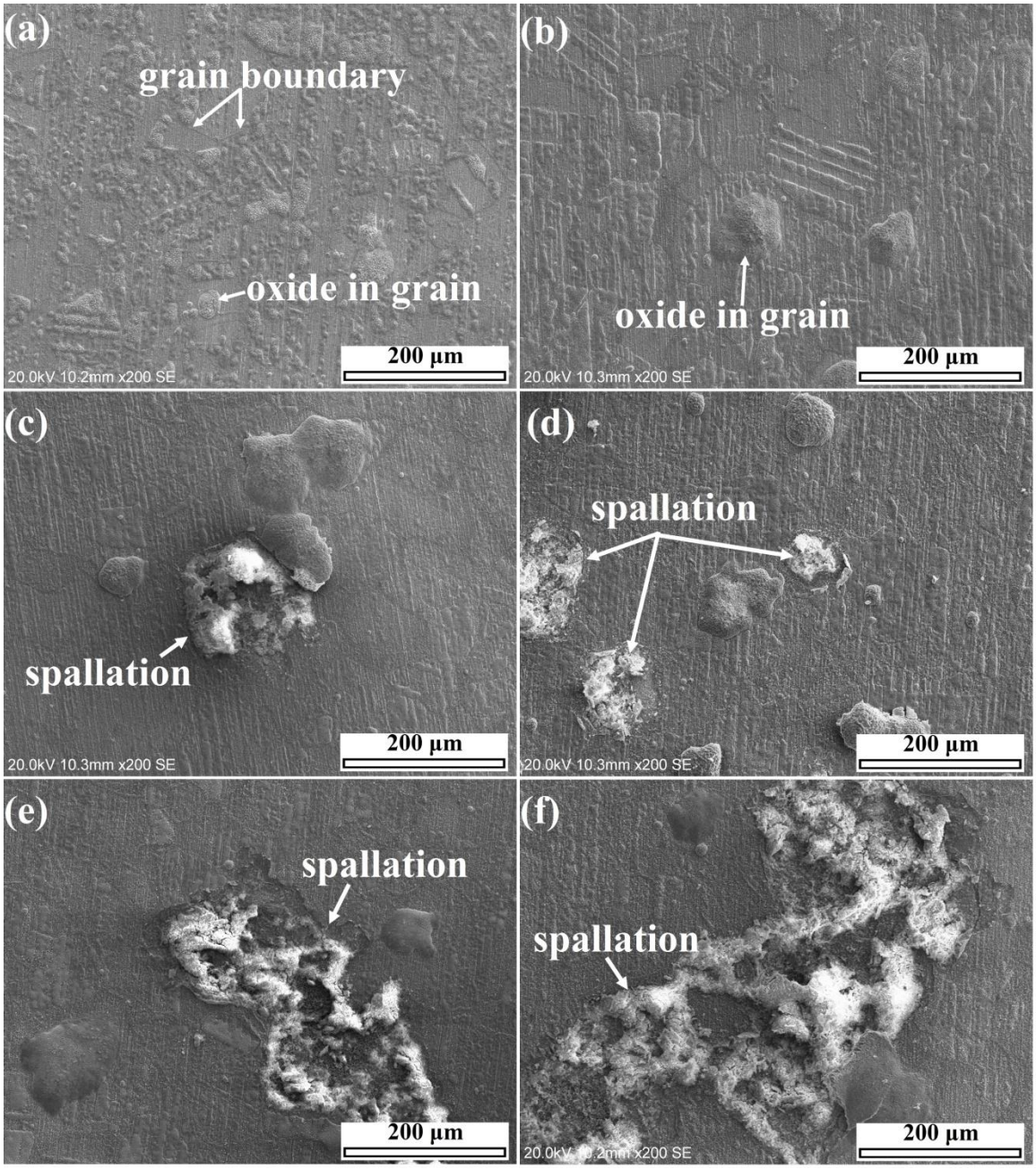

Fig. 3.5 Surface morphology of CGN after oxidation up to 1000 h at 800 ℃: (a) 50 h; (b) 100 h; (c) 300 h; (d) 500 h; (e) 700 h and (f) 1000 h.

with Fig. 3.6 (a). This phenomenon was more pronounced on the CGN sample after oxidation for 100 h as seen in Fig. 3.5 (b). On the one hand, the formation of oxides with different surface morphology on different grains may depend on the grain orientations as discussed in our previous works [138,139]. It was suggested that the crystallographic orientation had a critical effect on the oxidation behavior of face centered crystal (FCC) alloys [139]. The grain

orientation would affect both the oxide formation rate and the morphology of the oxide especially at the initial stage of the oxidation process. On the other hand, the formation of different oxide is related to the oxidation mechanism of the alloy which will be discussed in detail in the following sections.

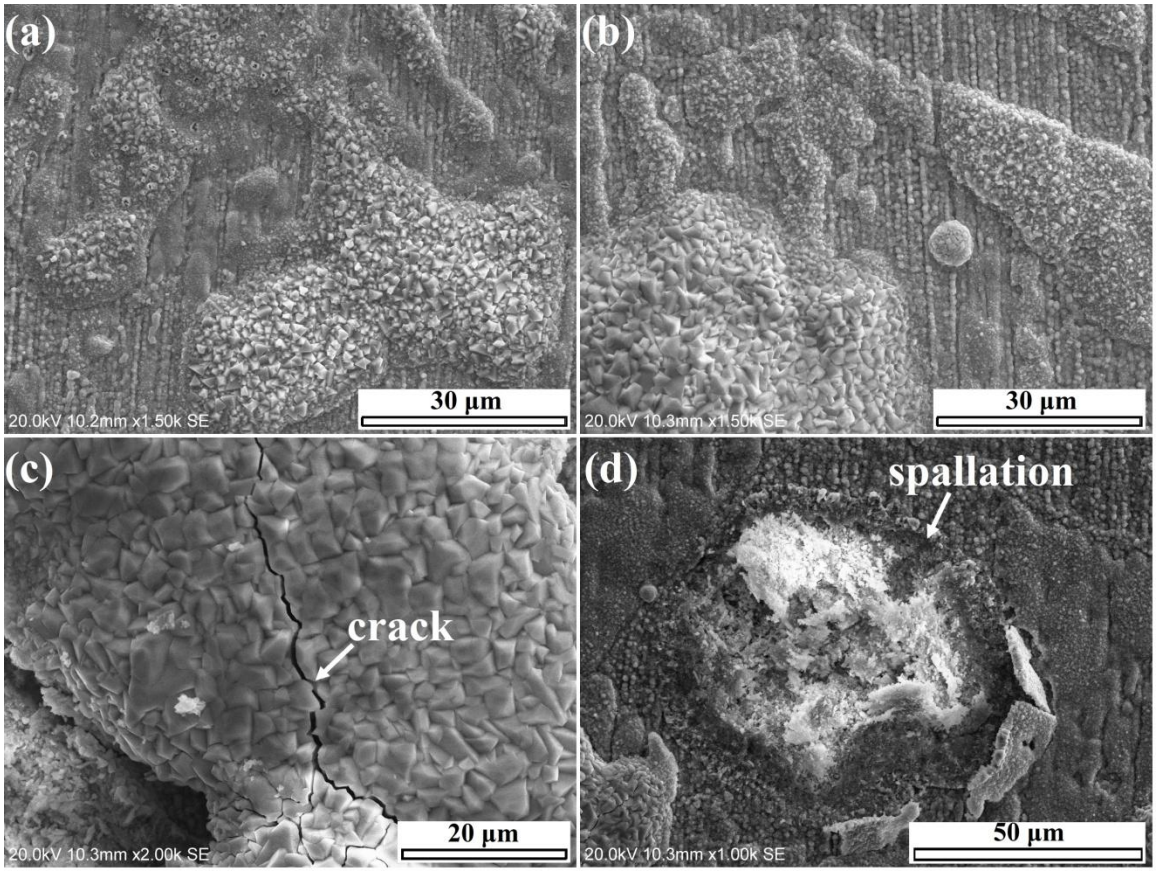

Fig. 3.6 High magnification surface morphology of CGN after oxidation for (a) 50 h; (b) 100 h; (c) 300 h and (d) 500 h.

Furthermore, oxide spallation started to happen after oxidizing the CGN for 300 h which confirms the mass loss detected through oxidation kinetics shown in Fig. 3.3 (b). It is noticed that the spallation only happens in the areas where the granular oxides were present as seen in Fig. 3.5 (c) to (f). Fig. 3.6 (c) shows a higher magnification image of the granular oxide area after oxidation for 300 h. Clearly, some micro-cracks were observed in the granular oxide area which indicates that the oxide layer containing granular oxides is not protective. These micro-cracks will facilitate the penetration of the oxygen into the substrate which will accelerate the oxidation rate of the alloy. Consequently, thicker oxide islands would form as shown in Fig. 3.5

(c) to (f) and possibly the penetration of the oxygen would result in the formation of internal oxide that will diminish the adhesion between the oxide layer and the substrate. As a result, the oxide islands scaled off from the substrate which is confirmed in Fig. 3.6 (d).

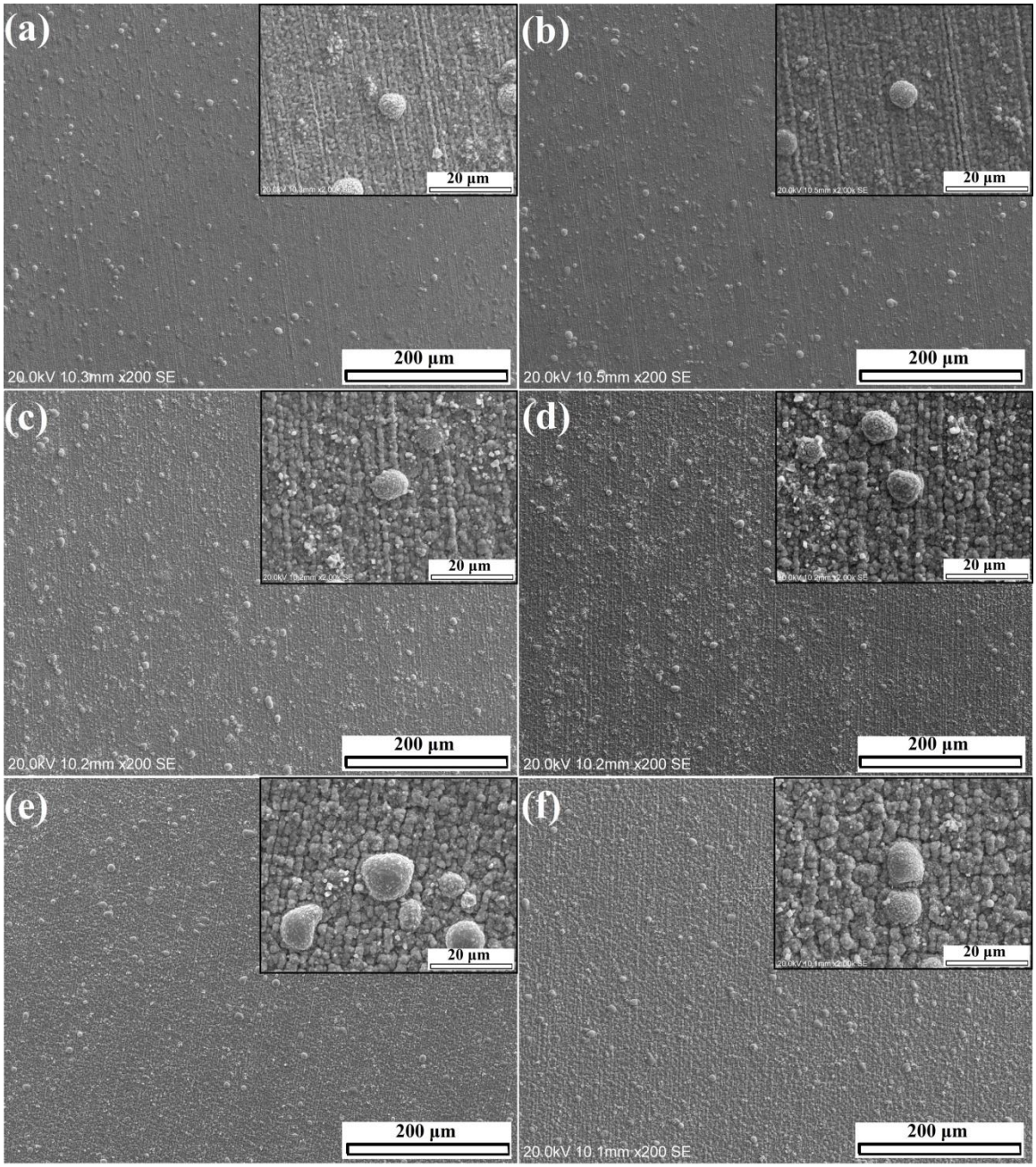

Fig. 3.7 Surface morphology of FGN after oxidation up to 1000 h at 800 ℃: (a) 50 h; (b) 100 h; (c) 300 h; (d) 500 h; (e) 700 h and (f) 1000 h.

Fig. 3.7 demonstrates the surface morphology of the FGN after oxidation at 800 ℃ for various periods. The higher magnification morphology of the oxidized sample is displayed as an inset image in each figure. As seen in Fig. 3.7 (a), some nodular oxides formed on top of a uniform oxide layer which covered the whole sample surface after oxidation for 50 h. The grain size of the uniform oxide layer gradually increased and the surface morphology becomed dense with the extending of oxidation time. However, the numbers of the nodules were not changing too much and only a slight increasing was observed for the sizes of the nodules. More importantly, no oxide spallation was seen after oxidizing the FGN for 1000 h which indicates that the formed oxide layers are protective. Consequently, the protective oxide layers could act as diffusion barriers which separated the substrate from the oxidizing environment that reduced the oxidation rate of alloy FGN. Therefore, it is concluded that the grain refinement process not only enhanced the oxidation resistance but also improved the adherence of the oxide layers of alloy N.

3.5.3.2 Identification of the oxide phases

To learn more about the oxidation mechanisms of the coarse and fine-grained substrates, the cross-sectional EDS analysis and XRD measurements were used to define the phases of the oxides formed on all the samples. Fig. 3.8 shows the cross-sectional EDS mapping and line scan measurement of the CG230 after oxidation for 50 h. A high-resolution surface morphology of the 50 h oxidized sample is also displayed in Fig. 3.8. It is clear to see that two oxide layers formed on the sample surface in the EDS mapping. The first layer is composed of Mn, Cr and O, while the second layer mainly contains Cr and O. From the line scanning along the red arrow marked in the cross-sectional SEM image, the first layer is recognized as $MnCr_2O_4$ with a thickness approximately 0.4 μm and the second layer is Cr_2O_3 with a thickness around 1.1 μm. Therefore, it can be concluded that the top granular oxide is $MnCr_2O_4$ and the flat area beneath it is Cr_2O_3 as marked in the surface morphology image.

Fig. 3.9 depicts the cross-section elemental composition and a high-resolution surface morphology image of the FG230 after oxidation for 50 h. Similarly, two oxide layers can be distinguished from the EDS mapping of the FG230. The first layer contains Mn, Cr and O and the second layer is composed of Cr and O which indicates the formation of $MnCr_2O_4$ and Cr_2O_3. The $MnCr_2O_4$ layer has a thickness of approximately 0.6 μm and the inner Cr_2O_3 layer has a thickness of 0.9 μm. In addition, the different types of oxides can be easily differentiated from

the different surface morphology as marked in the SEM image. The oxide layer formed on the FG230 has an almost same thickness as that formed on the CG230. Therefore, the similar thicknesses of oxide layers formed on these substrates confirm their similar oxidation kinetics as shown in Fig. 3.3 (a).

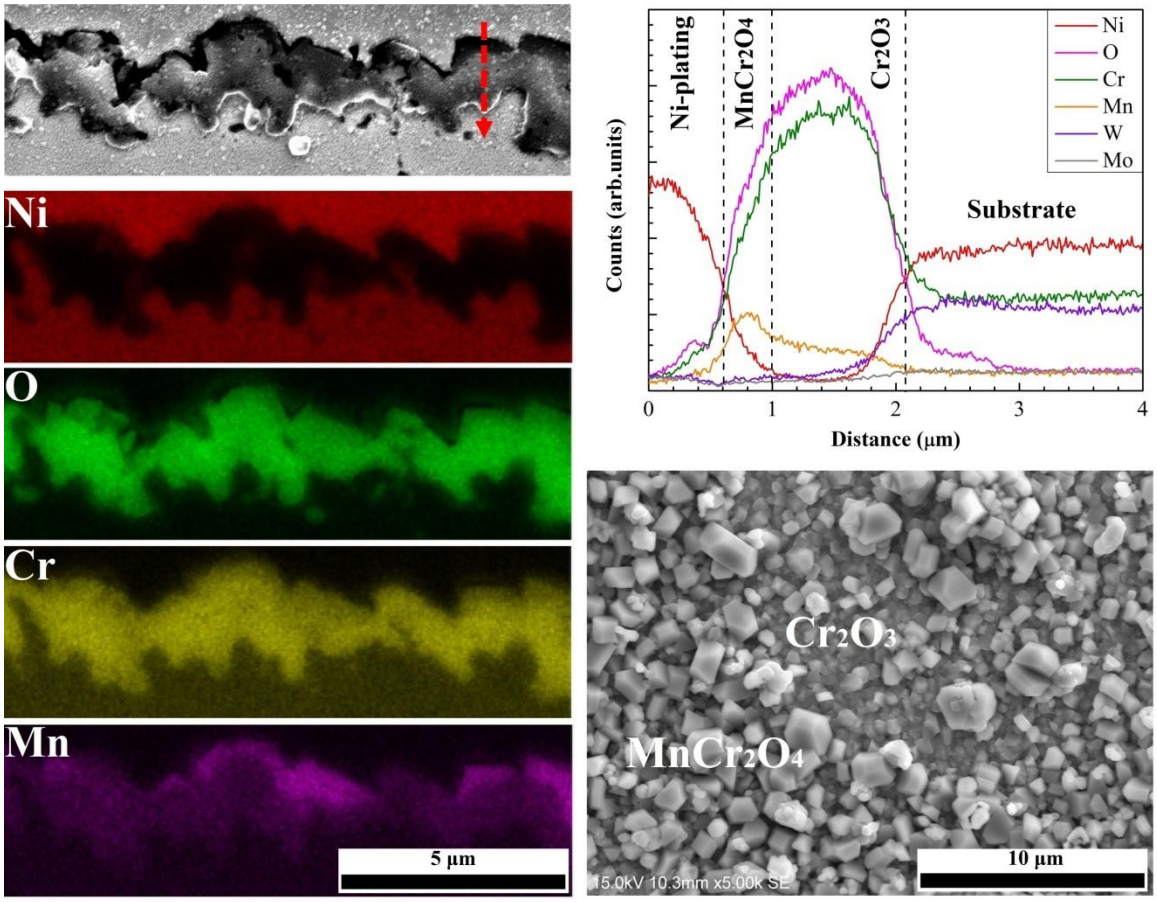

Fig. 3.8 Cross-sectional EDS mapping and line scan of CG230 after oxidation for 50 h at 800 ℃.

Fig. 3.10 illustrates the cross-sectional EDS results and a high-magnification surface morphology image of the CGN after oxidation for 50 h. Clearly, three oxide islands are observed from the cross-section morphology. In the case of the EDS mapping, the oxide islands can be separated into three oxide layers. The external oxide layer is composed of Ni and O, the middle layer contains the Fe and O while the internal layer contains Mn, Cr and O. For the EDS line scanning along the red arrow, the external layer is recognized as NiO and the central and internal layers can be considered as a mixed oxide layer. The mixed-oxide layer may contain Fe_2O_3, Cr_2O_3, $MnFe_2O_4$ or $MnCr_2O_4$ as expected from the line scanning result. The thickness of the NiO layer

is approximately 0.8 μm and that of the mixed-oxide layer is around 1.7 μm. Furthermore, an iron-rich oxide layer forms inside each oxide island. The formation of iron-rich oxide may have detrimental effects on the oxidation resistance of the substrate since it is generally loose and porous. In addition, it is clear to see the NiO islands and the mixed-oxide that is not covered by NiO from the surface morphology image. The thin oxide layer between the neighboring islands is composed of Mn, Cr and O which indicates the possible presence of Cr_2O_3 and/or $MnCr_2O_4$.

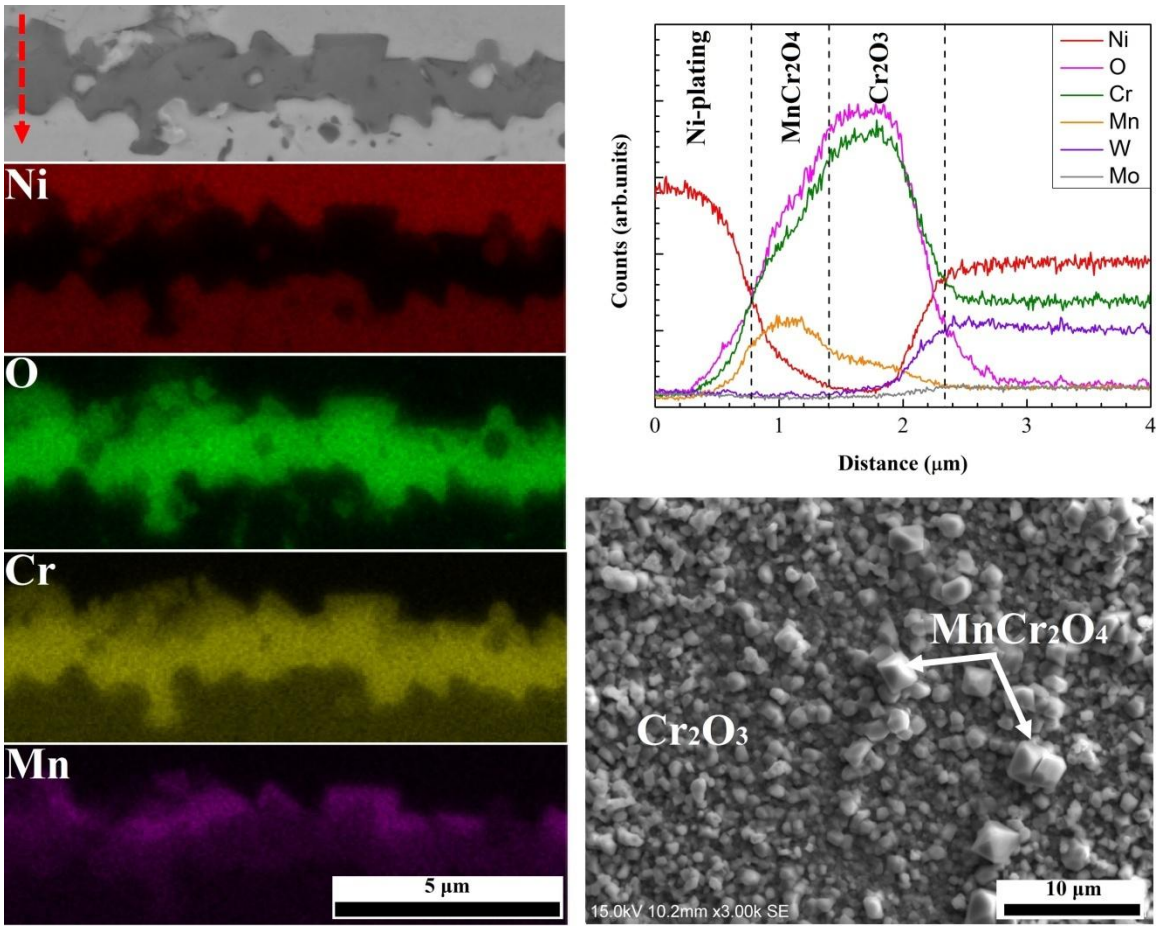

Fig. 3.9 Cross-sectional EDS mapping and line scan of FG230 after oxidation for 50 h.

Fig. 3.11 represents the cross-sectional EDS measurements and a high-resolution surface morphology of the FGN after oxidation for 50 h. Clearly, the oxide layer formed on the FGN is more continuous and homogeneous than that formed on the CGN as seen in the cross-sectional morphology image. A nodular oxide with a dimension approximately 10 μm is also observed in the cross-sectional image. From the EDS mapping result, it is seen that the Mn, Cr and O are concentrated in the nodular-oxide area and the oxide layer beneath the nodular-oxide is

composed of Cr and O. In the case of the line scanning cross the nodular-oxide, the nodular-oxide is recognized as $MnCr_2O_4$ with a thickness of 0.8 μm. The oxide layer beneath the nodule is defined as a thin Cr_2O_3 layer with a thickness of approximately 0.4 μm. The total oxide thickness is much thinner than that formed on the CGN after oxidation for 50 h which is in agreement with the lower mass gain obtained shown in Fig. 3.3 (b). Here, it is important to mention that NiO and iron-rich oxide are not observed in the EDS mapping. The formation of the thin Cr_2O_3 layer is believed to protect the substrate alloy from the oxidizing environment and will decrease the oxidation rate of the FGN.

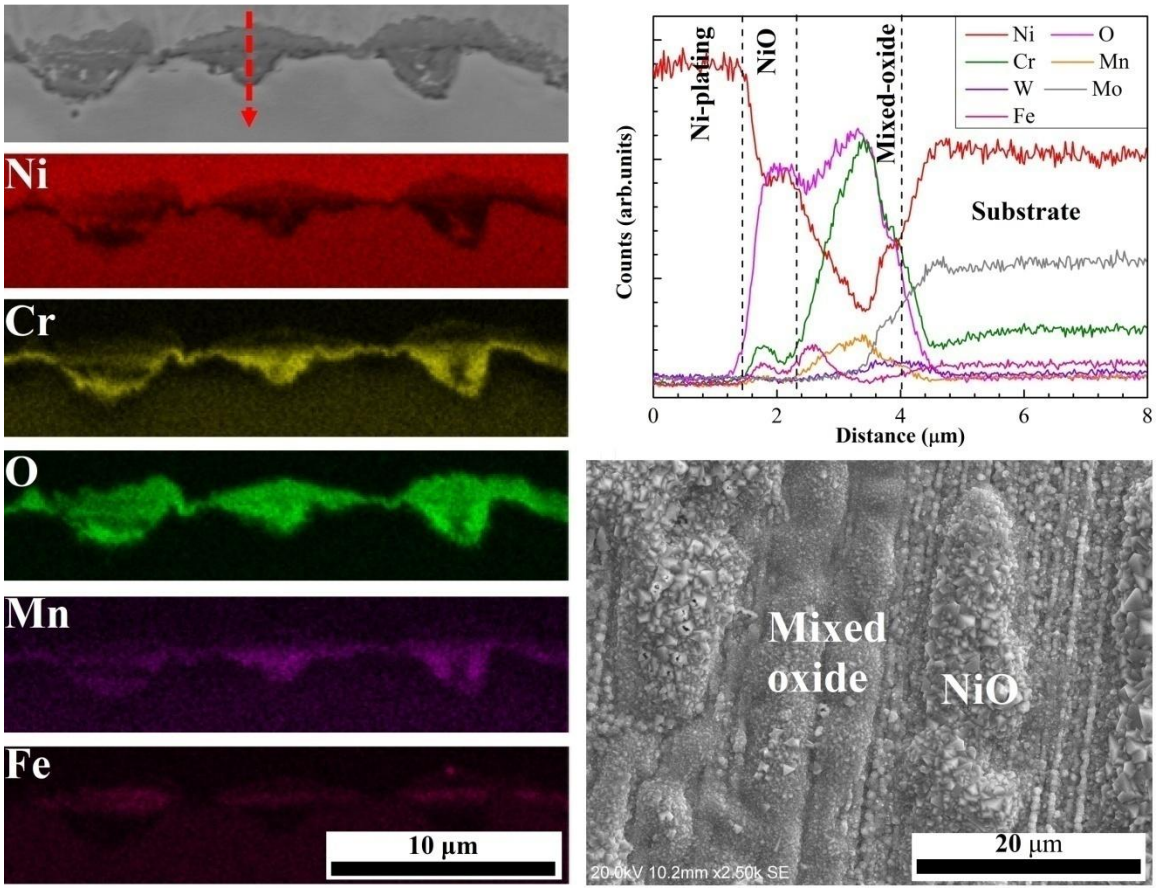

Fig. 3.10 Cross-sectional EDS mapping and line scan of CGN after oxidation for 50 h.

Fig. 3.12 presents the XRD patterns of the alloy 230 and N after oxidation at 800 and 900 ℃ for 1000 h. In the case of alloy 230, the same diffraction patterns are detected for CG230 and FG230 which implies that the grain refinement process will not change the chemical composition of the oxide formed on alloy 230. The detected $MnCr_2O_4$ and Cr_2O_3 phases verify the EDS mapping results shown in Fig. 3.8 and Fig. 3.9.

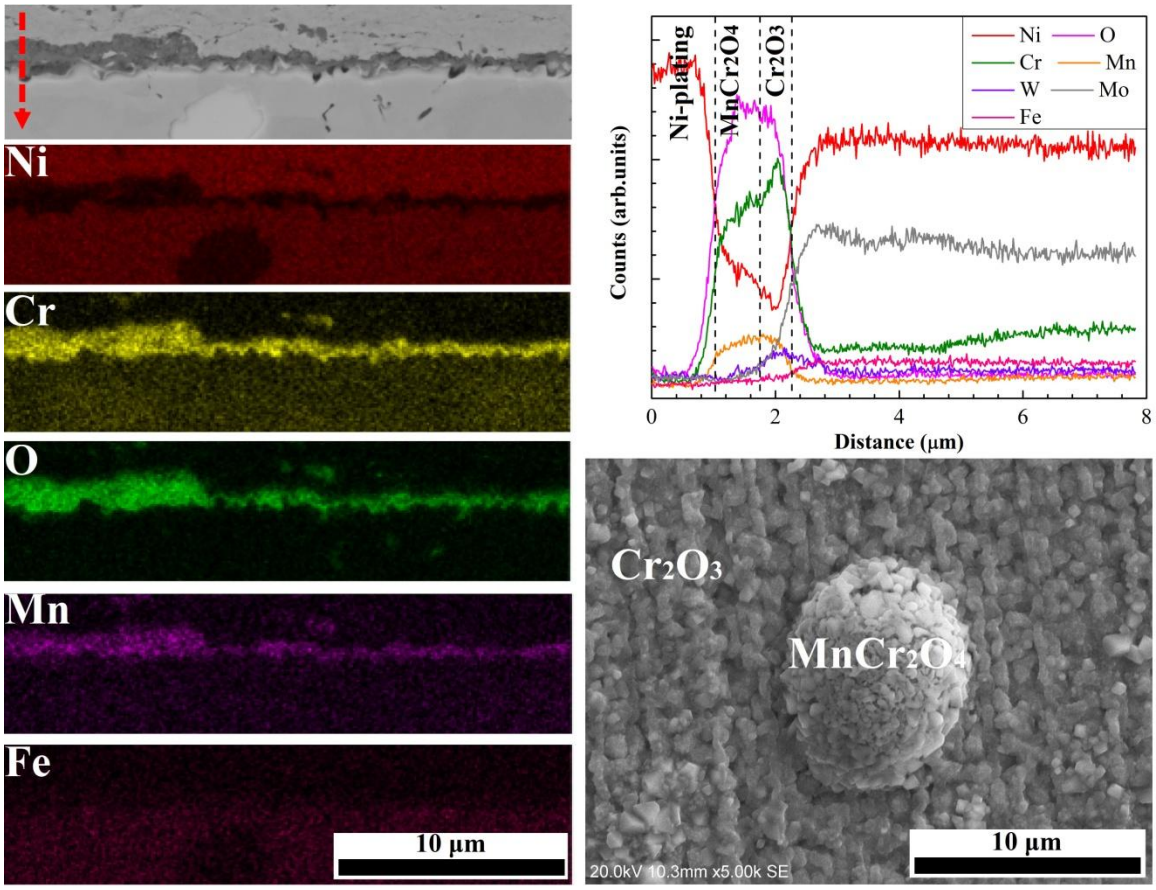

Fig. 3.11 Cross-sectional EDS mapping and line scan of FGN after oxidation for 50 h.

Fig. 3.12 (b) represents the diffraction patterns of the CGN and FGN. Generally, it is difficult to differentiate the Cr_2O_3 from Fe_2O_3 and $MnCr_2O_4$ from $MnFe_2O_4$ just based on the XRD measurements owing to their similar crystal parameters. Nevertheless, with the EDS results presented above, we can see that mixed oxides with Cr_2O_3 and Fe_2O_3, $MnCr_2O_4$ and $MnFe_2O_4$ formed on the CGN and Cr_2O_3 and $MnCr_2O_4$ were detected on FGN. More importantly, two obvious diffraction peaks of NiO were detected for the CGN while these peaks were not observed on the FGN. An enlarged image as displayed in Fig. 3.12 (b) clearly demonstrates the formation of NiO. The strongest peak of NiO indicates that a very thick NiO layer forms on the CGN after oxidation at 800 ℃ for 1000 h.

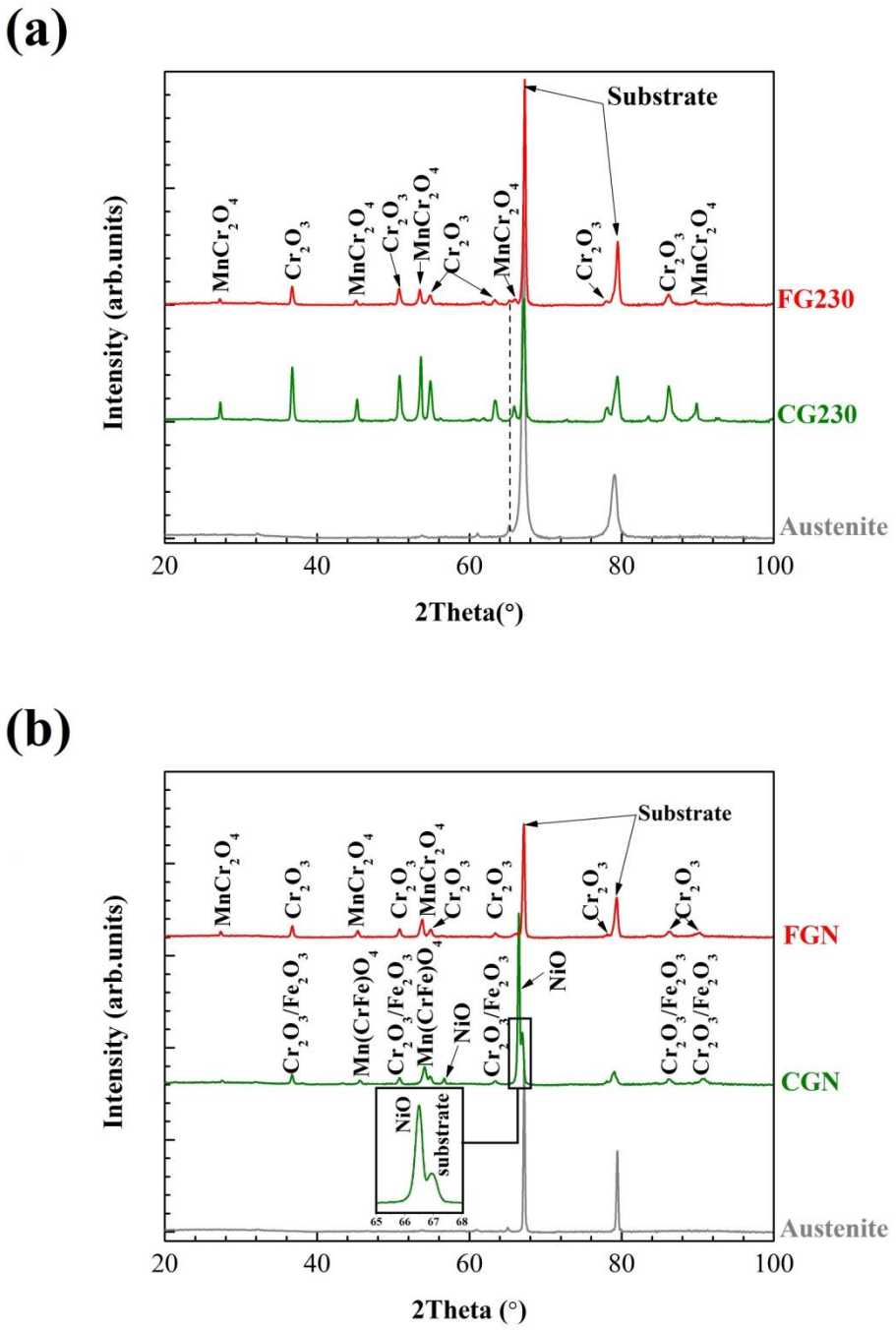

Fig. 3.12 XRD patterns of CG230, FG230, CGN and FGN after oxidation for 1000 h.

3.5.4 Oxidation mechanisms

In the above sections, the grain-refined samples were prepared to investigate the effect of grain size on the oxidation behavior of Hastelloy 230 and N. In the case of Hastelloy 230, the as-received sample was cold rolled with 70 % thickness reduction and annealed at 1000 ℃ to

prepare the FG230. However, the CG230 and FG230 tended to show similar oxidation kinetics and they had the similar mass gains even after oxidation for 1000 h. Furthermore, similar surface morphology was observed on the CG230 and FG230 after oxidation for various times. The oxide phases formed on the CG230 and FG230 are Cr_2O_3 and $MnCr_2O_4$. The obtained results imply that the grain refinement process only has a slight influence on the Hastelloy 230 with high Cr content.

For the high Cr content alloy, it is reasonable to assume that the formation of a protective Cr_2O_3 layer is possible even with low grain boundary density since there is a sufficient amount of Cr to maintain the formation of oxide. Actually, we observed that uniform Cr_2O_3 layers formed on both the CG230 and FG230 after oxidation for 50 h as shown in Fig. 3.8 and Fig. 3.9. The total thicknesses of the oxide layers formed on these two alloys are approximately 1.5 μm. The thickness of the Cr_2O_3 layer formed on the FG230 is 0.9 μm while it is 1.1 μm on the CG230 which is even thicker than that formed on the FG230. The Cr_2O_3 is well-known as dense and compact which can act as a protective barrier that separates the substrate alloy form the oxidizing environment [96]. Therefore, the fast formation of the Cr_2O_3 layer at the initial stage may result in the similar oxidation behavior of the CG230 and FG230. Consequently, the oxidation kinetics would be controlled by the ions diffusion through the formed Cr_2O_3 layers. The thin $MnCr_2O_4$ layer formed on top of the Cr_2O_3 may because of the faster diffusion rate of Mn than Cr through the Cr_2O_3 layer. It was reported that the diffusion coefficient of Mn through Cr_2O_3 is almost ten times higher than that of Cr [110]. Therefore, the fast outward diffusion of Mn would result in the formation of Mn-rich oxide on top of the existed Cr_2O_3 layer. However, thermodynamically, the formation of $MnCr_2O_4$ is more favorable than both of Cr_2O_3 or MnO owing to its more negative Gibbs free energy [135]. Consequently, the formed Mn-rich oxide would immediately react with the Cr_2O_3 which resulted in the formation of $MnCr_2O_4$.

For the low Cr content Hastelloy N, the as-received sample was rolled with a 70 % thickness reduction followed with annealing at different temperatures to prepare the CGN and FGN. In contrast with the Hastelloy 230, the grain refinement process results in an entirely different oxidation behavior of the CGN and FGN. Both of the FGN and CGN fast oxidized at the first 100 h but the mass gain of the CGN is almost five times higher than that of the FGN as shown in Fig. 3.3 (b). Furthermore, the oxide spallation happened which resulted in the mass loss of the

CGN after exposure for more than 100 h. On the contrary, the mass gain of the FGN slowly increased and no oxide spallation was observed up to 1000 h oxidation.

In addition, the surface morphology of the oxidized CGN and FGN are totally different as shown in Fig. 3.5 to Fig. 3.7. The thicker oxide layer containing NiO and mixed-oxide formed in the grain interior while a thin Cr-rich oxide is formed at the grain boundary areas in the CGN as shown in the Fig. 3.5 and Fig. 3.6. The thicker oxide layer formed in the center of the grain tended to crack which resulted in the detaching of the oxide layer from the substrate. Fig. 3.13 shows a typical cross-sectional EBSD scan of the CGN after oxidation for 500 h. Four spallation areas are clearly seen in the band contrast (BC) map as marked in Fig. 3.13 (a). Interestingly, all these spallations are in the center of grains as marked in the IPF map shown in Fig. 3.13 (b) which confirms the above observations. Nonetheless, a thin and uniform Cr-rich oxide layer with isolated $MnCr_2O_4$ covers the whole surface of the FGN as shown in Fig. 3.7. The formation of the uniform Cr-rich oxide layer obviously implies that the diffusivity of Cr was enhanced owing to the grain refinement process.

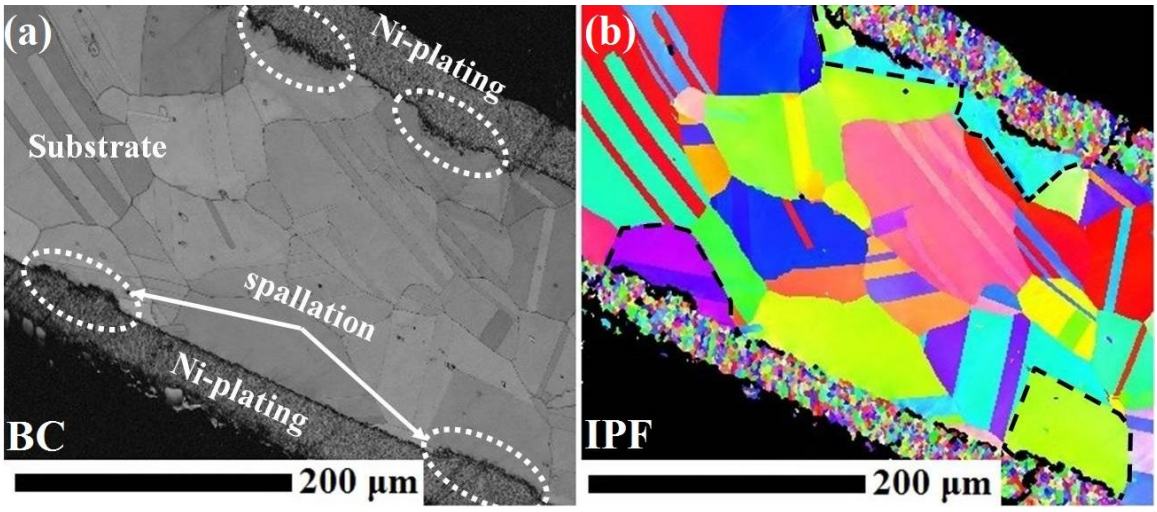

Fig. 3.13 EBSD scan showing the oxide spallation inside grain after oxidation for 500 h.

The decreasing of grain size introduces more grain boundaries in the grain-refined samples. In general, the grain boundaries are believed to show different properties with the bulk materials [137]. Consequently, it is reasonable to see the alloys with different grain sizes have different oxidation behavior especially for alloys with low Cr contents. In the case of low Cr content alloy with large grain size, it will be difficult to produce a uniform Cr_2O_3 layer since at least 12 wt%

Cr is needed [57]. The oxidation process is generally controlled by the diffusion of cations and anions through the oxide layer formed on the alloy surface at high temperature. The grain boundaries were suggested to act as short-circuit paths to transport metal and oxygen through oxide layers [5,140]. Therefore, a higher grain boundary density offering more of such paths will facilitate the diffusion of both cations and anions. Consequently, the facilitated diffusion may result in two possible outcomes. Firstly, the enhanced diffusion of cations like Cr may result in a fast formation of an external oxide layer which will act as a protective layer in the later stage. In the contrast, the strengthened diffusion of anions will benefit the penetration of the oxygen which contributes to the formation of internal oxide at a larger depth. However, the formation of internal oxide is undesirable since it may be detrimental for the adherence of the oxide layer.

In the case of Hastelloy N with 7 wt% Cr, the sample with an average grain size of 50 μm is impossible to be fully covered by Cr_2O_3 layer though the formation of the Cr_2O_3 film was observed on the grain boundary areas. The formation of the Cr_2O_3 layer around the grain boundary areas clearly indicates that the grain boundary diffusion dominated the oxidation process of Hastelloy N at 800 ℃. In contrast, the formation of a uniform Cr-rich oxide layer is possible for a higher grain boundary density substrate as confirmed by the results shown in Fig. 3.11. Consequently, the FGN had a lower oxidation rate and better spallation resistance. To demonstrate the enhancing of diffusion rate with decreasing of grain size, an effective diffusion coefficient D_{eff} composed of lattice diffusion coefficient D_L and grain boundary diffusion coefficient D_{GB} could be used as follows [7]:

$$D_{eff} = fD_{GB} + (1-f)D_L \qquad 3.1$$

where f is the area percentage of grain boundaries which can be represented as $2\delta/d$ if we assuming the grains have cubic structures. δ is the width of the grain boundary and d is the average grain size. For substrate with fine grain size, f is high and therefore the D_{eff} will mainly depend on the D_{GB}. In addition, it was reported that the activation energy of grain boundary diffusion is much lower than that of lattice diffusion and the D_{GB} is much higher than D_L [9,141–144]. For instance, it was suggested that the D_{GB} of Cr through Cr_2O_3 was five to six orders of magnitude higher than that of D_L. Therefore, the equation 3.1 can be rewritten as:

$$D_{eff} = \frac{2\delta}{d} D_{GB} + D_L \qquad 3.2$$

For alloy N, if taking the effective diffusion coefficient D_{eff}^{C} of the CGN (d = 50 μm) as a reference, the D_{eff}/D_{eff}^{C} can be used to describe the evolution of the effective diffusion coefficient with the decreasing of grain size with using δ = 0.5 nm as shown in Fig. 3.14 [7]. Clearly, the effective diffusion coefficient considerably increases with the decreasing of grain size.

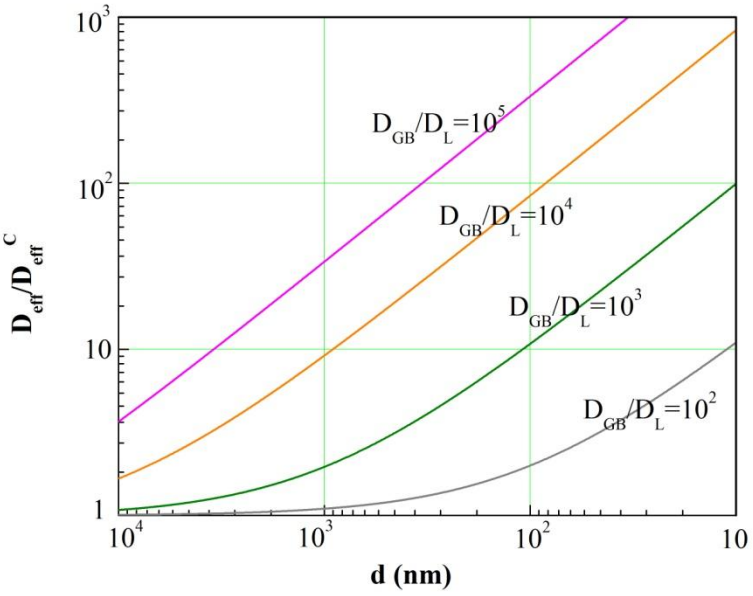

Fig. 3.14 Changes of D_{eff}/D_{eff}^{C} with the average grain size.

According to the discussions presented above, schematic models were developed to demonstrate the oxidation mechanisms of the high and low Cr alloys with coarse and fine grain sizes as shown in Fig. 3.15. For the high Cr content alloy, the Cr-rich oxide formed fast at the initial stage owing to the high affinity and content of Cr. Consequently, uniform and protective Cr-rich oxide layers form on both the coarse and fine-grained substrates. The sufficient supplying of Cr to form the Cr-rich oxide layer was able to minimize the influence of the grain boundary density. Therefore, the substrates with large and small grain sizes would show similar oxidation behavior. Specifically, the oxidation process would be controlled by the diffusion of ions through the formed Cr-rich layer. For instance, the ions like Mn or Fe which diffuse faster than Cr in the Cr_2O_3 layer may control the diffusion process. In the case of Hastelloy 230, the outward

diffusion of Mn ions resulted in the formation of the spinel of $MnCr_2O_4$ for both the CG230 and FG230.

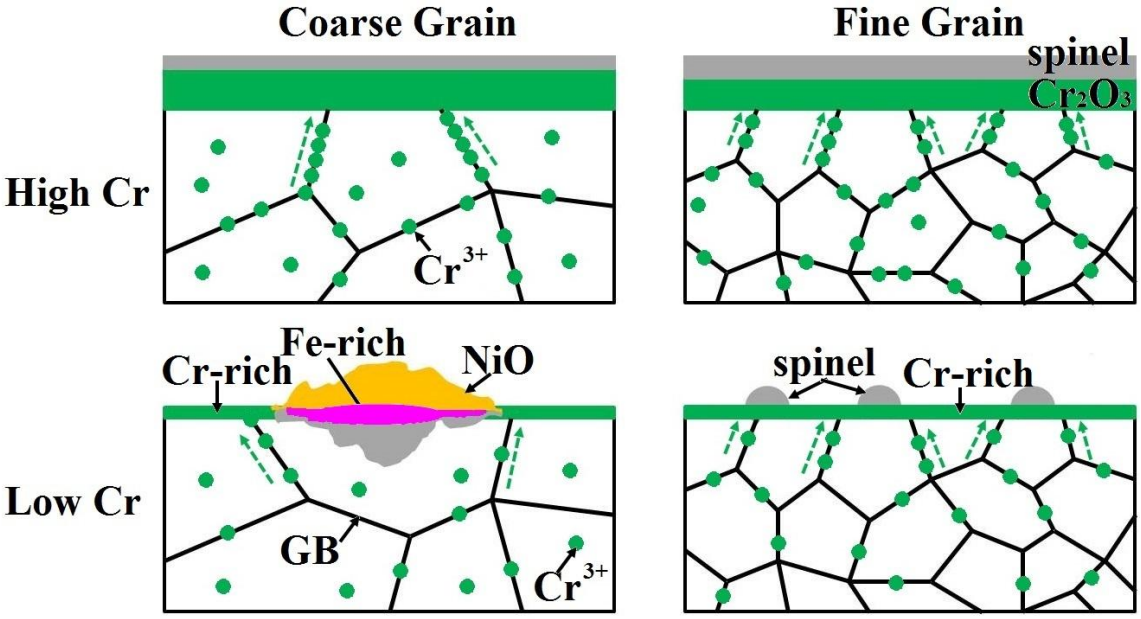

Fig. 3.15 Schematic models representing the oxidation mechanisms of high and low Cr content alloy with coarse and fine grain size.

On the contrary, the grain refinement process had a significant effect on the low Cr content alloy. For alloy with coarse grain, it was impossible to form a homogeneous Cr-rich oxide layer because of the lack of sufficient amount of Cr. However, the grain boundary could still affect the oxidation process which resulted in the formation of a thin Cr-rich film just on the grain boundary area. For CGN, the formation of the Cr-rich oxide layers on the grain boundary areas could not fully cover the entire sample surface. Consequently, the NiO would form on the Cr-depleted areas like grain interior owing to the high content (70 wt%) of nickel in the alloy. However, the NiO layer was not as dense or protective as a Cr_2O_3 layer and also tended to crack as shown in Fig. 3.6 (c). The porous and cracked NiO layer was unable to block the penetration of oxygen to the substrate matrix. Subsequently, a mixed inter oxide layer formed in the center of the grain. The components of the mixed oxide for CGN might be Fe_2O_3, Cr_2O_3, $MnFe_2O_4$ or $MnCr_2O_4$ as discussed above. For the substrate with higher grain boundary density, the grain boundaries facilitated the selective oxidation of Cr and enhanced its diffusion velocity. Therefore,

a uniform Cr-rich oxide layer was observed on the FGN as confirmed in Fig. 3.11. As a result, the FGN had a lower oxidation rate and better oxide spallation resistance than the CGN.

3.6 Conclusions

The oxidation behavior of Hastelloy 230 and N with large and small grain sizes is investigated. The surface morphology and chemical composition of the formed oxides are used to analyze the oxidation mechanisms of the prepared samples. The conclusions from the present work are drawn as below:

1) The substrates with different grain sizes and similar textures are prepared using cold rolling followed by different heat treatment for both Hastelloy 230 and N.

2) The grain refinement process has a slight influence on the oxidation behavior of Hastelloy 230 while it shows a significant effect on Hastelloy N. The surface morphology and chemical composition of the oxide formed on Hastelloy N are changed owing to the grain refinement process.

3) Thicker and complex oxide layers form in the grain interior and thin Cr-rich films are observed on the grain boundary areas for coarse-grained N. However, a uniform Cr-rich oxide forms on the fine-grained N which indicates that the higher grain boundary density enhances the diffusivity of Cr at the tested temperature.

Chapter 4 Optimizing cathodic electro-deposition parameters of ceria coating to enhance the oxidation resistance of a Cr_2O_3-forming alloy

4.1 Overview of chapter 4

The objective of this chapter is to optimize the deposition parameters for synthesizing RE coatings onto Ni-based alloys.

The current chapter was published as a manuscript # 4: Optimizing cathodic electro-deposition parameters of ceria coating to enhance the oxidation resistance of a Cr_2O_3-forming alloy. The contributions of the PhD candidate are 1) preparing all the samples; 2) operating all the electro-deposition experiments; 3) doing all post analysis of the deposits including XRD, SEM and Raman; 4) writing the manuscript.

This chapter was issued in the journal of *Thin Solid Films*:

- X. Wang, F. Fan, J.A. Szpunar, Optimizing cathodic electrodeposition parameters of ceria coating to enhance the oxidation resistance of a Cr_2O_3-forming alloy, Thin Solid Films, 611(2016) 12-20.

The differences of this chapter from the published paper are:

- The descriptions of the oxidation experiment and oxidation kinetics are removed in case of replication. The oxidation properties of this alloy are presented in the next chapter.
- The table depicting the nominal chemical composition of Hastelloy 230 is deleted to avoid repetition.

The references of the manuscript are listed at the end of this thesis. The permission of using this paper is attached in the Appendix section.

Optimizing cathodic electro-deposition parameters of ceria coating to enhance the oxidation resistance of a Cr_2O_3-forming alloy

Xu Wang, Fan Fan, Jerzy A. Szpunar

Department of Mechanical Engineering, University of Saskatchewan, Saskatoon, SK, S7N 5A9, Canada

4.2 Abstract

Nano-ceria coating is deposited onto a chromium oxide forming alloy through galvanostatic cathodic electro-deposition method in cerium nitrate electrolyte. The electrochemical behavior and influence of main deposition parameters of current density, deposition time, and temperature are studied. It is seen that the crystal size decreases with increasing of current density while micro-cracks are also observed at higher current density. A slightly increasing of crystal size and smoothing of surface morphology are seen with increasing of deposition time. It is reported that the bath temperature has the most significant effect on crystal size and surface morphology of the deposit. Green rust as corrosion product is also observed with deposition temperatures higher than 35 ℃. Optimized deposition parameters are used to produce homogeneous, continuous and green rust-free coatings. The electro-deposition process is found to be an accessible and efficient method to prepare nano-crystalline ceria coating.

Keywords: Ni-based superalloy; Electro-deposition; Current density; Deposition time; Bath temperature;

4.3 Introduction

Formation of protective oxide layers is necessary for alloys which are expected to be used in high-temperature environments. These protective layers, in general, are accepted as diffusion barriers which are high temperature stable, densely compact and well adhesive to the substrates [52]. Therefore, alloys which are able to form Cr_2O_3 or Al_2O_3 layers can be used for high-temperature applications. These alloys are named as Cr_2O_3-forming and Al_2O_3-forming alloys.

The addition of rare earth elements like Ce, Hf, Dy and Yb can significantly improve the high-temperature oxidation behavior of Cr_2O_3 and Al_2O_3-forming alloys. This improvement was primarily termed as rare earth effect (REE) since it was patented by Pfeil [53]. Recently, it was reported that not only the rare earth elements but also some other elements also have the similar influences on Cr_2O_3 and Al_2O_3-forming alloys. These previous works were summarized in several reviews [54–57]. Then the rare earth effect was re-named as reactive element effect (REE). Hereafter, the reactive element was defined as any element that has higher oxygen affinity than the oxide layer forming element which refers to Cr or Al. The benefits of REEs were mainly summarized as the reduction of oxidation rate and the enhancement of the adhesion between the oxide layer and the substrate. The postulate explains of how such a minor addition of REs could so strikingly enhance the oxidation behavior of materials were reported, but the exact reasons why this enhancement takes place are still not clearly known as summarized in a recent review [57].

Numerous methods have been used to add reactive elements either by alloying [58,59,62–64] or surface modification [72–74,76,77,145,146] in several materials. For instance, surface modification techniques like dip coating [49,73,146], sputtering [80], ion implantation [81], electro-deposition [86,87], MOCVD [90], solution precursor plasma spray (SPPS) [92] were widely studied. Among these approaches, the electro-deposition was considered as one of the most promising, efficient and environmental friend ways to produce stable and homogeneous metal oxide thin films. It was reported that the chemical composition, surface morphology and thickness of the produced film could be controlled by changing the deposition parameters of electrical potential, current density and bath temperature [145,147–150]. However, until now, studies on the influence of ceria coatings produced by electrochemical deposition were mainly focusing on Al_2O_3-forming alloys [87,88,150–155]. Research on the effect of electrochemical deposition of ceria on the oxidation behavior of Cr_2O_3-forming alloys was barely reported.

Therefore, the purpose of this work is to optimize the electro-deposition parameters such as the current density, deposition time and bath temperature to produce homogeneous ceria coatings which could be used to enhance the oxidation resistance of Cr_2O_3-forming alloys.

4.4 Experimental Procedure

4.4.1 Material

Nickel-based Hastelloy 230 was used in present work. As a promising candidate structural material for the VHTR, Hastelloy 230 is expected to be used at 900 to 1000 ℃ for at least 60 years. Therefore, many works have attempted to investigate the oxidation behavior of this alloy at different temperatures from 650 to 1150 ℃ [103,104,108,110–113,118]. However, the methods for enhancing the oxidation behavior of this alloy were barely reported.

The specimens with dimensions of 30 mm × 20 mm × 1 mm were cut from the alloy sheet and mechanically gound up to 1200 grit SiC emery paper. Then all the specimens were ultrasonically cleaned in acetone for 10 min, washed with deionized water and ethanol and immediately dried under flowing air before deposition of ceria coating.

4.4.2 Preparation of ceria coating

Ceria coating was synthesized by cathodic electrochemical deposition (CED) method. The CED was completed using a classical three-electrodes Gamry Interface 1000 experimental device which includes the sample as a working electrode, a Pt grid or graphite as a counter electrode and saturated calomel electrode (SCE) as a reference electrode. 0.1 M $Ce(NO_3)_3 \cdot 6\ H_2O$ was used as an electrolyte solution. All the specimen surfaces were deposited with ceria. To find a proper counter electrode and appropriate electro-deposition parameters, the potentiodynamic measurements with a linear sweep rate of 1 mV/s were recorded both with Pt and graphite counter electrode. The low sweep rate will offer enough time for the reactions to follow the potential change and arrive at a quasi-stationary state. Before application of current, all the electrodes were kept in the electrolyte for 10 min to establish a quasi-stable open-circuit potential. The galvanostatic mode was used to operate the deposition processes with different current densities of -0.5, -0.75, -1, -1.5, -2 and -2.5 mA/cm^2 to investigate how current density affect the formation of the ceria films. Furthermore, the ceria films were produced with different deposition times from 2 to 20 min to study the influence of deposition time. Finally, various bath temperatures were used to prepare the reactive element coatings. After depositing, the samples were washed with ethanol, dried by the hot dryer and then dried in a desiccator for 24 h before

any characterization. Cleaning of the deposits by ethanol will release the nitrides incorporated in the deposited films [145,148,149].

4.4.3 Characterization technique

The phase identification of the deposited ceria film was characterized using D8 Bruker discovery XRD with a Cr Kα radiation and 2D Hi-star detector at a scanning rate of 1 °/min and step size of 0.01 °. The voltage and current for XRD measurements were 40 kV and 40 mA. 2θ ranging from 20 ° to 100 ° was scanned for the sample. The surface morphology of deposit was characterized by Hitachi SU6600 SEM at 5 kV. The EDS system mounted on Hitachi SU6600 was used to determine the chemical components of the deposits at 15 kV. The EDS was done at a resolution of 1024 × 1024 with a pixel dwell time of 300 µs. Renishaw 2000 Raman microscope with laser source wavelength of 785 nm was also used to characterize the deposits.

4.5 Results and Discussions

4.5.1 Electrochemical characterization

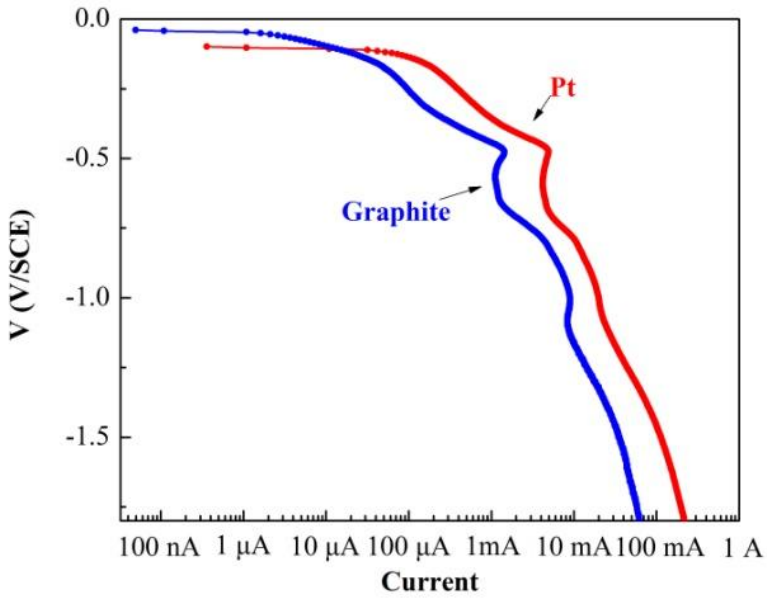

Fig. 4.1 Cathodic potentiodynamic scan of Hastelloy 230 with Pt and graphite counter electrode.

Fig. 4.1 shows the cathodic potentiodynamic scanning curve of Hastelloy 230 with Pt and graphite counter electrode. As can be seen from this figure, the electro-deposition process with Pt counter electrode gained a higher current density than that with a graphite electrode. In other words, the deposition potential needed for Pt electrode was reduced for the same current density. Therefore, Pt grid was used as the counter electrode since it could obtain a higher cathodic current efficiency.

The mechanism of electro-deposition using nitrate baths has been investigated and discussed by other researchers [145,148]. Three continuous steps were suggested by Bouchaud [145] and Hamlaoui [148,149] for the potentiodynamic curve. During the lower potential stage, the potential variation is because of the oxygen, nitrate reduction and the reactions 4.1 to 4.4 may present. Reaction 4.1 may also happen through two-step reactions as shown in 4.5 and 4.6.

$$O_2 + 2H_2O + 4e^- \rightarrow 4OH^- \quad (4.1)$$

$$2H_2O + 2e^- \rightarrow H_2 + 2OH^- \quad (4.2)$$

$$O_2 + 2H_2O + 2e^- \rightarrow 2OH^- + H_2O_2 \quad (4.3)$$

$$NO_3^- + H_2O + 2e^- \rightarrow NO_2^- + 2OH^- \quad (4.4)$$

$$O_2 + H_2O + 2e^- \rightarrow HO_2^- + OH^- \quad (4.5)$$

$$HO_2^- + H_2O + 2e^- \rightarrow 3OH^- \quad (4.6)$$

The second step corresponds to the potential drop which refers to the film deposition process. During this stage, a continuous and homogeneous deposit layer forms which may result from the reactions 4.7 to 4.9. The OH^- produced from the first step allows the formation of $Ce(OH)_3$ or $Ce(OH)_2^{2+}$.

$$Ce^{3+} + 3OH^- \rightarrow Ce(OH)_3 \quad (4.7)$$

$$4Ce^{3+} + O_2 + 4OH^- + 2H_2O \rightarrow 4Ce(OH)_2^{2+} \quad (4.8)$$

$$2Ce^{3+} + 2OH^- + H_2O_2 \rightarrow 2Ce(OH)_2^{2+} \quad (4.9)$$

The final step corresponds to the dehydration of deposit and/or oxidation of Ce^{3+} to Ce^{4+}. The reaction during this stage may be as follows:

$$Ce(OH)_3 \rightarrow CeO_2 + H_3O^+ + e^- \quad (4.10)$$

$$Ce(OH)_2^{2+} + 2OH^- \rightarrow CeO_2 + 2H_2O \quad (4.11)$$

4.5.2 Effect of current density

CED was operated with different current densities from -0.5 to -2.5 mA/cm^2 for 20 min at room temperature (25 ℃) to know the role of current density in the deposition process. The variation of potential during the deposition process is shown in Fig. 4.2. For all the deposition conditions, fast potential drops were recorded at the initial stages especially for the processes with current densities higher than -0.5 mA/cm^2 which indicates that the deposited films steadily become insulating. The drop may take several seconds and the drop time reduced with increasing of the current density. After the drop, the potential steadily became stable which indicates the formation of a continuously deposited layer. Thus, this layer is believed to decrease the electron conductivity of the interface between the substrate surface and the electrolyte [145]. The deposition process with a higher current density always became stable in a shorter time than the lower current density. However, transient stages were always seen for all the current densities.

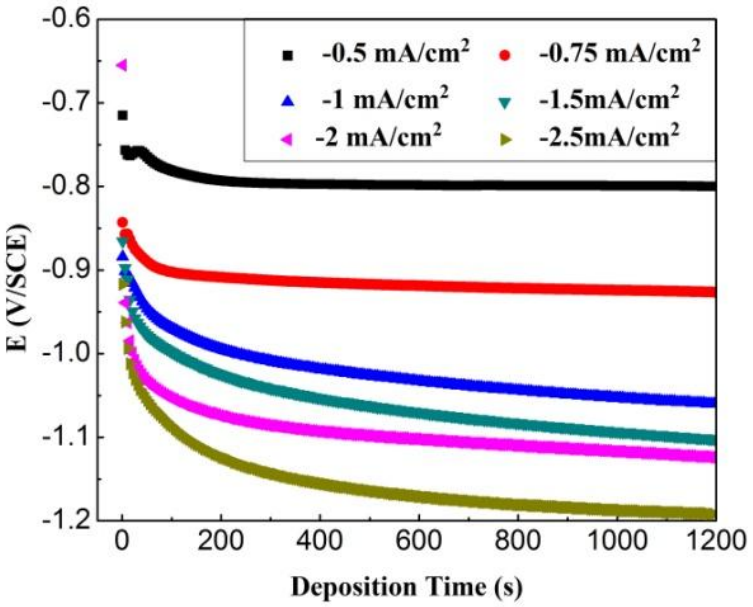

Fig. 4.2 Potential evolution against deposition time with deposition current density from -0.5 to -2.5 mA/cm^2.

The XRD patterns of the coatings deposited with different current densities are depicted in Fig. 4.3 (a). Four diffraction peaks of ceria which correspond to the diffraction planes of (111), (200), (220) and (311) were detected. As seen in this figure, the peaks of (111) and (220) are clearly observed even at a low current density of -0.5 mA/cm^2. With the increasing of current density, peaks of (200) and (311) were steadily detected. Further, the intensities of these four peaks were strengthening with the increase of current density which may indicate the thickening of the deposits. Moreover, peak widening for all the peaks was observed for ceria coatings regardless of the current density. This peak widening indicates the deposited ceria might be nano-crystalline. Therefore, the peak (111) was fitted with Gaussian equation, and the crystalline size was calculated according to Scherrer equation. The peak broadening of commercial 25 nm ceria purchased from Aldrich Company which annealed at 1200 ℃ for 20 h was used as a standard sample to remove the instrumental broadening. The XRD result for the standard sample was also depicted in Fig. 4.3.The equations used for calculating crystalline size are as follows:

$$D = \frac{K\lambda}{\beta \cos\theta} \tag{4.12}$$

$$\beta = \sqrt{\beta_m{}^2 - \beta_s{}^2} \tag{4.13}$$

where: D is the mean crystalline size, K is a shape factor or Scherrer constant, λ is the wavelength of X-ray, β is the full width at half of the maximum intensity (FWHM), θ is the Bragg diffraction angle, β_m is the FWHM of the peak measured from the deposit and β_s is the FWHM of the standard sample. Here in this work, K equals to 0.9 and λ equals to 0.22897 nm were used. Fig. 4.3 (b) depicts the effect of current density on the FWHM and the calculated crystalline size of deposited ceria. A slight decreasing of crystal size with the increasing of the current density was observed. Nucleation dominant and nuclei growth dominant were reported as two competition ways to form a continuous deposition layer from CED [149]. The decreasing of the crystal size with the increasing of the current density may indicate that the nucleation rate was enhanced and nuclei did not have sufficient time for growth. This finding is in agreement with the suggestion that the formation of the homogeneous layer of ceria at the higher current density was dominated by the nucleation rate rather than the growth rate of the nuclei [149].

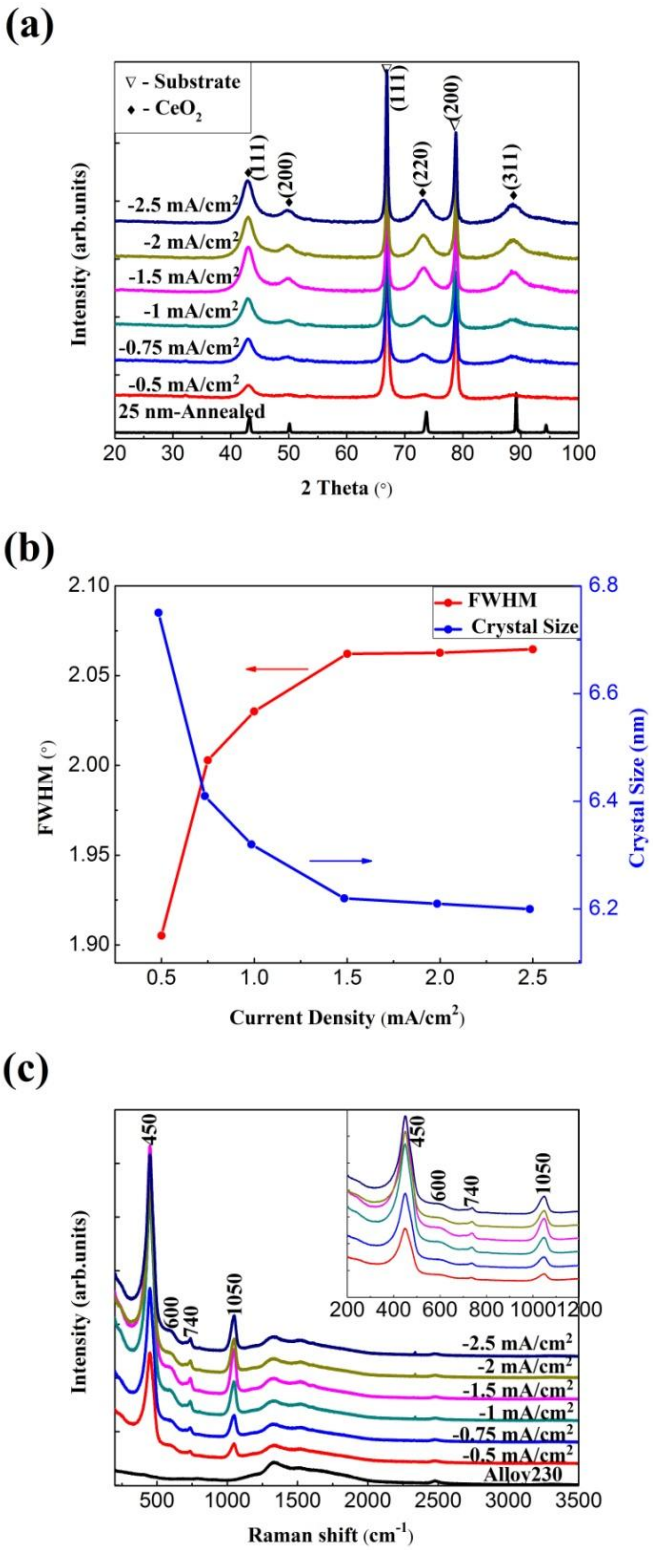

Fig. 4.3 XRD and Raman spectra characterization of ceria deposited with various current densities: (a) XRD results; (b) Variation of FWHM and grain size with current density; (c) Raman spectra.

Fig. 4.3 (c) depicts the Raman spectra of deposited ceria coatings with various current densities. The spectrum of the substrate Hastelloy 230 is also shown in Fig. 4.3 (c). Bulk ceria has a strong peak at the frequency of 465 cm^{-1} which depicts the symmetrical stretching mode of Ce-O vibration. The symmetrical mode is very sensitive to the lattice distortion and disorder in oxygen sub-lattice [156]. However, in this work, the strong peak shifted to the frequency of 450 cm^{-1} which indicates the lattice distortion owing to the reduction of grain size. The broadening and the asymmetry of the peaks at a frequency of 450 cm^{-1} all indicate the formation of nano-crystallized ceria which confirms the XRD results. It was reported that the content of Ce^{3+} will increase with the decreasing of ceria grain size. Therefore, the lattice distortion may arise from the existing of Ce^{3+} in the deposited CeO_2 layer. The containing of Ce^{3+} may lead to the lattice expansion of the ceria since the ionic radius of Ce^{3+} (1.143 Å) is much larger than that of Ce^{4+} (0.97 Å). This is confirmed by a slight peak shifting of the peak (111) from 42.99 °to 42.93 °for depositions with the current density from -0.5 to -2.5 mA/cm^2 measured from XRD. Furthermore, this defect is verified by the small Raman shift observed at a frequency of 600 cm^{-1} which is reported as the oxygen vacancy band for nano-crystallized ceria [157]. This formation of oxygen vacancy might relate to the reduction of two ions of Ce^{4+} to Ce^{3+} as follows [76]:

$$2Ce^{4+} + O^{2-} \rightarrow 2Ce^{3+} + \frac{1}{2}O_2 \qquad 4.14$$

Also, may express in Kroger-Vink notation as:

$$2Ce_{Ce}^{x} + O_O^{x} \rightarrow 2Ce_{Ce}^{'} + V_O^{\cdot\cdot} + \frac{1}{2}O_2 \qquad 4.15$$

However, the exit of Ce^{3+} might be not detected by XRD owing to the low volume fraction. The Raman peaks at frequencies of 740 and 1050 cm^{-1} were reported as the typical vibration of nitrate absorbed from the solution. However, the remaining nitrate in the deposited film is negligible after rinsing with ethanol as reported by Hamlaoui [148].

Fig. 4.4 shows the SEM images of the surface morphology of deposited ceria films with various current densities. As seen in these images, the deposited films cover the substrate surfaces and the morphologies vary significantly with the increasing of current densities. However, some ceria-free areas are still observed after deposition with the current density of -0.5 mA/cm^2 as seen in Fig. 4.4 (a). Moreover, micro-cracks are seen in the film especially with deposition

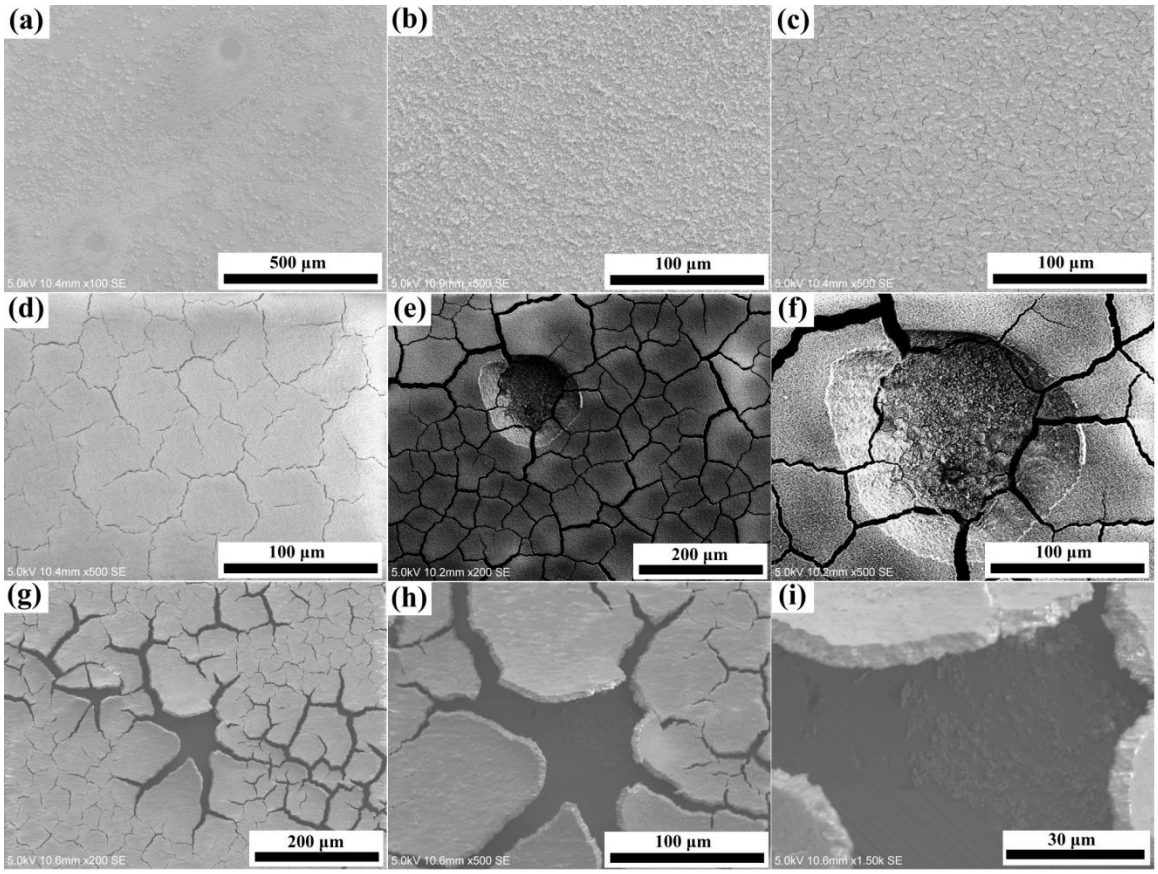

Fig. 4.4 Surface morphology of CeO_2 film formed by electro-deposition with different current density for 20 min: (a) -0.5 mA/cm^2; (b) -0.75 mA/cm^2; (c) -1 mA/cm^2; (d) -1.5 mA/cm^2; (e) and (f) -2 mA/cm^2; (g), (h) and (i) -2.5 mA/cm^2.

current density higher than -1 mA/cm^2. The width of the crack seems also increasing with the increasing of the current density. These micro-cracks may result from the stress accumulation during the formation of the homogeneous film, the release of hydrogen bubbles during the deposition stage and the dehydration of the deposited film during the drying process. Some pitting holes are observed in the specimen deposited with a current density of -2 mA/cm^2 and part of the film detaches from the substrate for deposition with a current density of -2.5 mA/cm^2. Therefore, new nuclei of ceria formed beneath the detached film as can be seen in the higher magnification image for current density with -2.5 mA/cm^2. The nucleation may form after the detaching of the film which resulted in the direct contact of the substrate and electrolytic solution. However, a homogeneous and continuous layer is observed with deposition current density of -

0.75 mA/cm^2. Therefore, the current density of -0.75 mA/cm^2 was used to investigate the role of deposition time within 20 min.

Fig. 4.5 depicts the EDS mapping results of an uncovered area with a current density of -0.5 mA/cm^2 and a detached area with a current density of -2 mA/cm^2. From these mapping results, two aspects can be observed. Firstly, the homogeneous distribution of Ce and O in the well-deposited area confirms the formation of ceria. Secondly, Ce and O are not seen in the uncovered area in Fig. 4.5 (a) while they are observed in the detached area in Fig. 4.5 (b). This indicates the increasing of the current density both increases the deposition volume and thickens the deposition film. However, the thickening of the film may decrease the adhesion strength of the film to the substrate. Therefore, the lower current density may be used to produce a film strongly adhesion to the substrate.

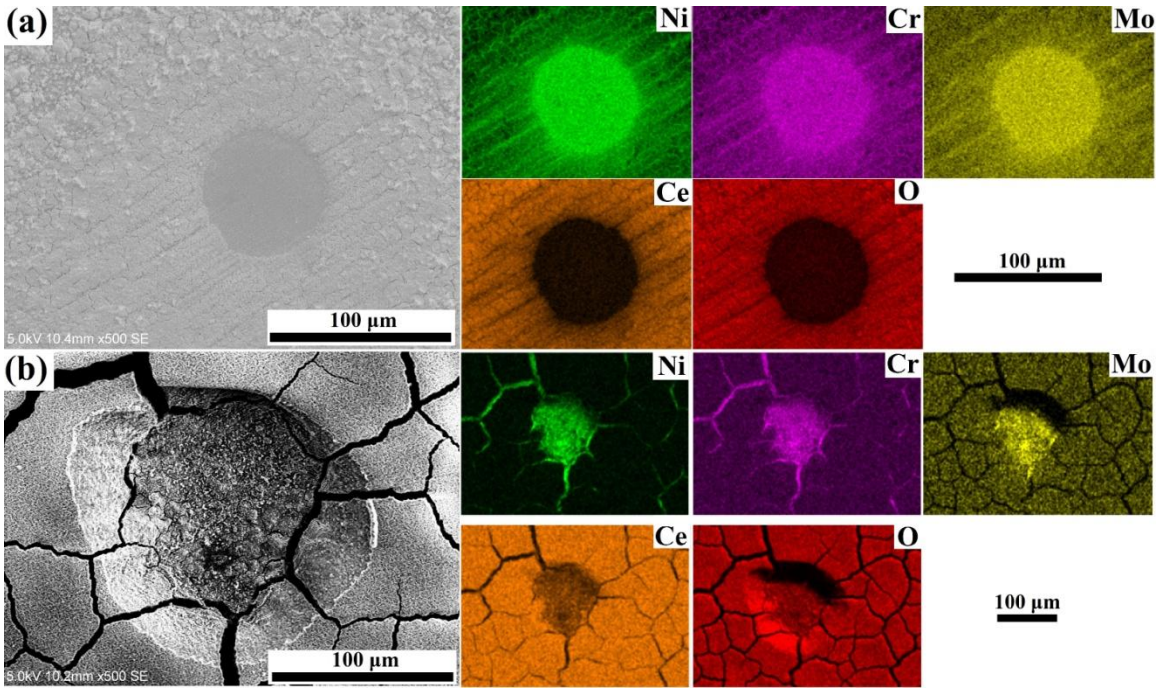

Fig. 4.5 EDS mapping for deposited film at different current density: (a) -0.5 mA/cm^2; (b) -2.0 mA/cm^2.

4.5.3 Effect of deposition time

Deposition time was reported to affect the particle size, thickness and surface morphology of the deposited film [86,149]. Therefore, the effect of deposition time on the deposition of ceria onto

Hastelloy 230 is investigated at a constant current density of -0.75 mA/cm^2. Fig. 4.6 shows the variation of potential during the deposition process with the deposition time from 2 to 15 min. Similar to the deposition processes with the various current density, potential drops followed with stable potential stages are observed at the initial stages of the deposition. The stable property of the potential indicates the formation of a homogeneous film even for the deposition with 2 min. Also, a similar variation trend of potential with increasing the deposition time shows the reproducibility of the deposition process.

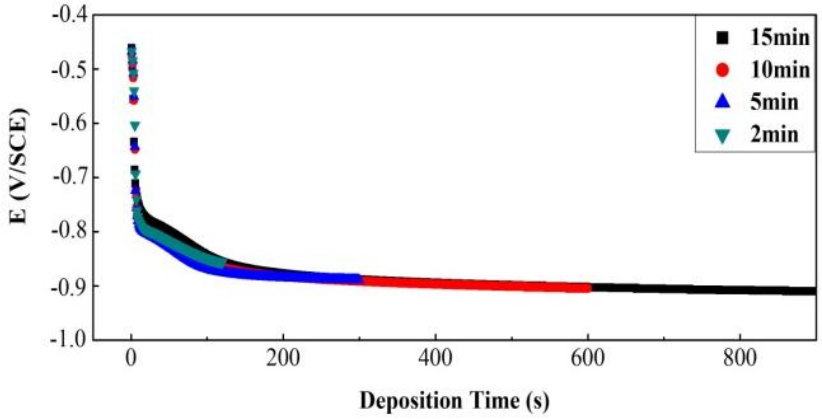

Fig. 4.6 Evolution of potential with deposition time with a current density of -0.75 mA/cm^2.

Fig. 4.7 depicts the XRD and Raman results of the deposits with different deposition times. As seen in Fig. 4.7 (a), the peaks for ceria are steadily detected with the increasing of deposition time. The strengthening of the peak along with increasing time indicates that the deposit is accumulating and the deposit thickness is increasing. The peak broadenings of (111) are again observed for all the depositions which indicate the formation of nano-crystalline ceria. Therefore, these peaks of (111) were fitted with Gaussian equation and the crystalline sizes are calculated by Scherrer equation as shown in the above section. Fig. 4.7 (b) demonstrates the FWHM and calculated crystal size for all the deposits with deposition times from 5 min to 20 min. A slight increasing of the crystal size is observed with the increasing deposition time. This implies that the growth of nuclei dominated the CED process at same current density with increasing deposition duration.

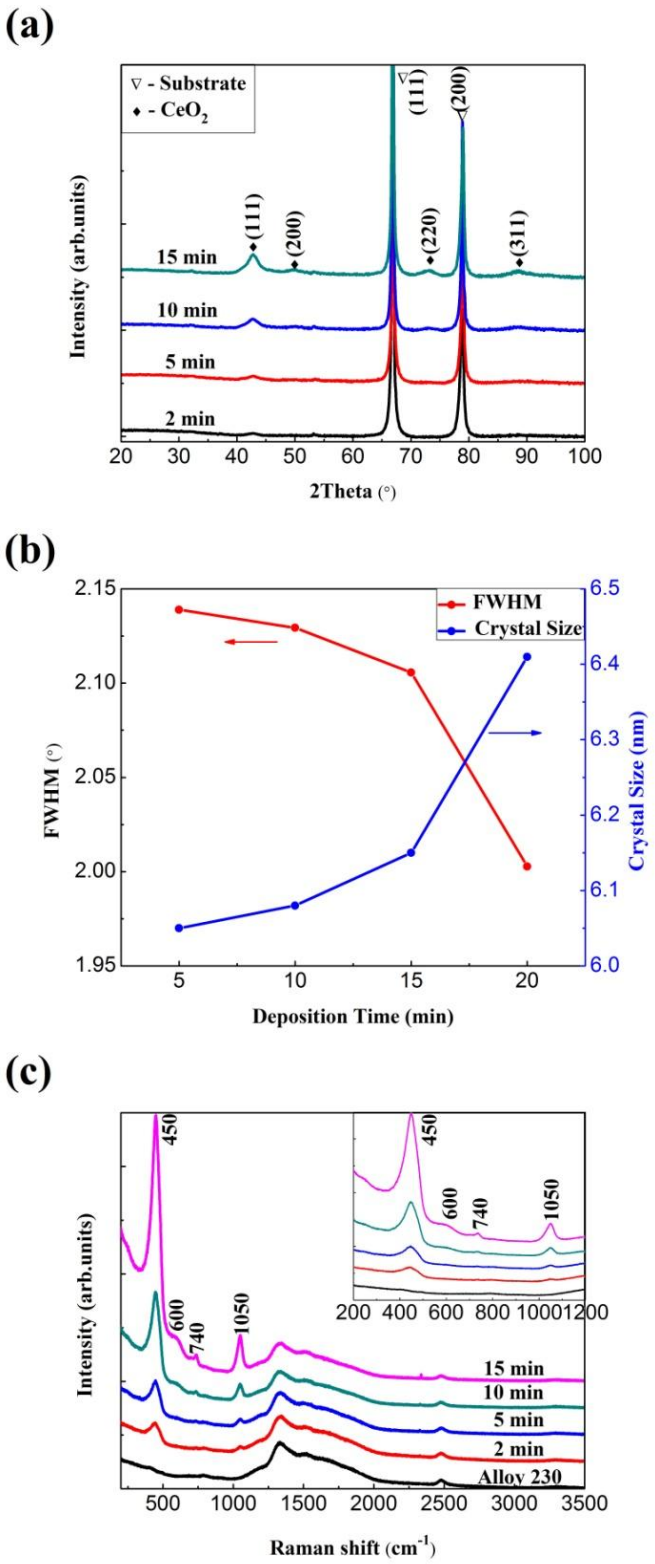

Fig. 4.7 XRD and Raman spectra characterization of ceria deposited with various deposition time: (a) XRD results; (b) Variation of FWHM and grain size with deposition time; (c) Raman spectra.

Fig. 4.7 (c) depicts the Raman spectra detected from the coatings obtained with various deposition times. Shifting of the strongest peak from 465 cm^{-1} to 450 cm^{-1} again reflects the lattice distortion of formed ceria. The broadening and asymmetry of the peak at 450 cm^{-1} confirms the formation of nano-crystalline ceria as denoted by XRD results. The Raman frequency of 600 cm^{-1} corresponds to the oxygen vacancy formation as demonstrated before and peaks of 740 cm^{-1} and 1050 cm^{-1} correspond to the residual nitrate in the films.

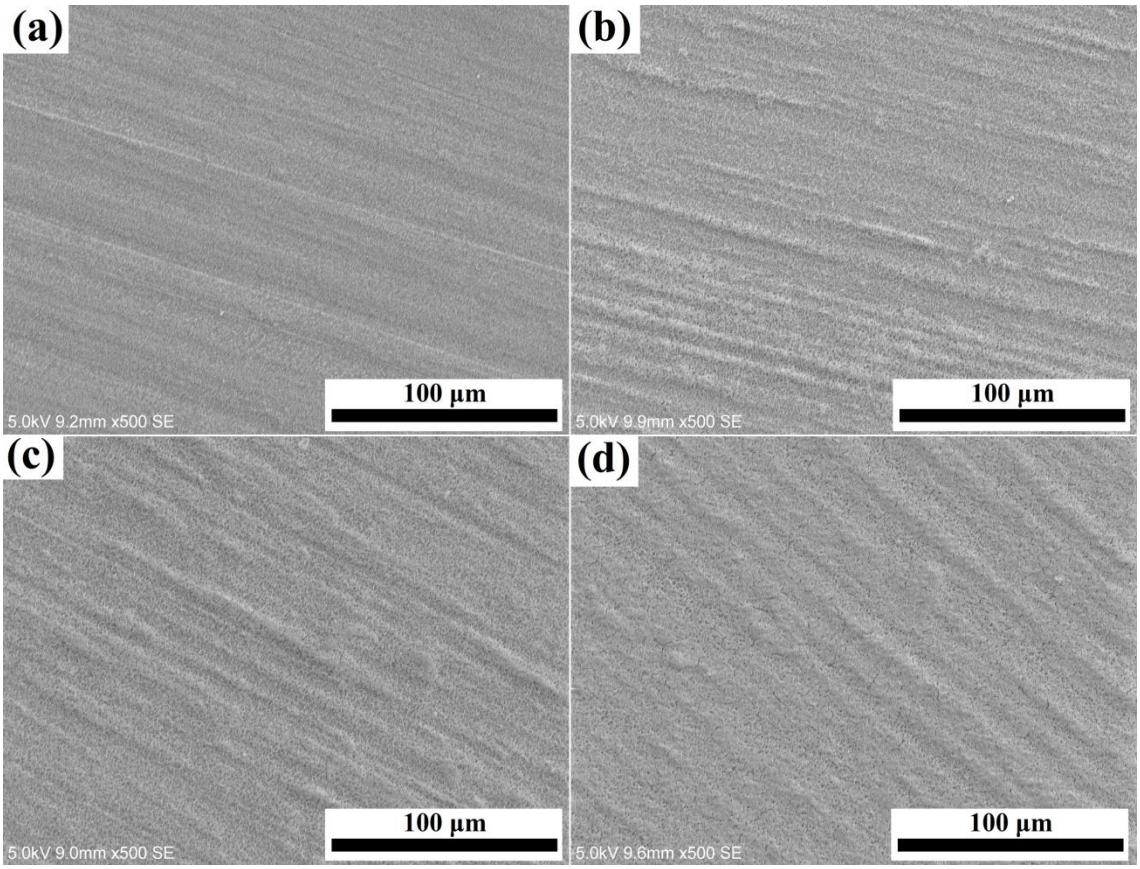

Fig. 4.8 Surface morphology of CeO_2 film formed by electro-deposition with different deposition time: (a) 2 min; (b) 5min; (c) 10 min; (d) 15 min.

Fig. 4.8 represents the surface morphology of the deposited ceria from 2 min to 15 min. Nucleation spreading along the polishing line is observed for the deposit and the surface morphology steadily becomes smooth with the time increasing. However, a more homogeneous and continuous film without seeing any of polishing line is observed on the surface with a deposition time of 20 min seen in Fig. 4.4 (b). Therefore, a deposition time of 20 min is needed

to produce a homogeneous and thick ceria layer even though the crystal size is increasing with increasing the deposition time.

4.5.4 Effect of deposition temperature

It was reported that the temperature of deposition bath would affect the crystalline structure, surface morphology, chemical composition and texture of the deposited film [149,158–160]. Therefore, the influence of bath temperature on ceria deposition is investigated to optimize the deposit structure. A bath temperature of 25 ℃ to 55 ℃ was used in this work.

Fig. 4.9 shows the XRD and Raman spectra characterization of the ceria coating deposited at temperatures from 25 ℃ to 55 ℃. Four diffraction peaks for ceria are detected as shown in Fig. 4.9. The peak of (111) was again used to calculate the crystal size of the deposit formed. Fig. 4.9 (b) plots the effect of bath temperature on the FWHM and crystallite size of formed ceria. The crystal size increases with the increasing of temperature indicates the growth of nuclei. Further, the bath temperature has a more significant effect on particle size than the current density and the deposition time since a significant crystal size increasing is observed.

Interestingly, a peak with diffraction angle 2θ at approximately 32 ° was detected with a deposition temperature of 35 ℃ to 55 ℃. This peak was reported corresponding to the formation of carbonated green rust (GR) which is a secondary product during the electro-deposition on carbon steel [161]. It was attributed to the pH drop at the deposit interface during the increasing of temperature [162]. The interfacial pH was reported to decrease a value of 1.5 with the bath temperature increasing from 10 ℃ to 40 ℃ during the deposition of ceria [162]. Therefore, degradation and corrosion of the substrate may occur on the substrate surface where corrosion products (e.g. GR) may form. The formation of such product may further affect the quality of the deposited film for corrosion protection. Fig. 4.9 (c) demonstrates the Raman spectra of deposits with different temperatures. The peak shifting of Ce-O vibration from 450 cm^{-1} to 455 cm^{-1} is observed with the increasing temperature which indicates the crystal size is changing with temperature variation. This is in agreement with the observed increase of the crystal size with temperature as calculated from the XRD result. Further, oxygen vacancy and nitrate are observed by Raman measurement. However, the intensity of nitrate seems to decrease with the increase of temperature which indicates the release of nitrate series.

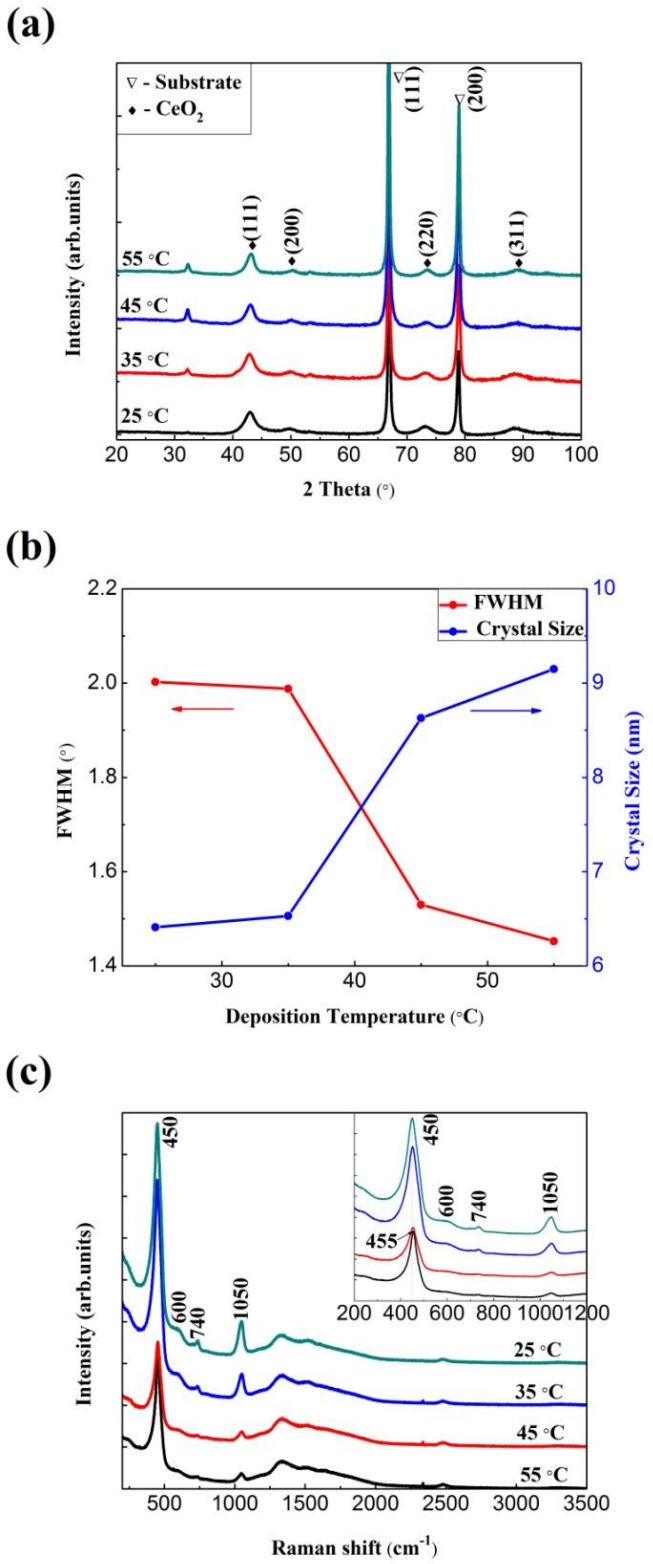

Fig. 4.9 XRD and Raman spectra characterization of ceria deposited with various temperature: (a) XRD results; (b) Variation of FWHM and grain size with deposition temperature; (c) Raman spectra.

Fig. 4.10 shows the surface morphology of ceria coatings deposited at different temperatures. Needle-like and petal-like ceria are seen at the deposition temperature of 35 ℃. With the increasing of bath temperature, needle-like ceria steadily disappeared and the leaves for petal-like ceria become thicker with double or triple leaves. Further, micro-cracks are seen with the increasing of bath temperature which is unexpected to prepare a uniform ceria coating. The significant changing of surface morphology with a variation of deposition temperature was also reported by other researchers [159,162]. Needle-like ceria was linked to the formation of $Ce(OH)_3$ in the film [145]. The vanish of needle-like ceria demonstrates further oxidation of $Ce(OH)_3$ to CeO_2 [145].

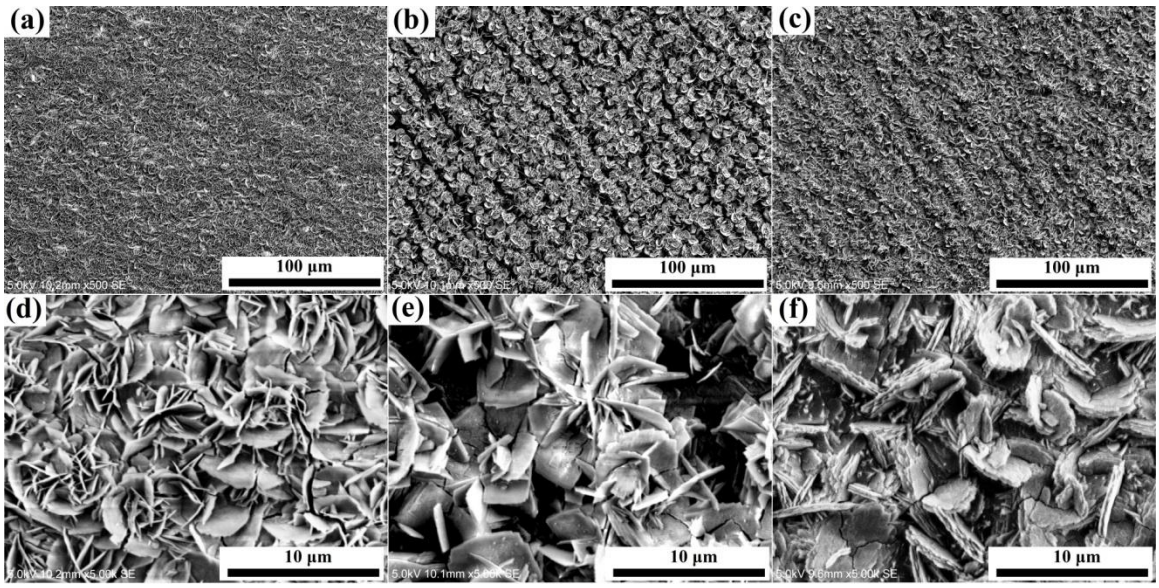

Fig. 4.10 Surface morphology of CeO_2 film formed by electro-deposition with different deposition temperature: (a) and (d) 35 ℃; (b) and (e) 45 ℃; (c) and (f) 55 ℃.

4.6 Conclusions

In conclusion, the effects of current density, deposition time and bath temperature on the cathodic electro-deposition of ceria are investigated. All these deposition parameters will affect the crystal size of the deposited film. A slight decrease of particle size is found with increasing the current density and decreasing of the deposition time. However, a more significant crystal size variation is observed with the increasing of bath temperature. The surface morphology of the deposit also varies with different current density, deposition time and deposition temperature.

Increasing current density will result in the formation of micro-cracks. Deposited film steadily becomes smooth and homogeneous with the increasing of deposition time. Needle-like and petal-like shape grains are found with the increasing of bath temperature. Corrosion product of green rust is detected by XRD with deposition temperature higher than 35 ℃. This corrosion product may affect the oxidation resistance. Homogeneous, continuous and GR-free ceria coating can be obtained with the optimized deposition parameters with the current density of -0.75 mA/cm^2 for 20 min at room temperature.

Chapter 5 Effect of CeO_2 coating on the isothermal oxidation behavior of Ni-based Hastelloy 230

5.1 Overview of Chapter 5

In the last chapter, the parameters for electro-deposition of ceria coating were optimized. The purpose of this chapter is to study the influence of optimized coating on the oxidation behavior of Hastelloy 230.

This chapter was accepted as a manuscript #5: Effect of CeO_2 coating on the isothermal oxidation behavior of Ni-based Hastelloy 230. The PhD candidate's contributions to this manuscript are a) polishing and coating all the samples; b) running the oxidation tests; c) characterizing all the samples after oxidation using XRD, SEM, EDS and EBSD; d) writing the manuscript.

This chapter is published in *Oxidation of Metals*:

- X. Wang, J.A Szpunar, Effect of CeO_2 on the isothermal oxidation behavior of Ni-based alloy 230, Oxidation of Metals, (2017) accepted

The differences of this chapter with the submitted one are as follows:

- The table displaying the nominal chemical composition of Hastelloy 230 is removed.

The listed references in the manuscript are presented at the end of this thesis.

Effect of CeO_2 coating on the isothermal oxidation behaviour of Ni-based Hastelloy 230

Xu Wang, Jerzy A.Szpunar

Department of Mechanical Engineering, University of Saskatchewan, Saskatoon, SK, S7N 5A9, Canada

5.2 Abstract

Ceria coating was deposited on Hastelloy 230 using an electro-deposition process in a cerium nitrate electrolyte. Reactive element effects were investigated by comparing the oxidation behaviour of the samples with and without the ceria coating. The prepared ceria coating reduced the oxidation rate and improved the adherence of the oxide layer. A thicker oxide layer with large spallation areas formed on the uncoated sample while a thin and protective oxide layer was found on the coated sample after oxidation for 1000 h at 900 ℃. The oxidation mechanisms of Hastelloy 230 with and without ceria coating were discussed. Furthermore, as the ceria coating changed the grain shapes of chromium oxides from columnar to an equiaxed structure, discussion also advanced proposals regarding the mechanisms of formation of these different oxides. The equiaxed grains enhanced the adhesion of the oxide to the alloy surface.

Keywords: High temperature oxidation; Ni-based superalloy; Electro-deposition; Reactive element effect (REE); Electron back-scattering diffraction (EBSD);

5.3 Introduction

The addition of REs such as Ce, Y, Ta and Yb or their oxides can either extensively improve the oxidation resistance of alloys or significantly prevent the descaling of the oxide layers from the substrate at high temperature [49,87,163]. These benefits were attributed to the REEs [57]. It was reported that the RE had significant effects on the oxidation behaviour of Cr_2O_3-forming and Al_2O_3-forming alloys [76]. For instance, the critical amount of Cr or Al needed for the formation of a continuous and homogeneous Cr_2O_3 or Al_2O_3 layer at high temperature would be reduced with the addition of REs [57]. Further, the adding of REs would reduce the time for forming a protective Cr_2O_3 or Al_2O_3 scale for those alloys that already contain a high amount of Cr or Al [55]. Intensive researches have been concentrated on investigating the influence of REs on the oxidation behaviour of Cr_2O_3 and Al_2O_3-forming alloys [59,66,74,76,84,87]. Consequently,

some hypotheses have been suggested to explain the mechanisms of the oxidation process with the reactive elements. For example, the segregations of REs on grain boundaries of Cr_2O_3 and Al_2O_3 were suggested to change the transportation mechanisms of ions [96,164–166]. Cotell et.al reported that the segregation of Y on to Cr_2O_3 grain boundaries changed the dominant transportation process from outward diffusion of Cr to inward diffusion of O [167,168]. Furthermore, the REs were believed to act as nucleation sites for Cr_2O_3 which reduced the distance of the neighbouring oxide grains and the oxide grain size [79,169]. Subsequently, the time needed to form a continuous and protective Cr_2O_3 layer would be shortened which resulted in a faster access to the steady state oxidation stage [169]. In addition, the reduced oxide grain size owing to the addition of REs was suggested to enhance the deformability of the oxide layer which improved the adherence of the oxide layer [79]. However, even though these hypotheses of oxidation have been suggested, the exact dominating mechanisms are still not fully clarified [96].

In the past 20 years, many attempts have been made to realize the benefits of REEs either for alloys or coatings [96]. Additionally, many methods have been developed to add REs to alloys or to prepare pure RE coatings. For example, surface modification methods such as dip coating [49,73,146,170], ion implantation [81], sputtering [80], solution precursor plasma spray (SPPS) [92] and the electro-deposition process were reported to successfully incorporate REs or their oxides into alloys [86,87]. Among these processes, electro-deposition was reported as one of the most effective and environment-friendly methods. It was suggested that the morphology, chemical composition and thickness of the deposited film can easily be restrained by varying the current density, deposition time and deposition temperature [145]. The effect of reactive element coating prepared through the electro-deposition process on the oxidation behaviour of alloys has been previously reported [151,154,155,171]. However, until now, the reactive element coating synthesized via this method has mainly been concentrated on the Al_2O_3-forming alloys. Therefore, we optimized the deposition parameters of ceria coating through the electro-deposition process for enhancing the oxidation resistance of Cr_2O_3-forming alloys in our previous work [172]. The objective of the present work is to investigate the mechanisms by which the oxidation behaviour of Cr_2O_3-forming alloys can be enhanced through the addition of RE coating.

5.4 Experimental Process

5.4.1 Material description

Ni-based Hastelloy 230 was used for oxidation tests in the present work. Its chemical composition is shown in Table 2.1. The high content of Cr (22 wt%) implies the possible formation of a protective Cr_2O_3 layer in the high-temperature oxidation environment [173]. Samples with dimensions of 18 × 12 × 1.5 mm were machined from the alloy strip. A small hole with a diameter of 1.5 mm was drilled in each sample. All the samples were mechanically ground with silicon carbide paper up to 1200 grit. Then the samples were ultrasonically cleaned in acetone for 10 min followed by cleaning in deionized water and ethanol prior to deposition of the ceria coating.

5.4.2 Experimental tests

To prepare ceria coatings on the ground specimens, a classical three-electrodes system was used [172]. This system contained the specimen as the cathode electrode, a platinum grid as the anode electrode and a SCE as the reference. 0.1 M cerium nitrate electrolyte solution was used to deposit ceria on all the specimen surfaces. The optimized deposition parameters with a current density of -0.75 mA/cm^2 were used to deposit ceria for 20 min at room temperature. After deposition, the samples were washed with ethanol, dried with an air drier and then placed in a desiccator for 24 h before further treatment. To eliminate the influence of resident free water on the weight change, the deposits were carefully scraped off and further heat-treated. They were heated from room temperature to 150 ℃ with a ramping rate of 20 ℃/min and held there for 30 min by using an SDT Q600 TA instrument. This method was used to see how long it would take to entirely vaporize the water molecular. Then, all the coated samples were also heat-treated in the same way in a box furnace.

Isothermal oxidation tests were conducted in a laboratory muffle furnace at 900 ℃ under static air atmosphere. The specimens were suspended in the crucible boat through a ceramic rod with a diameter of 0.8 mm. The specimens were removed from the furnace after different interval times of 50, 100, 300, 500, 700 and 1000 h to study the oxidation kinetics of both bare and coated substrates. A Mettler Toledo XS205 analytical balance with an accuracy of 0.01 mg was used to measure the weights of all the samples before and after oxidation.

A SEM SU6600 was used to characterize the surface and cross-section morphology of the oxidized samples. The oxide phase identification was defined by using a D8 Bruker discovery XRD with Cr Kα radiation at a scanning rate of 2 ?min. For analysis of the cross-section structures, the oxidized samples were electro-plated with nickel and mounted in a conductive resin. Then, the mounted samples were ground using silicon carbide papers up to 4000 grit followed by polishing with 3 μm and 1 μm solutions. Finally, the samples were polished using a BUEHLER Vibromet 2 vibratory polisher for 24 h. This final polishing provided a stress-free and extremely flat cross-section surface which allowed us to use EDS and EBSD for structure analysis. A fine scanning step size of 30 nm was used for the EBSD scanning.

5.5 Results and Discussions

5.5.1 Characterization of the coating

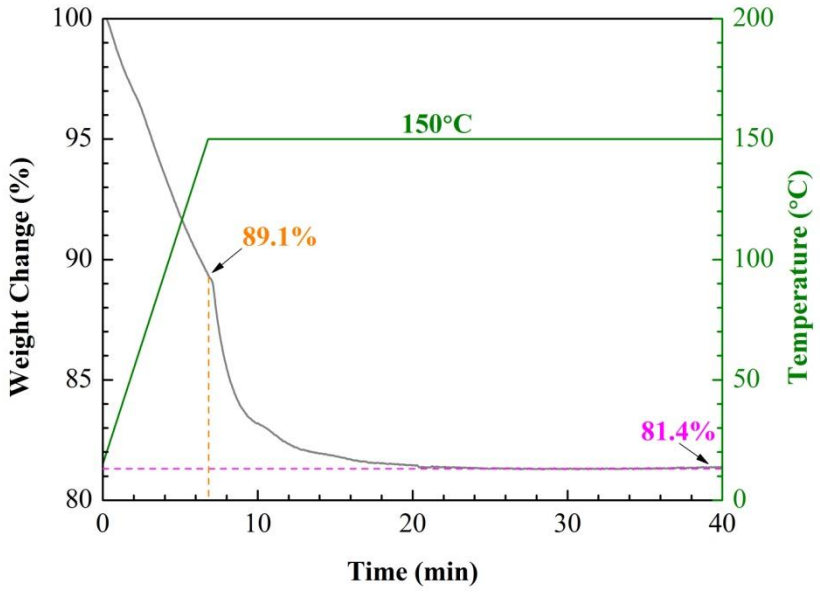

Fig. 5.1 Thermogravimetric analysis (TGA) shows the mass loss of the deposited ceria coating during the heating process.

Fig. 5.1 shows the mass changing of the scratched ceria coating during the heating process as described in the experimental section. The coating missed 10.9 % of its original mass after heating from room temperature (16 ℃) to 150 ℃ and steadily becomes stable after holding at

150 ℃ for 15 min. Therefore, all the coated samples for oxidation experiment were held at 150 ℃ for 20 min with two considerations: entirely removing the water and avoiding the increase of the coating crystal size with a long time heat treatment.

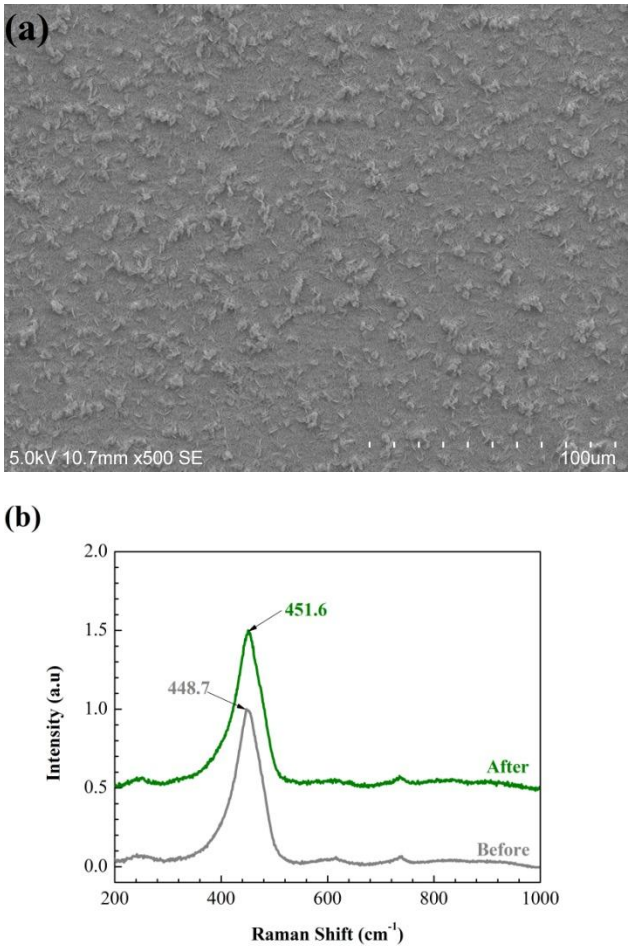

Fig. 5.2 Characterization of the coating: (a) SEM of the surface coating after heat treatment; (b) Raman spectra of the coated specimen surface after heating at 150 ℃ for 20 min.

Fig. 5.2 (a) describes the surface morphology of the deposited ceria coating after heat treatment. It is clear that the deposited ceria particles were uniformly spread on the whole specimen surface. Fig. 5.2 (b) depicts the Raman spectra of the coated ceria before and after annealing. Typically, the Raman frequency at 465 cm^{-1} represents the symmetrical stretching mode of Ce-O vibration in bulk CeO_2 [172]. However, the frequency shifted to 448.7 cm^{-1} before annealing and again shifted to 451.6 cm^{-1} after annealing as seen in Fig. 5.2 (b). The frequency shifting indicates the formation of nanocrystalline ceria that was confirmed in our previous work [172]. The slight

shift from 448.7 cm^{-1} to 451.6 cm^{-1} implies the additional crystallization of the deposited ceria during the heating process. The vibration at approximately 600 cm^{-1} indicates the presence of oxygen vacancies in the deposition film [145]. It was reported that the concentration of Ce^{3+} increased with the decreasing of ceria grain size that resulted in the formation of defective ceria film [145].

5.5.2 Oxidation kinetics

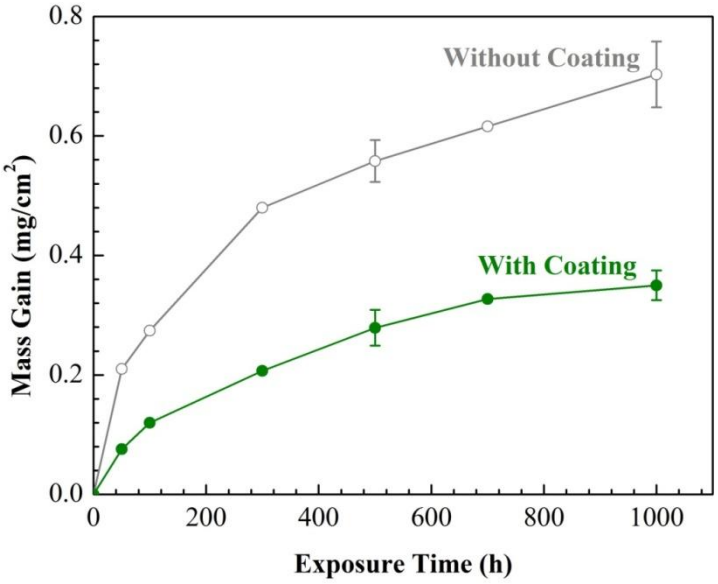

Fig. 5.3 Mass gain of samples with and without coating after oxidation at 900 ℃ for 1000 h.

Fig. 5.3 shows the mass gains of samples with and without coating after oxidation at 900 ℃ up to 1000 h. For the sample without coating, the sample was fast oxidized at the first 300 h where it obtained a mass gain of 0.48 mg/cm^2. Then the oxidation of alloy without coating gradually accessed to the steady stage where the mass gain increased slower than the initial stage. In contrast, the mass gain of the sample with coating increased smoothly at the initial stage and transferred to the steady stage with a faster speed than the uncoated sample. Clearly in the whole oxidation process, the samples without coating obtained higher average mass gains than the coated samples. The sample without coating obtained a more than two times higher mass gain than the coated sample after 1000 h exposure. This obviously demonstrates that the ceria coating reduced the oxidation rate of Hastelloy 230.

5.5.3 Characterization of oxide

Enhancing the oxidation resistance of materials through the addition of REs has been previously suggested as mentioned in the introduction. However, the dominant mechanisms of the REEs are not clearly understood. The current work will attempt to investigate the oxidation mechanisms of a Cr_2O_3-forming alloy with deposition of ceria coating.

To investigate the oxidation mechanism, XRD was used to define the oxide phases formed on top of the samples after the oxidation experiment. Fig. 5.4 shows the XRD patterns of all the samples after oxidation with different times up to1000 h. As seen from the diffraction patterns, the diffraction peak intensities of the substrates steadily decrease while those of the oxide phases strengthen with the increasing of exposure time. These phenomena imply the thickening of the oxide layer with the increasing of the oxidation time. The diffraction peaks of the substrate can be seen even after oxidation for 1000 h which indicates that the X-ray penetrated through all the oxide layers and identified all the oxide phases. It is also notable that the intensities of the oxides formed on the bare samples were always much higher than those of the coated samples with the same exposure time. The difference indicates that a thicker oxide layer formed on the sample without coating than the coated one which is in agreement with the higher mass it gained.

It is found that the ceria coating did not change the diffraction patterns of the formed oxides. This might imply that the ceria addition did not change the type of oxide formed. The detected oxide phases are mainly Cr_2O_3 and spinel as shown in Fig. 5.4. However, it is difficult to define the exact chemical composition of this spinel since formations of several different types have been previously reported for alloy 230. For instance, the formation of $MnCr_2O_4$ was previously suggested after oxidizing alloy 230 at 650 ℃ to 850 ℃ in the air up to 500 h [110]. Furthermore, $MnCr_2O_4$ formed after aging the alloy 230 in air at 850 ℃ to 1000 ℃ [173]. In another case, $NiCr_2O_4$ was found after an oxidation test of alloy 230 at 650 ℃ in supercritical carbon dioxide [174]. Therefore, in our case cross-section analysis along the depth direction was performed in order to know the oxide elemental composition.

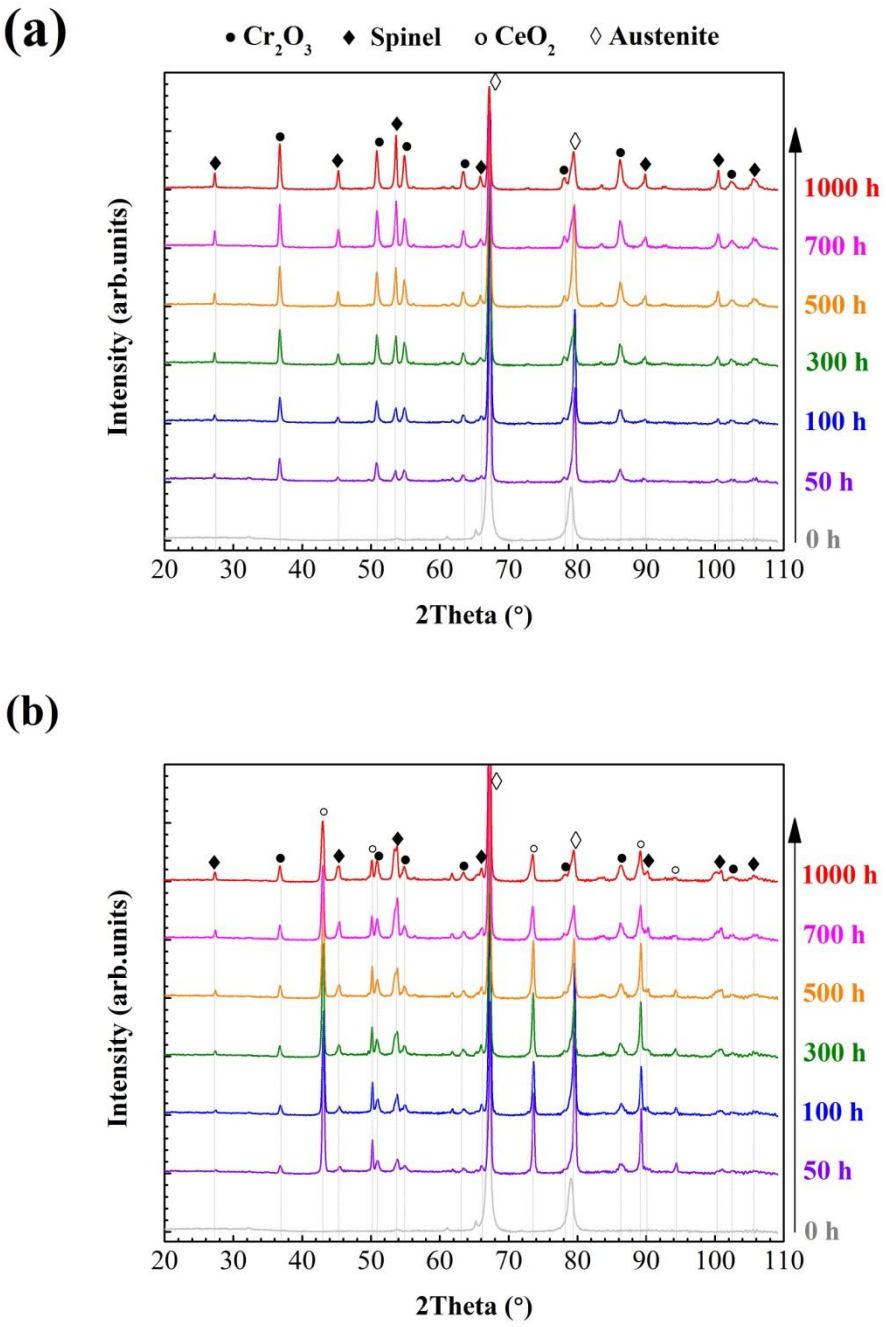

Fig. 5.4 XRD patterns for all the samples: (a) sample without coating; (b) sample with coating after oxidation at 900 ℃ up to 1000 h.

Fig. 5.5 (a) and (b) show the cross-section morphology of the oxidized samples without and with coating after exposure at 900 ℃ for 700 h. Fig. 5.5 (c) and (d) show the structures at a higher magnification. Obviously, a thicker external oxide layer was formed on the sample without coating compared with that of the coated one as seen from these images. The calculated external

oxide thickness after averaging five measurements was 6.8 μm for the uncoated sample and 3 μm for the coated one. Further, internal oxides formed and penetrated into the substrate along the grain boundaries in the uncoated sample. The average penetration depth of the internal oxide of the uncoated sample was around 15 μm. However, the internal oxides were barely observed on the sample with the ceria addition which indicates that the ceria coating suppressed the formation of the internal oxide. Finally, a small spallation area found on the uncoated sample is shown in Fig. 5.5 (a), while no spallation is visible on the coated sample which implies that the addition of ceria enhanced the adhesion of the oxide layer to the substrate.

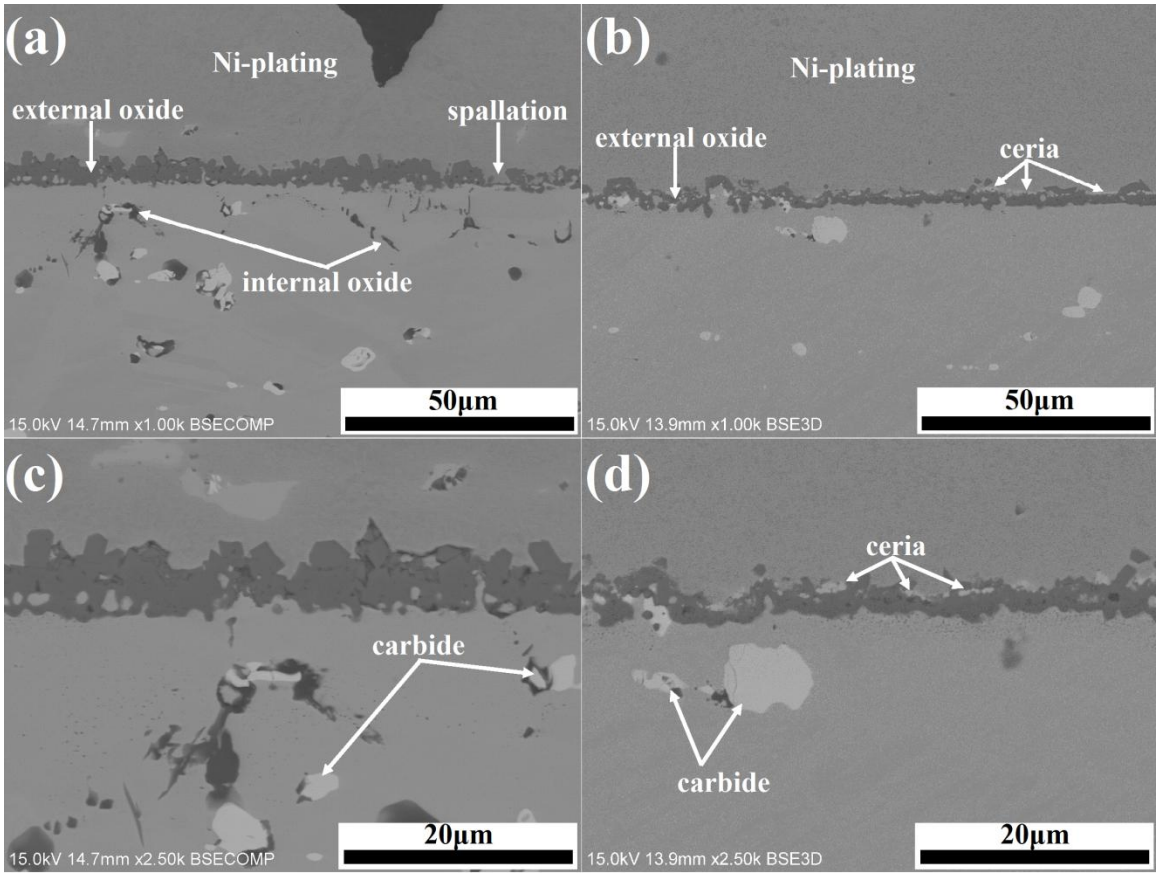

Fig. 5.5 Cross-sectional back-scattering electron images of the samples after oxidation at 900 ℃ for 700 h: (a) and (c) sample without coating; (b) and (d) sample with coating.

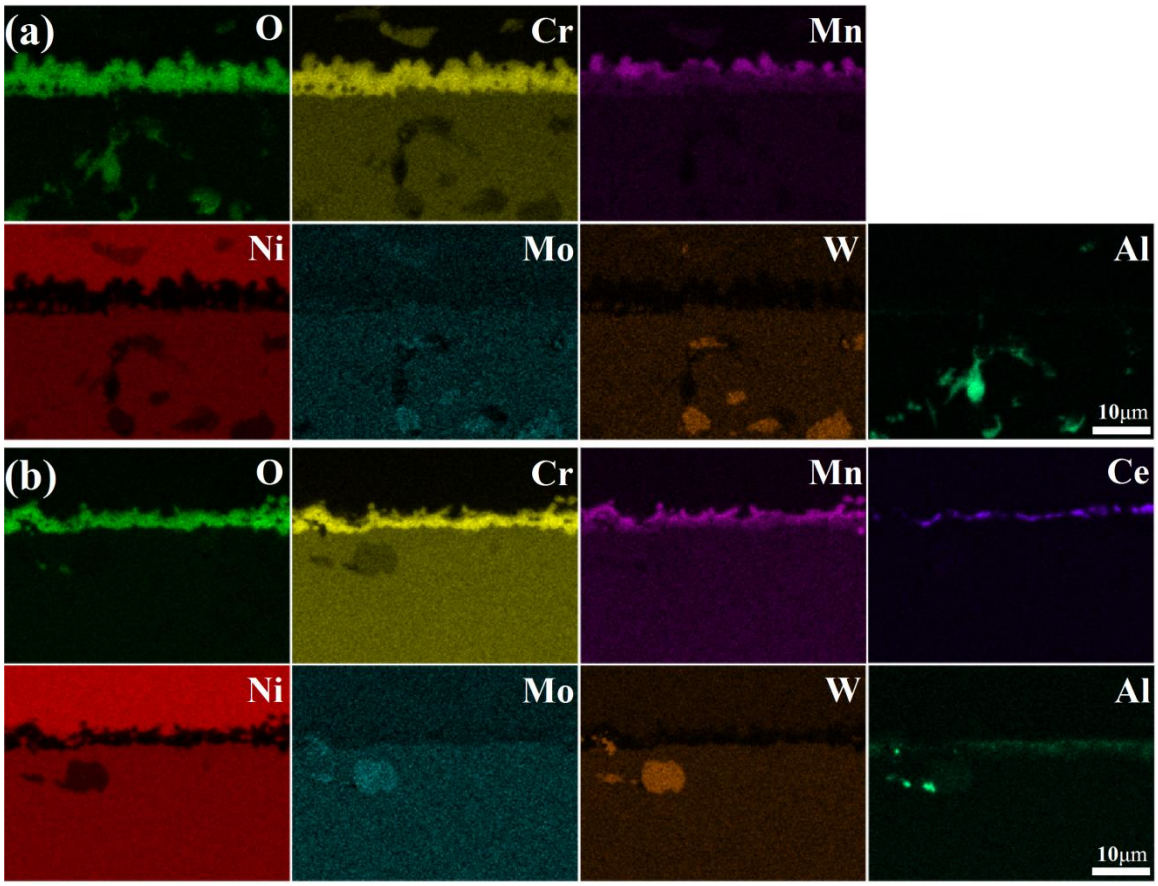

Fig. 5.6 Cross-section EDS mapping of samples after oxidation at 900 ℃ for 700 h: (a) sample without coating; (b) sample with coating. The SEM images of the EDS scanned areas are displayed in Fig. 5.5 (c) and (d).

Fig. 5.6 shows the cross-section EDS mapping results of samples after oxidation at 900 ℃ for 700 h shown in Fig. 5.5 (c) and (d). The external oxide formed on the sample without coating can be separated into two oxide layers. Fig. 5.6 (a) illustrates that Mn was concentrated on the topmost surface of the oxide layer which also contained O and a small volume of Cr. Therefore, the spinel detected by XRD could be $MnCr_2O_4$ based on this observation. The second layer of the external oxide was composed of Cr and O which confirms the formation of Cr_2O_3. Further, the internal oxide of Al_2O_3 was also found penetrating along grain boundaries and in carbide areas. In the case of the coated sample, the external oxide could also be separated into two layers of $MnCr_2O_4$ and Cr_2O_3. The thickness of oxide on the coated specimen was much thinner than that on the sample without coating. Additionally, the formation and penetration of the internal oxide were barely observed in the coated specimen. A much thinner Al_2O_3 layer formed beneath

the main oxide layer in the coated sample than that formed in the uncoated sample which indicates the ceria coating suppressed the formation of internal oxide. Based on this investigation, it seems that the addition of ceria did not change the composition of the formed oxides. It is also necessary to mention that the added ceria was observed mainly on the top of the formed oxide and that may help us to investigate the role of REE in the oxidation process.

5.5.4 Oxidation mechanism

Fig. 5.7 depicts the surface morphologies of the samples without ceria coating after oxidation for different times. Two types of oxides with different morphologies were observed after oxidation for 50 h. The oxide with granular morphology was $MnCr_2O_4$ as suggested by the EDS result shown in Fig. 5.6 (a). The Cr_2O_3 with flat morphology formed beneath the top $MnCr_2O_4$ layer. As exposure time increased, the granular oxide started spreading on the top surface which fully covered the inner oxide layer as shown in Fig. 5.7 (d). In addition, the grain size of the $MnCr_2O_4$ seemed to increase as the oxidation time was extended. Researchers previously suggested that the variation of the surface morphology is related to the changing of the oxidation kinetics and chemical reactions during the oxidation processes [175]. Variation of the oxidation rate could be resulted from different chemical reactions occurred in the oxidation processes as reported by others [135]. In the case of Hastelloy 230, several reactions can happen during the oxidation process as follows [135]:

$$\frac{4}{3}Cr(s)+O_2(g)=\frac{2}{3}Cr_2O_3(s) \qquad 5.1$$

$$\Delta G_T^{\theta}(kJ/mol)=-753.12+0.1826T$$

$$2Mn(s)+O_2(g)=2MnO(s) \qquad 5.2$$

$$\Delta G_T^{\theta}(kJ/mol)=-725.8+0.1498T$$

$$MnO(s)+Cr_2O_3(s)=MnCr_2O_4(s) \qquad 5.3$$

$$\Delta G_T^{\theta}(kJ/mol)=-1469.2+0.2798T$$

At the very beginning of the oxidation process, chromium was fast oxidized owing to its high affinity to oxygen, negative Gibbs free energy as shown in equation 5.1 and its high content in the alloy. Consequently, a thin protective Cr_2O_3 layer would have formed rapidly within a very short time. The fast formation of a Cr_2O_3 layer in Hastelloy 230 was also reported by other

researchers [176]. The initial 300 h oxidation would therefore have been controlled by the diffusion of elements through the thin Cr_2O_3 layer. The outward diffusion of Mn might have dominated the diffusion process at this stage since its diffusion velocity through the Cr_2O_3 layer was ten times higher than that of Cr [110]. The oxidation of Mn happened according to the equation 5.2. However, the formation of $MnCr_2O_4$ is more thermodynamically favourable than either Cr_2O_3 or MnO since it has a more negative Gibbs free energy as shown in equation 5.3. As a result, the formed MnO quickly reacted with the existing Cr_2O_3 and built the spinel structure. Consequently, the spinel was observed on the topmost surface of the oxide layer as seen in the Fig. 5.7 (a). The formation of MnO might not have been detected through XRD owing to its small volume and fast transformation to the spinel structure. Therefore, only Cr_2O_3 and $MnCr_2O_4$ were observed as shown in Fig. 5.7 (a). The left part of the initial stage relates to the gradual formation and growth of $MnCr_2O_4$, which attributes to the diffusion of Mn ions.

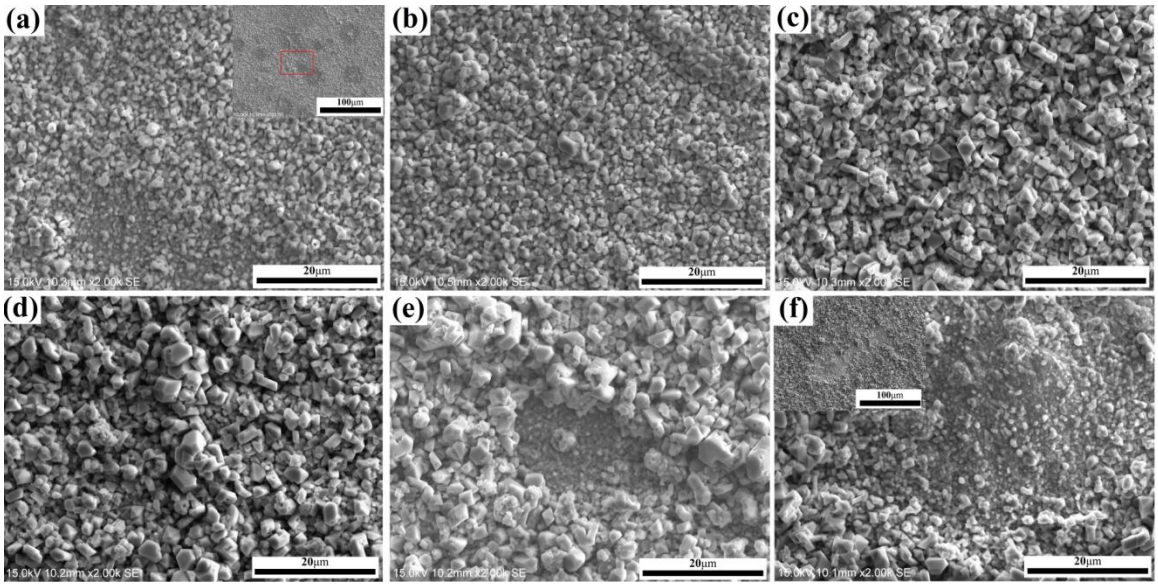

Fig. 5.7 Surface morphology of sample without coating after oxidation for (a) 50 h; (b) 100 h; (c) 300 h; (d) 500 h; (e) 700 h and (f) 1000 h.

However, the low content of Mn (0.5 wt%) in the alloy limited the continuous supply of Mn ions to produce the spinel structure as the oxidation time increased. Therefore, the consumption of Mn ions resulted in a Mn-depleted zone beneath the metal/oxide interface and it took a long time to reproduce a new Mn flux. Consequently, the dominant diffusion element changed back to Cr owing to its high content and the diffusion of Cr dominated in the steady oxidation stage. The

steady stage mainly contained the thickening of the Cr_2O_3 layer and the slow growth of $MnCr_2O_4$. Nevertheless, as mentioned earlier, the Cr diffused much slower than Mn in Cr_2O_3 layer which led to a reduction of oxidation kinetics for the steady oxidation stage. The oxide spallation observed after oxidation for 700 h as seen in Fig. 5.7 (e) was significant. Fig. 5.7 (f) shows the spallation was more pronounced after oxidation for 1000 h. The oxide spallation may occur at the cooling stage and/or at temperature. Obviously, a sudden decreasing of the sample temperature will probably result in the oxide spallation owing to the different thermal expansion coefficient of the scales and the substrate. In addition, the thermal stresses accumulated during the oxide growth process may also facilitate the oxide spallation. For Hastelloy 230 without coating, it is also notable that the spallation did not result in the direct exposure of the matrix alloy since no morphology of substrate was observed in the spallation area as seen in Fig. 5.7 (e) and (f). Further, Cr_2O_3 with some isolated $MnCr_2O_4$ particles were still seen in the spallation area as shown in Fig. 5.7 (f). Two assumption reasons might result in such a phenomenon: Firstly, it is generally accepted that the Cr_2O_3 layer can be a protective layer and has good adhesion to the substrate alloy. Therefore, the spallation might only occur on the $Cr_2O_3/MnCr_2O_4$ interfaces that resulting in the directly observed Cr_2O_3 in the spallation area. Secondly, oxide spallation might happen at the metal/Cr_2O_3 interfaces where the stress generated from the growth of the oxide layer is high. However, a new Cr_2O_3 layer would fast form and cover the spallation again since there is enough Cr in Hastelloy 230. Therefore, a thin Cr_2O_3 layer was still observed in the spallation area as illustrated in Fig. 5.7 (f). In this case, the reforming of spinel would depend heavily on how long it took to re-establish a new Mn flux since a Mn-depleted zone had already formed before spallation of the Cr_2O_3 layer. Therefore, the spinel might be barely visible in the spallation area as seen in Fig. 5.7 (f). To explore the reason for the spallation, a kernel average misorientation (KAM) map obtained from EBSD is used to display the strain distribution through local average misorientation (0 ~ 5 °) between each point and its neighbours. Fig. 5.8 (a) shows the cross-section image-quality map of a spallation area of the sample without coating after oxidation for 700 h and Fig. 5.8 (b) shows the KAM map of the same area. Two distinct oxide layers with partial spallation of $MnCr_2O_4$ are visible in Fig. 5.8 (a) where white arrows mark the internal oxides. The KAM map shows the strain concentrated on the internal oxide areas where it penetrated to the substrate/Cr_2O_3 interfaces as marked by the red circles. However, less strain is observed in the $Cr_2O_3/MnCr_2O_4$ interfaces as compared with the substrate/Cr_2O_3

interfaces. Therefore, the concentrated strain in the substrate/Cr_2O_3 interface must have weakened the adhesion of the Cr_2O_3 layer. Consequently, the weakly adhered oxide may promote oxide spallation at the oxidation temperature and/or at the cooling process. It was also suggested that the disconnection of scale and substrate resulted from the vacancy condensation in the substrate/scale interface owing to the fast outward diffusion of caitons [170]. Subsequently, the voids and defects on the substrate/scale interface would weak the oxide spallation resistance. However, for Hastelloy 230 without coating, the voids were not observed on the substrate/scale interface.

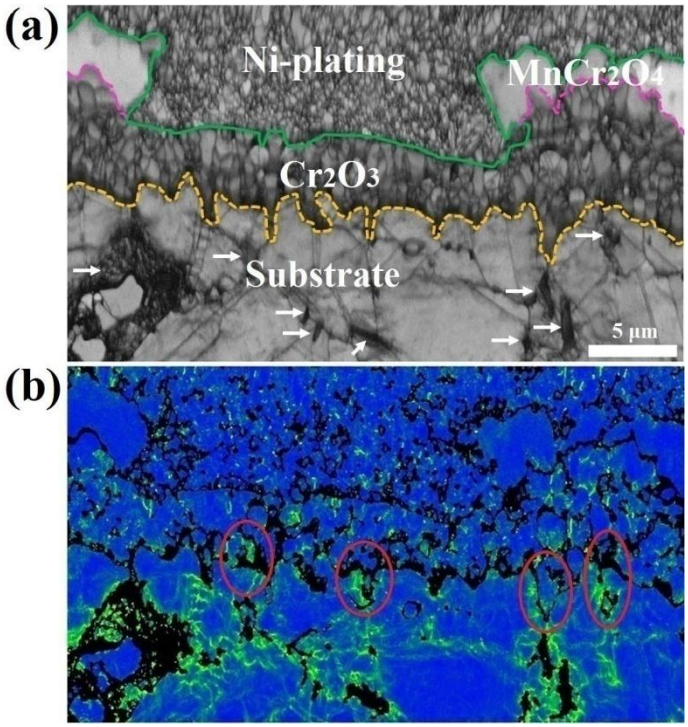

Fig. 5.8 Cross-sectional analysis showing a spallation area of the uncoated sample after oxidation at 900 ℃ for 700 h: (a) EBSD band contrast map; (b) Kernel average misorientation (KAM) map.

Fig. 5.9 shows the surface morphology of samples with ceria added after oxidation up to 1000 h. Network morphology ceria coating was observed after oxidation for 50 and 100 h as seen in Fig. 5.9 (a) and (b). However, no oxide particles or islands were observed on top of the ceria coating. A similar type of morphology was previously observed on an Al_2O_3-forming alloy [87]. The oxidation mechanism of this type of oxidation was attributed to the dominant inward diffusion of

oxygen. Therefore, the oxidation rate reduced since the inward diffusion of oxygen was much slower than the outward diffusion of ions through a Cr_2O_3 layer [177,178]. Consequently, the oxidation rate of the ceria coated sample reduced which resulted in a lower mass gain during the oxidation process. As the exposure time increased, the oxide particles gradually formed and the number of particles also increased as seen in Fig. 5.9 (c) to (f). However, no oxide spallation was detected during the whole oxidation process up to 1000 h which demonstrates that the ceria coating enhanced the adhesion strength between the oxide layer and substrate.

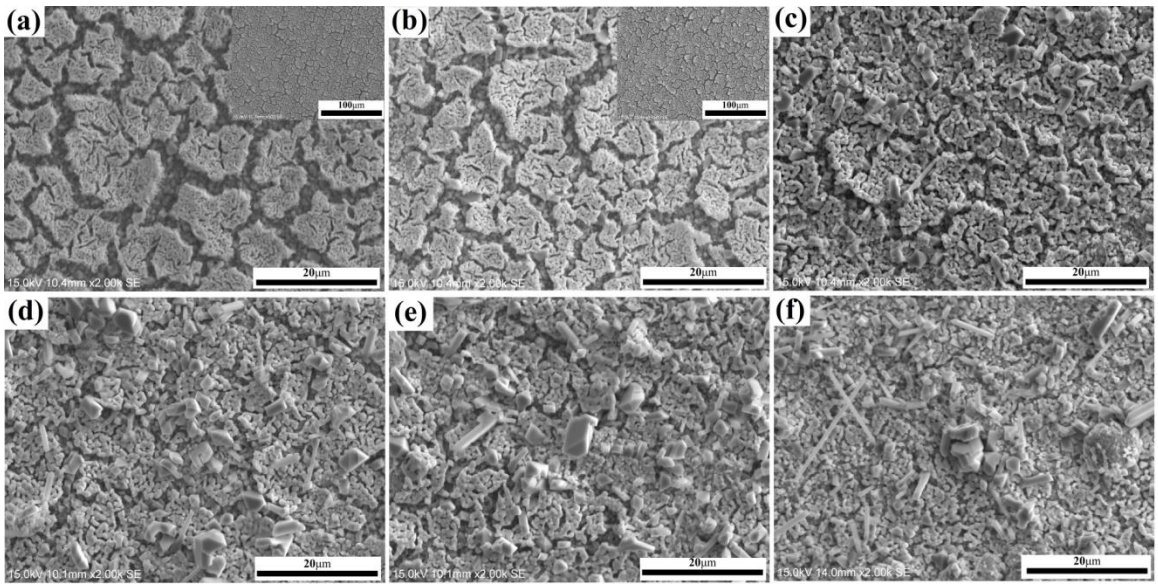

Fig. 5.9 Surface morphology of ceria coated sample after oxidation for various time: (a) 50; (b) 100; (c) 300; (d) 500; (e) 700 and (f) 1000h.

To know how the adhesion at the metal/oxide interfaces could be enhanced, EBSD was used to see the microstructure of the oxide through cross-section analysis. Fig. 5.10 shows the inverse pole figure (IPF), phase and EDS maps of the samples without and with ceria coating after oxidation for 700 h at 900 ℃. The IPF and phase maps were obtained from the cross-section EBSD map. EBSD mapping was reported as an efficient way to precisely illustrate the cross-section microstructure of the oxide [179]. The cross-section IPF, phase and EDS analysis of the spallation area of the uncoated sample are shown in Fig. 5.10 (a) to (c). The colour legends of the IPF maps and different phases are shown in the IPF map and the right bottom corner of Fig. 5.10 (c), respectively. In the case of the uncoated sample, two oxide layers can be found in the external layer as seen in the phase and EDS maps. The top oxide layer with large equiaxed grains

is acknowledged as $MnCr_2O_4$, while the inner layer with columnar grains is Cr_2O_3. Fig. 5.10 (d) to (f) shows the IPF, phase and EDS maps of a cross-section area of the coated sample. Similarly, two oxide layers could be also considered as the top layer was a mixed oxide layer of $MnCr_2O_4$ and ceria and the inner layer was Cr_2O_3. However, it is important to note that the microstructure of the Cr_2O_3 changed from columnar to the more equiaxed structure with the addition of the ceria coating. The changing of oxide microstructure owing to the addition of REs has rarely been reported. One similar phenomenon was reported by Wessel et.al. [60]. They suggested that the addition of Zr to FeCrAlY alloy changed the Al_2O_3 scale grain structure from the columnar to equiaxed. However, their sample with equiaxed oxide grains was oxidized much faster than that with columnar oxide grains which is completely opposite to the oxidation kinetics we observed. The researchers suggested that the higher grain boundary density of the small equiaxed grains enhanced the diffusion of ions which resulted in a higher oxidation rate of the Zr-added alloy [60]. Nevertheless, the grain size difference of the Cr_2O_3 formed with and without coating in our work was much smaller than they obtained for Al_2O_3 [60]. Therefore, the grain boundary density explanation is probably not correct in our case. In the current work, the columnar grains formed on the uncoated sample more likely attribute to the outward diffusion of ions. Research has shown that the growth of columnar structure is significantly related to the element diffusion mechanism and that the growth direction of the elongated grain will be along the direction of maximum diffusion [180]. In our case, the outward diffusion of Cr^{3+} dominated the oxidation process. The shortest path would be the favorable diffusion ways for ions which obtained the highest diffusion flux. In other word, the normal direction of the alloy/scale would be the right way that had the maximum diffusion. Consequently, the fast and massive diffusion of Cr^{3+} will accelerate the growth of Cr_2O_3 along the normal direction of the metal/scale interface. Finally, the columnar structure oxide grains will form.

However, in the case of the ceria coated sample, the dominant diffusion mechanism can be changed from outward diffusion to inward diffusion. The EDS mapping results in Fig. 5.10 (f) show the ceria particles clearly concentrated on the top surface of the oxidized sample. This may indicate that the inward diffusion of oxygen dominated the oxidation process assuming the immobility of ceria particles [181]. The coefficient of the oxygen diffusion in the Cr_2O_3 layer is around ten times lower than the chromium. Consequently, a lower oxidation velocity can be obtained for the sample with ceria coating. Fig. 5.11 shows the high-resolution back-scattering

electron (BSE), band contrast (BC) and phase maps of a small area surrounding the ceria particles after oxidation the coated sample for 700 h. The color legend of the phase map is same as displayed in Fig. 5.10. Ceria particles are marked by the white circles in the BSE map and shown as gray areas in the phase map. The ceria particles are shown to precipitate on the oxide grain boundaries although the area around the particles was not well-indexed owing to the very fine oxide grain size and limitation of the minimum step size of EBSD scanning. The segregation of reactive elements on the oxide grain boundaries was believed to suppress the outward diffusion of cations [164]. Therefore, the inward diffusion of oxygen likely controlled the oxidation process of the coated sample decreasing its oxidation kinetic. In addition, the ceria particles might have acted as heterogeneous nucleation sites for the formation of Cr_2O_3, which is confirmed by the very fine oxide grains close to the ceria particles seen in the BC map [69,76,93,182]. Thanneeru et.al demonstrated that the ceria coating offered additional nucleation sites for Cr_2O_3 which resulted in a fast formation of a homogeneous Cr_2O_3 layer on alloy 304 [76]. Lopez et.al also observed the similar phenomena after oxidation alloy 316 and 304 with ceria coating [93,182]. It was reported that the addition of ceria clearly reduced the time needed to form a protective Cr_2O_3 layer [182]. In addition, Guo et.al demonstrated that the REs enhanced the nucleation rate of α-Al_2O_3 for alloy NiAl after oxidation at 1200 ℃ [69]. In the case of Hastelloy 230, the increased nucleation sites would have reduced the distance between neighbouring grains of the oxides which promoted the formation of a homogeneous Cr_2O_3 layer. Furthermore, slow inward diffusion of anions would have offered enough time for the growth of oxide grains. Consequently, the granular structure of oxide would have been favourable for the coated sample. The formation of fine equiaxed grains was reported to be beneficial to the deformable properties of the metals [183] since the smaller grains tend to deform homogeneously. Therefore, the equiaxe-structured oxides may enhance the adhesion of an oxide layer since they are more likely to release the stress from the oxide growth process or the cooling process than the columnar oxide. As a result, the adhesion of the oxide would have been enhanced for the sample with ceria coating. More importantly, the internal oxidation was likely suppressed by the addition of ceria particles which enhanced the bonding strength of the metal/oxide interface.

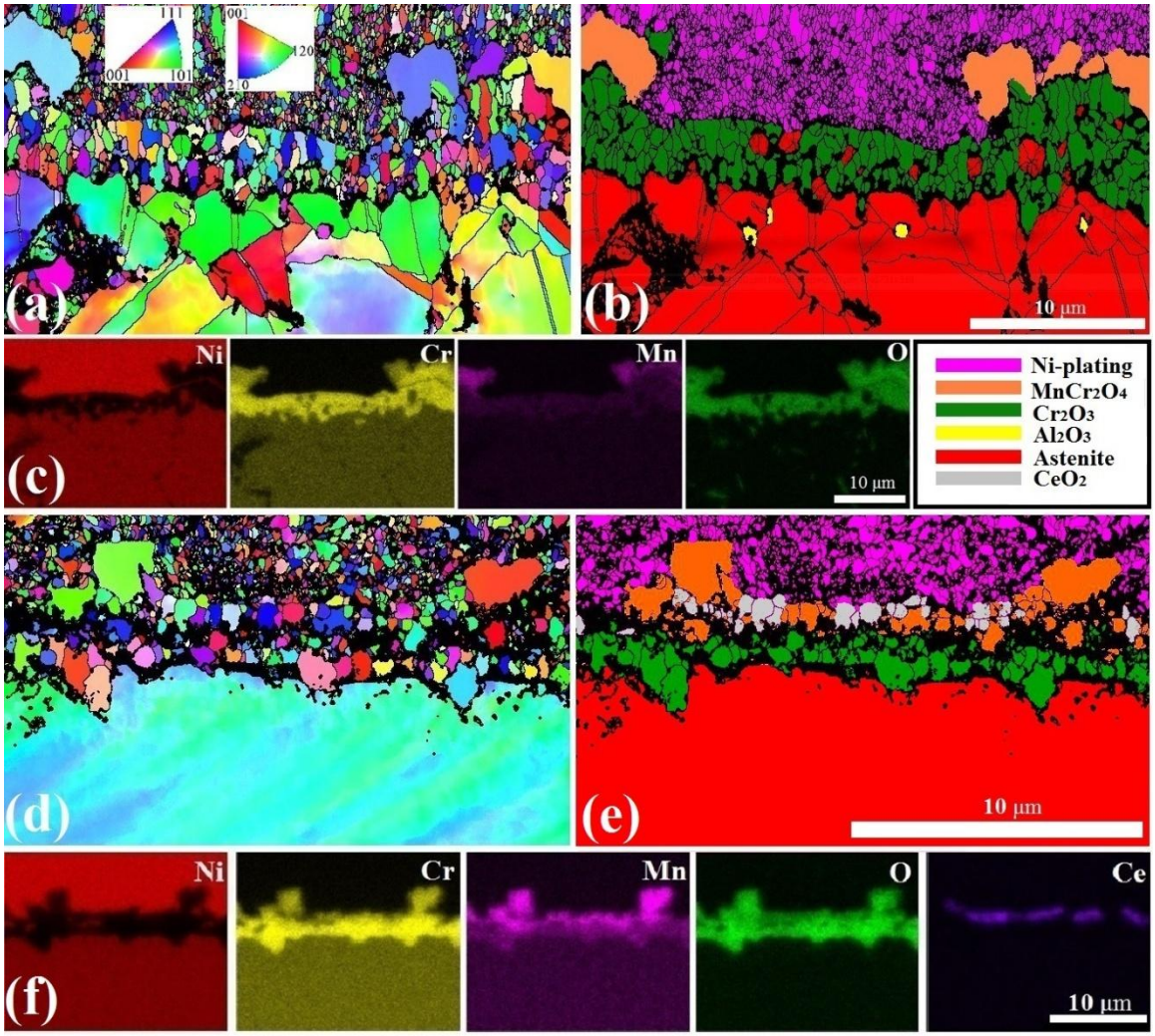

Fig. 5.10 Cross-section analysis of sample after oxidation at 900 ℃ for 700 h: (a) IPF, (b) phase and (c) EDS maps of the sample without coating; (d) IPF, (e) phase and (f) EDS maps of the sample with ceria coating.

Furthermore, the oxygen vacancies in the ceria coating may also have a chance to affect the oxidation behavior of alloys. Thanneeru et.al reported that the mass gains of the samples with ceria and La doped ceria were controlled by the inward diffusion of oxygen via the oxygen vacancies at the initial stage [76]. The oxygen vacancies increased with the increasing content of La doped in ceria which increased the nucleation sites for Cr_2O_3. Lopez et.al demonstrate that the existence of oxygen vacancies favored the inward diffusion of oxygen [93]. However, Pedraza et.al suggested that the oxygen vacancies would be immediately saturated with oxygen after annealing the ceria coating at 1050 ℃ for 1 h even with a low oxygen pressure [151]. Therefore,

the oxygen vacancies in the ceria coating might only affect the oxide formation at the very beginning of the oxidation process for Hastelloy 230. The ceria coating with high oxygen vacancies favored the inward diffusion of oxygen and offered more nucleation sites for Cr_2O_3 formation. Consequently, a faster access to steady stage was observed owing to the fast formation of a protective oxide layer.

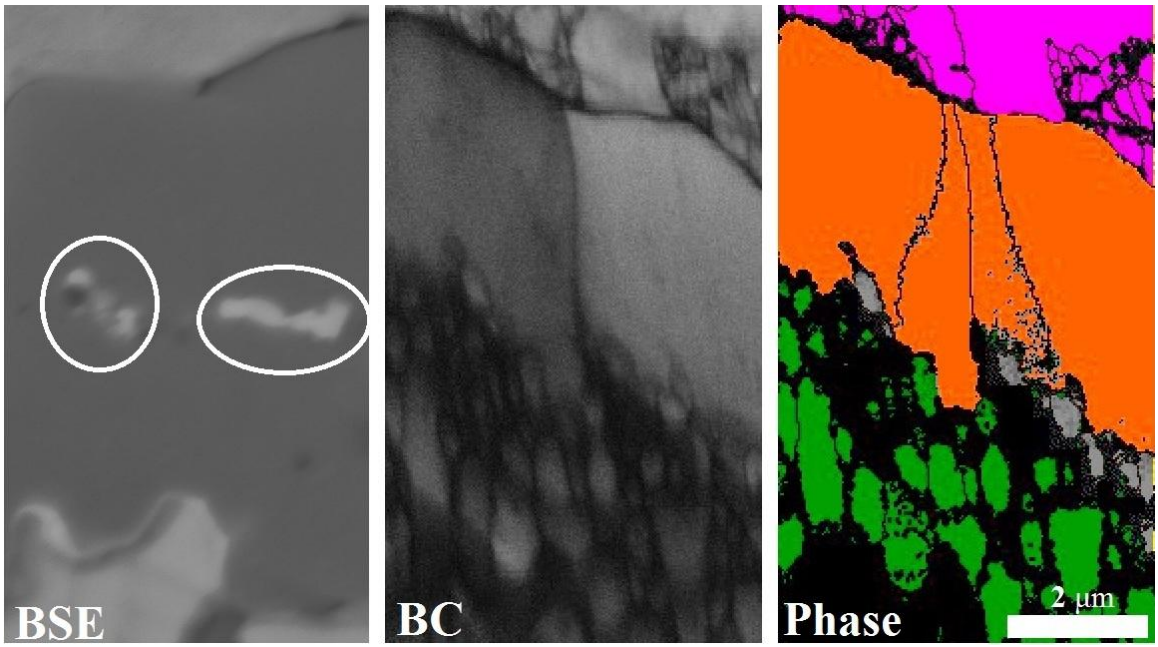

Fig. 5.11 Cross-sectional back-scattering electron image, band contrast (BC) and phase maps of the areas around ceria particles after oxidation for 700 h at 900 ℃. (The color legend of the phase map is shown in Fig. 5.10.

5.6 Conclusions

In conclusion, the mechanism of the oxidation behaviour of Hastelloy 230 with the addition of ceria coating was investigated. The following conclusions could be drawn from the current work:

(1) Electro-deposition process is used to synthesize ceria coating onto Hastelloy 230. The prepared ceria coating enhances the oxidation resistance of the substrate alloy and also improves the adherence of the oxide scale.

(2) The addition of ceria coating reduced the oxidation rate of Hastelloy 230 while it did not change the types of the formed oxides.

(3) The addition of ceria coating suppresses the formation of the internal oxide while severe internal oxidation occurs on the uncoated alloy. A larger depth of internal Al_2O_3 layer forms on uncoated Hastelloy 230 than on the coated alloy. The internal oxide weakens the bonding strength of the metal/oxide interface.

(4) The addition of ceria particles changes the oxidation mechanisms of coated Hastelloy 230 from outward diffusion to inward diffusion of oxygen. The incorporation of ceria particle changes the chromium oxide from columnar to an equiaxed structure which enhances the spallation resistance of the oxide layers.

Chapter 6 Ceria coating for controlling isothermal oxidation behavior of Ni-based Hastelloy 625

6.1 Overview of chapter 6

In the chapter 5, the influence of ceria coating on the oxidation behavior Hastelloy 230 was inspected. The aim of the present chapter is to understand the effect of ceria coating on the oxidation behavior of a Cr_2O_3-forming alloy which also can form iron oxide.

This chapter was submitted as a manuscript #6: Ceria coating for controlling the isothermal oxidation behavior of Ni-based Hastelloy 625. The Ph.D candidate's contributions to this manuscript are a) preparing all the samples; b) depositing ceria coating; c) performing the oxidation experiments; d) characterizing all the oxidized samples; e) writing the manuscript.

The manuscript is under reviewing in *Corrosion Science*:

- X. Wang, J.A Szpunar, Ceria coating for controlling the isothermal oxidation behavior of Ni-based alloy 625, Corrosion Science, (2016) under review.

The differences of this chapter with the submitted manuscript are as following:

- The description of the electro-deposition mechanisms is deleted;
- The description of the Scherrer equation is deleted to avoid repeating with that listed in Chapter 4;

The references of the submitted manuscript are listed at the end of the thesis.

Ceria coating for controlling the isothermal oxidation behavior of Ni-based Hastelloy 625

Xu Wang, Jerzy A. Szpunar

Department of Mechanical Engineering, University of Saskatchewan, Saskatoon, SK, S7N 5A9, Canada

6.2 Abstract

A ceria coating is electro-deposited on a chromium oxide forming Ni-based alloy to investigate the mechanisms of the reactive element effects. It is demonstrated that the ceria coating not only improves the oxidation resistance but also enhances the adherence between the oxide layer and the substrate alloy. The formation of iron oxide results in porous and cracked oxide layers on the bare sample. Oxide spallation starts to occur on the bare sample after exposure at 900 ℃ for 500 h. In contrast, a mixed iron-free oxide layer forms on the coated sample which is believed to enhance the oxidation resistance of the substrate. The change in oxidation mechanism of the coated sample from outward diffusion to inward diffusion is attributed to grain-boundary segregation of ceria particles. Furthermore, the formation of fine oxide grains on the coated sample improves the adhesion between the oxide layer and the matrix alloy. Schematic models of the oxidation mechanism are developed to interpret the oxidation behavior of the bare and coated samples.

Keywords: High-temperature oxidation; Ni-based alloy; Electron backscattering diffraction (EBSD); Reactive element effect (REE)

6.3 Introduction

Due to their properties of stability, density and slow growth, Cr_2O_3 and Al_2O_3 layers are accepted as protective oxide barriers for high-temperature alloys. Consequently, alloys that enable the formation of either Cr_2O_3 or Al_2O_3 can be used in high-temperature environments. Those alloys are then termed as Cr_2O_3 and Al_2O_3-forming alloys. It has been reported that the addition of reactive elements, such as Ce, Y, Ta, Re and Yb, can strikingly enhance the high-temperature oxidation resistance of Cr_2O_3 and Al_2O_3-forming alloys [49,87,94,163,184,185]. The primary effects of adding these elements were summarized as decreasing the oxidation rates of these alloys or enhancing the adherence of the oxide layer to the substrate matrix [73,86,186]. These

influences were called as REEs. However, the mechanisms for REEs are still not fully understood.

Various methods have been proposed to add reactive elements into alloys either by alloying [59,63] or suitable surface treatments such as sputtering [80], dip coating [49,73,146], ion implantation [81], MOCVD [187] and electro-deposition [87]. Among these methods, electro-deposition has been considered to be one of the most effective and environment-friendly ways to prepare homogeneous metal-oxide thin films [86]. The effect of ceria coating on the oxidation behavior of Al_2O_3-forming alloys synthesized through the electro-deposition process was previously investigated [86,87,145]. The formation of $CeAlO_3$ resulting from the reaction of ceria and alumina in the metal/oxide interface was attributed to the enhanced adhesion between the oxide layer and the substrate alloy [87]. However, the influence of the ceria coating on the oxidation behavior of the Cr_2O_3-forming alloy was barely discussed.

Alloy 625 is extensively used as a structural material in many industries utilizing high-temperature processes such as aerospace, chemical industries and nuclear industry applications. Therefore, high-temperature oxidation behavior is one of the most critical properties of this alloy. Consequently, the oxidation behavior of alloy 625 was previously investigated [174,188,189]. The high chromium content in alloy 625 clearly indicates it is a Cr_2O_3-forming alloy since the content of 12% is sufficient to form a continuous Cr_2O_3 layer [10]. It was demonstrated that alloy 625 could maintain its excellent oxidation resistance under a temperature of 815 ℃. However, its oxidation resistance would significantly decrease with increasing temperature. Consequently, to find new ways of enhancing the oxidation resistance of this alloy at high temperatures is extremely important based on the discussion above. Therefore, the objective of this work is to study the effect of a ceria coating prepared by the electro-deposition process on the oxidation behavior of a Cr_2O_3-forming Hastelloy 625.

6.4 Experimental Procedures

Hastelloy 625 with the nominal chemical composition shown in Table 6.1 was used in our work. All the samples were machined with dimensions of 18 × 12 × 1.5 mm from the alloy strip. To facilitate the oxidation experiment and to ensure all the sample surfaces were exposed to the oxidizing atmosphere, a small hole with a diameter of 1.5 mm was drilled in each sample. Next,

all of the samples were manually ground to 1200 grit and ultrasonically cleaned in acetone for 10 min. Finally, all of the samples were cleaned with deionized water and ethanol and dried in a desiccator for 24 h before further tests.

Table 6.1 Nominal chemical compositions of Hastelloy 625 (wt %)

Ni	Co	Fe	Cr	Mo	Cb+Ta	Mn	Si	Al	Ti	C
Bal	1	5	21	9	3.7	0.5	0.5	0.4	0.4	0.1

After drying in the desiccators, half of the polished samples were coated with ceria using an electro-deposition process. The detailed deposition processes were described in our previous work [172]. A cathodic electro-deposition process was performed through a classical three-electrodes Gamry Interface 1000 device with a sample as the working electrode, a Pt grid as a counter electrode and an SCE as a reference electrode. The electrolyte solution was 0.1 M $Ce(NO_3)_3 \cdot 6H_2O$ and samples were electro-deposited at a current density of -0.75 mA/cm^2 for 20 min at room temperature in the galvanostatic mode. Then all of the coated samples were dried in the desiccator again for 24 h to remove the possible presence of water from the coating. Finally, all the samples were annealed in a furnace at a temperature of 150 ℃ for 20 min to entirely remove all traces of molecular.

For the oxidation test, samples both with and without the coating were isothermally oxidized in a muffle furnace at 900 ℃. The samples were suspended in ceramic boats by ceramic rods with a diameter of 0.08 mm through the holes drilled as described above. The ceramic boats were regularly removed from the furnace after interval times of 50, 100, 300, 500, 700 and 1000 h which represented the time of exposure to the oxidizing atmosphere. A Mettler Toledo XS205 analytical balance having a resolution of 10^{-2} mg was used to measure the masses of the samples before and after oxidation.

After the oxidation experiment, a D8 Bruker discovery XRD system with Cr Kα (λ = 0.22897 nm) radiation was used to define the oxide phases formed on all samples. The surface and cross-section morphology of the oxidized sample was characterized using a Hitachi SU6600 FE-SEM at 15 kV. For the cross-section analysis, the oxidized sample was firstly electro-plated with nickel that was used to prevent the removal of the oxide layers during the polishing process. The

Ni-plated cross-section samples were then mounted with polyfast conductive resin. Finally, the mounted samples were manually ground using silicon carbide paper up to 4000 grit and polished with 3 and 1 μm polishing solution. After this treatment, all of the samples were polished using a BUEHLER Vibromet 2 vibratory polisher for 24 h. The gentle vibratory polishing produced a flat and stress-free cross-sectional surface and allowed both EBSD and EDS characterization. EBSD and EDS were performed at 30 kV. A small step size of 60 nm was used for EBSD scanning. HKL Channel 5 software was used to visualize the EBSD data.

6.5 Results and Discussions

6.5.1 Characterization of the ceria coating

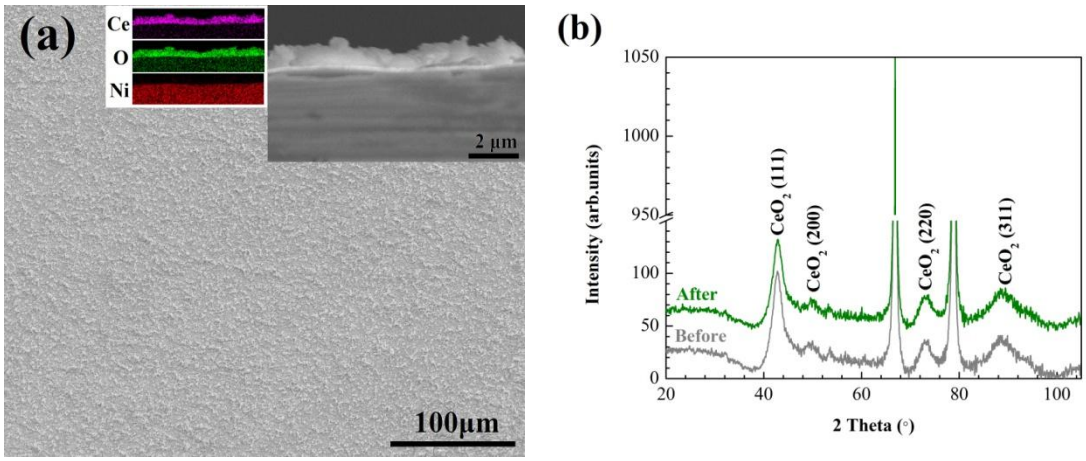

Fig. 6.1 Surface and cross-section morphology and XRD patterns of the ceria coating: (a) surface and cross-section morphology; (b) XRD patterns.

Fig. 6.1 (a) shows the surface and cross-section morphology of the ceria coating after heat treatment. Clearly, the ceria coating homogeneously spreads over the whole area and the thickness of the coating is approximately 1.5 μm as shown in the cross-section image. EDS mapping was used to confirm the formation of the ceria coating as shown in the inset image of Fig. 6.1 (a). Fig. 6.1 (b) shows the XRD pattern of the ceria coating before and after annealing. Four broadening diffraction peaks corresponding to CeO_2 are observed which indicates the possible formation of nano-crystalline ceria particles. Consequently, the crystal size of the coating is calculated based on the Scherrer equations described in 4.12 and 4.13. The commercial CeO_2 powders purchased from the Aldrich company were annealed at 1200 ℃ for 20 h and used as standard samples to discard the inherent instrumental broadening [172]. The diffraction peak

of (111) is fitted with the Gaussian equation to know the FWHM of the deposit before and after annealing. The calculated average crystal sizes for the coating before and after annealing are 6.5 and 6.7 nm, respectively. The average crystal size slightly increases after annealing but it is still nano-crystalline.

6.5.2 Oxidation kinetics

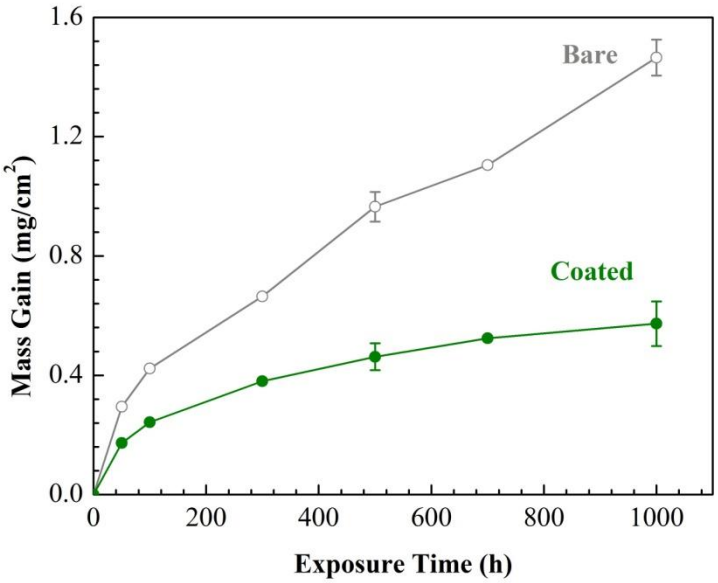

Fig. 6.2 Oxidation kinetics of the samples at 900 ℃ for 1000 h.

Fig. 6.2 shows the oxidation kinetics of all the samples after exposure at 900 ℃ up to 1000 h. The bare and coated samples are all rapidly oxidized during the initial stage. Next, the oxidation process of the coated sample gradually accesses to the steady stage where the mass gain steadily becomes stable. For the bare sample, the mass gain dramatically increases especially after oxidation for 300 h. It is observed that the sample without coating shows a mass gain almost three times higher than that of the coated sample after exposure for 1000 h. This clearly indicates that the ceria coating reduces the oxidation rate of the alloy.

6.5.3 Characterization of oxide

6.5.3.1 Surface morphology

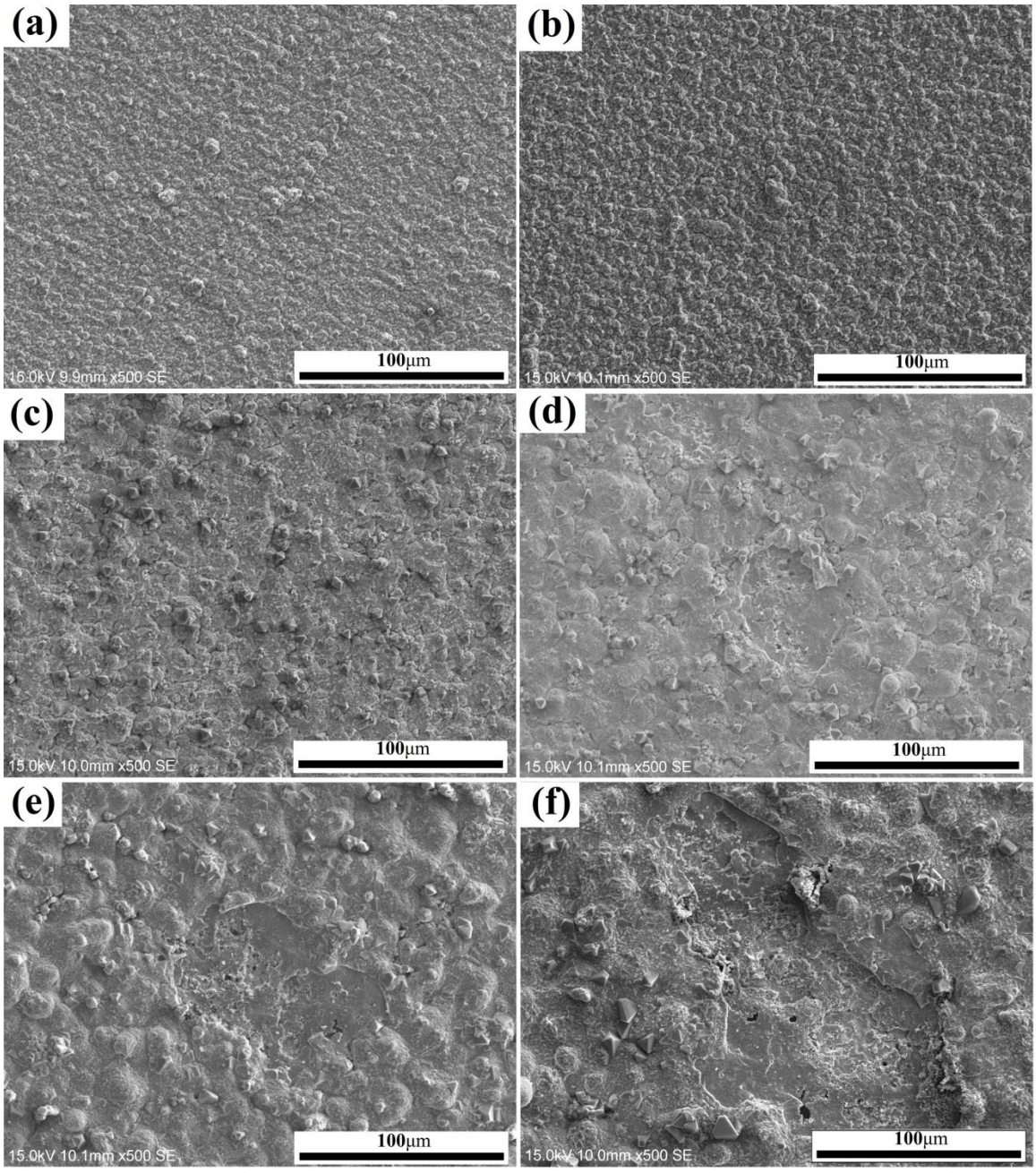

Fig. 6.3 Surface morphology of the bare sample after oxidation at 900 ℃: (a) 50 h; (b) 100 h; (c) 300 h; (d) 500 h; (e) 700 h; (f) 1000 h.

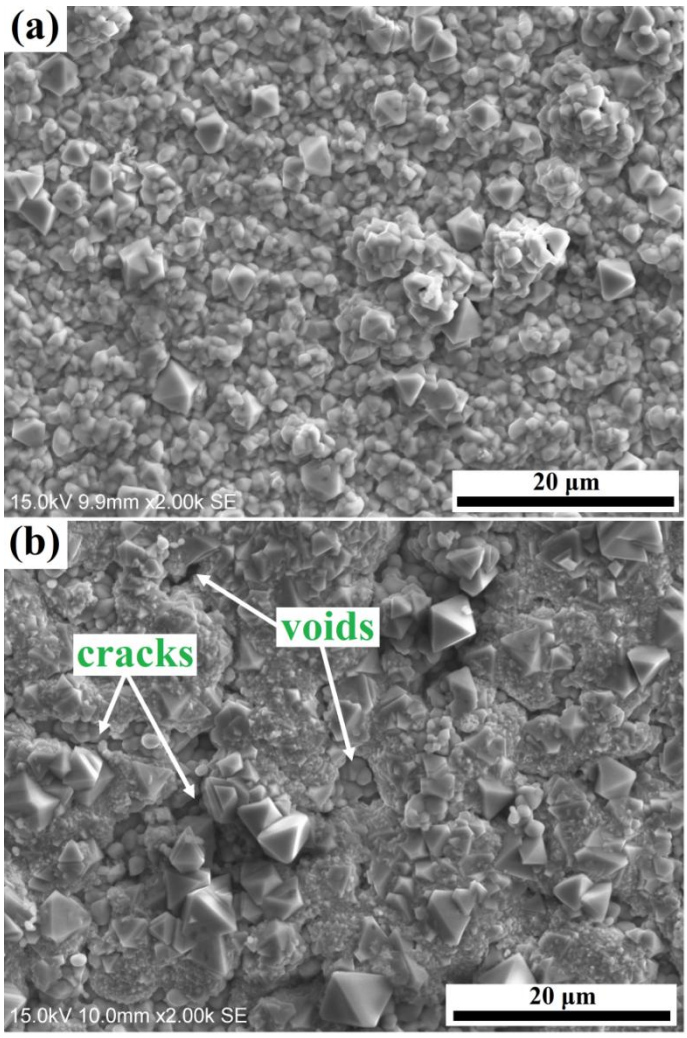

Fig. 6.4 High magnification surface morphology of the bare sample after oxidation at 900 ℃: (a) 50 h; (b) 300 h.

Fig. 6.3 shows the surface morphology of the bare samples after oxidation at 900 ℃ for different times. Fig. 6.4 depicts higher magnifications of the surface morphology of samples oxidized for 50 h and 300 h. The oxide formed on the sample surface seems dense and compact after oxidation for 50 h and 100 h as seen from Fig. 6.3 and Fig. 6.4 (a). However, many micro-cracks and pores starts to form inside the oxide layer of the sample oxidized for 300 h which indicates the oxide layer is poorly compacted as shown in Fig. 6.4 (b). Consequently, oxide spallation occurs after 500 h exposure and is clearly observed on the sample surface after 1000 h oxidation. Even worse, the matrix grains are directly exposed to the oxidizing environment. Many pores are observed both inside the oxide grains and in the grain boundary areas of the substrate. The

existence of micro-cracks and pores will facilitate the ingress of oxygen into the substrate matrix. Therefore, severe spallation and a greater depth of inner oxide occur which is detrimental to the oxidation resistance.

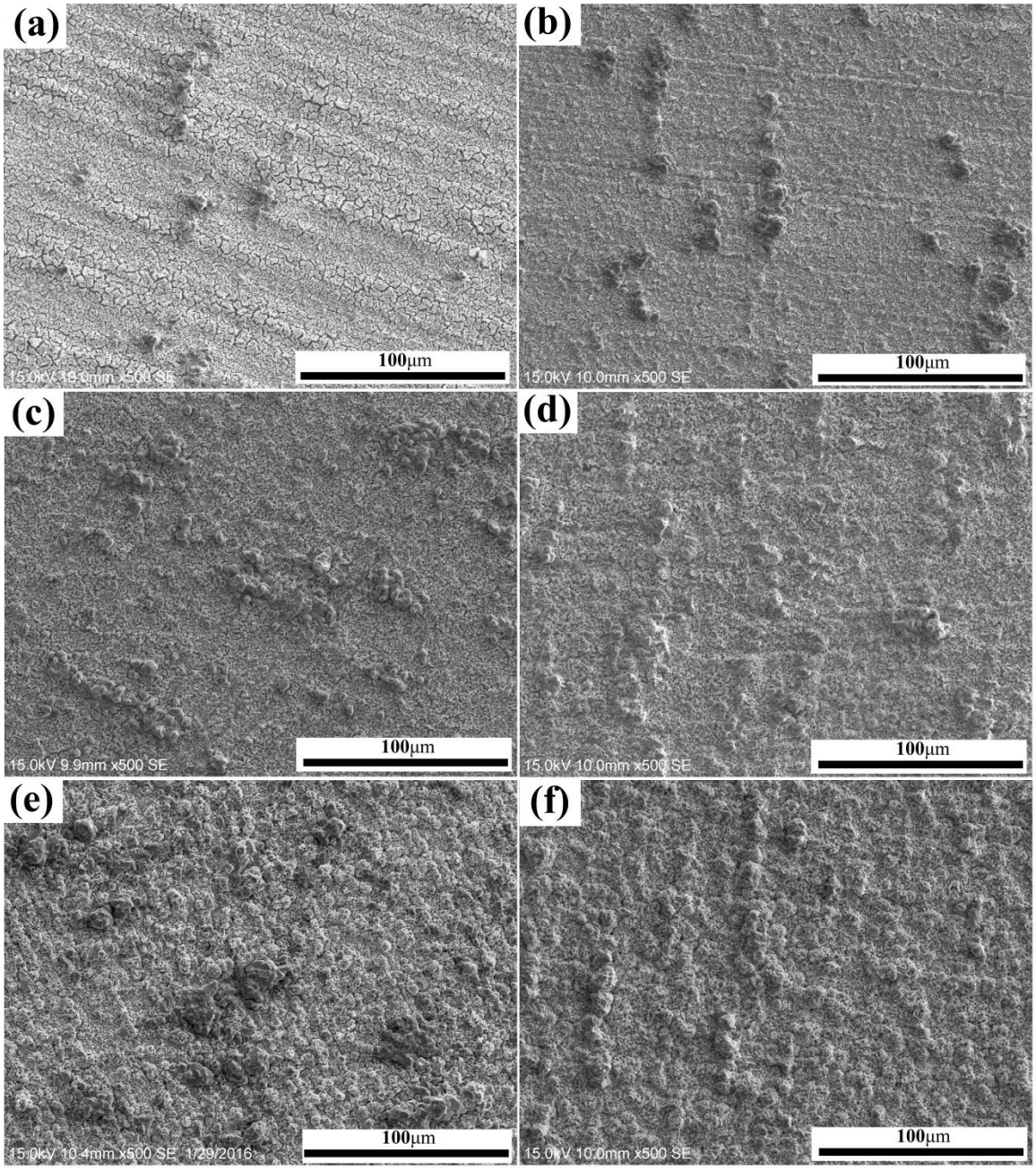

Fig. 6.5 Surface morphology of the ceria coated sample after oxidation at 900 ℃: (a) 50 h; (b) 100 h; (c) 300 h; (d) 500 h; (e) 700 h; (f) 1000 h.

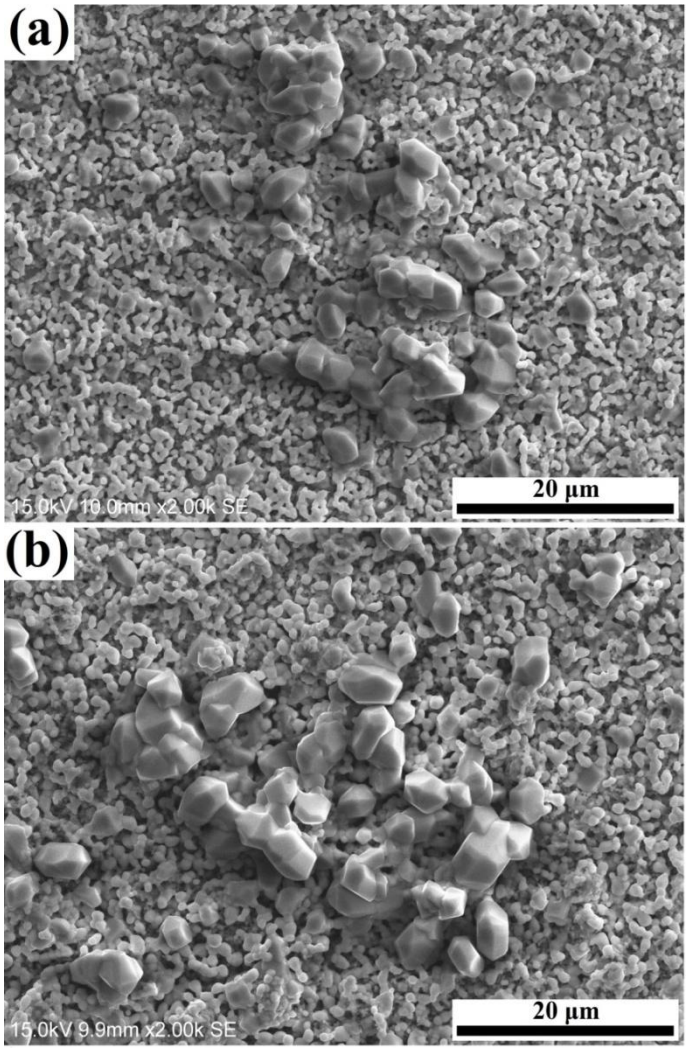

Fig. 6.6 High magnification surface morphology of the coated sample after oxidation at 900 ℃ for (a) 100 h; (b) 500 h.

Fig. 6.5 demonstrates the surface morphology of the ceria-coated sample after exposing at 900 ℃ for various periods. Fig. 6.6 shows the highly magnified morphology of the coated sample after oxidation for 100 h and 500 h. As seen in Fig. 6.5 (a), some isolated oxides start to form on top of the ceria coating after 50 h of oxidation and the number of islands steadily increases with increasing oxidation time. Meanwhile, the ceria coating cracks and it separates into many small isolated particles as seen in Fig. 6.6 (a). These particles will later saturate into the grain boundaries of the formed oxide which results in a mixed-oxide layer as seen in Fig. 6.5 (f) and Fig. 6.6. In addition, the average size of the isolated particles is still less than 500 nm after 500 h of oxidation as shown in Fig. 6.6 (b). In contrast with the bare samples, no oxide

spallation is observed for the coated sample until for the oxidation period reaches 1000 h. This observation definitely indicates that the ceria coating enhances the adhesion between the oxide layer and the substrate matrix.

6.5.3.2 Identification of oxide phase

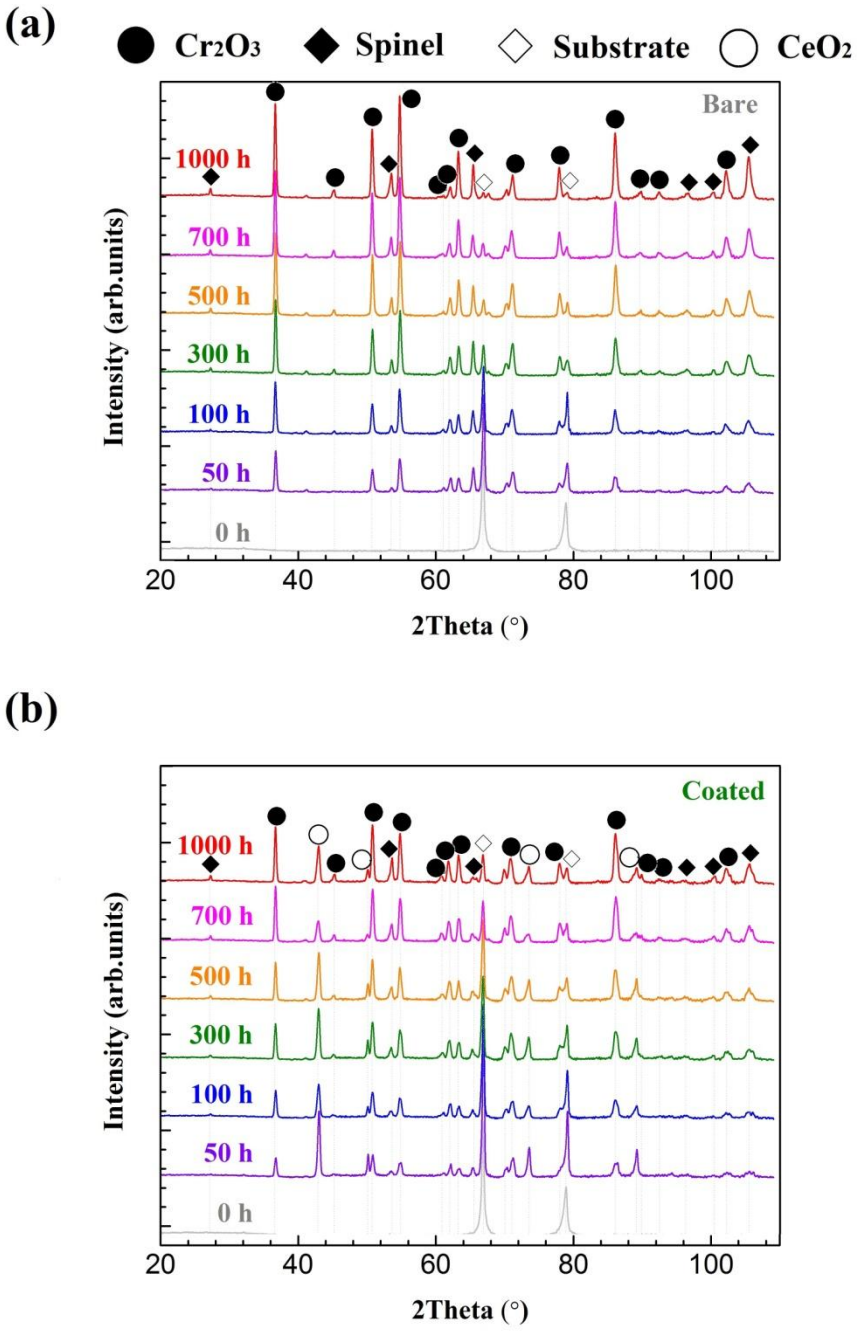

Fig. 6.7 X-ray diffraction (XRD) patterns of the bare and coated samples after exposure for different periods: (a) bare samples; (b) coated samples.

To understand how the deposited ceria coating can enhance both the oxidation resistance and the adhesion of the oxide layer, we attempt to use XRD to define the oxide phases formed on all the samples as shown in Fig. 6.7. For all of the XRD patterns, the intensity of the substrate steadily decreases while that of the oxide gradually increases with increasing oxidation period. This phenomenon implies that the thickness of the oxide layer gradually increases with increasing exposure time. Furthermore, the diffraction patterns of the substrates still can be observed in the sample oxidized for 1000 h which indicate that the X-ray penetrates through the whole oxide layer and all of the oxide phases are detected.

In the case of the detected patterns, the oxides formed on the bare samples always show higher diffraction intensities than those on the coated samples after exposure for the same period. The higher intensities imply that thicker oxide layers form on the bare samples than on the coated samples. In considering the oxide phases, the diffraction patterns fit with the Cr_2O_3 and spinel phases for all the samples regardless of the presence or absence of the ceria addition. However, it is difficult to determine the elemental compositions of the spinel phases, since several possible types of compositions can be formed. Therefore, cross-section analysis should be used to measure the distribution of elements along the depth direction.

Fig. 6.8 shows the cross-section morphology of bare and coated samples after oxidation at 900 ℃ for 700 h. Fig. 6.8 (a) and (c) show the cross-section morphology of the bare sample at low and high magnification. As observed from these images, a thick external oxide layer with many pores and micro-cracks forms on top of the bare sample. The average thickness of the external oxide layer is approximately 12.7 μm. Furthermore, a deep internal oxide layer with an average thickness approximately 11.8 μm forms on the high-angle grain boundary (HAGB) area. On the contrary, both the external and internal oxide layers formed on the coated sample are considerably thinner than those formed on the bare sample. The average thicknesses of the external and internal oxide layers are 6.3 and 6.1 μm, respectively. In addition, the oxide layer is much denser and more compacted than that formed on the bare sample. The ceria particles (marked by white arrows) are primarily observed on the uppermost surface of the oxide layer. This finding implies that the inward diffusion of oxygen dominates the oxidation process assuming that the ceria particles are immobile. The detailed mechanisms for the oxidation process will be discussed in the following section.

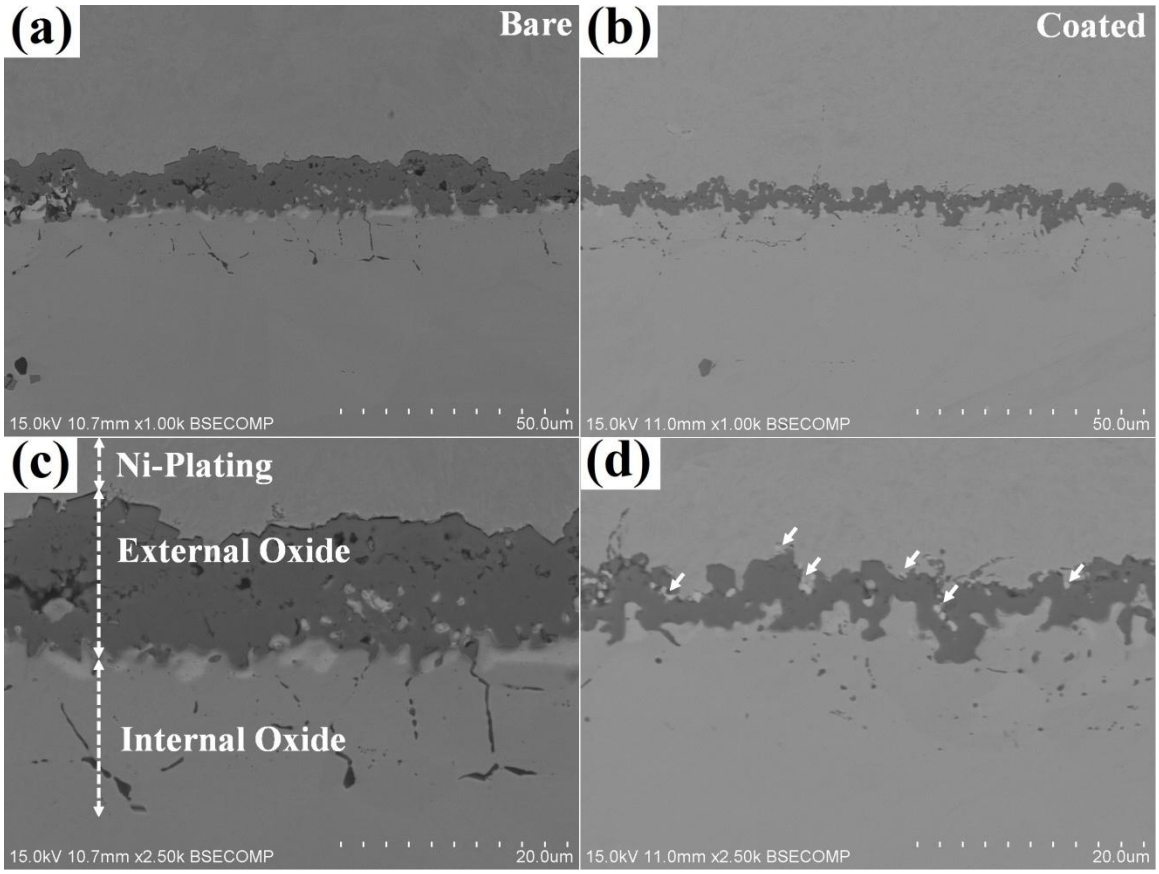

Fig. 6.8 Cross-section morphology of the bare and coated sample after oxidation at 900 ℃ for 700 h: (a) and (c) bare sample; (b) and (d) coated sample.

Fig. 6.9 demonstrates the EBSD band contrast map, phase map and EDS element distribution map of the bare sample after exposure for 700 h. The color legend of the phase map is displayed in the right bottom corner of Fig. 6.9 (c). Two distinctive sub-layers can be observed in the external oxide layer as seen in Fig. 6.9 (a) and (b). From the EDS mapping, Mn, Fe, Cr and O concentrate on the first layer which indicates that the spinel observed by XRD is $Mn(FeCr)O_4$. The average thickness of the first layer is approximately 1 μm as seen in the phase map. In addition, EDS mapping measured on the top surface of the sample oxidized for 50 h is used to verify the formation of the spinel as seen in Fig. 6.10. Clearly, the formation of isolated $Mn(FeCr)O_4$ can be observed. The second layer is dominated by Cr_2O_3 which is in agreement with the X-ray diffraction patterns. The internal layer is recognized as Al_2O_3 as seen in Fig. 6.9 (c). Occasionally, we observe some Al_2O_3 grains along HAGBs that are marked by the white circles in Fig. 6.9 (b). However, the scale/substrate interface is not well indexed in the band

contrast and phase map. It was reported that the scale/substrate interface was a very complex diffusion region of oxygen and many other elements [133]. Therefore, the oxides formed in this area might be non-stoichiometric crystals which will result in the poor imaging quality of the EBSD scan. In addition, this region is a Mo-rich layer as observed from the EDS distribution map. The concentration of Mo in this region may distort the crystal structure of Cr_2O_3 which further affects the indexing of EBSD pattern.

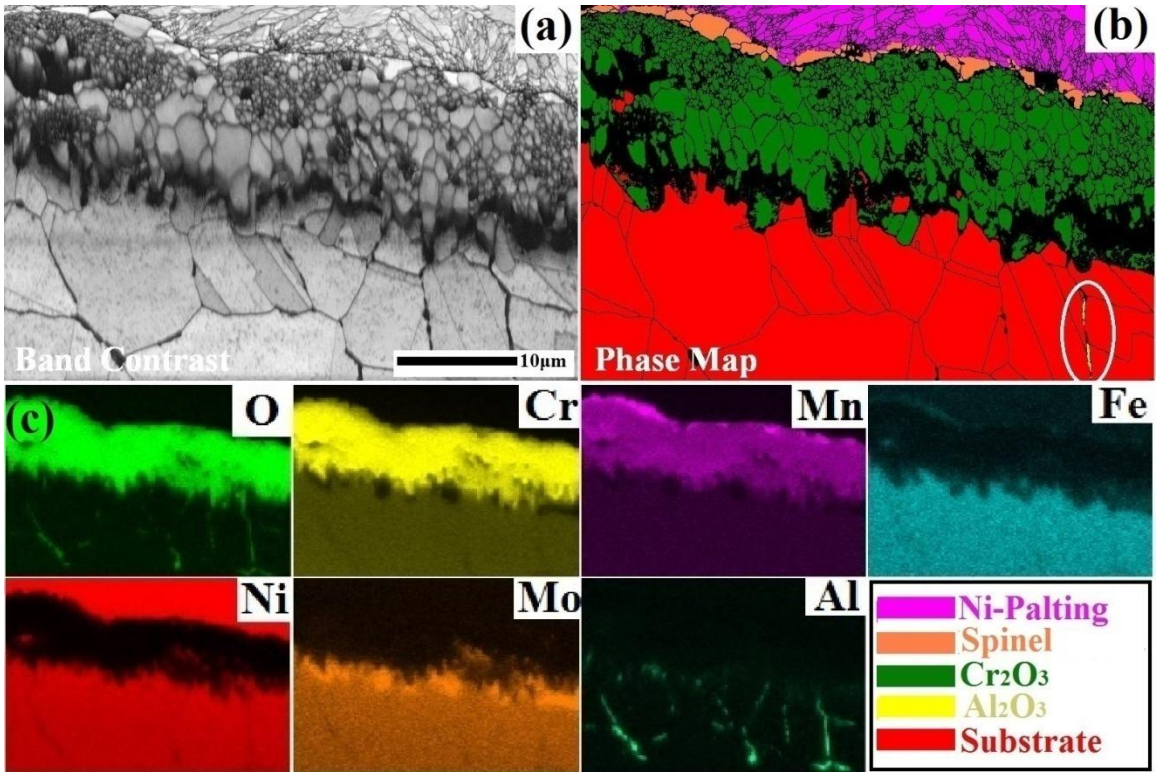

Fig. 6.9 Cross-sectional analysis of the bare sample after oxidation at 900 ℃ for 700 h: (a) EBSD band contrast map; (b) phase map; (c) EDS element distribution maps.

Fig. 6.11 shows the EBSD band contrast map, phase map and EDS element distribution mapping of the coated sample after oxidation for 700 h. The color legend of the phase map is the same as shown in Fig. 6.9 and a gray color is used to display the ceria particle here. In contrast with the bare sample, the EBSD patterns are poorly indexed owing to the much fine oxide grains and the limitation of minimum scanning step size of EBSD. Consequently, the ceria coating on top of the oxide cannot be properly indexed. Therefore, a small oxide layer area is scanned with a step size of 30 nm to display the small oxide grains. The selection of the small area rather than the whole

area for further scanning is primarily because of the striking increase in scanning time with decreasing scanning step size. The finer scanning step size significantly improves the EBSD pattern quality as seen in Fig. 6.11 (a) and (b). The grain sizes of most of the oxide grains clearly are smaller than 1 μm. Many nano-oxide grains are found surrounding the ceria particle which implies that the ceria particles can act as nucleation sites for the oxides.

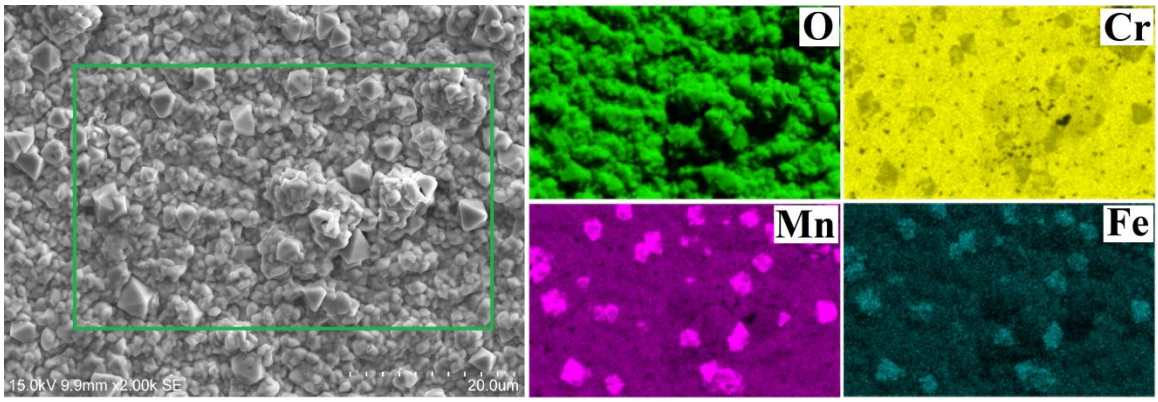

Fig. 6.10 Top surface EDS mapping of the uncoated sample after oxidation at 900 ℃ for 50 h.

As seen from Fig. 6.11 (b) and (c), mixed-oxide layer forms on the coated sample and no clearly separated layers are observed. However, it still can be observed that the ceria particles and spinel are distributed on the top surface of the mixed-oxide layer. Furthermore, it is observed that the ceria particles tend to segregate onto the oxide grain boundaries. The inner part of the external oxide layer is recognized as Cr_2O_3 which confirms its detection by XRD. In the case of the EDS element distribution maps, an obvious difference is observed for the spinel compared with that formed on the bare sample. No iron oxide is found in the external oxide layer, which indicates that the spinel detected by XRD is only $MnCr_2O_4$. Therefore, this difference in composition may result in the different oxidation behavior of the bare and coated samples.

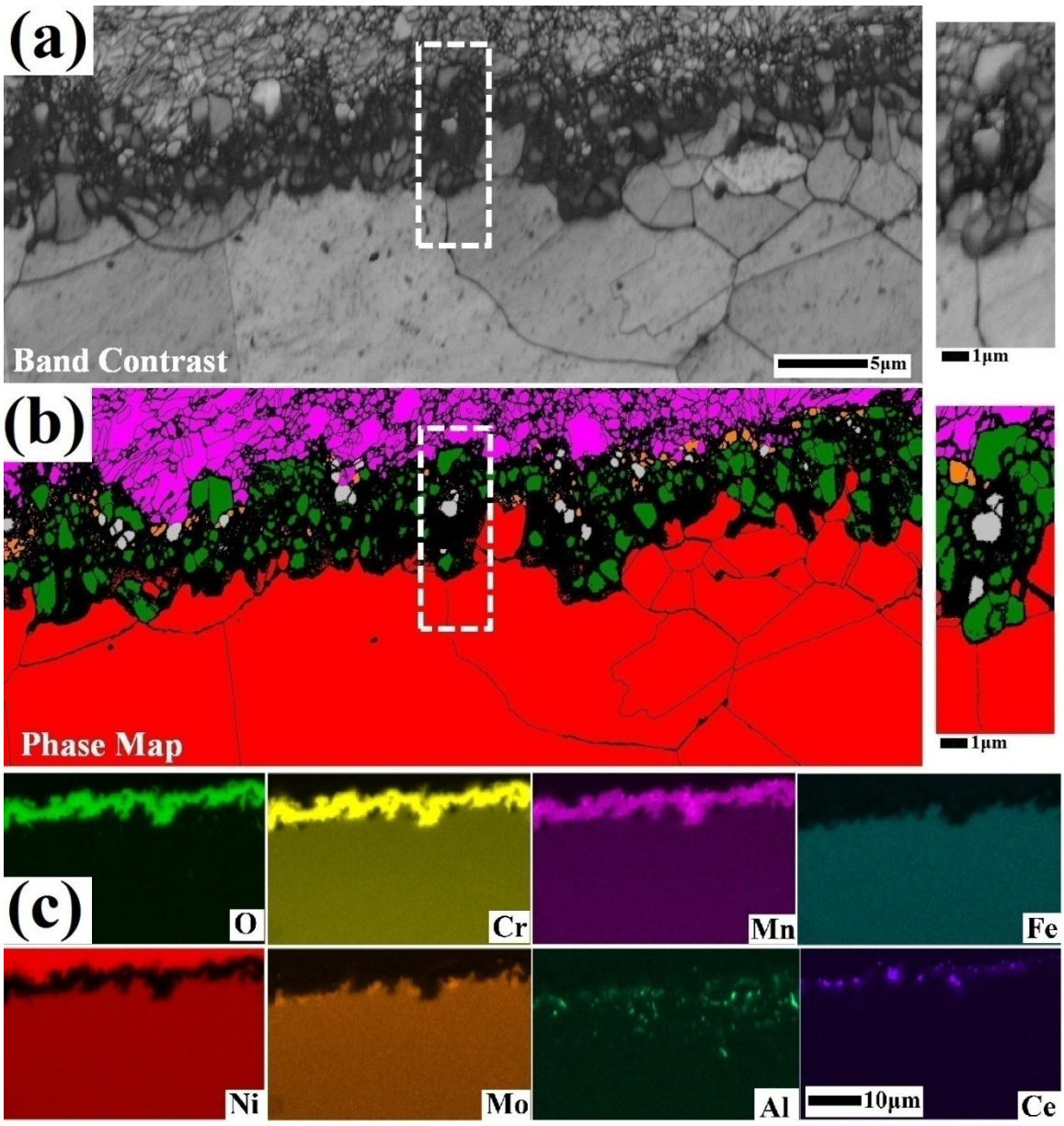

Fig. 6.11 Cross-sectional analysis of the coated sample after oxidation at 900 ℃ for 700 h: (a) EBSD band contrast map; (b) phase map and (c) EDS element distribution maps.

6.5.4 Oxidation mechanisms

The addition of reactive elements or their oxides to enhance the oxidation resistance of alloys has been previously reported [76,87,163,190]. However, the mechanisms of REEs have not been clearly understood until now [57]. Therefore, a ceria coating is prepared on a Cr_2O_3-forming alloy to propose the possible mechanisms of the REEs in the present work.

The oxidation process with different oxidation rates are recorded for the bare samples after oxidation at 900 ℃ up to 1000 h as seen in Fig. 6.2. Oxidation processes with two or three steps were also reported by other researchers [110,113,135]. The complex oxidation process was attributed to the formation of different types of oxides, such as spinel and corundum oxides. The slow growth rate of corundum and fast growth of spinel are important for understanding a change in the oxidation mechanism. In the present work, the surface morphology and phase identification of the oxide can help us to explain the variation of the oxidation rate. In the early stage of the oxidation process, the outward diffusion of Cr dominates the diffusion process owing to its high content and good oxygen affinity. Therefore, a thin Cr_2O_3 layer will immediately form which is confirmed by the XRD pattern of the sample oxidized for 50 h. The Cr_2O_3 layer thus formed will act as a diffusion barrier which will separate the substrate alloy from the oxidizing atmosphere, resulting in a slow oxidation rate. Consequently, a dense and compact oxide layer can still be found after an exposure of 300 h as shown in Fig. 6.3. However, later on the outward diffusion of Mn and Fe may dominate the diffusion process since these elements diffuse ten times faster than Cr in the dense Cr_2O_3 scale [110,135]. In consequence, this fast outward diffusion of Mn and Fe will result in the formation of a Mn-rich and Fe-rich oxide on top of the Cr_2O_3 scale and will increase the oxidation rate in the later stage. However, thermodynamically, the formations of $MnFe_2O_4$ and $MnCr_2O_4$ are more favorable than either the formation of either MnO or Fe_2O_3 owing to their more-negative Gibbs free energies [104,135]. Subsequently, the spinel-type oxides of $MnFe_2O_4$ and $MnCr_2O_4$ will form and spread at the Cr_2O_3/gas interface. Finally, a thin spinel layer forms after longer oxidation time as shown in the phase map of Fig. 6.9. This is confirmed by the increase in the XRD intensity of the spinel phase with increasing exposure time.

However, the formation of iron oxide can have detrimental effects on the oxidation resistance of the substrate. It was reported that the formation of iron oxide will result in a porous and loose surface morphology [14]. Therefore, in contrast with Cr_2O_3 or Al_2O_3, iron oxide cannot act as a protective barrier against oxidation. In the case of the bare sample, the fast diffusion of Fe will create many pores and micro-cracks in the oxide layer as shown in Fig. 6.4 (b). These pores and cracks can subsequently facilitate the diffusion of oxygen and weaken the adhesion between the oxide layer and the substrate. As a result, the oxidation kinetics of the substrates will increase, as observed in the second stage of the oxidation process. Furthermore, the cracks will result in the

spallation of the oxide with a longer exposure time as confirmed by the surface morphology in Fig. 6.3.

In contrast with the bare sample, a mixed-oxide layer with the composition of ceria, $MnCr_2O_4$ and Cr_2O_3 forms on the coated sample as seen in Fig. 6.11. In the early stage, ceria particles can act as additional heterogeneous nucleation sites for Cr_2O_3 scale as previously demonstrated [69,76,93,191]. With the growth of the oxide layer, ceria particles tend to segregate on the oxide grain boundaries and will block the outward diffusion of cations as confirmed in Fig. 6.11. In other words, blocking the diffusion of the cations will result in the growth of an oxide layer controlled by the inward diffusion of anions. Clearly, the concentration of ceria particles on the outer part of the external oxide layer indicates that the inward diffusion of oxygen dominates the diffusion process assuming the immobility of the ceria particles. The diffusion coefficients of ions and oxygen through the Cr_2O_3 layer were previously investigated by other researchers [177,178,192]. It was demonstrated that oxygen always had a lower diffusion coefficient than Cr both in the Cr_2O_3-forming alloy and synthetic Cr_2O_3 layer. The grain boundaries can act as short-circuit paths for oxygen and ions which will increase their diffusion velocities. The calculated diffusion coefficient of oxygen was ten times smaller than that of chromium in the Cr_2O_3 scale. Therefore, the transition from outward diffusion of ions to inward diffusion of oxygen will significantly decrease the oxidation rate of the alloy as seen in Fig. 6.2.

In addition, increasing the density of nucleation sites can decrease the distance of neighboring oxide grains which results in the formation of fine oxide grains [69]. This phenomenon is confirmed by observation of the nano-sized oxide grains in Fig. 6.11. The fine oxide grains will facilitate releasing of the stress that resulted from the rapid growth of oxide grains and the cooling process. Accordingly, the ductility of the oxide layer can be enhanced and oxide spallation will not happen. More importantly, no iron oxide is forming on the coated sample as shown in the EDS mapping of Fig. 6.11. Consequently, a non-porous and crack-free external oxide layer can form which separates the substrate from the oxidizing environment. Therefore, both the oxidation resistance and adhesion of the oxide to the substrate can be enhanced.

From the above discussions, we attempt to develop schematic models to represent the oxidation mechanisms of the bare and coated samples as shown in Fig. 6.12. For the bare samples, iron and manganese are the main elements diffusing outward after the formation of the chromium oxide

layer. The formation of iron oxide results in porous and cracked oxide layers which facilitate the outward diffusion of cations and penetration of oxygen into the substrate. Consequently, the oxidation rate increases significantly. In addition, the porous and cracked oxide layer weakens the bonding strength between the oxide layer and the sub-matrix which results in spallation of the oxide after a long period of exposure. However, in the case of the coated sample, the ceria particles can act as nucleation sites for oxides in the initial stage which then segregate on the oxide grain boundaries. The segregation of the ceria particles will prevent the outward diffusion of cations which changes the oxidation process from outward diffusion to inward diffusion of oxygen. Subsequently, the slow diffusion of oxygen through the oxide layers will result in a slow oxidation rate of the coated sample. Furthermore, the formation of fine oxide grains and an iron-free oxide layer are believed to enhance the ductility of the oxide layer and separate the matrix from the corrosive atmosphere. Finally, the changing of the oxidation process from initially outward diffusion to inward diffusion will result in the formation of a mixed-oxide layer.

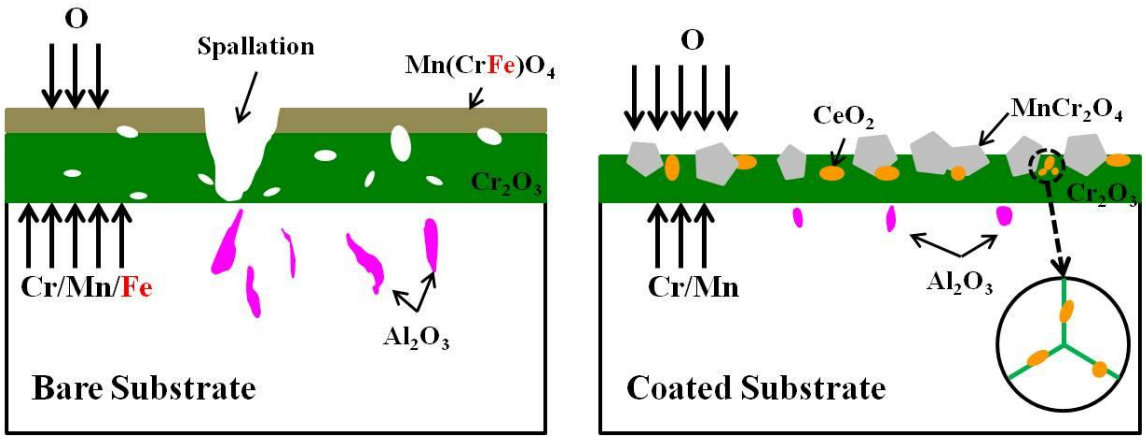

Fig. 6.12 Schematic models represent the oxidation mechanisms of the bare and coated sample.

6.6 Conclusions

The influence of the ceria coating on the oxidation behavior of the Cr_2O_3-forming Hastelloy 625 is investigated. The following conclusions can be drawn from the present work:

(1) A homogeneous coating of nano-sized ceria particles coating is deposited onto Hastelloy 625 through an electro-deposition process. The prepared ceria coating not only reduces the oxidation rate but also enhances the adhesion between the oxide layer and the substrate.

(2) The uncoated sample obtains a higher mass gain than the coated sample. Oxide spallation occurs on the uncoated sample after 300 h oxidation while no spallation is observed on the coated sample.

(3) The formation of iron oxide is believed to deteriorate the oxidation resistance of the bare sample and facilitates the formation of a porous and cracked oxide layer. However, an iron-free oxide layer is formed after the addition of the ceria coating that enhances the oxidation resistance of Hastelloy 625.

(4) The formation of fine oxide grains is related to the enhancement of the adherence between the oxide and the alloy substrate.

Chapter 7 Summary and Future works

7.1 Summary

In this thesis, the oxidation behavior of three Ni-based Hastelloys of 230, N and 625 is investigated. The oxidation resistance of these alloys is improved through grain refinement process and the addition of reactive element coating.

In the case of the grain refinement approach, the first objective of the present project is to define the effect of substrate texture on the oxidation behavior of Ni-based alloy. In Chapter 2, the electron back-scattering diffraction maps scanned on the same area before and after oxidation are compared and the obtained results clearly demonstrates the anisotropic oxidation behavior of grains with different crystallographic orientations. The combination of electron back-scattering diffraction and atomic force microscopy is successfully used to correlate the grain orientations with their oxidation behavior. Furthermore, the surface morphology of the oxide layer formed on different grain is also correlated with the grain orientations.

Based on the results presented in Chapter 2, Hastelloy 230 and Hastelloy N are used to study the influence of grain size on the oxidation behavior of alloys with different chromium contents in Chapter 3. Samples with different grain sizes and similar textures are prepared to evaluate the effect of grain size on the oxidation behavior of Hastelloy 230 and Hastelloy N which address the problem outlined in the second objective. Cross-sectional energy dispersive spectroscopy and X-ray diffraction are used to describe the oxide formed on the substrates with different grain size. The oxidation mechanisms of high and low Cr content alloys with different grain sizes are discussed.

In Chapter 4, the possible way to enhance the oxidation resistance of Ni-based Cr_2O_3-forming alloys through electro-deposition process is proposed which satisfies the third objective. A classical three electrodes system is used to deposit ceria coating on to Hastelloy 230 through galvanostatic mode. The deposition parameters like the current density, the deposition time and the bath temperature are optimized. X-ray diffraction is used to determine the phase constitution and the crystal size of the deposits. Scanning electron microscope is used to characterize changes of the surface morphology of the deposited films for different deposition parameters.

The optimized ceria coating is used to study the effect of the reactive element on the oxidation behavior of Hastelloy 230 and 625 which addresses the fourth objective. In Chapter 5, the influence of ceria coating on the oxidation behavior of Hastelloy 230 is investigated. X-ray diffraction, energy dispersive spectroscopy and orientation image mapping were used to characterize the microstructure and chemical composition of the oxide layer formed on the samples after oxidation for 700 h. The oxidation mechanisms of the coated and uncoated samples are discussed.

Finally, the ceria coating is also used to study the influence of reactive element coating on the oxidation behavior of Hastelloy 625 as shown in Chapter 6. The coated and uncoated samples are oxidized at 900 ℃ for 1000 h. Scanning electron microscope is used to characterize the surface morphology and cross-sectional morphology of the oxidized samples. Electron back-scattering diffraction is used to display the microstructure of the formed oxide. The mechanism of oxidation of the samples is discussed and the schematic models of oxidation are developed.

7.2 Conclusions

The following conclusions can be drawn from the whole project:

1) The texture has a critical role in the oxidation behavior of face-centered structure Ni-based alloys. The grains with deviation angles from ideal <111> direction lower than 20 °tend to have better oxidation resistance than the other grains. The oxidation rates of the grains are found to be in the order of (111) < (110) < (100). The surface morphology of the oxides formed on grains is also orientation dependant.

2) The grain size only has a small effect on the oxidation behavior of high Cr content Hastelloy230. The substrates with large and small grain sizes tend to show similar oxidation kinetics after oxidizing for 1000 h. The surface morphology and the chemical compositions of the oxides formed on Hastelloy 230 with different grain sizes are pretty similar.

3) The variation of grain size significantly changes the oxidation behavior of Hastelloy N with low Cr content. The grain refinement process substantially enhances the oxidation resistance and the oxide adherence of Hastelloy N. The oxidation rate of the coarse-grained alloy is more than two orders of magnitude higher than that of fine-grained one within 100 h oxidation. Oxide spallation happens on the Hastelloy N with large grains while no spallation is observed on the fine-grained substrate after 300 h oxidation. It is found that thick and complex oxide islands form inside the large grain interiors and thin Cr-rich oxide layers form on the grain boundaries for the coarse-grained Hastelloy N. However, for the fine-grained alloy, it is found that a uniform Cr-rich oxide layer forms on the whole surface of the sample. The finer grain size with higher grain boundary density enhanced the diffusivity of Cr toward the surface and resulted in the formation of the Cr-rich oxide layer on the surface.

4) For the electro-deposition process, the grain size of the deposited film decreases with the increasing of current density while micro-cracks also form at a higher current density. Extending the deposition time can produce more smooth deposited films and increase the grain size of the film. The bath temperature shows a more significant effect on the deposition process than other parameters like current density and deposition time. The electro-deposition process at a current density of – 0.75 mA/cm^2 for 20 min is used to prepare a uniform and homogeneous ceria coating on to Ni-based alloys at room temperature.

5) The ceria coating not only improves the oxidation resistance but also enhances the adherence between oxide layers and substrate for Hastelloy 230. The ceria coating does not change the chemical compositions of the oxides formed on the alloy while it significantly alters the surface morphology of the oxides. Oxide spallation occurs after oxidizing the bare sample for 700 h while no spallation is seen on the coated alloy after 1000 h oxidation. The addition of ceria coating substantially suppresses the internal oxidation of the alloy while severe internal oxidation is observed in the uncoated sample. The formation of internal oxide can reduce the adhesion between the oxide layer and the substrate that results in the oxide spallation. Furthermore, the

ceria coating changes the grain shape of Cr_2O_3 from columnar to an equiaxed structure, which is beneficial to enhance the oxide spallation resistance.

6) The ceria coating also enhances the oxidation resistance and the adherence of the oxide layers of Hastelloy 625. The formation of iron-oxide results in a porous and cracked oxide layer that covers the bare sample which results in the oxide spallation after 500 h oxidation. In contrast, ceria coating suppresses the formation of iron-oxide and promotes the formation of a thin and uniform Cr_2O_3 layer which enhances the oxidation resistance. The fine-grained oxides formed on the coated samples are able to enhance the adhesion of the oxide layer to the main substrate.

7.3 Future works

Although the main objectives of current project are realized, more works can be done in the future.

1) The effect of crystallographic orientation on the oxidation behavior of Hastelloy 230 can be studied by combing of EBSD and AFM in this project. It would be beneficial to measure the work functions of different grains and relates them with their grain orientations to further clarify the oxidation mechanisms of grains with different orientations;

2) According to the results obtained in Chapter 2, it is worth to prepare alloys that have different textures but similar grain sizes to evaluate how the texture affects the oxidation behavior. Especially, attempts to produce substrates with <111>//ND texture would enhance the oxidation resistance of alloys;

3) The effect of grain size on the oxidation behavior of alloys may be further studied. It will be interesting to produce a series of samples with different grain size but with similar texture to determine the critical grain size that enhance the oxidation resistance alloys.

4) The effect of ceria coating on the oxidation behavior of Hastelloy 230 and 625 are inspected where the nano-oxide formation is observed on the coated sample in this project. Therefore, it is meaningful to use high-resolution techniques like TEM to better understand the microstructure of the oxide.

REFERENCES

[1] N.E. Agency, Technology roadmap update for Generation IV nuclear energy systems, Gener. IV Int. Forum. (2014) 1–66.

[2] D.R. Baer, M.D. Merz, Differences in oxides on large-and small-grained 304 stainless steel, Metall. Trans. A. 11 (1980) 1973–1980. doi:10.1007/BF02655116.

[3] S.N. Basu, G.J. Yurek, Effect of alloy grain size and silicon content on the oxidation of austenitic Fe-Cr-Ni-Mn-Si alloys in pure O2, Oxid. Met. 36 (1991) 281–315. doi:10.1007/BF00662967.

[4] R.K. Singh Raman, A.S. Khanna, R.K. Tiwari, J.B. Gnanamoorthy, Influence of grain size on the oxidation resistance of 2 1/4 Cr-1Mo steel, Oxid. Met. 37 (1992) 1–12. doi:10.1007/BF00665627.

[5] Y.S. Li, Y. Niu, F. Gesmundo, F.H. Wang, Grain size effects on the oxidation of two-phase Cu-Fe alloys, Corros. Sci. 44 (2002) 1457–1468. doi:10.1016/S0010-938X(01)00153-6.

[6] P. Pérez, Influence of the alloy grain size on the oxidation behaviour of PM2000 alloy, Corros. Sci. 44 (2002) 1793–1808. doi:10.1016/S0010-938X(01)00182-2.

[7] X. Peng, J. Yan, Y. Zhou, F. Wang, Effect of grain refinement on the resistance of 304 stainless steel to breakaway oxidation in wet air, Acta Mater. 53 (2005) 5079–5088. doi:10.1016/j.actamat.2005.07.019.

[8] T.S. Jo, S.H. Kim, D.G. Kim, J.Y. Park, Y. Do Kim, Effects of grain refinement on internal oxidation of alloy 617, J. Nucl. Mater. 402 (2010) 162–166. doi:10.1016/j.jnucmat.2010.05.013.

[9] Z.Q. Cao, H.J. Sun, J. Lu, K. Zhang, Y. Sun, High temperature corrosion behavior of Cu–20Co–30Cr alloys with different grain size, Corros. Sci. 80 (2014) 184–190. doi:10.1016/j.corsci.2013.11.025.

[10] L. Liu, Z. Yang, C. Zhang, M. Ueda, K. Kawamura, T. Maruyama, Effect of grain size on the oxidation of Fe–13Cr–5Ni alloy at 973K in Ar–21vol%O2, Corros. Sci. 91 (2014) 195–202. doi:10.1016/j.corsci.2014.11.020.

[11] X. Yu, Z. Jiang, J. Zhao, D. Wei, C. Zhou, Q. Huang, Effect of a grain-refined microalloyed steel substrate on the formation mechanism of a tight oxide scale, Corros. Sci. 85 (2014) 115–125. doi:10.1016/j.corsci.2014.04.006.

[12] S. Samal, S.K. Mitra, Influence of grain shape, size, and grain boundary diffusion on high-temperature oxidation of pure metal Fe, Cu, and Zn, Metall. Mater. Trans. A. 46 (2015) 3324–3332. doi:10.1007/s11661-015-2987-0.

[13] H. Viitala, I. Galfi, P. Taskinen, Initial oxidation behaviour of niobium stabilized TP347H austenitic stainless steel - Effect of grain size and temperature, Mater. Corros. 66 (2015) 851–862. doi:10.1002/maco.201407948.

[14] J.H. Kim, D.I. Kim, S. Suwas, E. Fleury, K.W. Yi, Grain-size effects on the high-temperature oxidation of modified 304 austenitic stainless steel, Oxid. Met. 79 (2012) 239–247. doi:10.1007/s11085-012-9347-x.

[15] A.S. Taylor, P. Cizek, P.D. Hodgson, Orientation dependence of the substructure characteristics in a Ni–30Fe austenitic model alloy deformed in hot plane strain compression, Acta Mater. 60 (2012) 1548–1569. doi:10.1016/j.actamat.2011.11.048.

[16] G. Xie, L. Wang, J. Zhang, L.H. Lou, Orientational dependence of recrystallization in an Ni-base single-crystal superalloy, Scr. Mater. 66 (2012) 378–381. doi:10.1016/j.scriptamat.2011.11.037.

[17] E. Merson, R. Brydson, A. Brown, The effect of crystallographic orientation on the mechanical properties of titanium, J. Phys. Conf. Ser. 126 (2008) 12020. doi:10.1088/1742-6596/126/1/012020.

[18] S.N. Luo, J.G. Swadener, C. Ma, O. Tschauner, Examining crystallographic orientation dependence of hardness of silica stishovite, Phys. B Condens. Matter. 399 (2007) 138–142. doi:10.1016/j.physb.2007.06.011.

[19] F.H. Latief, K. Kakehi, Influence of heat treatment on anisotropic creep behavior of aluminide coating on a Ni-base single crystal superalloy, Mater. Des. 52 (2013) 134–142. doi:10.1016/j.matdes.2013.04.101.

[20] E. Martinez-Lombardia, Y. Gonzalez-Garcia, L. Lapeire, I. De Graeve, K. Verbeken, L. Kestens, et al., Scanning electrochemical microscopy to study the effect of

crystallographic orientation on the electrochemical activity of pure copper, Electrochim. Acta. 116 (2014) 89–96. doi:10.1016/j.electacta.2013.11.048.

[21] A. Schreiber, J.W. Schultze, M.M. Lohrengel, F. Kármán, E. Kálmán, Grain dependent electrochemical investigations on pure iron in acetate buffer pH 6.0, Electrochim. Acta. 51 (2006) 2625–2630. doi:10.1016/j.electacta.2005.07.052.

[22] A. Schreiber, C. Rosenkranz, M.M. Lohrengel, Grain-dependent anodic dissolution of iron, Electrochim. Acta. 52 (2007) 7738–7745. doi:10.1016/j.electacta.2006.12.062.

[23] M.V. Diamanti, M.P. Pedeferri, C.A. Schuh, Thickness of anodic Titanium oxides as a function of crystallographic orientation of the substrate, Metall. Mater. Trans. A. 39 (2008) 2143–2147. doi:10.1007/s11661-008-9558-6.

[24] P.J. Bedrossian, A.J. Schwartz, M. Kumar, W.E. King, Observation of localized corrosion of Ni-Based alloys using coupled orientation imaging microscopy and atomic force microscopy, MRS Proc. 586 (1999) 81. doi:10.1557/PROC-586-81.

[25] B.J. Wang, D.K. Xu, J.H. Dong, W. Ke, Effect of the crystallographic orientation and twinning on the corrosion resistance of an as-extruded Mg–3Al–1Zn (wt.%) bar, Scr. Mater. 88 (2014) 5–8. doi:10.1016/j.scriptamat.2014.06.015.

[26] M. Liu, D. Qiu, M.C. Zhao, G. Song, A. Atrens, The effect of crystallographic orientation on the active corrosion of pure magnesium, Scr. Mater. 58 (2008) 421–424. doi:10.1016/j.scriptamat.2007.10.027.

[27] C.A. Schuh, K. Anderson, C. Orme, Rapid assessment of anisotropic surface processes: experiments on the corrosion of Inconel 600, Surf. Sci. 544 (2003) 183–192. doi:10.1016/j.susc.2003.07.009.

[28] F. Reichel, L.P.H. Jeurgens, E.J. Mittemeijer, The effect of substrate orientation on the kinetics of ultra-thin oxide-film growth on Al single crystals, Acta Mater. 56 (2008) 2897–2907. doi:10.1016/j.actamat.2008.02.031.

[29] F.H. Latief, K. Kakehi, X. Fu, Y. Tashiro, Isothermal oxidation behavior characteristics of a second Generation Ni-base single crystal superalloy in air at 1000 and 1100 °C, Int. J. Electrochem. Sci. 7 (2012) 8369–8383.

[30] L.P. Bonfrisco, M. Frary, Effects of crystallographic orientation on the early stages of

oxidation in nickel and chromium, J. Mater. Sci. 45 (2009) 1663–1671. doi:10.1007/s10853-009-4144-x.

[31] R. Bès, S. Gavarini, N. Millard-Pinard, S. Cardinal, A. Perrat-Mabilon, C. Peaucelle, et al., Influence of crystallographic orientation on the early stages of oxidation of polycrystalline titanium nitride, J. Nucl. Mater. 427 (2012) 415–417. doi:10.1016/j.jnucmat.2012.03.031.

[32] E.A. Lewis, E.A. Irene, The effect of surface orientation on silicon oxidation kinetics, J. Am. Ceram. Soc. 134 (1987) 2332–2339. doi:10.1149/1.2100881.

[33] P.B. Sewell, M. Cohen, The oxidation of iron single crystals around 200 ℃, J. Electrochem. Soc. 111 (1964) 501. doi:10.1149/1.2426168.

[34] F.H. Latief, K. Kakehi, X. Fu, Influence of surface orientation on oxidation resistance of Ni- based single crystal superalloy CM186LC at 1100 °C in air, J. Electrochem. Soc. 7 (2012) 7608–7618.

[35] F.H. Yuan, E.H. Han, C.Y. Jo, T.F. Li, Z.Q. Hu, The effect of crystallographic orientation on the oxidation behavior of a single-crystal Nickel-base superalloy, Oxid. Met. 60 (2003) 211–224. doi:10.1023/A:1026077417712.

[36] F.H. Latief, K. Kakehi, E.-S.M. Sherif, High temperature oxidation behavior of aluminide on a Ni-based single crystal superalloy in different surface orientations, Prog. Nat. Sci. Mater. Int. 24 (2014) 163–170. doi:10.1016/j.pnsc.2014.03.006.

[37] L. Hu, D. Hovis, A.H. Heuer, The effect of substrate orientation on oxidation-induced void formation in β-Ni–40Al–5Cr–0.03Y, Scr. Mater. 61 (2009) 157–160. doi:10.1016/j.scriptamat.2009.03.023.

[38] R. Subbaraman, S.A. Deshmukh, S.K.R.S. Sankaranarayanan, Atomistic insights into early stage oxidation and nanoscale oxide growth on Fe(100), Fe(111) and Fe(110) surfaces, J. Phys. Chem. C. 117 (2013) 5195–5207. doi:10.1021/jp312514m.

[39] J. R.Ligenza, Effect of crystal orientation on oxidation rates of silicon in high pressure steam, J. Phys. Chem. 65 (1961) 2011–2014. doi:10.1021/j100828a020.

[40] G. Tammann, W. Nernst, W. Hirschberg, K. Zepernick, K. Rogóyski, A. Bogojawlenski, et al., The determination of crystallite orientation, J. Inst. Met. 44 (1930) 29.

[41] A.T. Gwathmey, A.F. Benton, The directional oxidation of a single crystal of copper by heating in air at reduced pressure, J. Chem. Phys. 8 (1940) 431. doi:10.1063/1.1750683.

[42] Allen.T.Gwathmey, Arthur.F.Benton., The reaction of gases on the surface of a single crystal of copper, J. Phys. Chem. 46 (1942) 969–980. doi:10.1021/j150422a021.

[43] Allan.T.Gwathmey, Arthur.F.Benton., Some experiments showing the directional reactivities of single crystals of copper, J.Electrochem.Soc. 59 (1940) 211–222. doi:10.1149/1.3521198.

[44] F.W. Young, J. V Cathcart, A.T. Gwathmey, The rates of oxidation of several faces of a single crystal of copper as determined with elliptically polarized light, Acta Metall. 4 (1956) 145–152. doi:10.1016/0001-6160(56)90132-8.

[45] J. V. Cathcart, G.F. Petersen, C.J. Sparks, The structure of thin oxide films formed on nickel crystals, J. Electrochem. Soc. 116 (1969) 664. doi:10.1149/1.2412003.

[46] R. Herehl, N.N. Khoi, T. Homma, W.W. Smeltzert, Short-circuit diffusion in the growth of Nickel oxide scales on Nickel crystal faces, Oxid. Met. 4 (1972) 35–49. doi:10.1007/BF00612506.

[47] M.J. Graham, R.J. Hussey, M. Cohen, Influence of oxide structure on the oxidation rate of nickel single crystals, J. Electrochem. Soc. 11 (1973) 1523–1529. doi:10.1149/1.2403296.

[48] N.N.Khoi, W.W.Smeltzer, J.D.Embury, Growth and structure of nickle oxide on nickle crystal faces, J. Electrochem. Soc. 122 (1975) 1495–1503. doi:10.1149/1.2134052.

[49] F. Czerwinski, J.A. Szpunar, The influence of crystallographic orientation of nickel surface on oxidation inhibition by ceria coatings, Acta Mater. 46 (1998) 1403–1417. doi:10.1016/S1359-6454(97)00240-1.

[50] F. Czerwinski, A. Zhilyaev, J.. Szpunar, Grain boundary character distribution in oxides formed on (100) and (111) nickel single crystals coated with ceria gel, Corros. Sci. 41 (1999) 1703–1713. doi:10.1016/S0010-938X(99)00006-2.

[51] J.J. Gray, B.S. El Dasher, C.A. Orme, Competitive effects of metal dissolution and passivation modulated by surface structure: An AFM and EBSD study of the corrosion of alloy 22, Surf. Sci. 600 (2006) 2488–2494. doi:10.1016/j.susc.2006.04.002.

[52] F.S.P. N.Birks, G.H. Meier, Introduction to the high temperature oxidation of metals, 2nd ed., Cambridge University Press, New York, 2006.

[53] L.B.Pfeil, Improvements in the manufacture of alloys, GB454926A, 1935.

[54] P.Y.Hou, J.Stringer, The effect of reactive element additions on the selective oxidation,growth and adhesion of chromia scales, Mater. Sci. Eng. A. 202 (1995) 1–10. doi:10.1016/0921-5093(95)09798-8.

[55] B.A. Pint, Progress in understanding the reactive element effect since the Whittle and Stringer literature review, in: P.F. Tortorelli, I.G. Wright, P.Y. Hou (Eds.), Proc. John Stringer Symp., High Temperature Corrosion, ASM international, Material Park, OH, 2003: pp. 9–19.

[56] P.Y. Hou, The reactive element effect – past, present and future, Mater. Sci. Forum. 696 (2011) 39–44. doi:10.4028/www.scientific.net/MSF.696.39.

[57] S. Chevalier, What did we learn on the reactive element effect in chromia scale since Pfeil 's patent?, Mater. Corros. 65 (2014) 109–115. doi:10.1002/maco.201307310.

[58] F.A. Golightly, F.H. Stott, G.C. Wood, The influence of yttrium additions on the oxide-scale adhesion to an iron-chromium-aluminum alloy, Oxid. Met. 10 (1976) 163–187. doi:10.1007/BF00612158.

[59] T. Amano, T. Taguchi, Spalling of the surface oxide formed on Ni-(20,40,60,80)Cr alloys with small additions of Ce and Si, J. Alloys Compd. 193 (1993) 20–22. doi:10.1016/0925-8388(93)90297-Z.

[60] E. Wessel, V. Kochubey, D. Naumenko, L. Niewolak, L. Singheiser, W. Quadakkers, Effect of Zr addition on the microstructure of the alumina scales on FeCrAlY-alloys, Scr. Mater. 51 (2004) 987–992. doi:10.1016/j.scriptamat.2004.07.023.

[61] Y. Wu, Y. Niu, Effect of silicon additions on the oxidation of a Ni–6at.%Al alloy at 1273K, Scr. Mater. 53 (2005) 1247–1252. doi:10.1016/j.scriptamat.2005.08.002.

[62] M.F. Pillis, E.G. de Araújo, L.V. Ramanathan, Effect of rare earth oxide additions on oxidation behavior of AISI 304L stainless steel, Mater. Res. 9 (2006) 375–379. doi:10.1590/S1516-14392006000400006.

[63] X. Zhang, P. Hu, J. Han, L. Xu, S. Meng, The addition of lanthanum hexaboride to zirconium diboride for improved oxidation resistance, Scr. Mater. 57 (2007) 1036–1039. doi:10.1016/j.scriptamat.2007.07.036.

[64] H.S. Seo, G. Jin, J.H. Jun, D.-H. Kim, K.Y. Kim, Effect of reactive elements on oxidation behaviour of Fe–22Cr–0.5Mn ferritic stainless steel for a solid oxide fuel cell interconnect, J. Power Sources. 178 (2008) 1–8. doi:10.1016/j.jpowsour.2007.12.026.

[65] P. Pérez, G. Salmi, A. Muñoz, M.A. Monge, Influence of yttria additions on the oxidation behaviour of titanium prepared by powder metallurgy, Scr. Mater. 60 (2009) 1008–1011. doi:10.1016/j.scriptamat.2009.02.040.

[66] J. Das, R. Mitra, S.K. Roy, Effect of Ce addition on the oxidation behaviour of Mo–Si–B–Al ultrafine composites at 1100 °C, Scr. Mater. 64 (2011) 486–489. doi:10.1016/j.scriptamat.2010.11.022.

[67] D. Li, H. Guo, D. Wang, T. Zhang, S. Gong, H. Xu, Cyclic oxidation of β-NiAl with various reactive element dopants at 1200 °C, Corros. Sci. 66 (2013) 125–135. doi:10.1016/j.corsci.2012.09.010.

[68] K. Yan, H. Guo, S. Gong, High-temperature oxidation behavior of minor Hf doped NiAl alloy in dry and humid atmospheres, Corros. Sci. 75 (2013) 337–344. doi:10.1016/j.corsci.2013.06.017.

[69] H. Guo, D. Wang, H. Peng, S. Gong, H. Xu, Effect of Sm, Gd, Yb, Sc and Nd as reactive elements on oxidation behaviour of β-NiAl at 1200 °C, Corros. Sci. 78 (2014) 369–377. doi:10.1016/j.corsci.2013.10.021.

[70] K. Yan, H. Guo, S. Gong, High-temperature oxidation behavior of β-NiAl with various reactive element dopants in dry and humid atmospheres, Corros. Sci. (2014) 1–8. doi:10.1016/j.corsci.2014.02.033.

[71] L. Wang, B. Gorr, H.-J. Christ, D. Mukherji, J. Rösler, The effect of alloyed nickel on the short-term high temperature oxidation behaviour of Co–Re–Cr-based alloys, Corros. Sci. 93 (2015) 19–26. doi:10.1016/j.corsci.2015.01.004.

[72] S. Seal, S.K. Bose, S.K. Royt, Improvement in the oxidation behavior of austenitic stainless steels by superficially applied cerium oxide coatings, Oxid. Met. 41 (1994) 139–

178. doi:10.1007/BF01196647.

[73] R. Haugsrud, On the influence of sol–gel derived CeO2 coatings on high-temperature oxidation of Co, Ni and Cu, Corros. Sci. 44 (2002) 1569–1582. doi:10.1016/S0010-938X(01)00155-X.

[74] A.S. Hamdy, Advanced nano-particles anti-corrosion ceria based sol gel coatings for aluminum alloys, Mater. Lett. 60 (2006) 2633–2637. doi:10.1016/j.matlet.2006.01.049.

[75] D.E. Alman, C.D. Johnson, W.K. Collins, P.D. Jablonski, The effect of cerium surface treated ferritic stainless steel current collectors on the performance of solid oxide fuel cells (SOFC), J. Power Sources. 168 (2007) 351–355. doi:10.1016/j.jpowsour.2007.03.035.

[76] R. Thanneeru, S. Patil, S. Deshpande, S. Seal, Effect of trivalent rare earth dopants in nanocrystalline ceria coatings for high-temperature oxidation resistance, Acta Mater. 55 (2007) 3457–3466. doi:10.1016/j.actamat.2007.01.043.

[77] C. Issartel, H. Buscail, R. Rolland, S. Perrier, A. Fleurentin, Effect of oxidation with lanthanum sol–gel coating on the 330Cb carburization at 900 °C, Oxid. Met. 80 (2013) 467–478. doi:10.1007/s11085-013-9390-2.

[78] J.G. Chęcmanowski, B. Szczygieł, Effect of a ZrO2 coating deposited by the sol–gel method on the resistance of FeCrAl alloy in high-temperature oxidation conditions, Mater. Chem. Phys. 139 (2013) 944–952. doi:10.1016/j.matchemphys.2013.02.060.

[79] M. Landkof, A. V Levy, D.H. Boone, R. Gray, E. Yaniv, The effect of surface additives on the oxidation of chromia-forming Alloys, Corrosion. 31 (1985) 344–357. doi:10.5006/1.3582016.

[80] R.J. Hussey, M.J. Graham, The influence of reactive-element coatings on the high-temperature oxidation of pure-Cr and high-Cr-content alloys, Oxid. Met. 45 (1996) 349–374. doi:10.1007/BF01046989.

[81] F.J. Pérez, E. Otero, M.P. Hierro, C. Gómez, F. Pedraza, J.L. De Segovia, et al., High temperature corrosion protection of austenitic AISI 304 stainless steel by Si , Mo and Ce ion implantation, Surf. Coatings Technol. 109 (1998) 127–131. doi:10.1016/S0257-8972(98)00685-9.

[82] H.M. Jin, A. Felix, M. Aroyave, Growing kinetics and structural characterization of oxide

film formed on La-doped Co–40Cr alloy, Chinese Chem. Lett. 18 (2007) 577–580. doi:10.1016/j.cclet.2007.02.016.

[83] J. Ma, Y. He, D. Wang, W. Gao, The effects of pre-oxidation and thin Y2O3 coating on the selective oxidation of Cr18–Ni9–Ti steel, Mater. Lett. 58 (2004) 807–812. doi:10.1016/j.matlet.2003.07.017.

[84] Y. Zhou, X. Peng, F. Wang, Cyclic oxidation of alumina-forming Ni–Al nanocomposites with and without CeO2 addition, Scr. Mater. 55 (2006) 1039–1042. doi:10.1016/j.scriptamat.2006.08.004.

[85] R. Siab, G. Bonnet, J.M. Brossard, J. Balmain, J.-F. Dinhut, Effect of an electrodeposited yttrium containing thin film on the high-temperature oxidation behaviour of TA6V alloy, Appl. Surf. Sci. 253 (2007) 3425–3431. doi:10.1016/j.apsusc.2006.07.057.

[86] B. Bouchaud, J. Balmain, G. Bonnet, F. Pedraza, Optimizing structural and compositional properties of electrodeposited ceria coatings for enhanced oxidation resistance of a nickel-based superalloy, Appl. Surf. Sci. 268 (2013) 218–224. doi:10.1016/j.apsusc.2012.12.065.

[87] B. Bouchaud, J. Balmain, D. Barrere, T. Delannoye, F. Pedraza, Effect of water drops on the oxidation mechanisms of a ceria coated nickel-based superalloy, Corros. Sci. 68 (2013) 176–185. doi:10.1016/j.corsci.2012.11.010.

[88] M. Brossard, B. Bouchaud, G. Bonnet, B. Rannou, F. Pedraza, Early stages of high temperature cyclic oxidation of an electrodeposited ceria coating on nickel superalloys under water-drop tests, Oxid. Met. 81 (2013) 95–104. doi:10.1007/s11085-013-9426-7.

[89] V.A.C. Haanappel, T. Fransen, B. Geerdink, P.J. Gellings, M.F. Stroosnijder, The properties of protective oxide scales containing cerium on alloy 800H in oxidizing and oxidizing/sulphidizing environments, Oxid. Met. 35 (1991) 405–414. doi:10.1007/BF00664711.

[90] S. Chevalier, C. Nivot, J.P. Larpin, Influence of reactive element oxide coatings on the high temperature oxidation behavior of alumina-forming alloys, Oxid. Met. 61 (2004) 195–217. doi:10.1023/B:OXID.0000025331.25452.35.

[91] F. Jia, H. Peng, L. Zheng, H. Guo, S. Gong, H. Xu, Effect of different B contents on the mechanical properties and cyclic oxidation behaviour of β-NiAlDy coatings, J. Alloys

Compd. 623 (2015) 83–88. doi:10.1016/j.jallcom.2014.10.116.

[92] V. Viswanathan, R. Filmalter, S. Patil, S. Deshpande, S. Seal, High-temperature oxidation behavior of solution precursor plasma sprayed nanoceria coating on martensitic steels, J. Am. Ceram. Soc. 90 (2007) 870–877. doi:10.1111/j.1551-2916.2006.01463.x.

[93] H.F. Lopez, H. Mendoza, B. Church, High-temperature oxidation resistance of a nanoceria spray-coated 316L stainless steel under short-term air Eexposure, Metall. Mater. Trans. A. 45 (2013) 1362–1370. doi:10.1007/s11661-013-2051-x.

[94] J.H. Park, J.K. Kim, B.H. Lee, H.S. Seo, K.Y. Kim, Effect of Zr addition on intergranular corrosion of low-chromium ferritic stainless steel, Scr. Mater. 76 (2014) 77–80. doi:10.1016/j.scriptamat.2014.01.001.

[95] R. Siab, G. Bonnet, J.M. Brossard, J. Balmain, J.-F. Dinhut, Effect of an electrodeposited yttrium containing thin film on the high-temperature oxidation behaviour of TA6V alloy, Appl. Surf. Sci. 253 (2007) 3425–3431. doi:10.1016/j.apsusc.2006.07.057.

[96] D. Naumenko, B.A. Pint, W.J. Quadakkers, Current thoughts on reactive element effects in alumina-forming systems : in memory of John Stringer, Oxid. Met. 86 (2016) 1–43. doi:10.1007/s11085-016-9625-0.

[97] B. Bouchaud, F. Pedraza, Oxidation behaviour of new electrolytically synthesized ceria modified platinum γ/γ′ coatings, Surf. Coatings Technol. 248 (2014) 74–80. doi:10.1016/j.surfcoat.2014.03.034.

[98] W.G. Kim, S.N. Yin, J.Y. Park, S.D. Hong, Y.W. Kim, An improved methodology for determining tensile design strengths of Alloy 617, J. Mech. Sci. Technol. 26 (2012) 379–387. doi:10.1007/s12206-011-1024-5.

[99] M. Katcher, D.L. Klarstrom, A review of Haynes® 230® and 617 alloys for high temperature gas cooled reactors, Mater. Sci. Forum. 595–598 (2008) 511–517. doi:10.4028/www.scientific.net/MSF.595-598.511.

[100] P. Kritzer, N. Boukis, E. Dinjus, Review of the corrosion of Nickel-based alloys and stainless steels in strongly oxidizing pressurized high-temperature solutions at subcritical and supercritical temperatures, Corrosion. 56 (2000) 1093–1104. doi:10.5006/1.3294394.

[101] W. Ren, R. Swindeman, A review on current status of alloys 617 and 230 for Gen IV

nuclear reactor internals and heat exchangers, J. Press. Vessel Technol. 131 (2009) 44002–1. doi:10.1115/1.3121522.

[102] S. Abraham, Nuclear power ' s new dawn, Nature. 429 (2004) 238–240. doi:10.1038/429238a.

[103] D. Kim, I. Sah, C. Jang, Effects of high temperature aging in an impure helium environment on low temperature embrittlement of Alloy 617 and Haynes 230, J. Nucl. Mater. 405 (2010) 9–16. doi:10.1016/j.jnucmat.2010.07.026.

[104] D.M. England, A. V Virkar, Oxidation kinetics of some Nickel-based superalloy foils and electronic resistance of the oxide scale formed in air Part I, J. Electrochem. Soc. 146 (1999) 3196–3202. doi:10.1149/1.1392454.

[105] B. Hua, F. Lu, J. Zhang, Y. Kong, J. Pu, B. Chi, et al., Oxidation behavior and electrical property of a Ni-based alloy in SOFC anode environment, J. Electrochem. Soc. 156 (2009) 1261–1266. doi:10.1149/1.3194788.

[106] S.J. Geng, J.H. Zhu, Z.G. Lu, Evaluation of several alloys for solid oxide fuel cell interconnect application, Scr. Mater. 55 (2006) 239–242. doi:10.1016/j.scriptamat.2006.04.008.

[107] S. Dewson, X. Li, Selection criteria for the high temperature reactor intermediate heat exchanger, Proc. ICAPP. (2005) 1–8.

[108] H.M. Tawancy, High-temperature oxidation behavior of a wrought Ni-Cr-W-Mn-Si-La alloy, Oxid. Met. 45 (1996) 323–348. doi:10.1007/BF01046988.

[109] D.M. England, A. V. Virkar, Oxidation kinetics of some Nickel-based superalloy foils in humidified hydrogen and electronic resistance of the oxide scale formed Part II, J. Electrochem. Soc. 148 (2001) A330. doi:10.1149/1.1354611.

[110] L. Jian, P. Jian, H. Bing, G. Xie, Oxidation kinetics of Haynes 230 alloy in air at temperatures between 650 and 850 ℃, J. Power Sources. 159 (2006) 641–645. doi:10.1016/j.jpowsour.2005.09.065.

[111] L. Jian, P. Jian, X. Guangyuan, W. Shunxu, X. Jianzhong, Heat resistant alloys as interconnect materials of reduced temperature SOFCs, J. Power Sources. 157 (2006) 368–376. doi:10.1016/j.jpowsour.2005.07.086.

[112] L. Jian, P. Jian, X. Jianzhong, Q. Xiaoliang, Oxidation of Haynes 230 alloy in reduced temperature solid oxide fuel cell environments, J. Power Sources. 139 (2005) 182–187. doi:10.1016/j.jpowsour.2004.07.019.

[113] D. Kim, C. Jang, W.S. Ryu, Oxidation characteristics and oxide layer evolution of alloy 617 and Haynes 230 at 900 ℃ and 1100 ℃, Oxid. Met. 71 (2009) 271–293. doi:10.1007/s11085-009-9142-5.

[114] C. Jang, D. Kim, D. Kim, I. Sah, W.-S. Ryu, Y. Yoo, Oxidation behaviors of wrought nickel-based superalloys in various high temperature environments, Trans. Nonferrous Met. Soc. China. 21 (2011) 1524–1531. doi:10.1016/S1003-6326(11)60891-1.

[115] D. Kim, I. Sah, D. Kim, W.S. Ryu, C. Jang, High temperature oxidation behavior of alloy 617 and Haynes 230 in impurity-controlled helium environments, Oxid. Met. 75 (2010) 103–119. doi:10.1007/s11085-010-9223-5.

[116] D. Kim, I. Sah, C. Jang, Effects of aging in high temperature helium environments on room temperature tensile properties of nickel-base superalloys, Mater. Sci. Eng. A. 528 (2011) 1713–1720. doi:10.1016/j.msea.2010.10.104.

[117] D. Kim, I. Sah, H.J. Lee, C. Jang, Hydrogen effects on oxidation behaviors of Haynes 230 in high temperature steam environments, Solid State Ionics. 243 (2013) 1–7. doi:10.1016/j.ssi.2013.04.010.

[118] F.R. Chien, R. Brown, Cyclic oxidation of Haynes 230 alloy, J. Mater. Sci. 27 (1992) 1514–1520. doi:10.1007/BF00542912.

[119] H.M. Tawancy, N.M. Abbas, An analytical electron microscopy study of the role of La and Y during high-temperature oxidation of selected Ni-based alloys, Scr. Metall. Mater. 29 (1993) 689–694. doi:10.1016/0956-716X(93)90420-W.

[120] Paul D.Jablonski, D. E.Alman, Surface modification of ferritic and Ni based alloys for improved oxidation resistance in SOFC application, Adv. Solid Oxide Fuel Cells. 26 (2008) 193–200. doi:10.1002/9780470291245.ch22.

[121] C.Y. Bai, C.H. Koo, C.C. Wang, Electrical discharge surface alloying of superalloy Haynes 230 with aluminum and molybdenum, Mater. Trans. 45 (2004) 2878–2885. doi:10.2320/matertrans.45.2878.

[122] C.Y. Bai, Effects of electrical discharge surface modification of superalloy Haynes 230 with aluminum and molybdenum on oxidation behavior, Corros. Sci. 49 (2007) 3889–3904. doi:10.1016/j.corsci.2007.05.009.

[123] S. Guillou, C. Desgranges, S. Chevalier, Influence of a coating on oxidation resistance and resistivity of a chromia former alloy for high temperature vapor electrolysis application, Oxid. Met. 80 (2012) 341–361. doi:10.1007/s11085-012-9319-1.

[124] L. Chen, N. Magdefrau, E. Sun, J. Yamanis, D. Frame, C. Burila, Strontium transport and conductivity of Mn1.5Co1.5O4 coated Haynes 230 and Crofer 22 APU under simulated solid oxide fuel cell condition, Solid State Ionics. 204–205 (2011) 111–119. doi:10.1016/j.ssi.2011.10.004.

[125] L. Chen, E.Y. Sun, J. Yamanis, N. Magdefrau, Oxidation kinetics of Mn 1.5Co1.5O4-coated Haynes 230 and Crofer 22 APU for solid oxide fuel cell interconnects, J. Electrochem. Soc. 157 (2010) B931. doi:10.1149/1.3391820.

[126] H.M. Tung, J.F. Stubbins, Incipient corrosion behavior of Haynes 230 under a controlled reducing atmosphere at high temperatures, J. Nucl. Mater. 427 (2012) 389–392. doi:10.1016/j.jnucmat.2012.05.016.

[127] H.M. Tawancy, High temperature creep behaviour of an N i - C r - W - B alloy, J. Mater. Sci. 27 (1992) 6481–6489. doi:10.1007/BF00576301.

[128] L. Dongmei, H. Rui, L. Jinshan, L. Yi, K. Hongchao, F. Hengzhi, Isothermal oxidation behavior of Haynes 230 alloy in air at 1100 ℃, Rare Met. Mater. Eng. 37 (2008) 1545–1548. doi:10.1016/S1875-5372(09)60040-0.

[129] C.J. Boehlert, S.C. Longanbach, A comparison of the microstructure and creep behavior of cold rolled HAYNES® 230 alloy™ and HAYNES® 282 alloy™, Mater. Sci. Eng. A. 528 (2011) 4888–4898. doi:10.1016/j.msea.2011.03.019.

[130] X. Peng, L. Li, F. Wang, Application of AFM in a study of the selective oxidation behavior of materials during the early oxidation stage, Scr. Mater. 60 (2009) 699–702. doi:10.1016/j.scriptamat.2008.12.056.

[131] J. Litz, A. Rahmel, M. Schorr, Selective carbide oxidation and internal nitridation of the Ni-base superalloys IN 738 LC and IN 939 in air, Oxid. Met. 30 (1988) 95–105.

doi:10.1007/BF00656646.

[132] H. Akhiani, M. Nezakat, S. Penttilä, J. Szpunar, The oxidation resistance of thermo-mechanically processed Incoloy 800HT in supercritical water, J. Supercrit. Fluids. 101 (2015) 150–160. doi:10.1016/j.supflu.2015.03.019.

[133] M. Nezakat, H. Akhiani, S. Penttilä, M. Sabet, J. Szpunar, Effect of thermo-mechanical processing on oxidation of austenitic stainless steel 316L in supercritical water, Corros. Sci. 94 (2015) 197–206. doi:10.1016/j.corsci.2015.02.008.

[134] P. Tunthawiroon, Y. Li, N. Tang, Y. Koizumi, A. Chiba, Effects of alloyed Si on the oxidation behaviour of Co–29Cr–6Mo alloy for solid-oxide fuel cellinterconnects, Corros. Sci. 95 (2015) 88–99. doi:10.1016/j.corsci.2015.02.036.

[135] L. Liu, S. Wu, Y. Dong, S. Lü, Effects of alloyed Mn on oxidation behaviour of a Co–Ni–Cr–Fe alloy between 1050 and 1250 ℃, Corros. Sci. 104 (2016) 236–247. doi:10.1016/j.corsci.2015.12.016.

[136] R.K.S. Raman, J.B. Gnanamoorthy, S.K. Roy, Synergistic influence of alloy grain size and Si content on the oxidation behavior of 9Cr-1Mo steel, Oxid. Met. 42 (1994) 335–355. doi:10.1007/BF01046754.

[137] K.D. Ralston, N. Birbilis, C.H.J. Davies, Revealing the relationship between grain size and corrosion rate of metals, Scr. Mater. 63 (2010) 1201–1204. doi:10.1016/j.scriptamat.2010.08.035.

[138] X. Wang, J.A. Szpunar, L. Zhang, Effect of surface crystallographic orientation on the oxidation behavior of Ni-based alloy, Appl. Surf. Sci. 327 (2014) 532–536. doi:10.1016/j.apsusc.2014.11.126.

[139] X. Wang, F. Fan, J.A. Szpunar, L. Zhang, Influence of grain orientation on the incipient oxidation behavior of Haynes 230 at 900 ℃, Mater. Charact. 107 (2015) 33–42. doi:10.1016/j.matchar.2015.06.029.

[140] C.K. Kim, L.W. Hobbs, Microstructural evidence for short-circuit oxygen diffusion paths in the oxidation of a dilute Ni-Cr alloy, Oxid. Met. 45 (1996) 247–265. doi:10.1007/BF01046984.

[141] A. Smith, G. Gibbs, Volume and grain-boundary diffusion in 20 Cr/25 Ni/Nb stainless

steel, Met. Sci. 3 (1969) 93–94. doi:10.1179/msc.1969.3.1.93.

[142] J.C. Fisher, Calculation of diffusion penetration curves for surface and grain boundary diffusion, J. Appl. Phys. 22 (1951) 74–77. doi:10.1063/1.1699825.

[143] J.R. Farver, R.A. Yund, Measurement of oxygen grain boundary diffusion in natural, fine-grained, quartz aggregates, Geochim. Cosmochim. Acta. 55 (1991) 1597–1607. doi:10.1016/0016-7037(91)90131-N.

[144] A.C.S. Sabioni, A.M. Huntz, L.C. Borges, F. Jomard, First study of manganese diffusion in Cr2O3 polycrystals and thin films by SIMS, Philos. Mag. 87 (2007) 1921–1937. doi:10.1080/14786430601120462.

[145] B. Bouchaud, J. Balmain, G. Bonnet, F. Pedraza, Correlations between electrochemical mechanisms and growth of ceria based coatings onto nickel substrates, Electrochim. Acta. 88 (2013) 798–806. doi:10.1016/j.electacta.2012.10.112.

[146] S. Patil, S.C. Kuiry, S. Seal, R. Vanfleet, Synthesis of nanocrystalline ceria particles for high temperature oxidation resistant coating, J. Nanoparticle Res. 4 (2002) 433–438. doi:10.1023/A:1021696107498.

[147] K. Kamada, K. Higashikawa, M. Inada, N. Enomoto, J. Hojo, Photoassisted anodic electrodeposition of ceria thin films, J. Phys. Chem. C. 111 (2007) 14508–14513. doi:10.1021/jp074999p.

[148] Y. Hamlaoui, F. Pedraza, C. Remazeilles, S. Cohendoz, C. Rébéré, L. Tifouti, et al., Cathodic electrodeposition of cerium-based oxides on carbon steel from concentrated cerium nitrate solutions, Mater. Chem. Phys. 113 (2009) 650–657. doi:10.1016/j.matchemphys.2008.08.027.

[149] Y. Hamlaoui, L. Tifouti, C. Remazeilles, F. Pedraza, Cathodic electrodeposition of cerium based oxides on carbon steel from concentrated cerium nitrate. Part II: Influence of electrodeposition parameters and of the addition of PEG, Mater. Chem. Phys. 120 (2010) 172–180. doi:10.1016/j.matchemphys.2009.10.042.

[150] M. Brossard, B. Bouchaud, F. Pedraza, Influence of water vapour on the oxidation behaviour of a conventional aluminide and a new thermal barrier coating system sintered from a slurry, Mater. Corros. 65 (2014) 161–168. doi:10.1002/maco.201307106.

[151] F. Pedraza, J. Balmain, G. Bonnet, B. Bouchaud, Novel concept of functional oxide coatings providing enhanced oxidation resistance to Ni-based superalloys, Mater. Res. Bull. 49 (2014) 384–387. doi:10.1016/j.materresbull.2013.09.017.

[152] M. Mollard, B. Rannou, B. Bouchaud, J. Balmain, G. Bonnet, F. Pedraza, Comparative degradation of nickel aluminized by slurry and by pack cementation under isothermal conditions, Corros. Sci. 66 (2013) 118–124. doi:10.1016/j.corsci.2012.09.009.

[153] B. Rannou, B. Bouchaud, J. Balmain, G. Bonnet, F. Pedraza, Comparative isothermal oxidation behaviour of new aluminide coatings from slurries containing Al particles and conventional out-of-pack Aluminide coatings, Oxid. Met. 81 (2013) 139–149. doi:10.1007/s11085-013-9427-6.

[154] F. Pedraza, B. Bouchaud, J. Balmain, G. Bonnet, J. Menuey, Electrosynthesis of rare earth oxide coatings for high temperature applications, Mater. Sci. Forum. 696 (2011) 336–341. doi:10.4028/www.scientific.net/MSF.696.336.

[155] F. Pedraza, B. Bouchaud, J. Balmain, G. Bonnet, J. Menuey, Enhanced cyclic oxidation resistance of a single crystal superalloy with an electrodeposited reactive element oxide coating, Mater. Sci. Forum. 696 (2011) 278–283. doi:10.4028/www.scientific.net/MSF.696.278.

[156] I. Kosacki, T. Suzuki, H.U. Anderson, P. Colomban, Raman scattering and lattice defects in nanocrystalline CeO2 thin films, Solid State Ionics. 149 (2002) 99–105. doi:10.1016/S0167-2738(02)00104-2.

[157] A. Siokou, S. Ntais, V. Dracopoulos, S. Papaefthimiou, G. Leftheriotis, P. Yianoulis, Substrate related structural, electronic and electrochemical properties of evaporated CeOx ion storage layers, Thin Solid Films. 514 (2006) 87–96. doi:10.1016/j.tsf.2006.02.077.

[158] Y.M. Wang, D.D. Zhao, Y.Q. Zhao, C.L. Xu, H.L. Li, Effect of electrodeposition temperature on the electrochemical performance of a Ni(OH)2 electrode, RSC Adv. 2 (2012) 1074–1082. doi:10.1039/c1ra00613d.

[159] A.Q. Wang, T.D. Golden, Electrodeposition of oriented cerium oxide films, Int. J. Electrochem. 2013 (2013) 1–10. doi:10.1155/2013/482187.

[160] W. Lu, P. Huang, K. Li, P. Yan, Y. Wang, B. Yan, Effect of bath temperature on the

microstructural properties of electrodeposited nanocrystalline FeCo films, Int. J. Electrochem. Sci. 8 (2013) 2354–2364.

[161] Y. Hamlaoui, F. Pedraza, L. Tifouti, Investigation of electrodeposited cerium oxide based films on carbon steel and of the induced formation of carbonated green rusts, Corros. Sci. 50 (2008) 2182–2188. doi:10.1016/j.corsci.2008.05.017.

[162] L. Arurault, P. Monsang, J. Salley, R.S. Bes, Electrochemical preparation of adherent ceria coatings on ferritic stainless steel, Thin Solid Films. 466 (2004) 75–80. doi:10.1016/j.tsf.2004.02.039.

[163] B. Han, Y. Ma, H. Peng, L. Zheng, H. Guo, Effect of Mo, Ta, and Re on high-temperature oxidation behavior of minor Hf doped β-NiAl alloy, Corros. Sci. 102 (2016) 222–232. doi:10.1016/j.corsci.2015.10.011.

[164] G.M. Ecer, G.H. Meier, The effect of cerium on the oxidation of Ni-50Cr alloys, Oxid. Met. 13 (1979) 159–180. doi:10.1007/BF00611977.

[165] H. Guo, D. Li, L. Zheng, S. Gong, H. Xu, Effect of co-doping of two reactive elements on alumina scale growth of β-NiAl at 1200 ℃, Corros. Sci. 88 (2014) 197–208. doi:10.1016/j.corsci.2014.07.036.

[166] B.A. Pint, Experimental observations in support of the dynamic-segregation theory to explain the reactive-element effect, Oxid. Met. 45 (1996) 1–37. doi:10.1007/BF01046818.

[167] C.M. Cotell, G.J. Yurek, R.J. Hussey, D.F. Mitchell, M.. Graham, The influence of grain-boundary segregation of Y in Cr2O3 on the oxidation of Cr metal, Oxid. Met. 34 (1990) 173–200. doi:10.1007/BF00665014.

[168] C.M. Cotell, G.J. Yurek, R.J. Hussey, D.F. Mitchell, M.. Graham, The influence of grain-boundary segregation of Y in Cr2O3 on the oxidation of Cr metal . II . effects of temperature and dopant concentration, 34 (1990) 201–216. doi:10.1007/BF00665015.

[169] J. Stringer, B.A. Wilcox, R.I. Jaffee, The high-temperature oxidation of nickel-20 wt. % chromium alloys containing dispersed oxide phases, Oxid. Met. 5 (1972) 11–47. doi:10.1007/BF00614617.

[170] G.M. Ecer, R.B. Singh, G.H. Meier, The influence of superficially applied oxide powders on the high-temperature oxidation behavior of Cr2O3-forming alloys, Oxid. Met. 18 (1982)

55–81. doi:10.1007/BF00656095.

[171] F. Pedraza, B. Bouchaud, J. Balmain, G. Bonnet, V. Kolarik, J. Menuey, On the development of a protective oxide system in rare earth oxide coated Nickel superalloy under isothermal oxidation conditions, Mater. Sci. Forum. 696 (2011) 284–289. doi:10.4028/www.scientific.net/MSF.696.284.

[172] X. Wang, F. Fan, J.A. Szpunar, Optimizing cathodic electrodeposition parameters of ceria coating to enhance the oxidation resistance of a Cr2O3-forming alloy, Thin Solid Films. 611 (2016) 12–20. doi:10.1016/j.tsf.2016.05.004.

[173] H.M. Tung, J.F. Stubbins, Incipient oxidation kinetics and residual stress of the oxide scale grown on Haynes 230 at high temperatures, Mater. Sci. Eng. A. 538 (2012) 1–6. doi:10.1016/j.msea.2011.10.114.

[174] V. Firouzdor, K. Sridharan, G. Cao, M. Anderson, T.R. Allen, Corrosion of a stainless steel and nickel-based alloys in high temperature supercritical carbon dioxide environment, Corros. Sci. 69 (2013) 281–291. doi:10.1016/j.corsci.2012.11.041.

[175] A.L. Marasco, D.J. Young, The oxidation of Iron-Chromium-Manganese alloys at 900 ℃, Oxid. Met. 36 (1991) 157–174. doi:10.1007/BF00938460.

[176] H.M. Tung, J.F. Stubbins, Incipient corrosion behavior of Haynes 230 under a controlled reducing atmosphere at high temperatures, J. Nucl. Mater. 427 (2012) 389–392. doi:10.1016/j.jnucmat.2012.05.016.

[177] A.C.S. Sabioni, B. Lesage, A.M. Huntz, J.C. Pivin, C. Monty, Self-diffusion in Cr2O3 I. Chromium diffusion in single crystals, Philos. Mag. A. 66 (1992) 333–350. doi:10.1080/01418619208201560.

[178] A. Sabioni, A. Huntz, F. Millot, C. Monty, Self-diffusion in Cr2O3 II. Oxygen diffusion in single crystals, Philos. Mag. A. 66 (1992) 351–360. doi:10.1080/01418619208201561.

[179] J.H. Kim, D.I. Kim, J.H. Shim, K.W. Yi, Investigation into the high temperature oxidation of Cu-bearing austenitic stainless steel using simultaneous electron backscatter diffraction-energy dispersive spectroscopy analysis, Corros. Sci. 77 (2013) 397–402. doi:10.1016/j.corsci.2013.08.015.

[180] G.N. Dubinin, On the columnar structure of a duffusion layer, Met. Sci. Heat Treat. 42

(2000) 89–93. doi:10.1007/BF02471341.

[181] J. Meng, Z. Ji, Effect of La2O3/CeO2 particle size on high-temperature oxidation resistance of electrodeposited Ni–La2O3/CeO2 composites, Trans. Nonferrous Met. Soc. China. 24 (2014) 3571–3577. doi:10.1016/S1003-6326(14)63503-2.

[182] H.F. Lopez, H. Zhang, Nanoceria coating imperfections and their effect on the high-temperature oxidation resistance of a 304 stainless steel, J. Mater. Sci. 49 (2013) 277–286. doi:10.1007/s10853-013-7702-1.

[183] E. Dahle, Grain refinement of high alloyed steel with cerium addition, Norwegian University of Science and Technology, 2011.

[184] H.F. Lopez, H. Zhang, The effect of particle size on the oxidation resistance of a nanoceria-coated 304 stainless steel, Metall. Mater. Trans. A. 45 (2014) 2297–2308. doi:10.1007/s11661-013-2159-z.

[185] F. Czerwinski, W.W. Smeltzer, The growth and structure of thin oxide films on ceria-sol-coated nickel, Oxid. Met. 40 (1993) 503–527. doi:10.1007/BF00666389.

[186] Y. Wu, S.K. Hwang, Microstructural refinement and improvement of mechanical properties and oxidation resistance in EPM TiAl-based intermetallics with yttrium addition, Acta Mater. 50 (2002) 1479–1493. doi:10.1016/S1359-6454(02)00006-X.

[187] S. Chevalier, G. Bonnet, J.C. Colson, J.P. Larpin, Influence of a reactive element oxide coating on the high temperature oxidation of chromia-former alloys, J. Chim. Phys. Physico-Chimie Biol. 95 (1998) 2083–2102. doi:10.1051/jcp:1998356.

[188] M.F. Li Jian, C.Y.Yuh, Oxidation behavior of superalloys in oxidizing and reducing environments, Corros. Sci. 42 (2000) 1573–1585. doi:10.1016/S0010-938X(00)00011-1.

[189] H. Buscail, R. Rolland, C. Issartel, F. Rabaste, F. Riffard, L. Aranda, et al., Effects of water vapour on the oxidation of a nickel-base 625 alloy between 900 and 1100 ℃, J. Mater. Sci. 46 (2011) 5903–5915. doi:10.1007/s10853-011-5544-2.

[190] J. He, Z. Zhang, H. Peng, S. Gong, H. Guo, The role of Dy and Hf doping on oxidation behavior of two-phase (γ′+β) Ni–Al alloys, Corros. Sci. 98 (2015) 699–707. doi:10.1016/j.corsci.2015.06.016.

[191] H.F. Lopez, H. Mendoza-Del Angel, Long term high temperature oxidation resistance of a nanoceria coated 316 SS under dry air conditions, Mater. Chem. Phys. 146 (2014) 204–211. doi:10.1016/j.matchemphys.2013.11.053.

[192] A.C.S. Sabioni, A.M. Huntz, F. Millot, C. Monty, Self-diffusion in Cr2O3 III. Chromium and oxygen grain-boundary diffusion in polycrystals, Philos. Mag. A. 66 (1992) 361–374. doi:10.1080/01418619208201562.

APPENDIX A

List of alloys used in the work

In this project, the oxidation behavior of three Ni-based alloys provided by Haynes international Inc. were evaluated. The chemical compositions of those alloys are shown in Table A-1.

Table A-1 Chemical compositions of Hastelloys used in the project

	Ni	Cr	W	Mo	Fe	Co	Mn	Si	Al	C	La	B	Ti	Cb+Ta
230	Bal*	22	14	2	3	5	0.5	0.4	0.3	0.1	0.02	0.01		
N	Bal*	7	0.5	16	5	0.2	0.8	1	0.35	0.08				
625	Bal*	21		9	5	1	0.5	0.5	0.4	0.1			0.4	3.7

Bal*: balance

These selected Ni-based alloys are widely used in the high temperature industry areas. For instance, they are used as combustion cans, turbine components and transition ducts, etc. Furthermore, they are promising candidate structure materials for the next generation nuclear reactors. Therefore, it is critical to evaluate the oxidation behavior of these alloys.

APPENDIX B

Equipments and main characterization techniques used in the project

To perform all the experiments to complete the whole project, several main characterization technique are used as follows:

1) Sample preparation

Fig. B-1 (a) shows the dimensions of the prepared samples for oxidation measurements. The as-received alloy sheet has a thickness of 1.5 mm. It was cut into 18 × 12 mm rectangular pieces for oxidation tests. A small hole with diameter of 1.5 mm was drilled on each sample before the grounding process. For oxidation experiment, the samples were hanged in the ceramic crucible by some ceramic rods with diameters of 0.8 mm as shown in Fig. B-1 (b).

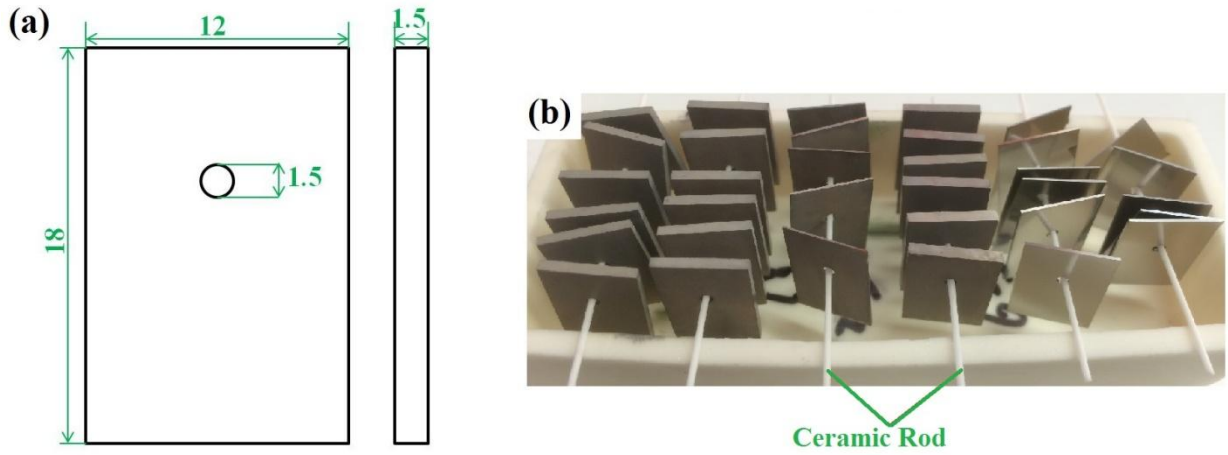

Fig. B-1 Dimensions of the specimen (a) (in mm) and hanging specimen in a ceramic crucible (b).

To prepared ceria coatings, all the samples were ground to 1200 grit and ultrasonically cleaned. A typical three electrodes Gamry Interface 1000 system was used to deposit ceria coating on to the samples with a galvanostatic mode as shown in Fig. B-2.

Fig. B-2 Gamry Interface 1000 equipment

2) Oxidation tests

Fig. B-3 (a) the Thermo Scientific Thermolyne Benchtop muffle furnace used for oxidation tests and (b) the METTLER TOLEDO XS205 analytical balance.

All the samples were oxidized in a Thermo Scientific Thermolyne Benchtop muffle furnace as shown in Fig. B-3 (a). The samples for oxidation measurements were hanged in the crucibles and inserted into the furnace at the same time and taken out from the furnace after specific interval

periods. A METTLER TOLEDO XS205 analytical balance with a resolution of 0.01 mg was used to measure the masses of the samples before and after oxidation as shown in Fig.B-3 (b).

3) Characterization techniques

A Bruker D8 Discovery XRD with Cr Kα radiation was used to define the phases of the deposited ceria and oxides as shown in Fig. B-4. The XRD was also used to collect the incomplete pole figure for texture measurements.

Fig. B-4 The Bruker D8 X-ray Diffraction.

For surface and cross-sectional morphology characterization, a Hitachi SU6600 field emission scanning electron microscope (FE-SEM) was used as shown in Fig. B-5. To know the element distributions of the oxide, the energy dispersive spectroscopy (EDS) mounted on the SEM was

used. Furthermore, the electron back-scattering diffraction equipped on the SEM was used to characterize the microstructure of the alloys and the cross-sectional oxide layers.

Fig. B-5 The Hitachi SU600 scanning electron microscope.

APPENDIX C

Copyright Permission of Manuscript #1:

ELSEVIER LICENSE

TERMS AND CONDITIONS

Apr 18, 2017

This Agreement between Xu Wang ("You") and Elsevier ("Elsevier") consists of your license details and the terms and conditions provided by Elsevier and Copyright Clearance Center.

License Number	4092000737868
License date	Apr 18, 2017
Licensed Content Publisher	Elsevier
Licensed Content Publication	Applied Surface Science
Licensed Content Title	Effect of surface crystallographic orientation on the oxidation behavior of Ni-based alloy
Licensed Content Author	Xu Wang, J.A. Szpunar, Lina Zhang
Licensed Content Date	1 February 2015
Licensed Content Volume Number	327
Licensed Content Issue Number	n/a
Licensed Content Pages	5
Start Page	532
End Page	536
Type of Use	reuse in a thesis/dissertation
Portion	full article
Format	Both print and electronic
Are you the author of this Elsevier article?	Yes
Will you be translating?	No
Order reference number	
Title of your	ENHANCING OXIDATION RESISTANCE OF Ni-BASED

thesis/dissertation	SUPERALLOYS FOR HIGH TEMPERATURE APPLICATIONS
Expected completion date	Apr 2017
Estimated size (number of pages)	200
Elsevier VAT number	GB 494 6272 12
Requestor Location	Xu Wang 57 Campus Drive Saskatoon, SK S7N5A9 Canada
Attn:	Xu Wang
Total	0.00 CAD

Terms and Conditions

INTRODUCTION

1. The publisher for this copyrighted material is Elsevier. By clicking "accept" in connection with completing this licensing transaction, you agree that the following terms and conditions apply to this transaction (along with the Billing and Payment terms and conditions established by Copyright Clearance Center, Inc. ("CCC"), at the time that you opened your Rightslink account and that are available at any time at http://myaccount.copyright.com).

GENERAL TERMS

2. Elsevier hereby grants you permission to reproduce the aforementioned material subject to the terms and conditions indicated.

3. Acknowledgement: If any part of the material to be used (for example, figures) has appeared in our publication with credit or acknowledgement to another source, permission must also be sought from that source. If such permission is not obtained then that material may not be included in your publication/copies. Suitable acknowledgement to the source must be made, either as a footnote or in a reference list at the end of your publication, as follows:

"Reprinted from Publication title, Vol /edition number, Author(s), Title of article / title of chapter, Pages No., Copyright (Year), with permission from Elsevier [OR APPLICABLE SOCIETY

COPYRIGHT OWNER]." Also Lancet special credit "Reprinted from The Lancet, Vol. number, Author(s), Title of article, Pages No., Copyright (Year), with permission from Elsevier."

4. Reproduction of this material is confined to the purpose and/or media for which permission is hereby given.

5. Altering/Modifying Material: Not Permitted. However figures and illustrations may be altered/adapted minimally to serve your work. Any other abbreviations, additions, deletions and/or any other alterations shall be made only with prior written authorization of Elsevier Ltd. (Please contact Elsevier at permissions@elsevier.com)

6. If the permission fee for the requested use of our material is waived in this instance, please be advised that your future requests for Elsevier materials may attract a fee.

7. Reservation of Rights: Publisher reserves all rights not specifically granted in the combination of (i) the license details provided by you and accepted in the course of this licensing transaction, (ii) these terms and conditions and (iii) CCC's Billing and Payment terms and conditions.

8. License Contingent Upon Payment: While you may exercise the rights licensed immediately upon issuance of the license at the end of the licensing process for the transaction, provided that you have disclosed complete and accurate details of your proposed use, no license is finally effective unless and until full payment is received from you (either by publisher or by CCC) as provided in CCC's Billing and Payment terms and conditions. If full payment is not received on a timely basis, then any license preliminarily granted shall be deemed automatically revoked and shall be void as if never granted. Further, in the event that you breach any of these terms and conditions or any of CCC's Billing and Payment terms and conditions, the license is automatically revoked and shall be void as if never granted. Use of materials as described in a revoked license, as well as any use of the materials beyond the scope of an unrevoked license, may constitute copyright infringement and publisher reserves the right to take any and all action to protect its copyright in the materials.

9. Warranties: Publisher makes no representations or warranties with respect to the licensed material.

10. Indemnity: You hereby indemnify and agree to hold harmless publisher and CCC, and their respective officers, directors, employees and agents, from and against any and all claims arising out of your use of the licensed material other than as specifically authorized pursuant to this license.

11. No Transfer of License: This license is personal to you and may not be sublicensed, assigned, or transferred by you to any other person without publisher's written permission.

12. No Amendment Except in Writing: This license may not be amended except in a writing signed by both parties (or, in the case of publisher, by CCC on publisher's behalf).

13. Objection to Contrary Terms: Publisher hereby objects to any terms contained in any purchase order, acknowledgment, check endorsement or other writing prepared by you, which terms are inconsistent with these terms and conditions or CCC's Billing and Payment terms and conditions. These terms and conditions, together with CCC's Billing and Payment terms and conditions (which are incorporated herein), comprise the entire agreement between you and publisher (and CCC) concerning this licensing transaction. In the event of any conflict between your obligations established by these terms and conditions and those established by CCC's Billing and Payment terms and conditions, these terms and conditions shall control.

14. Revocation: Elsevier or Copyright Clearance Center may deny the permissions described in this License at their sole discretion, for any reason or no reason, with a full refund payable to you. Notice of such denial will be made using the contact information provided by you. Failure to receive such notice will not alter or invalidate the denial. In no event will Elsevier or Copyright Clearance Center be responsible or liable for any costs, expenses or damage incurred by you as a result of a denial of your permission request, other than a refund of the amount(s) paid by you to Elsevier and/or Copyright Clearance Center for denied permissions.

LIMITED LICENSE

The following terms and conditions apply only to specific license types:

15. Translation: This permission is granted for nonexclusive world English rights only unless your license was granted for translation rights. If you licensed translation rights you may only

translate this content into the languages you requested. A professional translator must perform all translations and reproduce the content word for word preserving the integrity of the article.

16. Posting licensed content on any Website: The following terms and conditions apply as follows: Licensing material from an Elsevier journal: All content posted to the web site must maintain the copyright information line on the bottom of each image; A hypertext must be included to the Homepage of the journal from which you are licensing at http://www.sciencedirect.com/science/journal/xxxxx or the Elsevier homepage for books at http://www.elsevier.com;

Central Storage: This license does not include permission for a scanned version of the material to be stored in a central repository such as that provided by Heron/XanEdu.

Licensing material from an Elsevier book: A hypertext link must be included to the Elsevier homepage at http://www.elsevier.com . All content posted to the web site must maintain the copyright information line on the bottom of each image.

Posting licensed content on Electronic reserve: In addition to the above the following clauses are applicable: The web site must be password protected and made available only to bona fide students registered on a relevant course.

This permission is granted for 1 year only. You may obtain a new license for future website posting.

17. For journal authors: the following clauses are applicable in addition to the above:

Preprints:

A preprint is an author's own write-up of research results and analysis, it has not been peer-reviewed, nor has it had any other value added to it by a publisher (such as formatting, copyright, technical enhancement etc.).

Authors can share their preprints anywhere at any time. Preprints should not be added to or enhanced in any way in order to appear more like, or to substitute for, the final versions of articles however authors can update their preprints on arXiv or RePEc with their Accepted Author Manuscript (see below).

If accepted for publication, we encourage authors to link from the preprint to their formal publication via its DOI. Millions of researchers have access to the formal publications on ScienceDirect, and so links will help users to find, access, cite and use the best available version. Please note that Cell Press, The Lancet and some society-owned have different preprint policies. Information on these policies is available on the journal homepage.

Accepted Author Manuscripts: An accepted author manuscript is the manuscript of an article that has been accepted for publication and which typically includes author-incorporated changes suggested during submission, peer review and editor-author communications.

Authors can share their accepted author manuscript:

- immediately

  via their non-commercial person homepage or blog

  by updating a preprint in arXiv or RePEc with the accepted manuscript

  via their research institute or institutional repository for internal institutional uses or as part of an invitation-only research collaboration workgroup

  directly by providing copies to their students or to research collaborators for their personal use

  for private scholarly sharing as part of an invitation-only work group on commercial sites with which Elsevierhas an agreement

- after the embargo period

  via non-commercial hosting platforms such as their institutional repository

  via commercial sites with which Elsevier has an agreement

In all cases accepted manuscripts should:

- link to the formal publication via its DOI
- bear a CCBYNCND license- this is easy to do

- if aggregated with other manuscripts, for example in a repository or other site, be shared in alignment with our hosting policy not be added to or enhanced in any way to appear more like, or to substitute for, the published journal article.

Published journal article (JPA): A published journal article (PJA) is the definitive final record of published research that appears or will appear in the journal and embodies all value-adding publishing activities including peer review coordination, copyediting, formatting, (if relevant) pagination and online enrichment.

Policies for sharing publishing journal articles differ for subscription and gold open access articles:

Subscription Articles: If you are an author, please share a link to your article rather than the full-text. Millions of researchers have access to the formal publications on ScienceDirect, and so links will help your users to find, access, cite, and use the best available version.

Theses and dissertations which contain embedded PJAs as part of the formal submission can be posted publicly by the awarding institution with DOI links back to the formal publications on ScienceDirect.

If you are affiliated with a library that subscribes to ScienceDirect you have additional private sharing rights for others' research accessed under that agreement. This includes use for classroom teaching and internal training at the institution (including use in course packs and courseware programs), and inclusion of the article for grant funding purposes.

Gold Open Access Articles: May be shared according to the author-selected end-user license and should contain a **CrossMark logo**, the end user license, and a DOI link to the formal publication on ScienceDirect.

Please refer to Elsevier's posting policy for further information.

18. For book authors the following clauses are applicable in addition to the above: Authors are permitted to place a brief summary of their work online only. You are not allowed to download and post the published electronic version of your chapter, nor may you scan the printed edition to

create an electronic version. Posting to a repository: Authors are permitted to post a summary of their chapter only in their institution's repository.

19. Thesis/Dissertation: If your license is for use in a thesis/dissertation your thesis may be submitted to your institution in either print or electronic form. Should your thesis be published commercially, please reapply for permission. These requirements include permission for the Library and Archives of Canada to supply single copies, on demand, of the complete thesis and include permission for Proquest/UMI to supply single copies, on demand, of the complete thesis. Should your thesis be published commercially, please reapply for permission. Theses and dissertations which contain embedded PJAs as part of the formal submission can be posted publicly by the awarding institution with DOI links back to the formal publications on ScienceDirect.

Elsevier Open Access Terms and Conditions

You can publish open access with Elsevier in hundreds of open access journals or in nearly 2000 established subscription journals that support open access publishing. Permitted third party reuse of these open access articles is defined by the author's choice of Creative Commons user license. See our open access license policy for more information.

Terms & Conditions applicable to all Open Access articles published with Elsevier:

Any reuse of the article must not represent the author as endorsing the adaptation of the article nor should the article be modified in such a way as to damage the author's honour or reputation. If any changes have been made, such changes must be clearly indicated.

The author(s) must be appropriately credited and we ask that you include the end user license and a DOI link to the formal publication on ScienceDirect.

If any part of the material to be used (for example, figures) has appeared in our publication with credit or acknowledgement to another source it is the responsibility of the user to ensure their reuse complies with the terms and conditions determined by the rights holder.

Additional Terms & Conditions applicable to each Creative Commons user license:

Posting or linking by commercial companies for use by customers of those companies.

20. Other Conditions:

v1.8

Questions? customercare@copyright.com or +18552393415 (toll free in the US) or +19786462777.

Copyright Permission of Manuscript #2:

ELSEVIER LICENSE

TERMS AND CONDITIONS

Apr 18, 2017

This Agreement between Xu Wang ("You") and Elsevier ("Elsevier") consists of your license details and the terms and conditions provided by Elsevier and Copyright Clearance Center.

License Number	4092001043902
License date	Apr 18,2017
Licensed Content Publisher	Elsevier
Licensed Content Publication	Materials Characterization
Licensed Content Title	Influence of grain orientation on the incipient oxidation behavior of Haynes 230 at 900 ℃
Licensed Content Author	Xu Wang, Fan Fan, Jerzy A. Szpunar, Lina Zhang
Licensed Content Date	September 2015
Licensed Content Volume Number	107
Licensed Content Issue Number	n/a
Licensed Content Pages	10
Start Page	33
End Page	42
Type of Use	reuse in a thesis/dissertation
Intended publisher of new work	other
Portion	full article
Format	both print and electronic
Are you the author of this Elsevier article?	Yes
Will you be translating?	No
Order reference number	
Title of your thesis/dissertation	ENHANCING OXIDATION RESISTANCE OF Ni-BASED SUPERALLOYS FOR HIGH TEMPERATURE APPLICATIONS

Expected completion dat	Apr 2017
Estimated size (number of pages)	200
Elsevier VAT number	GB 494 6272 12
Requestor Location	Xu Wang 57 Campus Drive Saskatoon, SK S7N5A9 Canada
Attn:	Xu Wang
Total	0.00 USD

Terms and Conditions

INTRODUCTION

1. The publisher for this copyrighted material is Elsevier. By clicking "accept" in connection with completing this licensing transaction, you agree that the following terms and conditions apply to this transaction (along with the Billing and Payment terms and conditions established by Copyright Clearance Center, Inc. ("CCC"), at the time that you opened your Rightslink account and that are available at any time at http://myaccount.copyright.com).

GENERAL TERMS

2. Elsevier hereby grants you permission to reproduce the aforementioned material subject to the terms and conditions indicated.

3. Acknowledgement: If any part of the material to be used (for example, figures) has appeared in our publication with credit or acknowledgement to another source, permission must also be sought from that source. If such permission is not obtained then that material may not be included in your publication/copies. Suitable acknowledgement to the source must be made, either as a footnote or in a reference list at the end of your publication, as follows:

"Reprinted from Publication title, Vol /edition number, Author(s), Title of article / title of chapter, Pages No., Copyright (Year), with permission from Elsevier [OR APPLICABLE SOCIETY COPYRIGHT OWNER]." Also Lancet special credit "Reprinted from The Lancet, Vol. number, Author(s), Title of article, Pages No., Copyright (Year), with permission from Elsevier."

4. Reproduction of this material is confined to the purpose and/or media for which permission is hereby given.

5. Altering/Modifying Material: Not Permitted. However figures and illustrations may be altered/adapted minimally to serve your work. Any other abbreviations, additions, deletions and/or any other alterations shall be made only with prior written authorization of Elsevier Ltd. (Please contact Elsevier at permissions@elsevier.com)

6. If the permission fee for the requested use of our material is waived in this instance, please be advised that your future requests for Elsevier materials may attract a fee.

7. Reservation of Rights: Publisher reserves all rights not specifically granted in the combination of (i) the license details provided by you and accepted in the course of this licensing transaction, (ii) these terms and conditions and (iii) CCC's Billing and Payment terms and conditions.

8. License Contingent Upon Payment: While you may exercise the rights licensed immediately upon issuance of the license at the end of the licensing process for the transaction, provided that you have disclosed complete and accurate details of your proposed use, no license is finally effective unless and until full payment is received from you (either by publisher or by CCC) as provided in CCC's Billing and Payment terms and conditions. If full payment is not received on a timely basis, then any license preliminarily granted shall be deemed automatically revoked and shall be void as if never granted. Further, in the event that you breach any of these terms and conditions or any of CCC's Billing and Payment terms and conditions, the license is automatically revoked and shall be void as if never granted. Use of materials as described in a revoked license, as well as any use of the materials beyond the scope of an unrevoked license, may constitute copyright infringement and publisher reserves the right to take any and all action to protect its copyright in the materials.

9. Warranties: Publisher makes no representations or warranties with respect to the licensed material.

10. Indemnity: You hereby indemnify and agree to hold harmless publisher and CCC, and their respective officers, directors, employees and agents, from and against any and all claims arising

out of your use of the licensed material other than as specifically authorized pursuant to this license.

11. No Transfer of License: This license is personal to you and may not be sublicensed, assigned, or transferred by you to any other person without publisher's written permission.

12. No Amendment Except in Writing: This license may not be amended except in a writing signed by both parties (or, in the case of publisher, by CCC on publisher's behalf).

13. Objection to Contrary Terms: Publisher hereby objects to any terms contained in any purchase order, acknowledgment, check endorsement or other writing prepared by you, which terms are inconsistent with these terms and conditions or CCC's Billing and Payment terms and conditions. These terms and conditions, together with CCC's

Billing and Payment terms and conditions (which are incorporated herein), comprise the entire agreement between you and publisher (and CCC) concerning this licensing transaction. In the event of any conflict between your obligations established by these terms and conditions and those established by CCC's Billing and Payment terms and conditions, these terms and conditions shall control.

14. Revocation: Elsevier or Copyright Clearance Center may deny the permissions described in this License at their sole discretion, for any reason or no reason, with a full refund payable to you. Notice of such denial will be made using the contact information provided by you. Failure to receive such notice will not alter or invalidate the denial. In no event will Elsevier or Copyright Clearance Center be responsible or liable for any costs, expenses or damage incurred by you as a result of a denial of your permission request, other than a refund of the amount(s) paid by you to Elsevier and/or Copyright Clearance Center for denied permissions.

LIMITED LICENSE

The following terms and conditions apply only to specific license types:

15. Translation: This permission is granted for nonexclusive world English rights only unless your license was granted for translation rights. If you licensed translation rights you may only

translate this content into the languages you requested. A professional translator must perform all translations and reproduce the content word for word preserving the integrity of the article.

16. Posting licensed content on any Website: The following terms and conditions apply as follows: Licensing material from an Elsevier journal: All content posted to the web site must maintain the copyright information line on the bottom of each image; A hypertext must be included to the Homepage of the journal from which you are licensing at http://www.sciencedirect.com/science/journal/xxxxx or the Elsevier homepage for books at http://www.elsevier.com;

Central Storage: This license does not include permission for a scanned version of the material to be stored in a central repository such as that provided by Heron/XanEdu.

Licensing material from an Elsevier book: A hypertext link must be included to the Elsevier homepage at http://www.elsevier.com . All content posted to the web site must maintain the copyright information line on the bottom of each image.

Posting licensed content on Electronic reserve: In addition to the above the following clauses are applicable: The web site must be password protected and made available only to bona fide students registered on a relevant course.

This permission is granted for 1 year only. You may obtain a new license for future website posting.

17. For journal authors: the following clauses are applicable in addition to the above:

Preprints:

A preprint is an author's own write-up of research results and analysis, it has not been peer-reviewed, nor has it had any other value added to it by a publisher (such as formatting, copyright, technical enhancement etc.).

Authors can share their preprints anywhere at any time. Preprints should not be added to or enhanced in any way in order to appear more like, or to substitute for, the final versions of articles however authors can update their preprints on arXiv or RePEc with their Accepted Author Manuscript (see below).

If accepted for publication, we encourage authors to link from the preprint to their formal publication via its DOI. Millions of researchers have access to the formal publications on ScienceDirect, and so links will help users to find, access, cite and use the best available version. Please note that Cell Press, The Lancet and some society-owned have different preprint policies. Information on these policies is available on the journal homepage.

Accepted Author Manuscripts: An accepted author manuscript is the manuscript of an article that has been accepted for publication and which typically includes author-incorporated changes suggested during submission, peer review and editor-author communications.

Authors can share their accepted author manuscript:

- immediately

  via their non-commercial person homepage or blog

  by updating a preprint in arXiv or RePEc with the accepted manuscript

  via their research institute or institutional repository for internal institutional uses or as part of an invitation-only research collaboration workgroup

  directly by providing copies to their students or to research collaborators for their personal use

  for private scholarly sharing as part of an invitation-only work group on commercial sites with which Elsevierhas an agreement

- after the embargo period

  via non-commercial hosting platforms such as their institutional repository

  via commercial sites with which Elsevier has an agreement

In all cases accepted manuscripts should:

- link to the formal publication via its DOI
- bear a CCBYNCND license- this is easy to do

- if aggregated with other manuscripts, for example in a repository or other site, be shared in alignment with our hosting policy not be added to or enhanced in any way to appear more like, or to substitute for, the published journal article.

Published journal article (JPA): A published journal article (PJA) is the definitive final record of published research that appears or will appear in the journal and embodies all value-adding publishing activities including peer review coordination, copyediting, formatting, (if relevant) pagination and online enrichment.

Policies for sharing publishing journal articles differ for subscription and gold open access articles:

Subscription Articles: If you are an author, please share a link to your article rather than the full-text. Millions of researchers have access to the formal publications on ScienceDirect, and so links will help your users to find, access, cite, and use the best available version.

Theses and dissertations which contain embedded PJAs as part of the formal submission can be posted publicly by the awarding institution with DOI links back to the formal publications on ScienceDirect.

If you are affiliated with a library that subscribes to ScienceDirect you have additional private sharing rights for others' research accessed under that agreement. This includes use for classroom teaching and internal training at the institution (including use in course packs and courseware programs), and inclusion of the article for grant funding purposes.

Gold Open Access Articles: May be shared according to the author-selected end-user license and should contain a **CrossMark logo**, the end user license, and a DOI link to the formal publication on ScienceDirect.

Please refer to Elsevier's posting policy for further information.

18. For book authors the following clauses are applicable in addition to the above: Authors are permitted to place a brief summary of their work online only. You are not allowed to download and post the published electronic version of your chapter, nor may you scan the printed edition to

create an electronic version. Posting to a repository: Authors are permitted to post a summary of their chapter only in their institution's repository.

19. Thesis/Dissertation: If your license is for use in a thesis/dissertation your thesis may be submitted to your institution in either print or electronic form. Should your thesis be published commercially, please reapply for permission. These requirements include permission for the Library and Archives of Canada to supply single copies, on demand, of the complete thesis and include permission for Proquest/UMI to supply single copies, on demand, of the complete thesis. Should your thesis be published commercially, please reapply for permission. Theses and dissertations which contain embedded PJAs as part of the formal submission can be posted publicly by the awarding institution with DOI links back to the formal publications on ScienceDirect.

Elsevier Open Access Terms and Conditions

You can publish open access with Elsevier in hundreds of open access journals or in nearly 2000 established subscription journals that support open access publishing. Permitted third party reuse of these open access articles is defined by the author's choice of Creative Commons user license. See our open access license policy for more information.

Terms & Conditions applicable to all Open Access articles published with Elsevier:

Any reuse of the article must not represent the author as endorsing the adaptation of the article nor should the article be modified in such a way as to damage the author's honour or reputation. If any changes have been made, such changes must be clearly indicated.

The author(s) must be appropriately credited and we ask that you include the end user license and a DOI link to the formal publication on ScienceDirect.

If any part of the material to be used (for example, figures) has appeared in our publication with credit or acknowledgement to another source it is the responsibility of the user to ensure their reuse complies with the terms and conditions determined by the rights holder.

Additional Terms & Conditions applicable to each Creative Commons user license:

Posting or linking by commercial companies for use by customers of those companies.

20. Other Conditions:

v1.8

Questions? customercare@copyright.com or +18552393415 (toll free in the US) or +19786462777.

Copyright Permission of Manuscript #4:

ELSEVIER LICENSE

TERMS AND CONDITIONS

Apr 18, 2017

This Agreement between Xu Wang ("You") and Elsevier ("Elsevier") consists of your license details and the terms and conditions provided by Elsevier and Copyright Clearance Center.

License Number	4092001204315
License date	Apr 18, 2017
Licensed Content Publisher	Elsevier
Licensed Content Publication	Thin Solid Films
Licensed Content Title	Optimizing cathodic electrodeposition parameters of ceria coating to enhance the oxidation resistance of a Cr_2O_3 forming alloy
Licensed Content Author	Xu Wang, Fan Fan, Jerzy A. Szpunar
Licensed Content Date	29 July 2016
Licensed Content Volume Number	611
Licensed Content Issue Number	n/a
Licensed Content Pages	9
Start Page	12
End Page	20
Type of Use	reuse in a thesis/dissertation
Intended publisher of new work	other
Portion	full article
Format	both print and electronic
Are you the author of this Elsevier article?	Yes
Will you be translating?	No
Order reference number	

Title of your thesis/dissertation	ENHANCING OXIDATION RESISTANCE OF Ni-BASED SUPERALLOYS FOR HIGH TEMPERATURE APPLICATIONS
Expected completion date	Apr 2017
Estimated size (number of pages)	200
Elsevier VAT number	GB 494 6272 12
Requestor Location	Xu Wang 57 Campus Drive Saskatoon, SK S7N5A9 Canada
Attn:	Xu Wang
Total	0.00 USD

Terms and Conditions

INTRODUCTION

1. The publisher for this copyrighted material is Elsevier. By clicking "accept" in connection with completing this licensing transaction, you agree that the following terms and conditions apply to this transaction (along with the Billing and Payment terms and conditions established by Copyright Clearance Center, Inc. ("CCC"), at the time that you opened your Rightslink account and that are available at any time at http://myaccount.copyright.com).

GENERAL TERMS

2. Elsevier hereby grants you permission to reproduce the aforementioned material subject to the terms and conditions indicated.

3. Acknowledgement: If any part of the material to be used (for example, figures) has appeared in our publication with credit or acknowledgement to another source, permission must also be sought from that source. If such permission is not obtained then that material may not be included in your publication/copies. Suitable acknowledgement to the source must be made, either as a footnote or in a reference list at the end of your publication, as follows:

"Reprinted from Publication title, Vol /edition number, Author(s), Title of article / title of chapter, Pages No., Copyright (Year), with permission from Elsevier [OR APPLICABLE SOCIETY

COPYRIGHT OWNER]." Also Lancet special credit "Reprinted from The Lancet, Vol. number, Author(s), Title of article, Pages No., Copyright (Year), with permission from Elsevier."

4. Reproduction of this material is confined to the purpose and/or media for which permission is hereby given.

5. Altering/Modifying Material: Not Permitted. However figures and illustrations may be altered/adapted minimally to serve your work. Any other abbreviations, additions, deletions and/or any other alterations shall be made only with prior written authorization of Elsevier Ltd. (Please contact Elsevier at permissions@elsevier.com)

6. If the permission fee for the requested use of our material is waived in this instance, please be advised that your future requests for Elsevier materials may attract a fee.

7. Reservation of Rights: Publisher reserves all rights not specifically granted in the combination of (i) the license details provided by you and accepted in the course of this licensing transaction, (ii) these terms and conditions and (iii) CCC's Billing and Payment terms and conditions.

8. License Contingent Upon Payment: While you may exercise the rights licensed immediately upon issuance of the license at the end of the licensing process for the transaction, provided that you have disclosed complete and accurate details of your proposed use, no license is finally effective unless and until full payment is received from you (either by publisher or by CCC) as provided in CCC's Billing and Payment terms and conditions. If full payment is not received on a timely basis, then any license preliminarily granted shall be deemed automatically revoked and shall be void as if never granted. Further, in the event that you breach any of these terms and conditions or any of CCC's Billing and Payment terms and conditions, the license is automatically revoked and shall be void as if never granted. Use of materials as described in a revoked license, as well as any use of the materials beyond the scope of an unrevoked license, may constitute copyright infringement and publisher reserves the right to take any and all action to protect its copyright in the materials.

9. Warranties: Publisher makes no representations or warranties with respect to the licensed material.

10. Indemnity: You hereby indemnify and agree to hold harmless publisher and CCC, and their respective officers, directors, employees and agents, from and against any and all claims arising out of your use of the licensed material other than as specifically authorized pursuant to this license.

11. No Transfer of License: This license is personal to you and may not be sublicensed, assigned, or transferred by you to any other person without publisher's written permission.

12. No Amendment Except in Writing: This license may not be amended except in a writing signed by both parties (or, in the case of publisher, by CCC on publisher's behalf).

13. Objection to Contrary Terms: Publisher hereby objects to any terms contained in any purchase order, acknowledgment, check endorsement or other writing prepared by you, which terms are inconsistent with these terms and conditions or CCC's Billing and Payment terms and conditions. These terms and conditions, together with CCC's

Billing and Payment terms and conditions (which are incorporated herein), comprise the entire agreement between you and publisher (and CCC) concerning this licensing transaction. In the event of any conflict between your obligations established by these terms and conditions and those established by CCC's Billing and Payment terms and conditions, these terms and conditions shall control.

14. Revocation: Elsevier or Copyright Clearance Center may deny the permissions described in this License at their sole discretion, for any reason or no reason, with a full refund payable to you. Notice of such denial will be made using the contact information provided by you. Failure to receive such notice will not alter or invalidate the denial. In no event will Elsevier or Copyright Clearance Center be responsible or liable for any costs, expenses or damage incurred by you as a result of a denial of your permission request, other than a refund of the amount(s) paid by you to Elsevier and/or Copyright Clearance Center for denied permissions.

LIMITED LICENSE

The following terms and conditions apply only to specific license types:

15. Translation: This permission is granted for nonexclusive world English rights only unless your license was granted for translation rights. If you licensed translation rights you may only translate this content into the languages you requested. A professional translator must perform all translations and reproduce the content word for word preserving the integrity of the article.

16. Posting licensed content on any Website: The following terms and conditions apply as follows: Licensing material from an Elsevier journal: All content posted to the web site must maintain the copyright information line on the bottom of each image; A hypertext must be included to the Homepage of the journal from which you are licensing at http://www.sciencedirect.com/science/journal/xxxxx or the Elsevier homepage for books at http://www.elsevier.com;

Central Storage: This license does not include permission for a scanned version of the material to be stored in a central repository such as that provided by Heron/XanEdu.

Licensing material from an Elsevier book: A hypertext link must be included to the Elsevier homepage at http://www.elsevier.com . All content posted to the web site must maintain the copyright information line on the bottom of each image.

Posting licensed content on Electronic reserve: In addition to the above the following clauses are applicable: The web site must be password protected and made available only to bona fide students registered on a relevant course.

This permission is granted for 1 year only. You may obtain a new license for future website posting.

17. For journal authors: the following clauses are applicable in addition to the above:

Preprints:

A preprint is an author's own write-up of research results and analysis, it has not been peer-reviewed, nor has it had any other value added to it by a publisher (such as formatting, copyright, technical enhancement etc.).

Authors can share their preprints anywhere at any time. Preprints should not be added to or enhanced in any way in order to appear more like, or to substitute for, the final versions of

articles however authors can update their preprints on arXiv or RePEc with their Accepted Author Manuscript (see below).

If accepted for publication, we encourage authors to link from the preprint to their formal publication via its DOI. Millions of researchers have access to the formal publications on ScienceDirect, and so links will help users to find, access, cite and use the best available version. Please note that Cell Press, The Lancet and some society-owned have different preprint policies. Information on these policies is available on the journal homepage.

Accepted Author Manuscripts: An accepted author manuscript is the manuscript of an article that has been accepted for publication and which typically includes author-incorporated changes suggested during submission, peer review and editor-author communications.

Authors can share their accepted author manuscript:

- immediately

  via their non-commercial person homepage or blog

  by updating a preprint in arXiv or RePEc with the accepted manuscript

  via their research institute or institutional repository for internal institutional uses or as part of an invitation-only research collaboration workgroup

  directly by providing copies to their students or to research collaborators for their personal use

  for private scholarly sharing as part of an invitation-only work group on commercial sites with which Elsevierhas an agreement

- after the embargo period

  via non-commercial hosting platforms such as their institutional repository

  via commercial sites with which Elsevier has an agreement

In all cases accepted manuscripts should:

- link to the formal publication via its DOI

- bear a CCBYNCND license- this is easy to do
- if aggregated with other manuscripts, for example in a repository or other site, be shared in alignment with our hosting policy not be added to or enhanced in any way to appear more like, or to substitute for, the published journal article.

Published journal article (JPA): A published journal article (PJA) is the definitive final record of published research that appears or will appear in the journal and embodies all value-adding publishing activities including peer review coordination, copyediting, formatting, (if relevant) pagination and online enrichment.

Policies for sharing publishing journal articles differ for subscription and gold open access articles:

Subscription Articles: If you are an author, please share a link to your article rather than the full-text. Millions of researchers have access to the formal publications on ScienceDirect, and so links will help your users to find, access, cite, and use the best available version.

Theses and dissertations which contain embedded PJAs as part of the formal submission can be posted publicly by the awarding institution with DOI links back to the formal publications on ScienceDirect.

If you are affiliated with a library that subscribes to ScienceDirect you have additional private sharing rights for others' research accessed under that agreement. This includes use for classroom teaching and internal training at the institution (including use in course packs and courseware programs), and inclusion of the article for grant funding purposes.

Gold Open Access Articles: May be shared according to the author-selected end-user license and should contain a **CrossMark logo**, the end user license, and a DOI link to the formal publication on ScienceDirect.

Please refer to Elsevier's posting policy for further information.

18. For book authors the following clauses are applicable in addition to the above: Authors are permitted to place a brief summary of their work online only. You are not allowed to download and post the published electronic version of your chapter, nor may you scan the printed edition to

create an electronic version. Posting to a repository: Authors are permitted to post a summary of their chapter only in their institution's repository.

19. Thesis/Dissertation: If your license is for use in a thesis/dissertation your thesis may be submitted to your institution in either print or electronic form. Should your thesis be published commercially, please reapply for permission. These requirements include permission for the Library and Archives of Canada to supply single copies, on demand, of the complete thesis and include permission for Proquest/UMI to supply single copies, on demand, of the complete thesis. Should your thesis be published commercially, please reapply for permission. Theses and dissertations which contain embedded PJAs as part of the formal submission can be posted publicly by the awarding institution with DOI links back to the formal publications on ScienceDirect.

Elsevier Open Access Terms and Conditions

You can publish open access with Elsevier in hundreds of open access journals or in nearly 2000 established subscription journals that support open access publishing. Permitted third party reuse of these open access articles is defined by the author's choice of Creative Commons user license. See our open access license policy for more information.

Terms & Conditions applicable to all Open Access articles published with Elsevier:

Any reuse of the article must not represent the author as endorsing the adaptation of the article nor should the article be modified in such a way as to damage the author's honour or reputation. If any changes have been made, such changes must be clearly indicated.

The author(s) must be appropriately credited and we ask that you include the end user license and a DOI link to the formal publication on ScienceDirect.

If any part of the material to be used (for example, figures) has appeared in our publication with credit or acknowledgement to another source it is the responsibility of the user to ensure their reuse complies with the terms and conditions determined by the rights holder.

Additional Terms & Conditions applicable to each Creative Commons user license:

Posting or linking by commercial companies for use by customers of those companies.

20. Other Conditions:

v1.8

Questions? customercare@copyright.com or +18552393415 (toll free in the US) or +19786462777.

Copyright Permission of Manuscript #5:

ELSEVIER LICENSE

TERMS AND CONDITIONS

Apr 18, 2017

This Agreement between Xu Wang ("You") and Elsevier ("Elsevier") consists of your license details and the terms and conditions provided by Elsevier and Copyright Clearance Center.

License Number	4092010328102
License date	Apr 18, 2017
Licensed Content Publisher	Springer
Licensed Content Publication	Oxidation of Metals
Licensed Content Title	Effect of CeO_2 coating on the isothermal oxidation behaviour of Ni-based alloy 230
Licensed Content Author	Xu Wang, Jerzy A. Szpunar
Licensed Content Date	Jan 1, 2017
Type of Use	Thesis/Dissertation
Portion	full article
Number of copies	1
Author of this Springer article	Yes and you are a contributor of the new work
Order reference number	
Format	both print and electronic
Title of your thesis/dissertation	ENHANCING OXIDATION RESISTANCE OF Ni-BASED SUPERALLOYS FOR HIGH TEMPERATURE APPLICATIONS
Expected completion date	Apr 2017
Estimated size (number of pages)	200
Requestor Location	Xu Wang 57 Campus Drive Saskatoon, SK S7N5A9 Canada
Attn:	Xu Wang
Billing Type	Invoice

Billing Address	Xu Wang 57 Campus Drive Saskatoon, SK S7N5A9 Canada
Total	0.00 USD

Terms and Conditions

Introduction

The publisher for this copyrighted material is Springer. By clicking "accept" in connection with completing this licensing transaction, you agree that the following terms and conditions apply to this transaction (along with the Billing and Payment terms and conditions established by Copyright Clearance Center, Inc. ("CCC"), at the time that you opened your Rightslink account and that are available at any time at http://myaccount.copyright.com).

Limited License

With reference to your request to reuse material on which Springer controls the copyright, permission is granted for the use indicated in your enquiry under the following conditions:

- Licenses are for onetime use only with a maximum distribution equal to the number stated in your request.

- Springer material represents original material which does not carry references to other sources. If the material in question appears with a credit to another source, this permission is not valid and authorization has to be obtained from the original copyright holder.

- Thispermission

  • is nonexclusive

  • is only valid if no personal rights, trademarks, or competitive products are infringed.

  • explicitly excludes the right for derivatives.

- Springer does not supply original artwork or content.

- According to the format which you have selected, the following conditions apply accordingly:

• **Print and Electronic:** This License include use in electronic form provided it is password protected, on intranet, or CDRom/DVD or Ebook/Ejournal. It may not be republished in electronic open access.

• **Print:** This License excludes use in electronic form.

• **Electronic:** This License only pertains to use in electronic form provided it is password protected, on intranet, or CDRom/DVD or Ebook/Ejournal. It may not be republished in electronic open access.

For any electronic use not mentioned, please contact Springer at permissions.springer@spiglobal.com.

- Although Springer controls the copyright to the material and is entitled to negotiate on rights, this license is only valid subject to courtesy information to the author (address is given in the article/chapter).

- If you are an STM Signatory or your work will be published by an STM Signatory and you are requesting to reuse figures/tables/illustrations or single text extracts, permission is granted according to STM Permissions Guidelines: http://www.stmassoc.org/permissionsguidelines/

For any electronic use not mentioned in the Guidelines, please contact Springer at

permissions.springer@spiglobal.com. If you request to reuse more content than stipulated in the STM Permissions Guidelines, you will be charged a permission fee for the excess content.

Permission is valid upon payment of the fee as indicated in the licensing process. If permission is granted free of charge on this occasion, that does not prejudice any rights we might have to charge for reproduction of our copyrighted material in the future.

- If your request is for reuse in a Thesis, permission is granted free of charge under the following conditions:

This license is valid for onetime use only for the purpose of defending your thesis and with a maximum of 100 extra copies in paper. If the thesis is going to be published, permission needs to be reobtained.

- includes use in an electronic form, provided it is an author-created version of the thesis on his/her own website and his/her university's repository, including UMI (according to the definition on the Sherpa website: http://www.sherpa.ac.uk/romeo/);

- is subject to courtesy information to the coauthor or corresponding author.

Geographic Rights: Scope

Licenses may be exercised anywhere in the world.

Altering/Modifying Material: Not Permitted

Figures, tables, and illustrations may be altered minimally to serve your work. You may not alter or modify text in any manner. Abbreviations, additions, deletions and/or any other alterations shall be made only with prior written authorization of the author(s).

Reservation of Rights

Springer reserves all rights not specifically granted in the combination of (i) the license

details provided by you and accepted in the course of this licensing transaction and (ii) these terms and conditions and (iii) CCC's Billing and Payment terms and conditions.

License Contingent on Payment

You hereby indemnify and agree to hold harmless Springer and CCC, and their respective officers, directors, employees and agents, from and against any and all claims arising out of your use of the licensed material other than as specifically authorized pursuant to this license.

No Transfer of License

This license is personal to you and may not be sublicensed, assigned, or transferred by you without Springer's written permission.

No Amendment Except in Writing

This license may not be amended except in a writing signed by both parties (or, in the case of Springer, by CCC on Springer's behalf).

Objection to Contrary Terms

Springer hereby objects to any terms contained in any purchase order, acknowledgment, check endorsement or other writing prepared by you, which terms are inconsistent with these terms and conditions or CCC's Billing and Payment terms and conditions. These terms and conditions, together with CCC's Billing and Payment terms and conditions (which are incorporated herein), comprise the entire agreement between you and Springer (and CCC) concerning this licensing transaction. In the event of any conflict between your obligations established by these terms and conditions and those established by CCC's Billing and Payment terms and conditions, these terms and conditions shall control.

Jurisdiction

All disputes that may arise in connection with this present License, or the breach thereof, shall be settled exclusively by arbitration, to be held in the Federal Republic of Germany, in accordance with German law.

Other conditions:

V 12AUG2015

Questions? customercare@copyright.com or +18552393415 (toll free in the US) or +19786462777.